THE UNIVERSITY OF CHICAGO

PARTICLES TAKING SELFIES: INVESTIGATIONS INTO LIGHT DARK MATTER USING SILICON CHARGE COUPLED DEVICES

A DISSERTATION SUBMITTED TO
THE FACULTY OF THE DIVISION OF THE PHYSICAL SCIENCES
IN CANDIDACY FOR THE DEGREE OF
DOCTOR OF PHILOSOPHY

DEPARTMENT OF PHYSICS

BY
KARTHIK RAMANATHAN

CHICAGO, ILLINOIS
DECEMBER 2020

TABLE OF CONTENTS

LIST OF FIGURES

LIST OF TABLES

ACKNOWLEDGMENTS

An undertaking of this scope would be nigh on impossible without the support of very many people. First and foremost, many thanks to my supervisor Paolo Privitera for his mentorship and guidance. Paolo exemplifies what it means to be a great advisor and his patience, good humor, and insightful advice will be sorely missed. Next, a big thank you to Alvaro Chavarria for his scientific guidance, and Juan Collar for his unwavering support of my graduate career and his presence on my committee. Many thanks too to the other committee members William Irvine and Carlos Wagner.

I am also grateful to every current and former member of DAMIC at UChicago including Ryan Thomas, Ariel Matalon, Radomir Smida, Dan Baxter, Danielle Norcini, Grayson Rich, Julian Cuevas, Sugata Paul, and Carly KleinStern for being excellent and supportive colleagues. I would further like to highlight the strong support of Javier Tiffenberg, Pitam Mitra, Alex Piers, Bjorn Scholz, Juan Estrada, Noah Kurinsky, Todd Hossbach, Ian Lawson, Alan Robinson and Ian Wisher in helping me at various key moments during my graduate career. Many thanks also to my French collaborators Antoine Letessier-Selvon, Mariangela Settimo, João da Rocha, and Romain Gaior among others. Similarly, many thanks to João R. Torres de Mello Neto., Diego T. Machado and Clara Watanabe for hosting me in Brazil.

To my office mates, work colleagues, and other physics friends: Evan S., John F., Aaron O., Lipi G., Joel F., Alex K., Mark S., and Mark L., thanks for all the good memories and even better tacos. To everyone in the class of 2015, thanks for the wonderful FTY memories and many laughs over the years. I also really appreciate the help of Amy Schulz, Putri Kusmo, Valeri Galtsev, Mark Zaskowski, and David Reid in navigating both the bureaucratic and technical complexities of graduate school.

I am indebted to James Davis at the University of Toronto, Jean-Pierre Zigrand from the London School of Economics, and Andrew Mann from Viognier Capital who all felt confident enough in my abilities to support what felt at the time like a quixotic attempt at applying to graduate school. To my London and Toronto friends, thank you for the great times and for always being there for me.

To Vidya, who came into my life halfway through the PhD. but who has made the last

few years a blessing, thanks for being by my side.

All of my achievements rest on the love and support of my family. Many thanks to my sisters Usha and Seetha — not to mention my nieces Shreya and Annikka, and nephew Rohan — for their unending support. My parents Meenal and Ramanathan have been there with me every step of the way, and their sacrifices in supporting our family will never be forgotten — this thesis is dedicated to them.

ABSTRACT

Recent null results in searches for WIMP (Weakly Interacting Massive Particle) dark matter (DM) from both accelerator and nuclear recoil direct detection experiments have increased the particle physics community's interest in exploring other areas of DM parameter space. In particular, experiments have started looking for lighter mass candidates such as hidden photons or light dark matter recoiling off electrons. Common to these alternatives, however, is that the energy deposited in a detector will often be of $\mathcal{O}$(eV), requiring experiments with low thresholds and high sensitivity.

An experiment uniquely tuned to searching for low energy events is DAMIC (Dark Matter in CCDs) which uses scientific grade silicon charge-coupled devices (CCDs) to detect ionization signals from external radiation. These pixelated devices provide unprecedented spatial resolution on the order of 15 μm, effectively taking pictures of interactions allowing for discrimination between different particle types. Additionally, their excellent read noise on the order of 2 e^-makes for a very low energy reconstruction threshold of 50 eV_{ee}[1]. Two consecutive iterations of the DAMIC experiment have been deployed at SNOLAB — an underground Canadian laboratory — since 2012 and have provided stringent limits on WIMP dark matter cross-sections for masses less than 10 GeV c^{-2}.

However, probing for light dark matter with even smaller energy deposits with the current DAMIC experiment requires a) a good understanding of the backgrounds that might be present at this level, b) an empirically validated model of the microphysics of ionization response at these energies and c) some way that can be used to extend the reach of the experiment below threshold. This work explores and provides answers for these three challenges.

The first major contribution in this thesis is in accurately measuring the background from small-angle scattering of environmental γ-rays, considered a dominant background for solid state detectors. By exposing a CCD setup at the University of Chicago to ^{57}Co and ^{241}Am radioactive sources, we measured the electron recoil background between 60 eV and 4 keV.

1. eV_{ee} is the *electron equivalent* energy which is measured through the ionization channel vs. the total energy that may have been deposited for example in a nuclear recoil event.

The observed spectra were found to agree with theoretical predictions, but more interestingly we report for the first time a measurement of "Compton Steps", a series of step like spectral features associated with the atomic structure of the silicon target. We further provide a parametrization of this Compton background applicable to background estimations for any silicon based dark matter detection experiment.

Secondly, in order to reconstruct the energy of any event in a silicon ionization detector, we need an accurate charge yield model that converts between the energy deposited and the number of charge carriers ionized. We reviewed existing literature measurements of charge yield in silicon and identified a calibration gap between 12-50 eV, referred to as the UV-gap. We synthesized a phenomenological model of impact ionization with a simplified model of silicon band structure to provide ionization probability curves p_n, arguing that these are more appropriate than the single number calibration constant and Fano factor traditionally used to describe ionization in detector target materials.

Thirdly, we set constraints on unexplored parameter space for dark matter recoiling off e^- with masses between 0.6 and 100 MeV c^{-2} and hidden photon dark matter with masses in the range 1.2–9 eV c^{-2} by exploiting the impressively low leakage current ($< 10^{-21}$ A cm^{-2}) of DAMIC CCDs. Generically, by interpreting the dark current present in our setup as coming instead from flux of light species that deposits energy below our reconstruction threshold, we can trade off between a model of this dark matter and a model of our leakage current to resolve the relative contributions of both. This method is shown to be competitive with traditional dark matter limit setting approaches.

Finally, this work introduces and reports on R&D progress at UChicago in using "Skipper" instrumented CCDs — a novel readout technique that allows for counting of individual charge pairs, with a demonstrated resolution of 0.07 e^-, which ushers in a new era of sensitivity to low-energy interactions. We delve into the ongoing challenges in using these devices for scientific applications, particularly in reducing their leakage current, and briefly touch on their deployment for the next generation DAMIC-M experiment currently funded for operation.

CHAPTER 1
INTRODUCTION TO DARK MATTER AND ITS DIRECT DETECTION

1.1 What is Dark Matter?

The term "Dark Matter" (DM) often conjures up visions of a nebulous, sinister entity permeating our universe. And while there is a kernel of truth to that mental image, the phrase is nothing more than a parameterization of our ignorance — we know there is something out there that behaves like "matter", felt through its gravitational tug on normal matter, but that is "dark" to both our senses and to most extensions of our senses.

This missing gravity problem is observed only at large scales ($\sim$ galactic distances), and its anomalous effect was first rigorously picked up by Fritz Zwicky in his 1933 study of extragalactic nebulae [1]. Using the virial theorem to relate the potential and kinetic energies of a cluster of galaxies, along with mass estimates based on luminosity, he was able to posit the existence of unexplained mass and thus coined the term 'dunkle Materie' [Dark Matter]. Further work, exploiting this concept of mass-to-light ratios, continued to show deviations between expected and observed motion for both galaxy clusters and specific galaxies [2, 3]. This state of affairs, with observation and theory disagreement, persisted benignly for roughly 3 decades due to broad unknowns in the behaviour of galaxy clusters, questions over the assumptions underpinning mass-to-light ratios, and beliefs about large observational systematics.

However, beginning in 1978, Vera Rubin and co-authors demonstrated large deviations in the expected rotation profile of many galaxies [4]. These galactic rotation curves outlined the velocity of stars as a function of distance from the center of the galaxy. The data did not show an exponential drop-off, a signature of the Newtonian physics expectation, but rather clearly showed a plateauing of velocities (Fig. 1.1 Left), implying that the velocity of stars at the edges was much too high to be gravitationally bound if the sole source of gravity was the visible matter contained within the galaxy. An example curve from *NGC 6503* taken from Ref. [5], with visible matter constituents marked, is shown in Figure 1.1 right.

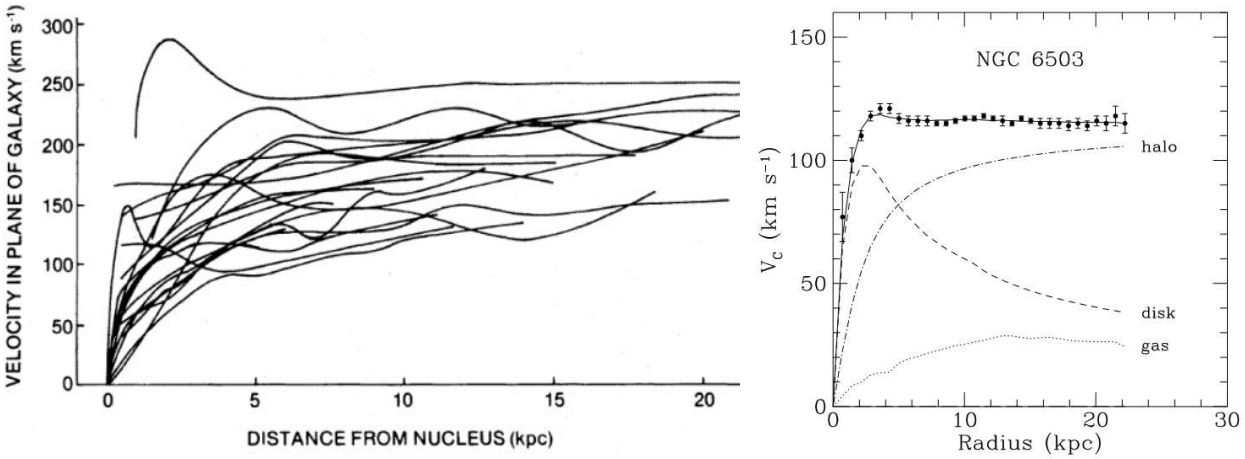

Figure 1.1: Left: Compendium of rotation curves extracted from [4]. Right: Galactic rotation curve of NGC 6503, showing the velocity profile of stars measured from distance to the center, taken from Begeman et al [5]. The contribution of disk and gas matter is insufficient to reconstruct the full profile without a contribution from a dark matter 'halo' component.

The intervening decades have strengthened the case for DM substantially. Review articles like Refs. [6, 7] thoroughly explore the current status of DM, so it suffices to briefly point out a few more key lines of evidence below, along with the crown jewel of modern cosmology ΛCDM (Λ [Dark Energy] Cold Dark Matter).

Gravitational Lensing: This is the General Relativistic phenomenon whereby light is distorted by the presence of matter. The overlapping techniques of weak and strong lensing, looking for distortion due to diffuse or single gravitational sources, and applied to structures like the *Bullet Cluster* reveal the signature of DM [8]. The Bullet Cluster was formed in the merger of two clusters, but because DM appears to have negligible self-interaction, the lens informed mass distribution varies significantly from the x-ray derived plasma distribution (which can undergo frictional self-interaction), easily seen in the difference between mass contours and gas location in Fig. 1.2.

Cosmic Microwave Background (CMB): This is the leftover radiation "relic" due to cosmological processes in the early universe. It is effectively an initially constant temperature bath of photons, that as it time evolves, carries an imprint of the local structure of gravity when it was created. By measuring the thermal anisotropy and fitting a cosmological model,

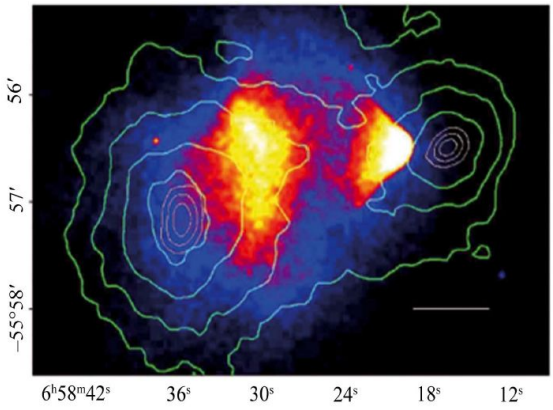

Figure 1.2: Weak lensing reconstructed mass contours (green, inner contours have more mass) and Chandra space telescope x-ray data that traces the density of hot plasma in a galaxy (colored regions: blue least dense to white most dense), showing the discrepancy between the location of the plasma and where the lensed mass is inferred to be. Taken from Ref. [8],

e.g. the 6 parameter ΛCDM, one can infer the constituents of the universe. Results from the Planck space mission are shown in Fig. 1.3 [9].

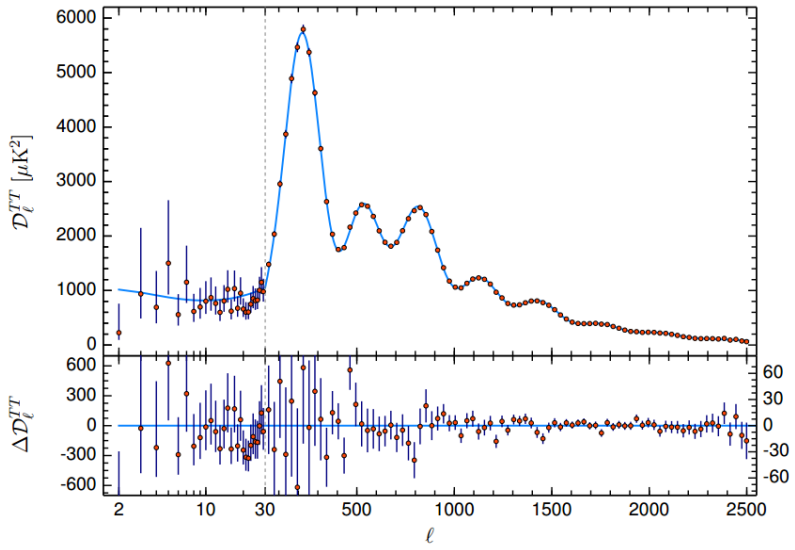

Figure 1.3: CMB temperature power spectrum from final Planck 2018 results [9] with the best fit from ΛCDM cosmological model overlaid. Residuals shown below.

The Planck data determines a total baryonic density of $\Omega_b h^2 = 0.02233 \pm 0.00015$ and a cold dark matter density of $\Omega_c h^2 = 0.1198 \pm 0.0012$, which shows that there is roughly ∼5.4

times as much DM as regular baryonic matter [9].

1.2 What it (probably) isn't

The assumption throughout this dissertation is that DM is a non-baryonic particle. One might argue that a parsimonious explanation to the missing mass anomaly might be either that our understanding of gravity is incomplete, or there is a lot of non-luminous baryonic matter.

Modifying Gravity: The dominant paradigm to modify gravity is MOND (MOdified Newtonian Dynamics), proposed by Milgrom [10]. This hypothesis modifies Newton's second law in the very small acceleration limit to be $F = m(a^2/a_0)$ for $a << a_0$ ($\mathcal{O}(10^{-10})$ ms^{-2}) and is able to match rotation curve data. In conjunction with the relativistic extension, Tensor-Vector-Scalar (TeVeS) theory proposed by Bekenstein in [11], MOND has been able to accurately describe missing mass anomalies at the galactic scale but cannot yet replicate fits to the CMB (though very recent work by Skordis and Złosnik [12] may surmount this issue) or fully explain phenomena like the Bullet Cluster [13]. Moreover recent observational work by Van Dokkum et al. [14] has shown that some galaxies seem to lack DM completely, which is hard for modified gravity to grapple with, disfavouring but not ruling out these theories at present.

Baryonic DM and Neutrinos: The standard bearers in this category are MACHOs (Massive Compact Halo Objects), primordial black holes, or neutrinos. MACHOs, interpreted as things like brown dwarf stars, accounting for the totality of the DM have been strongly ruled out by microlensing studies, observational data, and simulations [15, 16]. Primordial black holes, a subcategory of MACHOs, have experienced a renaissance as an explanation of DM [17], but have been heavily constrained by gravitational lensing studies like Ref. [18], though with some mass windows remaining open. Finally, both regular neutrinos and exotic non-interacting sterile neutrinos were once proposed as viable DM candidates, as in Ref. [19]. Regular neutrinos would however be "hot" dark matter (relativistic) and would be unable to allow observed structure formation [20], while sterile neutrinos have run into

strong astrophysical bounds [21].

1.3 The cold facts

For an experimentalist it is of prime importance to know global constraints, regardless of what specific type of DM might exist, on the DM that might interact with our detectors. Two key quantities are the local density and velocity profile, ρ_{DM} and $f(\vec{v})$, as these will directly inform the expected flux and energy of any interaction we might hope to witness.

The velocity distribution can be quite complex but under the classic assumption that one can model DM as a self-gravitating isothermal sphere of ideal gas, because the DM particles appear to move freely without much interaction, one can simplify the *velocity* distribution to be Maxwell-Boltzmann of the form:

$$f(\vec{v}) = \frac{1}{v_0^3 \pi^{3/2}} \exp\left(- \frac{|\tilde{\mathrm{v}}|^2}{\mathrm{v}_0^2} \right) \tag{1.1}$$

valid in a heliocentric frame and where v_0 is the most probable velocity:

$$v_0 = \sqrt{\frac{2k_B T}{m}} = \sqrt{\frac{2}{3}} \sigma_{\vec{v}} \tag{1.2}$$

where $\sigma_{\vec{v}}$ is the RMS speed (≈ 120 kms$^-$1 in the Milky Way) and m is the DM mass. It is interesting to note that this implies a "temperature" of the DM:

$$T \sim 10^4 \left[\frac{m}{\mathrm{GeV}} \right] \mathrm{K} \tag{1.3}$$

The addition of a galactic escape velocity v_{esc} above which the DM particle would escape, and local earth motion complicates matters slightly. Thorough accounting for all relative velocities between galactic motion, solar system motion, and Earth motion nets us, as in Refs. [22, 23] and known in the literature as the Standard Halo Model (SHM), the speed

distribution:

$$f(v) = \begin{cases} \exp(-\frac{(\mathrm{v}-\mathrm{v_E})^2}{\mathrm{v_0^2}}) - \exp(-\frac{(\mathrm{v}+\mathrm{v_E})^2}{\mathrm{v_0^2}}) & v \leq v_{esc} - v_E \\ \exp(-\frac{(\mathrm{v}-\mathrm{v_E})^2}{\mathrm{v_0^2}}) - \exp(-\frac{\mathrm{v_{esc}^2}}{\mathrm{v_0^2}}) & v_{esc} - v_E < v \leq v_esc + v_E \\ 0 \qquad v > v_{esc} + v_E \end{cases} \tag{1.4}$$

where the Earth velocity, giving rise to an annual modulation in any signal, is:

$$v_E(t) \approx v_E^0 + v_{rel}\cos\left(\frac{2\pi}{365\ \mathrm{d}}(\mathrm{t} - \mathrm{t_0})\right) \tag{1.5}$$

with $t_0 \approx 152$ d.

Strictly speaking, all these velocities and densities are inferred from observational data looking at the motion of stars within the Milky Way — an involved undertaking requiring deep astrophysical modelling of various stellar streams and processes. It suffices to say that literature values shown in Fig. 1.4 Left for ρ_{DM} and Right for $f(v)$ represent current best knowledge.

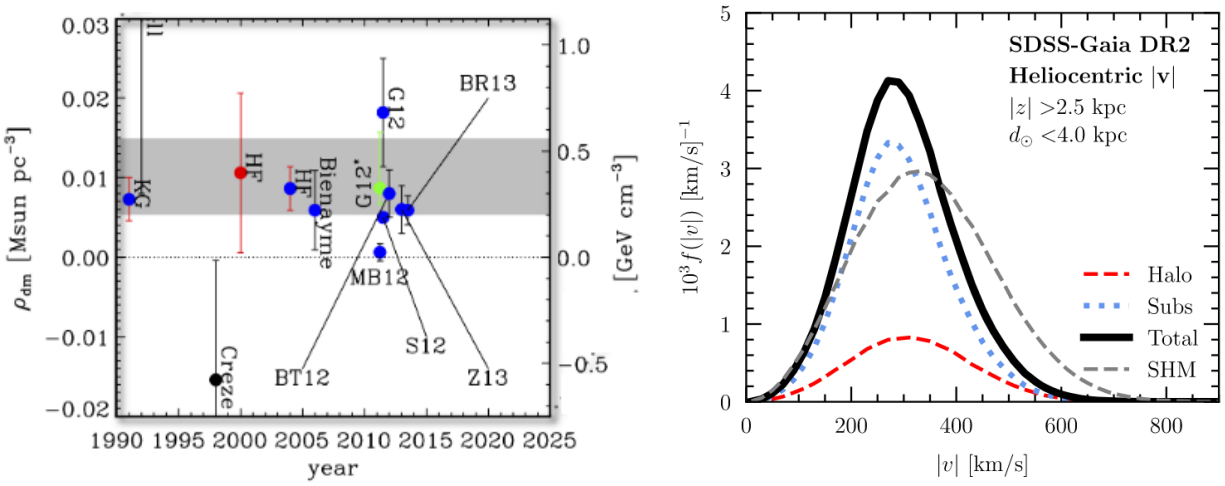

Figure 1.4: Left: Collected measurements of ρ_{DM} taken from Ref. [24] Right: Heliocentric DM velocity profile from an analysis of the European Space Agency (ESA) Gaia Satellite Data Release 2 which shows that the SHM likely overestimates DM velocities, taken from [25]

However, the experimental community has chosen to informally standardize on a set of

Parameter	Value
v_0	220 km s^{-1}
v_E^0	232 km s^{-1}
v_{esc}	544 km s^{-1}
v_{rel}	29.8 km s^{-1}
ρ_{DM}	0.3 GeV cm^{-3}

Table 1.1: Dark matter velocity and density parameters used in most direct detection analyses.

values for the Milky Way, listed in Table 1.1, that while superseded, have continued to be historically favored so as to allow comparison between experiments.

1.4 Candidates

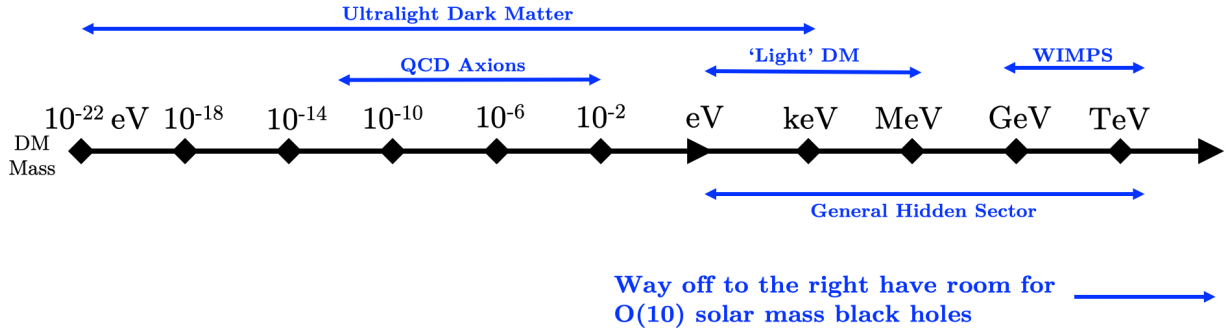

Figure 1.5: Mass ranges for potential dark matter candidates, with key families outlined in blue.

Within the constraints laid out previously, there are still over 80 orders of magnitude in mass for potential DM candidates, as shown in Fig. 1.5. The lower bound comes from requiring the wavelength of a DM particle to fit within dwarf galaxy scales of ~ 1 kpc:

$$\lambda_{DM} \sim \frac{h}{mv_0} \approx 10^{-11}\ m \cdot \left[\frac{eV}{m_{DM}}\right] \tag{1.6}$$

which works out to be roughly 10^{-22} eV. We infer that dark matter would have to be bosonic if of this mass due to phase space degeneracy restrictions. Applying this phase space

constraint, the lower bound on fermionic dark matter is approximated in Ref. [26] as being $m_{DM} \gtrapprox 25$ eV.

Within this diversity of potential DM models we can follow a useful rule-of-thumb classification laid out in Ref. [27] and identify candidates as belonging to one of four categories in decreasing orders of technical stringency as seen in Table 1.2.

Category	**Description**	**Examples**
1. Well Motivated	Solve some fundamental question in particle physics other than being the DM	WIMPs (concordance with supersymmetry), QCD Axion (solves strong CP problem)
2. "Why Not"	Technically natural and stable even if not motivated by a specific problem	Hidden Photons, Sterile-ν, Electron-Recoil DM
3. Gap Filling	Fit some observational anomaly but otherwise contrived	Superfluids, Fuzzy DM
4. Unnatural	Perhaps technically unnatural and not motivated by or fitting under any existing framework	Chameleon DM

Table 1.2: Dark matter classifications proposed by Pospelov [27] for different modelling criteria, with select examples elucidated later. For a discussion of naturalness, which is well beyond the scope of this document, see [28]

In the following sections we will discuss Weakly Interacting Massive Particles (WIMPs), Hidden Photons, and Sub-GeV DM, only briefly touching on other candidates.

1.4.1 WIMPs

While the vanilla Standard Model (SM) of particle physics has proven remarkably successful in explaining almost all terrestrial particle physics phenomena, puzzles like the Hierarchy Problem (i.e. differences in the strength of known forces) and gauge coupling unification (i.e. the hypothesized merger of the known forces at higher energies) remain. One avenue to resolve these tensions is to extend the SM by adding Supersymmetry (SUSY) which postulates a counterpart to every known SM particle (boson $\leftrightarrow$ fermion) [6]. A feature of this class of models is that they admit a stable uncharged lightest Supersymmetric particle

(LSP) —a *neutralino* [29].

On the other hand, working through the cosmological implications of the abundance measurements mentioned in Sec. 1.3, assuming some unknown particle χ in thermal equilibrium with the SM in the early universe, we can trace the evolution of this χ to present day as thoroughly outlined in Ref. [29]. After a period of annihilation, χ will "freeze-out" when the universe sufficiently cools and expands. The velocity averaged annihilation cross-section $\langle \sigma v \rangle$ is shown to be:

$$\langle \sigma v \rangle \approx 3 \cdot 10^{-26} \text{ cm}^3\text{s}^{-1} \tag{1.7}$$

The tantalizing concordance linking SUSY and cosmology, often called the "WIMP Miracle" is that the predicted cross-sections are in line with a weak-scale interaction expected for the spectrum of SUSY neutralinos. Thus DM is a natural extension of the attempt to expand on the SM and why such a candidate is considered tier 1 in reference to Table 1.2. A terminological caveat is that weak refers to the scale of the force, not that it is specifically the Weak force that mediates any interaction. WIMPs are hypothesized to be detectable in lab experiments by elastic recoil off nuclei. We will not delve further into WIMP phenomenology as this thesis is only tangentially concerned with constraining WIMP dark matter.

Rate Setting: We will discuss the interaction rate of DM in a terrestrial detector generally, canonically derived for WIMPS but basically applicable for almost any DM candidate. The event rate of any interaction on a single free target (whether it be a nucleus or an electron or a barn door), can be written purely with the help of dimensional analysis as:

$$R = n_\chi \sigma \langle v \rangle \tag{1.8}$$

where R is the event rate [s^{-1}], n is the number density of candidate particles [cm^{-3}], σ is the interaction cross section [cm^2] and $\langle v \rangle$ is the averaged velocity [cm s^{-1}] ($\equiv \int v f(v)$). Relevant for the experiment is the event rate as a function of deposited energy E in our detector:

$$\frac{dR}{dE} = \frac{\rho_\chi}{m_\chi} \frac{d\sigma}{dE} \int_{v_{min}}^{\infty} d^3v v f(v) \tag{1.9}$$

where $f(v)$ is a velocity profile of the form seen in Eq. 1.4.

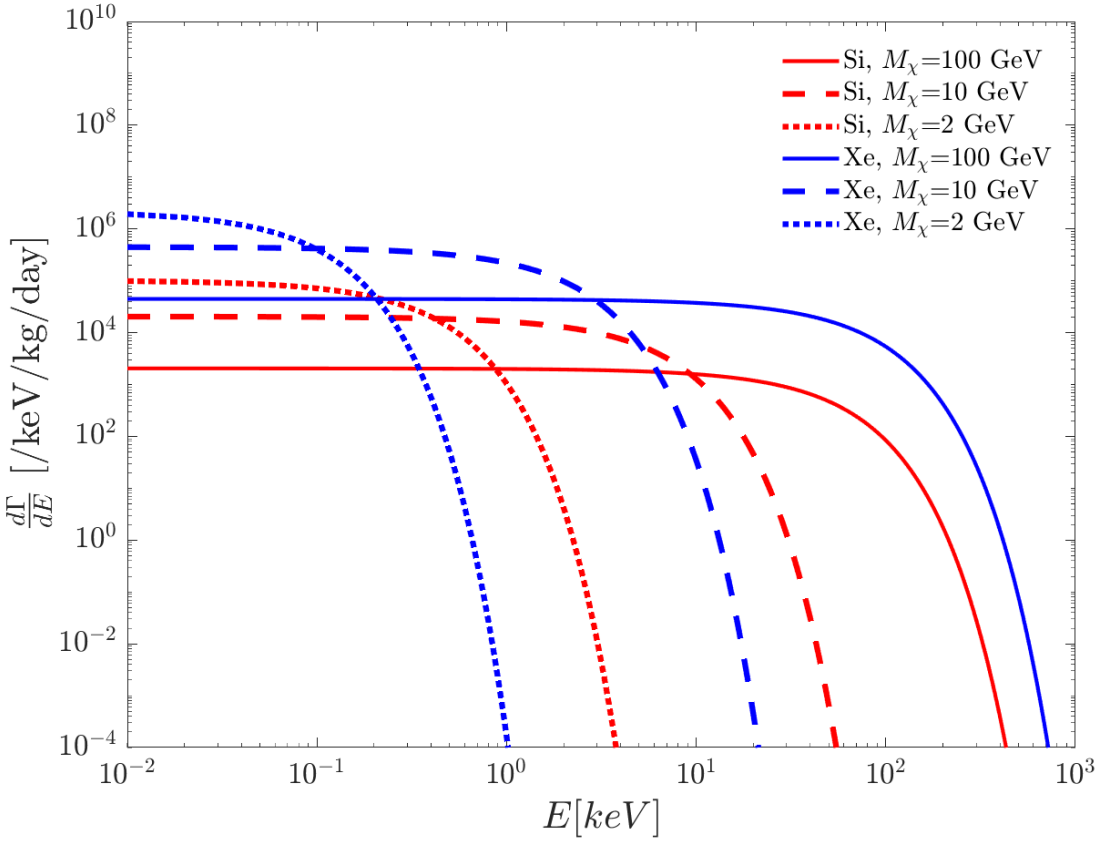

Figure 1.6: Calculated WIMP recoil spectrum, under the simplification F(q)≈ 1, with different target nuclei (Si in red, Xe in blue) for DM masses of 2 GeV (dotted), 10 GeV (dashed), 100 GeV (solid), $\sigma_{wn} = 10^{-36}$ cm^2, showing dependence of recoil rate on kinematic factors.

In the specific case of a WIMP, where we consider an elastic recoil of nuclei with mass m_n at non-relativistic velocities in a detector of mass M, one can follow the machinery of Ref. [29] and end with the detector event rate Γ:

$$\frac{d\Gamma}{dE} = M\frac{\sigma_0\rho_\chi}{2m_T^2 m_\chi}F^2(q)\int_{v_{min}}^{v_\infty} d^3v\frac{f(v)}{v} \tag{1.10}$$

where the energy dependence comes in through the astrophysical integration limits, σ has been factorized into a reference value σ_0 at an unphysical q=0 momentum transfer with the target material momentum dependence baked into the form factor F^2(q), and m_T is

the reduced mass ($\equiv \frac{m_n m_\chi}{m_n+m_\chi}$). For the case of spin-independent (meaning the WIMPs do not preferentially couple to nuclei with spins) scattering σ_0 is proportional to $A^2\sigma_{wn}$ (the WIMP-nucleon scattering cross-section), and for a given σ_{wn} we see from Fig. 1.6 that different targets masses will be most sensitive to similar DM masses.

A useful figure of merit is the maximum energy transfer in an elastic two-body collision,

$$E_{max} \approx \frac{2m_T^2(v_{esc}+v_E)}{m_T} \approx \begin{cases} 400 \text{ keV}\left(\frac{\mathrm{m_n}}{28\mathrm{GeV}}\right) & m_\chi >> m_n \\ 500 \text{ eV}\left(\frac{\mathrm{m_\chi}}{1\mathrm{GeV}}\right)^2\left(\frac{28\mathrm{GeV}}{\mathrm{m_n}}\right) & m_\chi << m_n \end{cases} \tag{1.11}$$

where we have preemptively used the mass of Silicon. This gives a sense of how important the lower energy threshold of a detector is when probing DM on the lighter end of the mass scale.

We avoid discussing here any other complexity like the nature of the nuclear form factor and spin-dependent cross-sections, and instead refer the reader to the thorough discussions found in Refs. [22, 29].

The upshot is that an experiment that can detect nuclear recoils sets constraints on σ_{wn} for a given m_χ resulting in exclusion plots like Fig. 1.7 taken from Ref. [30].

However the last 3 decades of searching for WIMPs have come up short. The parameter space as shown continues to be heavily constrained with every new experiment, while the theoretical foundations of SUSY are undercut by consistent null searches for Supersymmetry at the LHC (Large Hadron Collider) as reviewed by Ref. [31]. In addition, experiments are likely to hit the *neutrino floor* in the next decade, seen in Fig. 1.7 orange dashed line, wherein neutrinos will coherently scatter similar to WIMPs and produce an irreducible indistinguishable background. As such, community attention has begun to turn to other candidates for DM, a few of which are elucidated in the following sections.

1.4.2 Hidden Photons

Hidden Photons (HPs), also known as Dark Photons in literature, are massive Spin-1 vector bosons. They were originally conceived as "para-photons" by Okun [32], Holdom [33] but

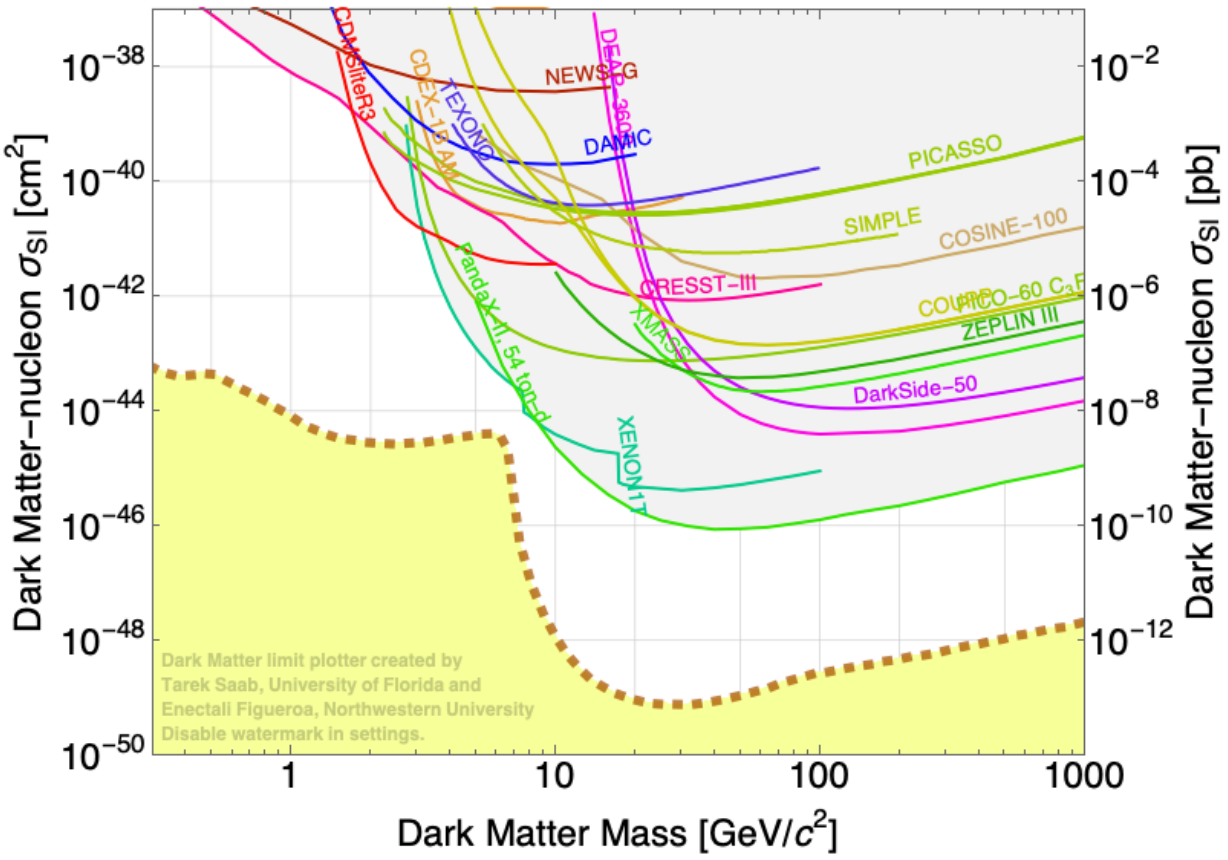

Figure 1.7: Exclusion plot showing spin-independent WIMP cross-section parameter space excluded (above a line) by a given labeled experiment, from Ref. [30]

received new life as possible Dark Matter constituents in the late 2000s [34]. These can act as a portal to a whole dark sector, but one can obtain a flavor of the physics involved by solely looking at HPs and their interaction with the SM sector. From our table in the previous section, we can see they fit under the category of "why not" physics and are considered in the literature as Warm Dark Matter in that they are relativistic with masses in the range of 10^{-7} eV-10^5 eV.

We start by following [35] and positing the existence of an extra $U(1)_D$ gauge field which is coupled to the standard model via kinetic mixing with the hypercharge field strength κ:

$$\mathcal{L} \supset -\frac{1}{4}V_{\mu\nu}^2 - \frac{\kappa}{2}V_{\mu\nu}F_{\mu\nu} - \frac{m_V^2}{2}V_\mu V^\nu - J_\mu A^\mu \tag{1.12}$$

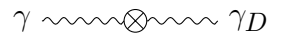

where the only other new terms are related to the existence of this new Hidden Photon: V_μ is the HP gauge field, $V_{\mu\nu} = \partial_\mu V_\nu - \partial_\nu V_\mu$ is the HP field strength tensor, and m_V is the mass of the hidden photon. Applying a transformation $A \to A - \kappa V$, we can get rid of any interactions and have mass eigenstates composed of a massless photon and a heavy photon:

$$\mathcal{L} \supset -\frac{1}{4}V_{\mu\nu}^2 - \frac{m_V^2}{2}V_\mu V^\nu - J_\mu(A^\mu - \kappa V^\mu) \tag{1.13}$$

We notice here that the electromagnetic current has picked up a small "dark charge" component: $\kappa V_\mu J^\mu_{EM}$. We can reach the flavor eigenstates, the interaction/propagation basis, by rotating with $\tilde{A} = A - \kappa V$ and $\tilde{V} = V + \kappa A$. This mixes the mass terms and we get:

$$\mathcal{L} \supset -\frac{1}{4}\tilde{V}_{\mu\nu}\tilde{V}^{\mu\nu} - \frac{m^2}{2}((\tilde{V}_\mu - \kappa\tilde{A}_\mu)(\tilde{V}^\mu - \kappa\tilde{A}^\mu) + J_\mu\tilde{A}^\mu \tag{1.14}$$

$$\overset{\Longrightarrow}{mass\ mixing} \propto \begin{pmatrix} 0 & \kappa \\ \kappa & 1 \end{pmatrix} m^2 \tag{1.15}$$

But if this 'kinetic mixing' parameter is very small, we can effectively treat the mass mixing matrix as diagonal and still think in terms of a massless photon and a massive hidden photon. We appeal to the intuitive picture of the neutrino sector and think of the HP and photon as oscillating:

This model has 2 free parameters, the mass of the HP m_V and the kinetic mixing parameter κ which are allowed to take almost any value. The mass is protected by the $\mathrm{U}(1)_D$ symmetry and the theory is technically natural with the understanding that the renormalized values are of similar size to the bare values for a cutoff $\sim \Lambda_{pl}$. It should also be noted that the vector mass term $m^2 V_\mu V^\mu$ is not manifestly gauge invariant and is introduced in the literature via a standard Higgs or Stueckelberg mechanism.

Restricting ourselves to the electron-photon sector, important processes in the context of DM detection are the coupling to photons and electrons. If the energy $E_D \geq 2m_e$ the favorable interaction is the decay $V \to e^+e^-$, while at lower energies the dominant

mechanism is $V \to 3\gamma$. We look at these in turn.

$V \to e^- e^+$**:** From the highlighted dark charge component we have the diagram shown in Fig. 1.8 Left. Rotating the diagram we can think of detecting a Hidden Photon by absorption or scattering off an electron, following the work of Ref. [36] perhaps with emission of a phonon Φ for momentum conservation purposes like in the following two diagrams:

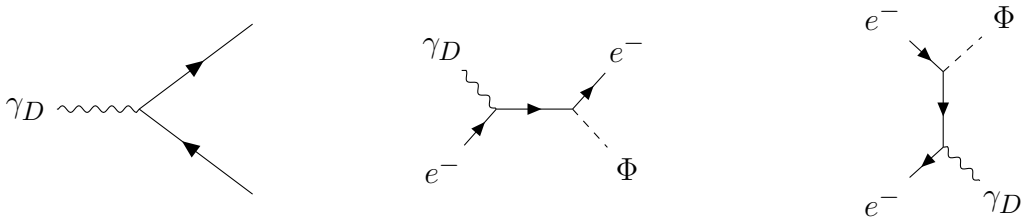

Figure 1.8: Left: Feynman diagram of $V \to e^- e^+$ decay process. Right: rotating diagram, and with addition of Φ phonon channel.

The matrix element is going to be pretty simple in that these processes behave almost exactly like a regular photon being absorbed or scattered off an electron. We can thus write:

$$\mathcal{M}|^2 = \kappa^2 |\mathcal{M}_\gamma|^2 \tag{1.16}$$

Where we can identify a suppression in the rate due to the κ^2 especially if the coupling is small. The upshot of this is that any physical process or experiment that measures a flux of photons can be exploited to measure Hidden Photons.

$V \to 3\gamma$**:** For completeness we mention the case where a HP can couple to 3 photons at the loop level (while decays to 2 photons are forbidden due to the Landau-Yang theorem [7]). This signal is useful due to the belief that DM decay and annihilation processes contribute to the excess gamma ray astrophysical background detectable by telescopes such as Fermi-LAT [37].

$V \to \gamma \to V$**:** Finally, the oscillatory nature identified previously can also be exploited. Shining a light through a wall should cause some photons to oscillate through the barrier. Thinking classically in terms of ($\vec{E}$, $\vec{B}$) fields, HPs imply that any electromagnetic field can leak through shields and perfect conductors. The source detection can be termed as in Ref. [38] wherein $(\vec{E}, \vec{B})_{\text{detected}} \sim \kappa^2 (\vec{E}, \vec{B})_{\text{source}}$. Further, production of photons in the

sun and other stars will propagate away some energy through the hidden photon channel and differences in produced and measured energy from various measurements (i.e. solar neutrinos) can be exploited to set limits on HPs [38].

Rate Setting in a detector: The effective interaction rate of these Hidden Photons in a detector (per detector mass and unit time) is:

$$\Gamma_{int} = \frac{\rho_{DM}}{m_V}\sigma_V v \tag{1.17}$$

where σ_V is the HP cross section in units of area per mass, and v is the local DM velocity. Now following An et al. [39] we can relate the HP interaction cross section to the photoelectric cross section of the medium, at a given energy E, to first order by:

$$\sigma_V(E = m_V)v_{rel} \approx \kappa^2\sigma_\gamma(E = m_V)c \tag{1.18}$$

However, this is an incomplete story without accounting for in-medium dispersion effects of our target material. Again following Refs. [36, 39], and introducing the polarization tensor $\Pi(E)$ which is related to the complex conductivity of the medium $\hat{\sigma}(E) = \sigma_1 + i\sigma_2$, which is itself related to the complex index of refraction of the medium $\hat{n}^2 = 1 + i\hat{\sigma}E$, we replace κ with an *effective* mixing parameter of:

$$\kappa^2_{eff} = \frac{\kappa^2 m_V^4}{[m_V^2 - Re(\Pi(E))]^2 + [Im(\Pi(E))]^2} \tag{1.19}$$

The net result being an effective interaction rate of:

$$\Gamma_{\text{int}} = \frac{\rho_{DM}}{m_V}\kappa^2_{eff}\sigma_\gamma(m_V)c \tag{1.20}$$

Of note in Eq. 1.20 is the lack of dependency on local DM velocity, in contrast to regular WIMPs, implying no potential annual modulation in detection. We will expand on working with the mentioned terms and setting constraints on HPs in Chapter 6.

1.4.3 Sub-GeV Dark Matter

With the aforementioned collapsing of the WIMP parameter space and move into more speculative theories, community interest has shifted towards a whole new class of models in the "light DM" range (see Fig. 1.5). Of course one immediate problem is the kinematic mismatches of light DM. We can refer to our handy rule of thumb in Eq. 1.11 and see that sub-GeV particles would only deposit $\mathcal{O}(100$ eV) against a Silicon nucleus and even if we were to scatter off electrons (among the lightest known stable and controllable particles) these sub-GeV particles would only deposit $\mathcal{O}(1$ eV) — a vanishingly small amount.

However, recent phenomenological work by Essig et. al. [40] has opened the door to look for *inelastic* DM-electron couplings for these sub-GeV mass particles. As the reference notes, the bound state electron momenta are indefinite and can be arbitrarily large with energy transfer of the $\mathcal{O}(1$ keV) scale. Hence these DM candidates become reasonably probe-able by current and future experiments due to their electronic interactions, which dominate their nuclear scattering. Unfortunately, modelling DM-e^- interactions presents challenges precisely due to the bound nature of the electrons and crystalline band structure of the target, implying one cannot treat electrons as free unlike nuclei. Thus, from Ref. [41] the differential event rate in the detector for a DM mass m_χ, with transferred energy E_e, and momentum q is parametrized as:

$$\frac{dR}{dE_e} \propto \bar{\sigma_e} \int \frac{dq}{q^2}\, \eta(m_\chi, q, E_e)|F_{DM}(q)|^2|f_c(q, E_e)|^2 \tag{1.21}$$

where $\bar{\sigma_e}$ is a reference cross section for free electron scattering, η includes properties of the incident flux of galactic DM particles, F_{DM} is the dark matter form factor, and the crystal form factor $f_c(q, E_e)$ quantifies the atomic transitions of bound-state electrons.

The dark matter form factor expresses the model dependent momentum transference in an interaction, generically as $F_{DM} = (\alpha m_e)/q^n$ $\{n = 0, 1, 2\}$. The $n = 0$ case corresponds to point like interactions with heavy mediators or a magnetic dipole coupling, the $n = 1$ case to an electric dipole coupling, and $n = 2$ for massless or ultra-light mediators. The crystal form factor encodes target material properties and is numerically derived from a DFT (density

functional theory) approach, with results taken from [41] for Silicon. We will setting limits on this type of DM in Chap. 6.

1.4.4 Axions

To round out the discussion we briefly touch on the one other well motivated category of particle DM, axions, that we however do not consider in the rest of this work. Basically, the *Strong CP* (Charge-Parity) problem is the observation that the descriptive theory of strong force, Quantum Chromodynamics (QCD), appears to respect CP symmetry, unlike the weak sector. Peccei and Quinn [42] proposed that a light pseudoscalar, the *axion* could resolve this puzzle. While immediately ruled out by particle physics experimental constraints, later phenomenological work showed that there are many plausible flavors of axions, like "DFSZ" or "KSVZ", that could also fully make up the DM in the universe [43], hence placing axions in the "well motivated" category of Table. 1.2 Ref. [44]. Even more generically, Axion Like Particles (ALPS) loosen energy-momentum dispersion relations that the axion satisfies and themselves form a class of potential DM [44].

1.5 Direct Detection

In the previous sections we have obtained a high-level picture of the phenomenology of DM candidates and where appropriate have stated how they might interact with SM particles. Now we turn our attention to exploring the wide array of existing "Direct Detection" efforts — terrestrial experiments seeking to record interactions of DM particles with SM particles. However, we first touch on other methodological approaches one can take, as laid out in Fig. 1.9. Depending on the orientation of the figure with respect to the outside arrows representing initial to final states, one can rely on "Annihilation" where DM particles create SM particles or "Production" where SM particles create DM. The former is expected to occur only where $\rho_\chi \gg \rho_{\mathrm{DM,local}}$, such as in the center of the Milky Way, resulting in e.g. γ-ray emission detectable by telescopes [37]. The latter can occur in astrophysical processes or potentially at accelerators like the LHC. Direct detection is the holy-grail however because

the other avenues are indirect "negative" inferences — production relies on inferring missing momenta in an accelerator, while annihilation is dependent on observing an excess count of SM particles than otherwise expected.

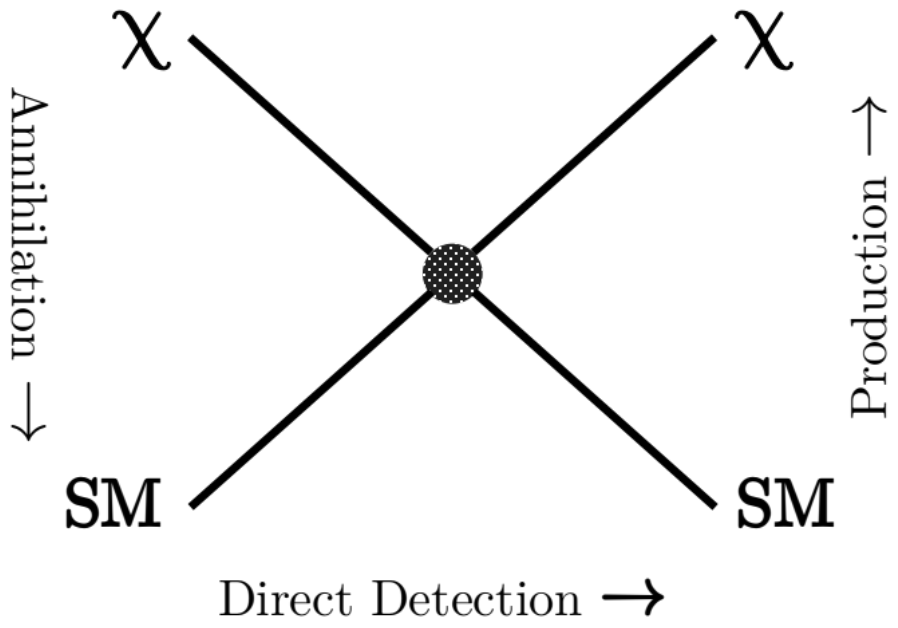

Figure 1.9: Cartoon Feynman diagram representation showing DM detection strategies, depending on labeled orientation of initial to final states.

1.5.1 Principles and key experiments

Since the coupling of DM to the SM is unknown, there are a plethora of experiment types in the event that target selection is important. However common to all of them are the issue of *backgrounds*, signals originating from physical sources that need to be distinguished from any potential DM signal. *Radiogenic* backgrounds are caused by radioactive contaminants that decay and release energy into the detector. *Cosmogenic* backgrounds are particles produced externally, e.g. in the atmosphere or in a subsequent interaction with the earth, that pass through the detector. Here we will very briefly lay out a non-exhaustive list of important detection techniques and example experiments.

Scintillation: As the name implies, any particle interaction of $\mathcal{O}$(keV) releases a

burst of photons which are then recorded, usually with photomultiplier tubes (PMTs). A classic example is the DAMA/LIBRA experiment that uses solid NaI(Tl) crystals and has continued to claim positive detection of DM since the mid 90s [45]. Another technology, Time Projection Chambers (TPCs) — based on pressure vessels usually filled with a separate layer of gaseous and liquid Xenon or Argon — are perhaps the dominant category of DM experiments at present. An interaction in the larger liquid volume produces prompt photons, while ionized electrons are accelerated through the gaseous phase to produce a secondary signal. Experiments like XenonNT are able to set world leading constraints for a variety of DM signals [46].

Ionization: Ionization refers to the process of releasing electrons from either an amorphous or crystalline material, which are then collected. The canonical materials to build ionization detectors are the crystalline semiconductors Germanium and Silicon with band gaps (a proxy for the energy required to free an electron) of $\mathcal{O}$(eV). We will thoroughly explore the process of ionization and detector response in Silicon in Chapter 4. The DAMIC experiment, the focus of this thesis, is an example of an ionization detector. Recent theoretical work has suggested a whole class of new materials with tunable band gaps in the $\mathcal{O}$(meV) range, Dirac Semi-metals [47], that promise to improve sensitivities of ionization detectors dramatically.

Phonons & Other: The excitation of collective modes in a material, with energies of $\mathcal{O}$(meV), is also another avenue to record deposited energy. One flavour of the SuperCDMS experiment [48] records phonons, lattice vibrations, to reconstruct energy deposits primarily through registering temperature changes of the detector sitting at cryogenic temperatures. One other unique technique is bubble chambers, like the PICO experiment [49]. A $\mathcal{O}$(keV) energy deposit in the superheated target fluid (e.g. C_3F_8) induces local nucleation and creation of a bubble. Acoustic and visual properties of the bubbles can be used to extract information about the initial deposit. This technique is particularly interesting because of its ability to probe spin-dependent interactions along with having very low to no electron-recoil backgrounds [49].

References

[1] Fritz Zwicky. Die rotverschiebung von extragalaktischen nebeln. *Helvetica physica acta*, 6:110–127, 1933.

[2] Sinclair Smith. The mass of the virgo cluster. *The Astrophysical Journal*, 83:23, 1936.

[3] Horace W Babcock. The rotation of the andromeda nebula. *Lick Observatory Bulletin*, 19:41–51, 1939.

[4] Vera C Rubin, W Kent Ford Jr, and Norbert Thonnard. Rotational properties of 21 sc galaxies with a large range of luminosities and radii, from ngc 4605/r= 4kpc/to ugc 2885/r= 122 kpc. *The Astrophysical Journal*, 238:471–487, 1980.

[5] KG Begeman, AH Broeils, and RH Sanders. Extended rotation curves of spiral galaxies: Dark haloes and modified dynamics. *Monthly Notices of the Royal Astronomical Society*, 249(3):523–537, 1991.

[6] Gianfranco Bertone, Dan Hooper, and Joseph Silk. Particle dark matter: Evidence, candidates and constraints. *Physics reports*, 405(5-6):279–390, 2005.

[7] Gianfranco Bertone and Dan Hooper. History of dark matter. *Reviews of Modern Physics*, 90(4):045002, 2018.

[8] Douglas Clowe, Maruša Bradač, Anthony H Gonzalez, Maxim Markevitch, Scott W Randall, Christine Jones, and Dennis Zaritsky. A direct empirical proof of the existence of dark matter. *The Astrophysical Journal Letters*, 648(2):L109, 2006.

[9] N Aghanim, Yashar Akrami, M Ashdown, J Aumont, C Baccigalupi, M Ballardini, AJ Banday, RB Barreiro, N Bartolo, S Basak, et al. Planck 2018 results. vi. cosmological parameters. *arXiv preprint arXiv:1807.06209*, 2018.

[10] Mordehai Milgrom. A modification of the newtonian dynamics as a possible alternative to the hidden mass hypothesis. *The Astrophysical Journal*, 270:365–370, 1983.

[11] Jacob D Bekenstein. Relativistic gravitation theory for the modified newtonian dynamics paradigm. *Physical Review D*, 70(8):083509, 2004.

[12] Constantinos Skordis and Tom Złosnik. A new relativistic theory for modified newtonian dynamics. *arXiv preprint arXiv:2007.00082*, 2020.

[13] Scott Dodelson. The real problem with mond. *International Journal of Modern Physics D*, 20(14):2749–2753, 2011.

[14] Pieter Van Dokkum, Shany Danieli, Yotam Cohen, Allison Merritt, Aaron J Romanowsky, Roberto Abraham, Jean Brodie, Charlie Conroy, Deborah Lokhorst, Lamiya Mowla, et al. A galaxy lacking dark matter. *Nature*, 555(7698):629–632, 2018.

[15] Jaiyul Yoo, Julio Chaname, and Andrew Gould. The end of the macho era: limits on

halo dark matter from stellar halo wide binaries. *The Astrophysical Journal*, 601(1): 311, 2004.

[16] Timothy D Brandt. Constraints on macho dark matter from compact stellar systems in ultra-faint dwarf galaxies. *The Astrophysical Journal Letters*, 824(2):L31, 2016.

[17] Bernard Carr, Florian Kühnel, and Marit Sandstad. Primordial black holes as dark matter. *Physical Review D*, 94(8):083504, 2016.

[18] Hiroko Niikura, Masahiro Takada, Naoki Yasuda, Robert H Lupton, Takahiro Sumi, Surhud More, Toshiki Kurita, Sunao Sugiyama, Anupreeta More, Masamune Oguri, et al. Microlensing constraints on primordial black holes with subaru/hsc andromeda observations. *Nature Astronomy*, 3(6):524–534, 2019.

[19] Scott Dodelson and Lawrence M Widrow. Sterile neutrinos as dark matter. *Physical Review Letters*, 72(1):17, 1994.

[20] Gianfranco Bertone and David Merritt. Dark matter dynamics and indirect detection. *Modern Physics Letters A*, 20(14):1021–1036, 2005.

[21] Kevork Abazajian and Savvas M Koushiappas. Constraints on sterile neutrino dark matter. *Physical Review D*, 74(2):023527, 2006.

[22] JD Lewin and PF Smith. Review of mathematics, numerical factors, and corrections for dark matter experiments based on elastic nuclear recoil. Technical report, SCAN-9603159, 1996.

[23] Katherine Freese, Mariangela Lisanti, and Christopher Savage. Colloquium: Annual modulation of dark matter. *Reviews of Modern Physics*, 85(4):1561, 2013.

[24] JI Read. The local dark matter density. *Journal of Physics G: Nuclear and Particle Physics*, 41(6):063101, 2014.

[25] Lina Necib, Mariangela Lisanti, and Vasily Belokurov. Inferred evidence for dark matter kinematic substructure with sdss–gaia. *The Astrophysical Journal*, 874(1):3, 2019.

[26] Edward A Baltz. Dark matter candidates. *arXiv preprint astro-ph/0412170*, 2004.

[27] M. Pospelov. Cosmological probes of light weakly coupled fields. Perimter Institute Invited Talk, 2014.

[28] Gian Francesco Giudice. Naturally speaking: the naturalness criterion and physics at the lhc. *Perspectives on LHC physics*, pages 155–178, 2008.

[29] Gerard Jungman, Marc Kamionkowski, and Kim Griest. Supersymmetric dark matter. *Physics Reports*, 267(5-6):195–373, 1996.

[30] Tarek Saab. Dark matter limit plotter v5.14. `https://supercdms.slac.stanford.edu/dark-matter-limit-plotter`. Accessed: 2020-05-23.

[31] William James Fawcett. *Supersymmetry searches at the LHC and their interpretations*. PhD thesis, University of Oxford, 2017.

[32] Lev Borisovich Okun. Limits of electrodynamics: paraphotons. Technical report, Gosudarstvennyj Komitet po Ispol'zovaniyu Atomnoj Ehnergii SSSR, 1982.

[33] Bob Holdom. Two u (1)'s and charge shifts. *Physics Letters B*, 166(2):196–198, 1986.

[34] Javier Redondo and Marieke Postma. Massive hidden photons as lukewarm dark matter. *Journal of Cosmology and Astroparticle Physics*, 2009(02):005, 2009.

[35] Ann E Nelson and Jakub Scholtz. Dark light, dark matter, and the misalignment mechanism. *Physical Review D*, 84(10):103501, 2011.

[36] Yonit Hochberg, Tongyan Lin, and Kathryn M Zurek. Absorption of light dark matter in semiconductors. *Physical Review D*, 95(2):023013, 2017.

[37] M Ackermann, M Ajello, A Albert, WB Atwood, L Baldini, J Ballet, G Barbiellini, D Bastieri, R Bellazzini, E Bissaldi, et al. The fermi galactic center gev excess and implications for dark matter. *The Astrophysical Journal*, 840(1):43, 2017.

[38] Javier Redondo and Georg Raffelt. Solar constraints on hidden photons re-visited. *Journal of Cosmology and Astroparticle Physics*, 2013(08):034, 2013.

[39] Haipeng An, Maxim Pospelov, Josef Pradler, and Adam Ritz. Direct detection constraints on dark photon dark matter. *Physics Letters B*, 747:331–338, 2015.

[40] Rouven Essig, Jeremy Mardon, and Tomer Volansky. Direct detection of sub-gev dark matter. *Phys. Rev. D*, 85:076007, Apr 2012. doi: 10.1103/PhysRevD.85.076007. URL `https://link.aps.org/doi/10.1103/PhysRevD.85.076007`.

[41] Rouven Essig, Marivi Fernndez-Serra, Jeremy Mardon, Adrin Soto, Tomer Volansky, and Tien-Tien Yu. Direct detection of sub-gev dark matter with semiconductor targets. *Journal of High Energy Physics*, 2016(5):46, 2016. doi: 10.1007/JHEP05(2016)046.

[42] Roberto D Peccei and Helen R Quinn. Cp conservation in the presence of pseudoparticles. *Physical Review Letters*, 38(25):1440, 1977.

[43] Marco Battaglieri, Alberto Belloni, Aaron Chou, Priscilla Cushman, Bertrand Echenard, Rouven Essig, Juan Estrada, Jonathan L Feng, Brenna Flaugher, Patrick J Fox, et al. Us cosmic visions: new ideas in dark matter 2017: community report. *arXiv preprint arXiv:1707.04591*, 2017.

[44] M. Tanabashi et al. Review of particle physics. *Phys. Rev. D*, 98:030001, Aug 2018. doi: 10.1103/PhysRevD.98.030001. URL `https://link.aps.org/doi/10.1103/PhysRevD.98.030001`.

[45] R Bernabei, P Belli, F Cappella, R Cerulli, CJ Dai, A dAngelo, HL He, A Incicchitti, HH Kuang, JM Ma, et al. First results from dama/libra and the combined results with

dama/nai. *The European Physical Journal C*, 56(3):333–355, 2008.

[46] XENON Collaboration, E Aprile, J Aalbers, F Agostini, M Alfonsi, L Althueser, FD Amaro, M Anthony, F Arneodo, L Baudis, et al. Dark matter search results from a one ton-year exposure of xenon1t. *Physical Review Letters*, 121(11):111302, 2018.

[47] Yonit Hochberg, Yonatan Kahn, Mariangela Lisanti, Kathryn M Zurek, Adolfo G Grushin, Roni Ilan, Sinead M Griffin, Zhen-Fei Liu, Sophie F Weber, and Jeffrey B Neaton. Detection of sub-mev dark matter with three-dimensional dirac materials. *Physical Review D*, 97(1):015004, 2018.

[48] R Agnese, AJ Anderson, M Asai, D Balakishiyeva, R Basu Thakur, DA Bauer, J Billard, A Borgland, MA Bowles, D Brandt, et al. Search for low-mass weakly interacting massive particles using voltage-assisted calorimetric ionization detection in the supercdms experiment. *Physical review letters*, 112(4):041302, 2014.

[49] C Amole, M Ardid, IJ Arnquist, DM Asner, D Baxter, E Behnke, M Bressler, B Broerman, G Cao, CJ Chen, et al. Dark matter search results from the complete exposure of the pico-60 c 3 f 8 bubble chamber. *Physical Review D*, 100(2):022001, 2019.

CHAPTER 2

THE DAMIC EXPERIMENT

The DAMIC (Dark Matter in CCDs) experiment uses scientific-grade Silicon CCDs (charge-coupled devices) to search for energy deposits left by dark matter interactions. The experiment originated as a Fermilab R&D project in 2010 [1]; The demonstrator Stage I experiment with 3 CCDs was deployed at the SNOLAB underground facility in 2012 and concluded data taking in 2015; Stage II, DAMIC at SNOLAB with 7 CCDs, commenced operation in 2017 and terminated operation in early 2019; Stage III, DAMIC-M at Modane with a projected 50 CCDs, is under design and scheduled for a first deployment in 2021. Stage I and Stage II experiments utilized "conventional" CCDs, a term that will be defined in Sec. 2.1.1 while Stage III will use state of art, single electron resolution "Skipper" devices which we will hold off discussing until Chap. 7.

This section will introduce relevant background for the reader: what are CCDs, how do they work, how are they operated, and what is the DAMIC experiment. Readers are recommended to peruse Refs. [2–4] to attain a fuller picture of the experiment, its future, or for any operational details not discussed here.

2.1 Charge Coupled Devices

CCDs are pixelated ionization collection devices. They were originally invented in 1969 at Bell AT&T labs [5] by Willard Boyle and George E. Smith, the latter a PhD. alumnus from UChicago. Originally designed as memory storage units, and given the name "Charge Bubble Devices", CCDs have instead been universally adopted for their ability to image incident radiation (usually light) and miniature image sensors following their key principles have found their way into consumer electronics, notably smartphone cameras. The DAMIC CCDs we discuss here though are essentially macroscopic 2D devices made of Silicon, with the largest so far tested having linear dimensions of 9 cm, broken into square pixels of 15 μm $\times$ 15 μm, and thicknesses of 675 μm, an example of which can be seen in Fig. 2.1. A CCD quoted as 4k$\times$2k has roughly 4000 columns and 2000 rows, which are also referred to as the x and y dimensions respectively.

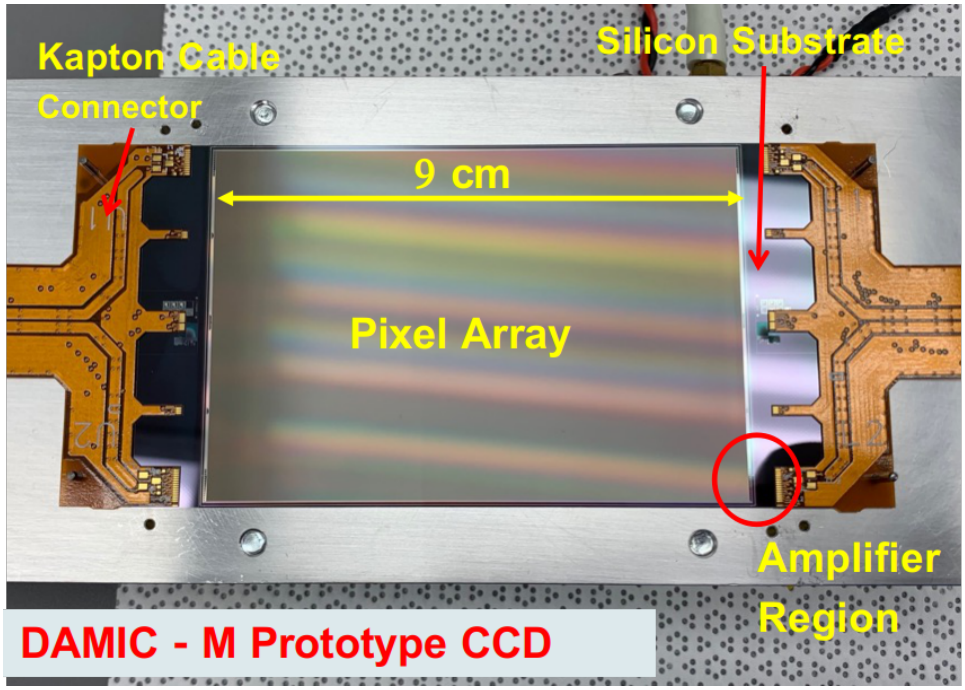

Figure 2.1: A labeled prototype DAMIC-M CCD mounted on a Silicon substrate, showing the extant pixel array, the Kapton cables with wirebonded pads that carry signals to and from the CCD, and the amplifier region where charge is read out.

2.1.1 CCD microstructure & operation

To understand how a CCD functions, it is useful to work at the level of an individual pixel as seen in the cross-sectional diagram of Fig. 2.2. The CCD can be approximated as a MOS (Metal Oxide Semiconductor) capacitor sandwich consisting of polysilicon metal gate contacts on top of an SiO_2 oxide insulator with a pn-junction below. The buried p-channel is a 1 μm thick layer of Boron doped p-type Silicon while the very thick n-type substrate is Phosphorous doped, with a substrate resistivity of $\geq$10 KΩ cm. This substantial thickness of 675 μm is needed for the high quantum efficiency and mass exposure requirements of a DM search. Thankfully, the high resistivity makes for a low donor density of $\mathcal{O}(10^{11})$ cm^{-3}, which means that the device can be fully depleted with a relatively low bias potential of $\sim$40 V [6]. This bias potential V_{sub} is applied to the backside contact of the CCD and creates the potential profile seen in Fig. 2.2 Bottom. Referencing the diagram, the order of operation in detecting external radiation is as follows:

1. An incoming particle, say DM, with energy E_p enters the device.

2. The particle deposits an energy E_r which if greater than the band-gap of Silicon

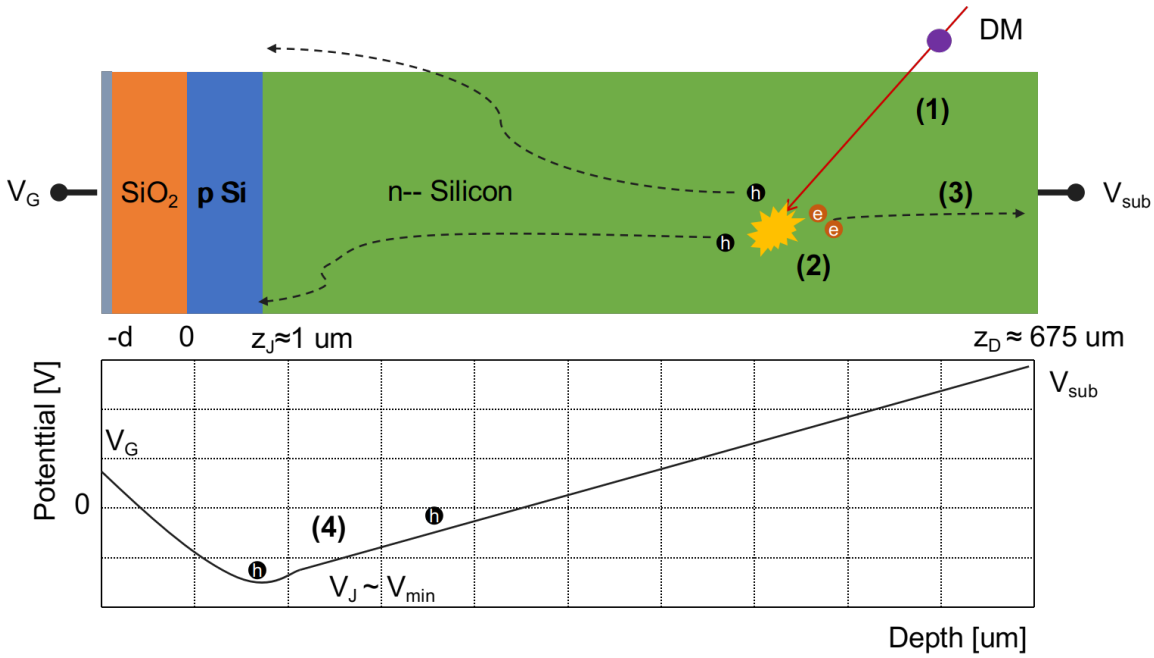

Figure 2.2: Top: Pixel cross section diagram showing labeled internal structure. The z coordinate runs along the thickness of the CCD and should be interpreted as the depth. A bias voltage V_{sub} applied to the backside contact generates an electric field that fully depletes the device. Bottom: The voltage profile as a function of depth. The junction location z_J is close to the minimum potential V_J. See text for description of device operation under irradiation.

E_g (∼1.12 eV) creates charge-pairs (electron-hole pairs) in a process referred to as *ionization*.

3. The electric field sweeps electrons to the backside (z_D) while pushing holes towards the top ($z \approx 0$) gate structure held at voltage V_G.

4. The holes undergo a diffusive random walk during their drift and are then collected at the minimum of the potential which lies just above the pn interface. Depending on the strength of the diffusion, these charges can collect in pixels that are horizontally far away from the interaction location.

Each pixel will continue to collect charge as long as the device is exposed with the voltages held constant. In Fig. 2.3 we can see that each pixel is actually equipped with 3 gate contacts $P_{1,2,3}$ (making it a 3-phase CCD) and the judicious application of gate voltages, switching them independently from low to high or vice versa, allows for charge to be moved from pixel to pixel in a procedure called *clocking*. Now zooming out to the level of the entire CCD array, schematically seen in Fig. 2.4 Right, we observe that pixels along the vertical axis

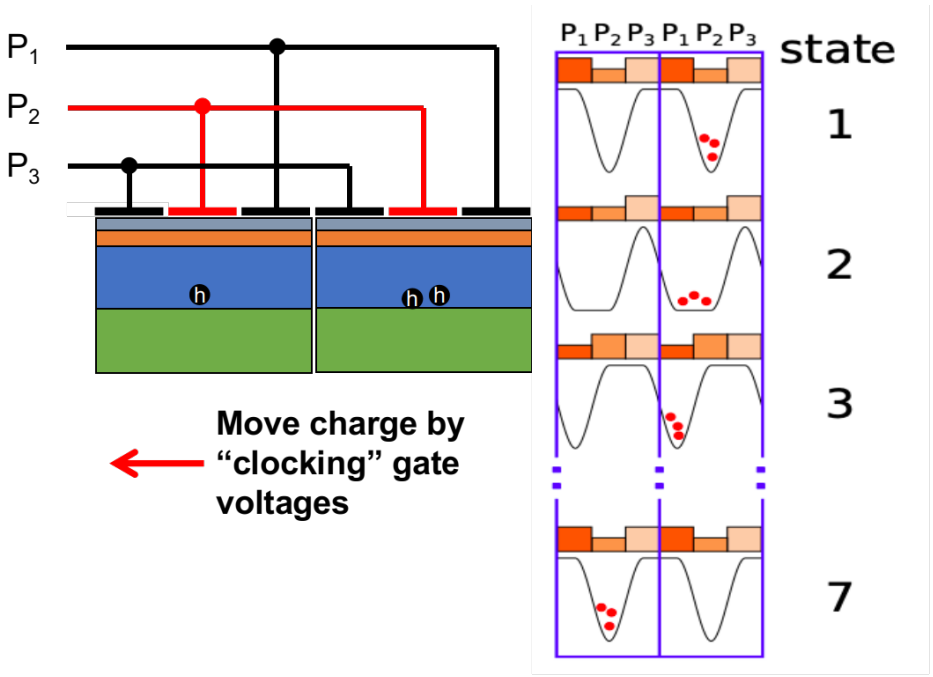

Figure 2.3: Left: Cross section of multiple pixels showing the 3-phase gate structure. Right: 7 step clock sequence on how to move charge from pixel to pixel by changes in Voltage stage, taken from Ref. [2].

(y-direction) are connected allowing charge to be transferred along the column. Channels stops, n-type implants between columns (purple), prevent charge from moving horizontally. Since every gate in a column of the same number is connected to the same clock source, a single clock cycle will move *all* the charge in the CCD in the same vertical direction from one pixel to the next. The last row abuts the Transfer Gate potential barrier (TG, dark yellow). If the transfer gate is open, charge is allowed to flow into the *serial/horizontal register*. The serial register is also wired up for 3-phase clocking but now moves the charge orthogonal (x-direction) to the rest of the CCD. At the end of the serial register is the readout output amplifier.

Pixel readout is accomplished courtesy of a series of source follower layout amplifiers as seen in Fig. 2.5 Left circuit diagram. At its simplest, when charge exits the serial register it is passed through a series of successive gates, the *Summing Well* (SW) and the *Output Gate* (OG), before being dumped into a *Sense Node* (SN). The SN is basically a capacitor and the injected charge Q_c changes the potential by:

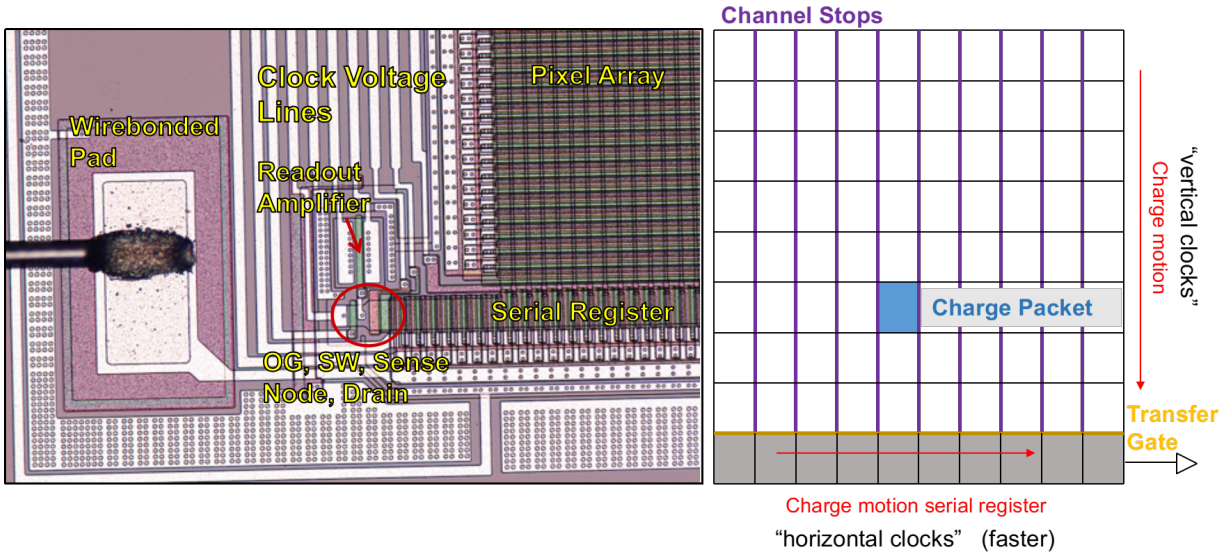

Figure 2.4: Left: Micrograph of a conventional design CCD, courtesy of PNNL, with relevant features labeled. Right: Schematic drawing of the 2D charge clocking process with labeled features as discussed in text.

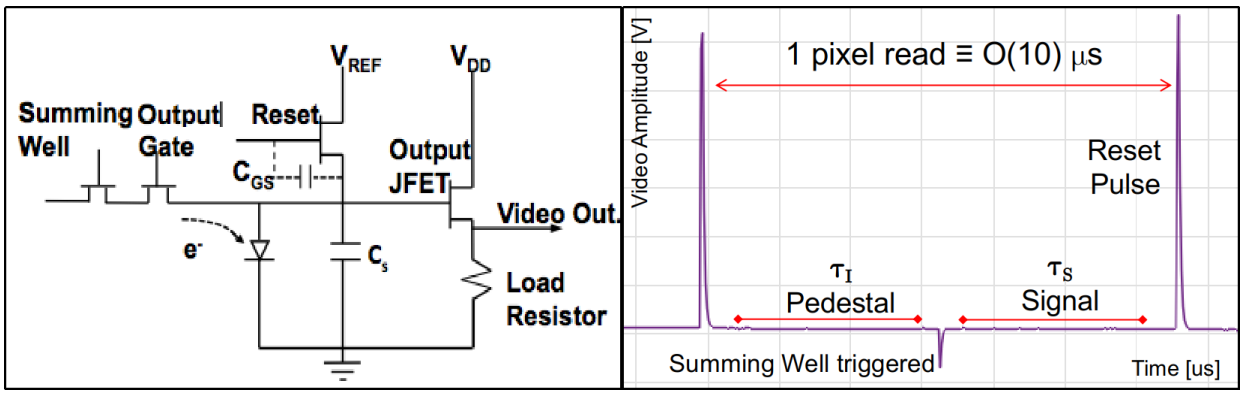

Figure 2.5: Left: Circuit diagram for readout amplifier showing the source follower configuration leading to the Video Output. Right: Video signal with highlighted features discussed in text.

$$\begin{aligned} \Delta V_c &= \frac{Q_c}{C_s} \\ &\approx 3 - 10\,\mu V e^{-1} \end{aligned} \tag{2.1}$$

This μV signal is then amplified by an output JFET and is the *Video* signal sent out of the CCD. Charge is cleared by means of a *Reset* pulse that triggers a flush by V_{ref}. One

issue this introduces is that the reset pulse can inject spurious charge into the SN. This reset noise can be significantly reduced by performing a differential measurement of the charge — before adding Q_c and then immediately after placing it in the SN. To reduce noise we also integrate the video signals for the measurement in a technique called *Correlated Double Sampling* (CDS).

The readout process is summarized in the video traces shown in Fig. 2.5 Right and can be stated as:

1. Clock the vertical register once cycle, moving all charge in the CCD down and dumping one row into the serial register.
2. Clock the horizontal register one cycle, dumping charge into the SW.
3. Measure the integral of the sense node value for an *integration time* τ_I. This is called the Pedestal.
4. Clock the SW to move charge through the OG into the SN.
5. Integrate the video signal for τ_I again, this value is called the Signal.
6. Trigger the reset pulse to flush charge.
7. Repeat from Step 2 until the horizontal register is completely read out.
8. Return to Step 1 to move another row down.

The advantage of this readout technique can be visualized in Fig. 2.7. If we had a perfect readout the pedestal and signal video outputs would be perfectly stable as the top panel shows. In real systems, the introduction of noise degrades performance. However if the noise is high frequency as in the middle panel, this jitter in the signal can be compensated for by the CDS integration, essentially by the central limit theorem. Unfortunately if the noise is of sufficiently low frequency, then even CDS will be unable to construct a reasonable estimator for ΔV_c as the bottom panel shows. The choice of τ_I is set by the noise profile of the entire electronics chain, and is often determined experimentally as in Fig. 2.6. The amplifier system mentioned here is called a *conventional readout* and we will discuss ways of getting around low frequency noise in Chapter. 7.

Fig. 2.4 Left shows an optical micrograph of a CCD, courtesy of Pacific Northwest National Labs (PNNL), where one can visually see the etched surface with all the components discussed above in the text.

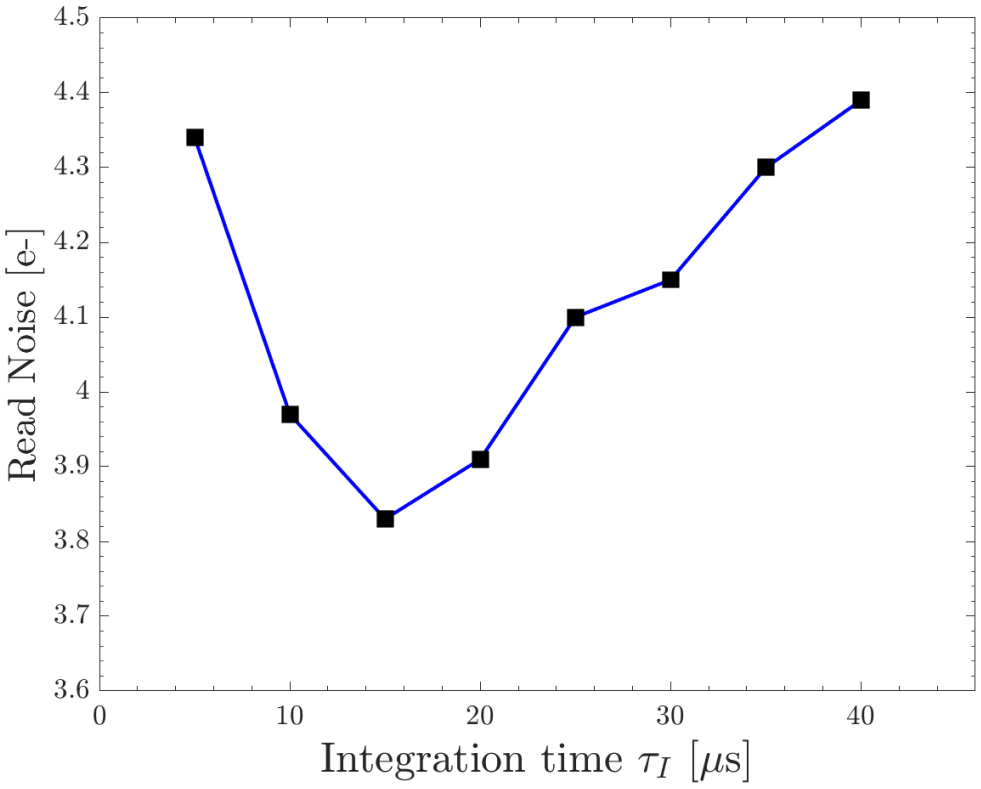

Figure 2.6: Read noise for the UW1601S CCD, see Chap. 7, as a function of integration time, with a clear minimum around 12 μs.

Every clock cycle and charge transfer process has the potential to lose charge back into the substrate. This loss is quantified by the *Charge Transfer Inefficiency* (CTI) which is a measure of the expected fractional loss during a transfer and is less than 1 part in 10^7 [7] in modern day CCDs. This low CTI has practically no influence on DAMIC science capability.

2.1.2 Images, overscans, pixel distributions, and energy spectra

Once the CCD has been clocked and charge read in the Sense Node, the output is fed through the readout electronics (specifically an ADC, Analog-to-Digital Converter) and then sent over a fiber optic cable to a computer where the information is stored in a FITS file format [8]. If multiple CCDs are read out, each is labeled with an *extension* number. The output information is best described and reconstructed as an *image* due to the pixelated nature of the CCD and the historic use case of CCDs. Fig. 2.8 Left is an example of a raw image taken with a DAMIC CCD at the University of Chicago while Right shows the same patch after processing. The CCD images contain a two-dimensional (2D) stacked history (projected on

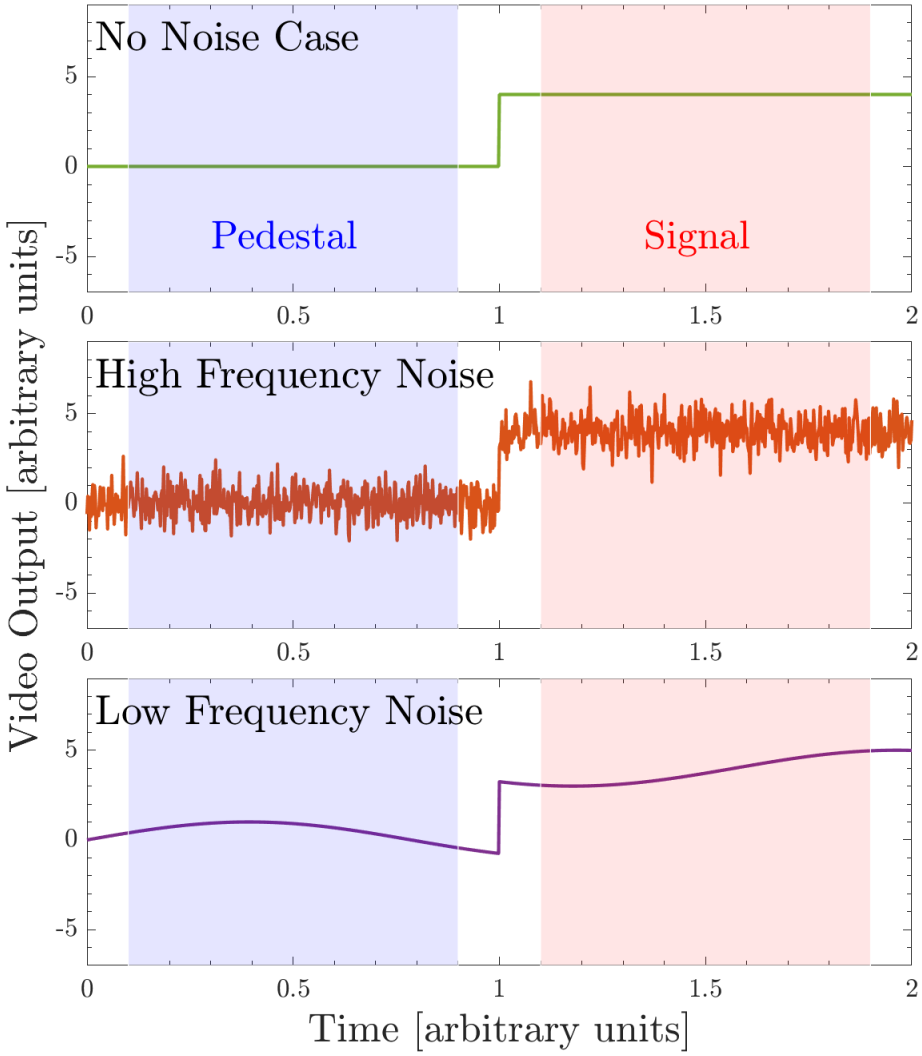

Figure 2.7: Video signal in the 3 regimes of noise for the Correlated Double Sampling method. Top panel is with no noise; Middle is an injection of high frequency noise; and Bottom panel for low frequency noise.

the x-y plane) of all ionization produced throughout an exposure, where each image pixel value is proportional to the collected number of charge carriers. The pixel values are in ADU (Analog-to-Digital Units), a 16 bit number (0 to 65535) in the current version of the readout electronics. The ADU value is related to the number of electrons counted at the sense node by way of the *gain* k [ADU per e^- counted during readout] — a constant based on operating condition and is derived from calibration (see Chap. 3). A *calibration constant* [ADU per keV of energy deposited] is then derived from the gain taking into account the energy required to

produce an electron-hole pair (see Chap. 4). Sections discussing calibration will explicitly mention the units of the terms being used.

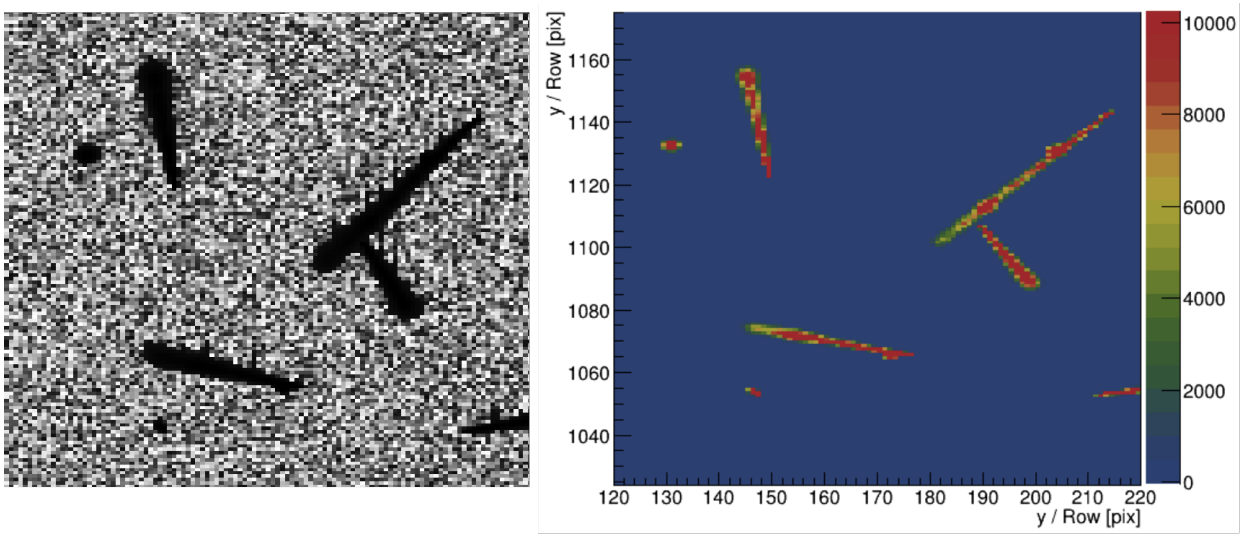

Figure 2.8: Left: Raw image taken with a DAMIC CCD, showing clusters of elevated pixels that belong to particles that deposited energy in the CCD. Right: Same image patch after algorithmic processing. Pixel locations are identified by their row and column index and the color is the ADU content, a proxy for the amount of charge contained within the pixel.

Current generation CCDs can be read out with up to 4 amplifiers at once, one in each corner of the device. These can be operated to not read charge since one can clock all the charge in a direction opposite to the amplifier. Reading the serial register past the length of a row will mean one gets an image that is larger in x than the size of the sensor. These extra pixels will by definition contain almost no charge since they will have only been exposed for the amount of time it took to read the entirety of a row (usually milliseconds). These 0 exposure pixels make up the *x-overscan* and provide a snapshot of the *baseline* or *pedestal* of an image— the ADU value associated with no charge. However if a CCD is clocked more rows in y than exist in the sensor, these rows will actually be "real" rows as they contain exposure equal to the amount of time it took to clock the full image before it (which can be seconds to hours). This horizontal patch of the image is called the *y-overscan*. Fig. 2.9 shows an image read out with 2 amplifiers and overlaid with all these terms where one can visually see the difference between regions for a given amplifier, where brightness has been used as a proxy for the ADU value. Note the baselines are different for each amplifier, which **does not mean** that one has more charge since charge is only proportional to the pixel content **after** pedestal subtraction (also known as *equalization*). Neighboring pixels can be read out simultaneously if they are dumped into the readout stage together, a process called

binning. For example if an image is binned 2×3 then 2 pixels were dropped into the readout stage from the serial register (x-binning) and 3 rows were vertically pushed into the serial register before it was clocked horizontally (y-binning) .

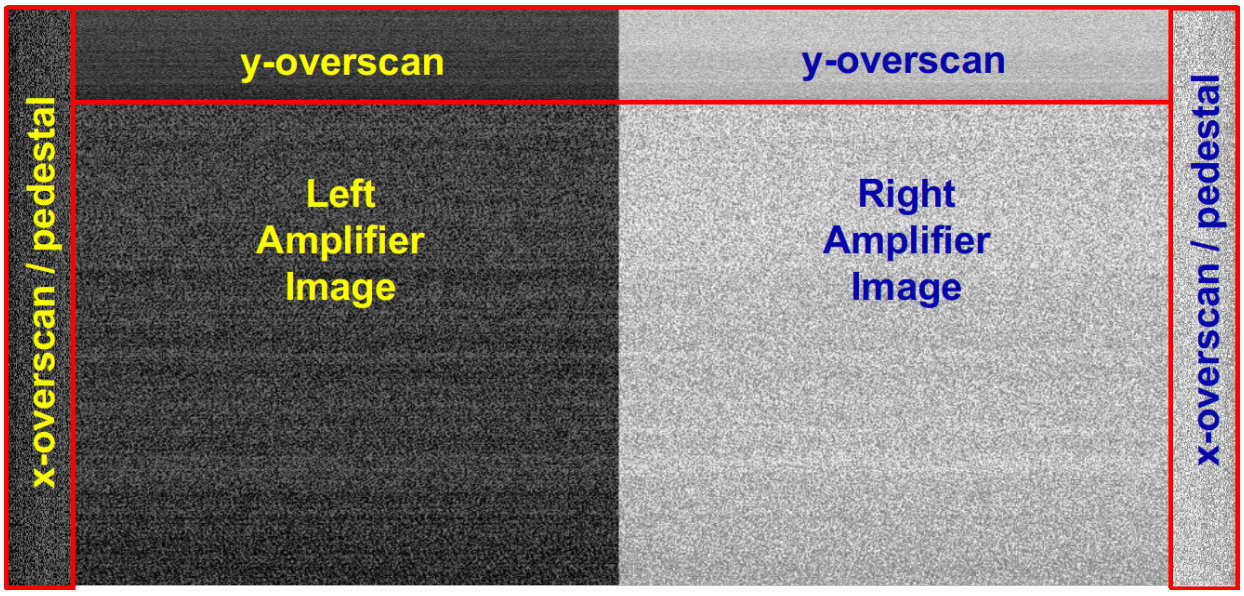

Figure 2.9: Labeled sections of CCD raw image output showing the image region, x and y-overscans, and simultaneous read out by dual amplifiers.

In the following we will refer to the *pixel distribution* as the histogram of the pixel values in an image. If there is no charge present in the pixels, we expect this distribution to be a Gaussian with mean $\mu = 0$ and width σ_{pix} equal to the *read noise* of the device. The read noise is the inherent fluctuation introduced by the amplifier and readout electronics. An example of a pixel distribution for a calibrated device can be seen in Fig. 2.10, showing the already impressive σ_{pix}=1.9 e^- read noise achieved with these CCDs. Note that since σ_{pix} is dominated by the last step in the charge readout, a hardware binned pixel features the same noise even if it contains charge from multiple pixels. A $M \times N$ region read out with 1x1 binning (i.e. no binning) and summed together downstream of the CCD will have a read noise contribution of $\sigma_{\text{M}\times\text{N}} = \sqrt{MN}\sigma_{\text{pix}}$ while a hardware binned region of the same size will still only have σ_{pix} resolution. This maybe advantageously used to improve the resolution on the charge measurement.

Once σ_{pix} is determined, we can devise an algorithm to associate pixels with charge (having values above a certain number of σ_{pix}) into clusters representative of the *tracks* left by ionizing particles. As discussed in Sec. 2.1.1, charge *diffuses* and ends up horizontally displaced in $x - y$ after travelling in z. Refs. [6, 9] work out that the expected profile of

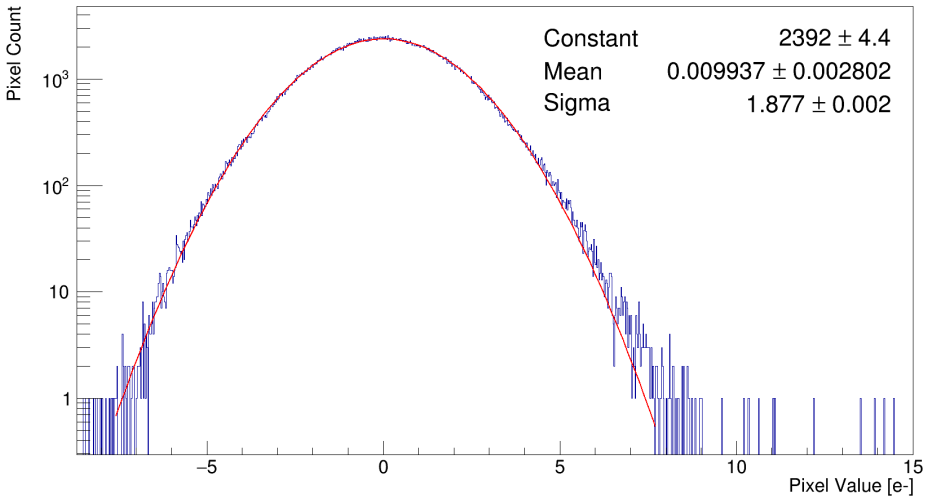

Figure 2.10: Pixel distribution histogram of a CCD image after pedestal subtraction and calibration, with a Gaussian fit overlaid showing both that read noise is effectively described by Gaussian white noise and that σ_{pix} is roughly $1.9e^-$ once calibrated.

diffusion is a 2D Gaussian centered around the point of impact with diffusion width $\sigma_{xy}(z)$ as,

$$\begin{aligned} \sigma_{xy} &= -Aln|1-bz| \\ A &= \frac{\epsilon}{\rho_n}\frac{2k_BT}{e} \\ b &= \left(\frac{\epsilon}{\rho_n}\frac{V_{\text{sub}}-V_j}{z_D}+\frac{z_D}{2}\right)^{-1} \end{aligned} \tag{2.2}$$

where ϵ is the permittivity of Silicon, ρ_n is the donor charge density of the substrate, k_B is the Boltzmann constant, T is the operating temperature, e is the electron charge, V_j is the junction voltage (voltage at the p-n interface) and z_D is the thickness of the device. In practice the parameters A & b are determined from data rather than from calculation. Note that Eq. 2.2 can be used to estimate the depth of the interaction z thus providing a 3D reconstruction of the energy deposit [9].

Once the charge has reached the surface, deciding whether the pixel it has landed in is part of a track or not is effectively an exercise in judgement and multiple algorithms can be used. The basic flow of the image processing and cluster reconstruction code developed in Ref. [2] for previous analyses is roughly:

1. Determine the pedestal value by estimating it independently for each column of an

image by a Gaussian fit to the pixel value distribution of that column and then subtract the mean value from each pixel in that column.

2. Repeat the previous procedure but now applied to each row of the image.

3. Starting from one corner of the image, increment over every pixel until a pixel with content above some *clustering threshold* (usually taken to be $> 4\sigma_{\rm pix}$) is found.

   3.1. Use this seed as a starting point and apply a recursive search with the same threshold cut to identify contiguous pixels.

   3.2. Categorize these groups of pixels as a cluster and mark them as already searched.

4. If the energy of the cluster is <10 keV (the initial track length will be much smaller than a pixel), perform a 2nd cluster search under the validated assumption that it will be well described by a 2D Gaussian.

   4.1. Generate a square moving window of 11×11 pixels.

   4.2. For each window position, compute the difference in log-likelihood (ΔLL) between the hypotheses of white noise and that of a 2D Gaussian distribution

   4.3. If the 2D Gaussian hypothesis is more credible, move the window in increments around the start position to find the ΔLL extremum, thereby centering the window.

   4.4. Perform a fit for a 2D Gaussian with free parameters x-position, y-position, σ_{xy}, and energy E

5. Restart the search from Step 3 until the entire image has been searched.

The choice of clustering threshold is taken to exclude the majority of noise pixels. In a 4k×4k CCD with a threshold of $4\sigma_{\rm pix}$ ($\approx 4\times 2e^{-}$=30 eV) we expect no more than (1-CDF($4\sigma_{\rm pix}$)$\times N_{\rm pix} \approx 500$) noise clusters. However, the *analysis threshold* is set at 50 eV based on the reconstruction efficiency, taking into account charge diffusion, investigated in previous work [10] which has shown that the acceptance drops to 10% for simulated clusters at 50 eV.

The clustering process reveals the excellent spatial resolution of a CCD and gives DAMIC the ability to *discriminate* and identify particles from each other as seen in Fig. 2.11. A *diffusion-limited* cluster is a low energy $\mathcal{O}$(keV) deposit whose morphology follows a 2D Gaussian, as it does not have the energy to create spatially elongated features.

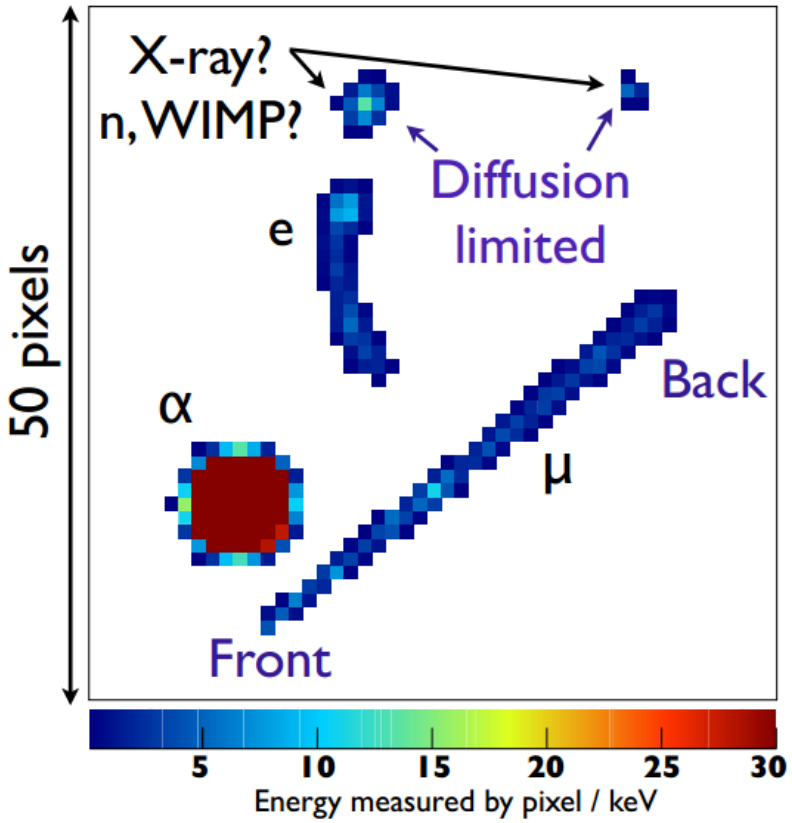

Figure 2.11: Image region showing types of tracks commonly found in CCD exposures, highlighting the excellent spatial discrimination of a CCD as a particle detector. Long straight tracks are likely muons or Minimum Ionizing Particles (MIPs). Note how we can identify the front vs. back of the track due to larger width at the back caused by charge carriers having to travel a longer distance causing them to diffuse more. Curved tracks are likely electrons while the large blobs are α's. The lower energy diffusion limited candidates could be photons, neutrons or hopefully DM candidates. Figure taken from Ref. [2].

Once clusters have been reconstructed we can add their pixels value to obtain an estimate of the cluster energy. An example of *energy spectrum* — the distribution of cluster energy — is given in Fig 2.12 where the CCD was exposed to an ^{59}Fe source with particles of known energy thus giving rise to peaks (see caption for details). The variance inherent to measuring a specific energy is called the *energy resolution* and comes from both the read noise and the Fano factor. Binning will trade worse spatial resolution for better energy resolution because read noise is acquired, as the name says, only during and after readout.

A energy spectrum can be used to calculate the background rate of events which is then expressed in *d.r.u* (differential rate units) equivalent to [keV^{-1} kg^{-1} d^{-1}] allowing scaling and comparison between experiments with wildly differing exposures.

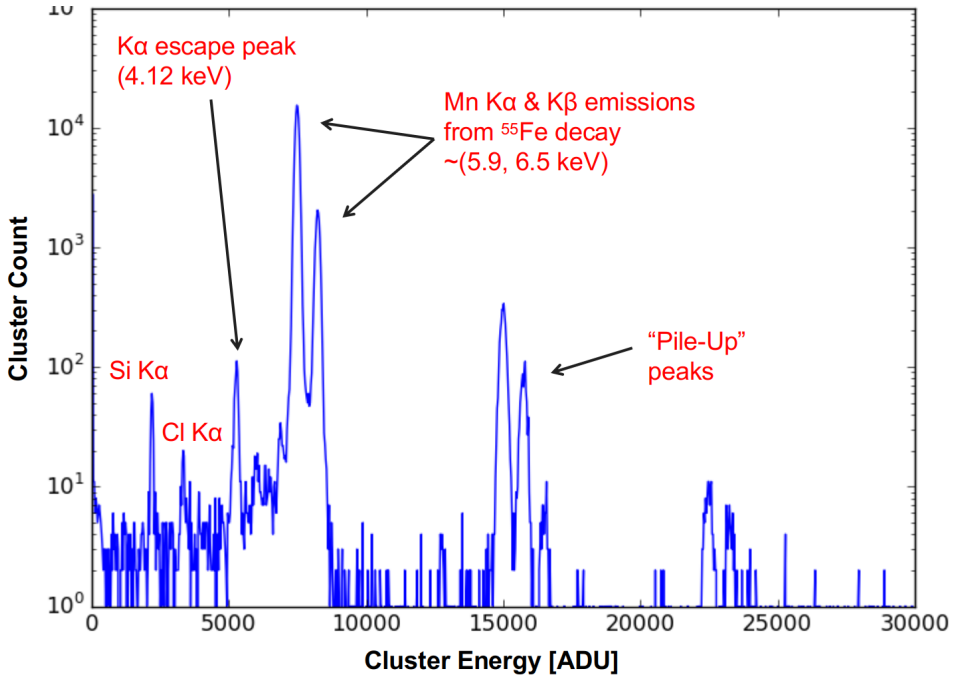

Figure 2.12: Energy spectrum of events found in an image taken during exposure to an ^{59}Fe source. The triple peaks of the $K\alpha$ and $K\beta$ emissions are seen clearly, along with other features like escape lines and pile-up. Knowledge of the energies of these spectral features allows one to determine the calibration constant.

2.2 The DAMIC experiment

2.2.1 at SNOLAB

The Stage I and Stage II science grade DAMIC experiments were installed at the SNOLAB underground laboratory near Sudbury, Ontario, Canada [11]. The facility is located 2 km underground in the Vale Creighton Mine, an active nickel mine, with a water equivalent depth of approx. 6 km. The CCD packaging and layout of the Stage II experiment can be seen in Fig. 2.13. The CCDs are epoxied (Epotek 301) to a silicon backing piece, over which is placed a copper frame. Control voltages and read out signals are ferried over a Kapton cable glued to the silicon backing. The cable is wirebonded to electrical contacts etched on the surface of the CCD. A copper bar over the narrow lip of the Kapton securely fastens the Kapton-CCD-frame unit. This packaged CCD is slid into a copper box hung below a 7" lead block. The lead blocks background radiation produced by the Vacuum Interface Board (VIB) electronic card where the Kapton cables are fastened to. This entire structure is then inserted into a copper vacuum vessel (10^{-6} mbar) where the CCD box is cooled

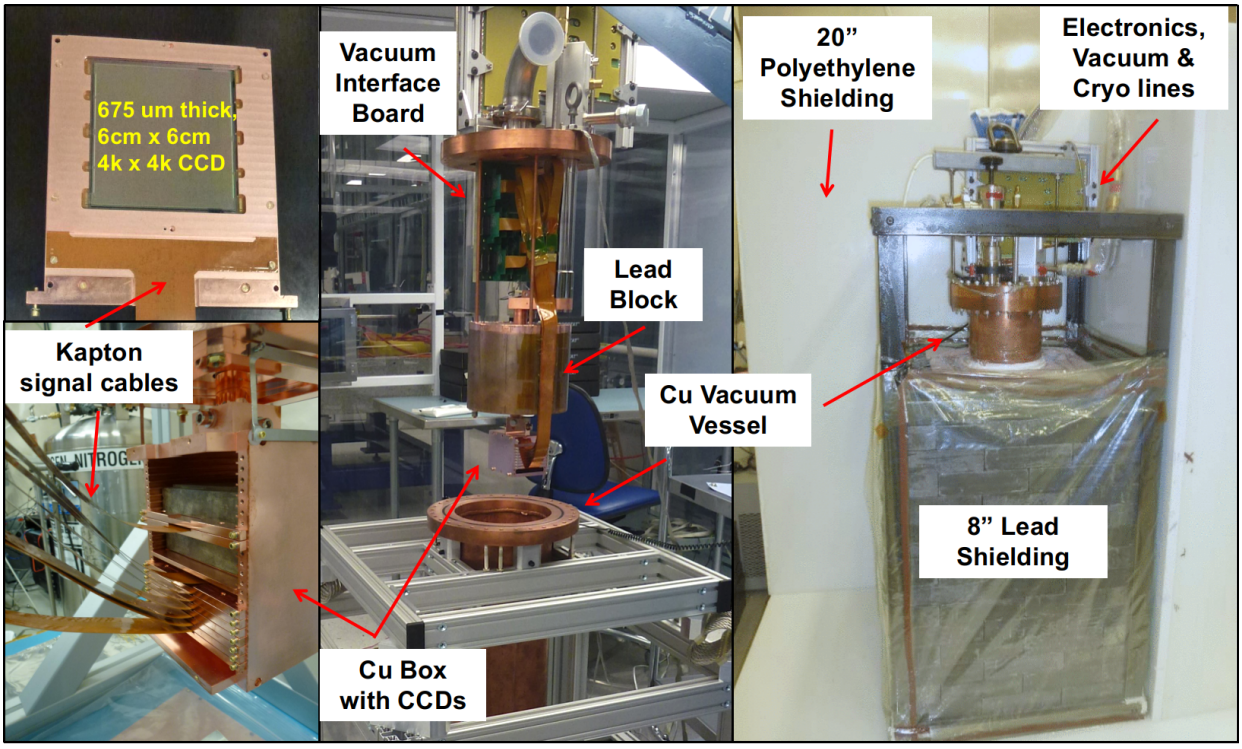

Figure 2.13: Clockwise from top: 4k x 4k CCD used in DAMIC at SNOLAB experiment; Components internal to Copper vacuum vessel, showing CCD holder box hanging off lead block, above which is the Vacuum Interface Board where Kapton signal cables are connected to; 20" polyethylene neutron shield surrounding 8" of lead used as a gamma shield, with vacuum, cryocooler and electronic lines snaking in from the top; Close up of the Cu box showing mounted CCDs along with lead blocks shielding Ext. 1

via a cryogenic tip connected to a cryocooler (PCC Compressor with PT-30 Cooler). The vacuum vessel is then mounted in a frame and surrounded by an 8" thick lead castle to block environmental γ-rays. Mos of the internal 1" of lead is “ancient” — recovered from a sunken Spanish galleon and a Roman ship — and is particularly radiopure having survived long enough to decay away radioactive ^{210}Pb and other isotopes. A 20" polyethylene shield completes the shielding, attenuating and absorbing incident neutrons primarily produced by spallation within the rock of the underground cavern. The entire shielding is enclosed in an aluminium box continuously flushed with N_2 gas to reduce the level of radon gas from $\sim$100 Bq m^{-3} in the SNOLAB experimental hall to $<$1 Bq m^{-3}.

We will not discuss the readout electronics in detail since an off the shelf system, the MONSOON [12], was obtained and used while leveraging tools and principles developed from Fermilab involvement in astronomical instrumentation. Suffice to say the MONSOON provides all voltages, clocks, and timings for the operation of all the CCDs. The entire

system, including the slow control interfacing with the cryogenics, vacuum, and power, was built for remote operation and data taking.

Briefly, the fabrication history of the CCDs deployed for the Stage II experiment is:

1. Crystalline Silicon ingots were grown at the TOPSIL facility in Denmark and then sliced into wafers, whereupon they were polished in TOPSIL Taiwan, around Nov. 2009

2. CCD pre-processing steps (e.g. depositing in-situ doped silicon on the backside) were done at the Teledyne DALSA facility in Canada while front-side polishing took place at OMNISIL in the United States, which all took place in 2010. The Silicon wafers were then stored at DALSA.

3. The design of the CCDs was done by the CCD group at Lawrence Berkeley National Labs (LBNL). The actual 11 step CCD fabrication took place in mid-2014 and was done at DALSA, see Ref. [13] for some details on this process. The large wafers were diced at LBNL into multiple CCDs of format 4k×2k and 4k×4k.

4. The packaging of the CCDs (gluing the support and Kapton cables and mounting the CCDs) took place at Fermilab.

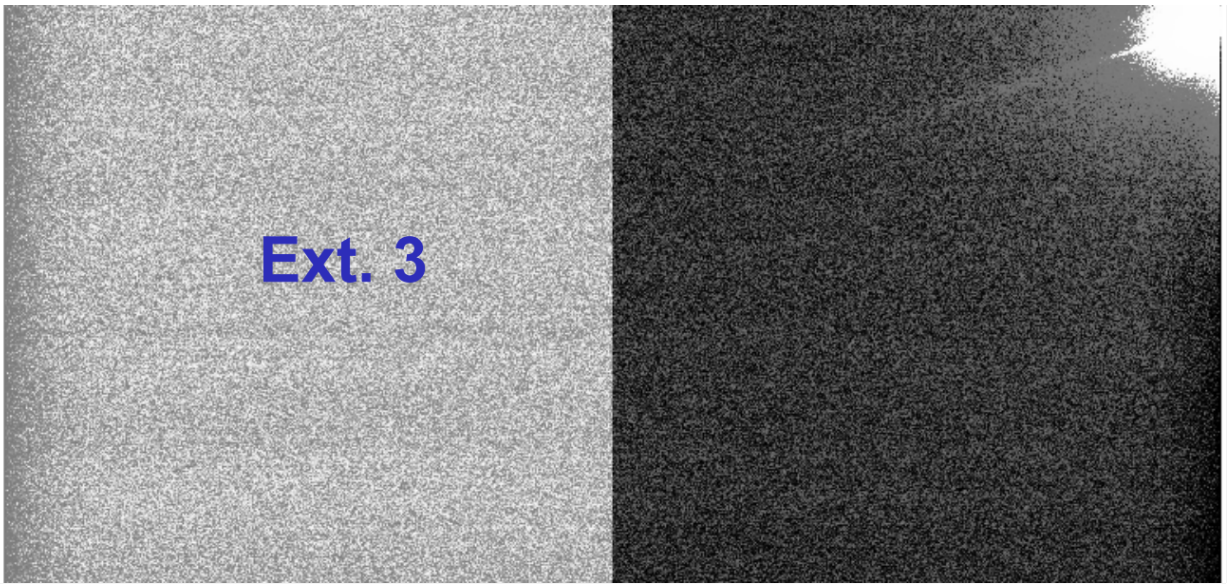

Figure 2.14: Ext. 3 image taken during original deployment of Stage II experiment. Excess charge blob, termed glowing, visible in upper right corner.

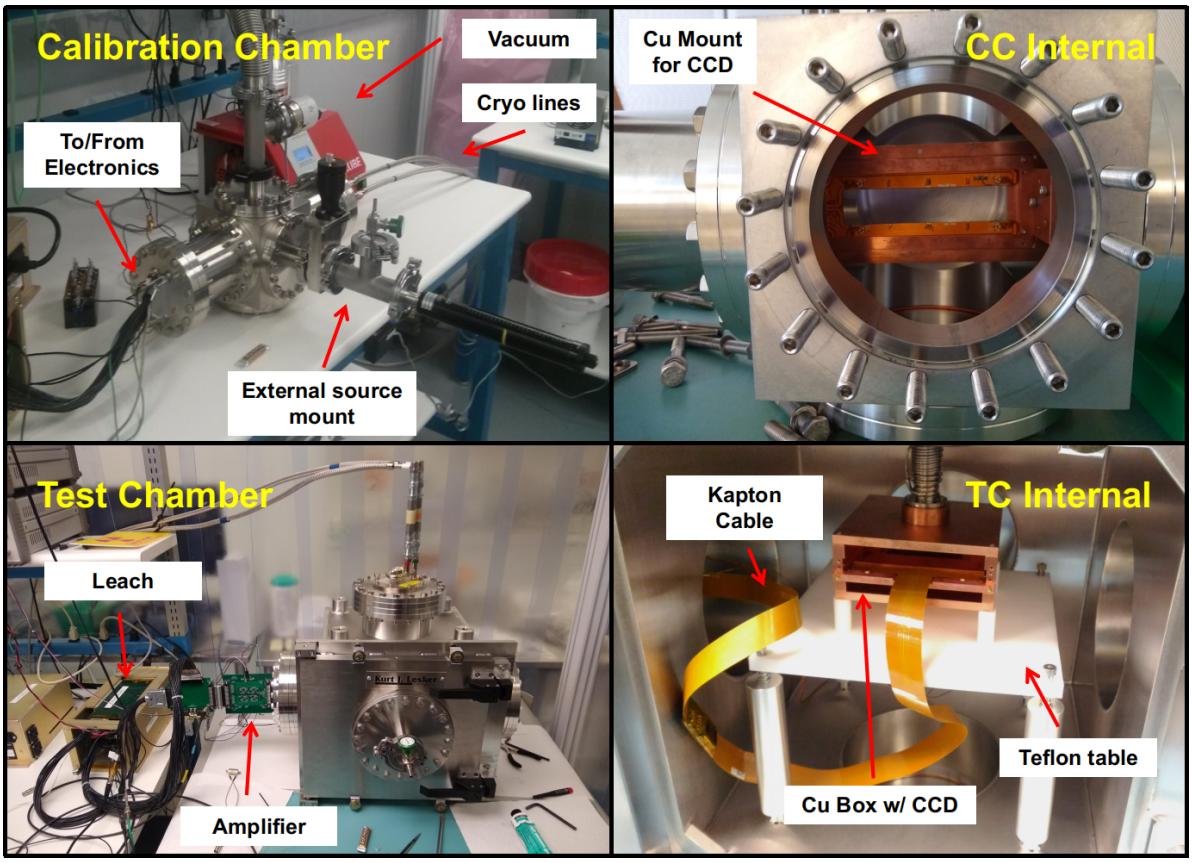

Figure 2.15: Dual R&D setup at the University of Chicago. Top panels are the calibration chamber where the Compton measurement in Chap. 5 was taken. Bottom panels are of the large test chamber setup with the Leach electronics and external amplifier circuitry highlighted. Inside one can see a copper box mimicking the one found at SNOLAB, mounted on a Teflon table to thermally isolate the CCDs from the chamber walls.

The Stage II experiment was initially deployed in late 2015/early 2016 with a design capacity of 18 CCDs for an active mass of 100 g. First light on a batch of 8 installed CCDs was achieved in early 2016 but the CCDs appeared to be defective. In particular, large amounts of glowing were noticed in images across all extension, as seen in Fig. 2.14. This was indicative of either an electronic or mechanical issue in the experiment. Remote and onsite debugging proved ineffective and the CCDs were taken out and shipped back to Fermilab to undergo testing. It was later determined that 7 CCDs were functional (Ext. 1, 2, 3, 4, 6, 11, 12). A second deployment occurred in early 2017 and these 7 CCDs were installed at SNOLAB. Ext. 1 was mounted in an electroformed copper frame and sandwiched between two 1" ancient lead blocks. The eventual measured background rate for Ext. 1 was 5 d.r.u while the remaining CCDs had a background of roughly 11 d.r.u. each. Science runs

started in late 2017 and completed in early 2019.

2.2.2 at the University of Chicago

R&D work is conducted at the University of Chicago across multiple CCDs operated in a similar fashion to those at SNOLAB. Two key differences are that individual chambers only operate one CCD at at time and the readout uses the LEACH electronics system [14], which provides similar functionality to the MONSOON. Activities are conducted in two setups, called the *calibration chamber* and the *test chamber*, seen in Fig. 2.15. The calibration chamber is a 6" cube with 2 cylindrical arms, one containing the cryocooler while the other houses the signal cables. The selected CCD is mounted in a copper frame directly attached to the cold finger. The larger test chamber is a 12" internal box with a front opening door. CCDs are mounted inside a copper box that is supported on a Teflon table.

References

[1] Juan Estrada. Direct dark matter search using ccds. In *Journal of Physics: Conference Series*, volume 203, page 012033. IOP Publishing, 2010.

[2] Jing Zhou. *Direct dark matter detection with the DAMIC experiment at SNOLAB*. PhD thesis, The University of Chicago, 2015.

[3] Alvaro E Chavarria, Javier Tiffenberg, Alexis Aguilar-Arevalo, Dan Amidei, Xavier Bertou, Gustavo Cancelo, Juan Carlos DOlivo, Juan Estrada, Guillermo Fernandez Moroni, Federico Izraelevitch, et al. Damic at snolab. *Physics Procedia*, 61:21–33, 2015.

[4] Mariangela Settimo. Search for low-mass dark matter with the damic experiment. *arXiv preprint arXiv:2003.09497*, 2020.

[5] Willard S Boyle and George E Smith. Charge coupled semiconductor devices. *Bell System Technical Journal*, 49(4):587–593, 1970.

[6] Stephen E Holland, Donald E Groom, Nick P Palaio, Richard J Stover, and Mingzhi Wei. Fully depleted, back-illuminated charge-coupled devices fabricated on high-resistivity silicon. *IEEE Transactions on Electron Devices*, 50(1):225–238, 2003.

[7] James R Janesick. *Scientific charge-coupled devices*, volume 83. SPIE press, 2001.

[8] JD Ponz, RW Thompson, and JR Munoz. The fits image extension. *Astronomy and Astrophysics Supplement Series*, 105:53–55, 1994.

[9] DE Groom, PH Eberhard, SE Holland, ME Levi, NP Palaio, S Perlmutter, RJ Stover, and M Wei. Point-spread function in depleted and partially depleted ccds. 1999.

[10] A Aguilar-Arevalo, D Amidei, D Baxter, G Cancelo, BA Vergara, AE Chavarria, JC d'Olivo, J Estrada, F Favela-Perez, R Gaior, et al. Results on low-mass weakly interacting massive particles from a 11 kg-day target exposure of damic at snolab. *arXiv preprint arXiv:2007.15622*, 2020.

[11] NJT Smith. The snolab deep underground facility. *The European Physical Journal Plus*, 127(9):108, 2012.

[12] Nick C Buchholz and Philip N Daly. The monsoon generic pixel server software design. In *Advanced Software, Control, and Communication Systems for Astronomy*, volume 5496, pages 364–372. International Society for Optics and Photonics, 2004.

[13] SE Holland, CJ Bebek, KS Dawson, HT Diehl, F Dion, JH Emes, J Estrada, R Frost, R Groulx, A Karcher, et al. Fabrication of large format, fully depleted ccds for the dark energy survey camera.

[14] Robert W Leach and Frank J Low. Ccd and ir array controllers. In *Optical and IR Telescope Instrumentation and Detectors*, volume 4008, pages 337–343. International Society for Optics and Photonics, 2000.

CHAPTER 3

CCD CHARACTERIZATION

While the previous Chapter introduced CCDs, this section discuss areas where the author has made a useful contribution to the experiment that do not rise to the level of requiring separate chapters. In particular, we focus on ideas related to calibration, device optimization, and overall characterization of CCDs. Readers are again encouraged to look at Refs. [1–3] for any DAMIC experiment details not touched here.

3.1 Correlated Noise Subtraction

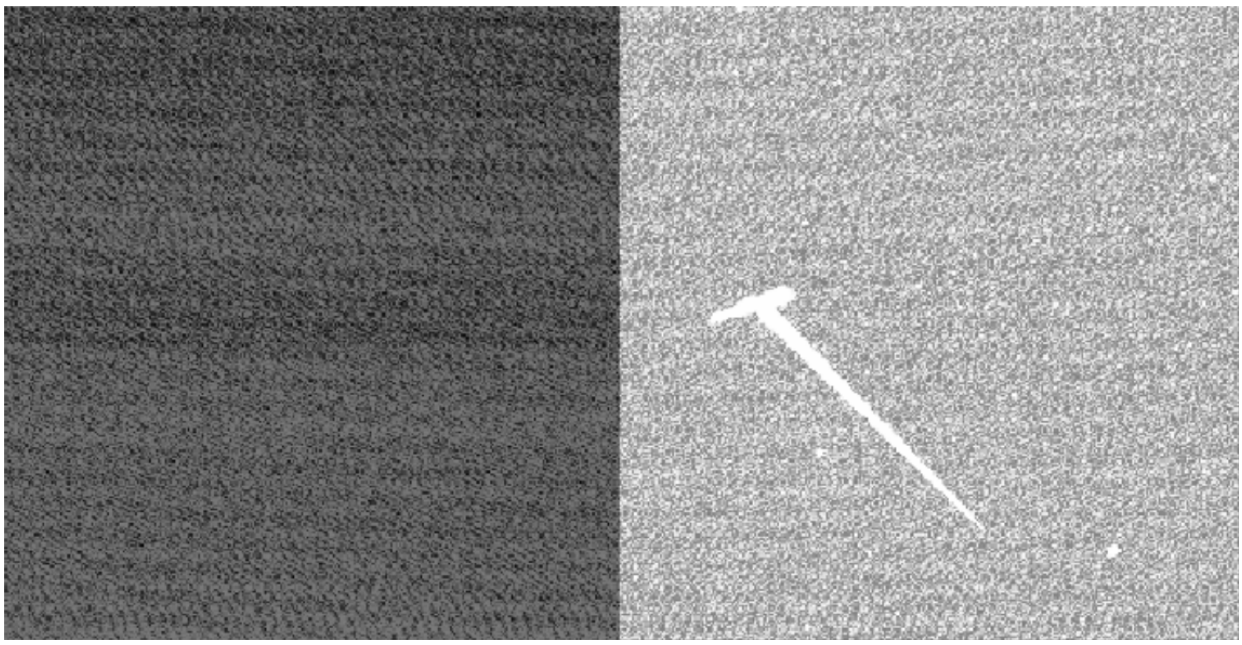

Figure 3.1: Selected image region read out with Left and Right amplifier showing correlated noise features (diagonal stripes) common to both images. Note that only Right amplifier images contain non-zero exposure pixel values, as seen by the track.

Due to the imaging nature of the CCDs noise often results in *spatial* patterns in an image, as seen in the diagonal striping of Fig. 3.1. The corresponding power spectrum is shown in Fig. 3.2. In this image the left and right portions are independent readouts by the two amplifiers in the same serial register — however charge has only been clocked to the Right amplifier, meaning the Left should just be reading noise (a "blank" image). The presence of identical features suggests a noise source in the readout chain downstream of the

CCD itself and common to both amplifiers. The previous methodology [1] to remove this correlated effect relies on fitting to the data a relationship between every pixel value of the right amplifier, R_i, and the value its corresponding Left amplifier pixel, L_i, of the form:

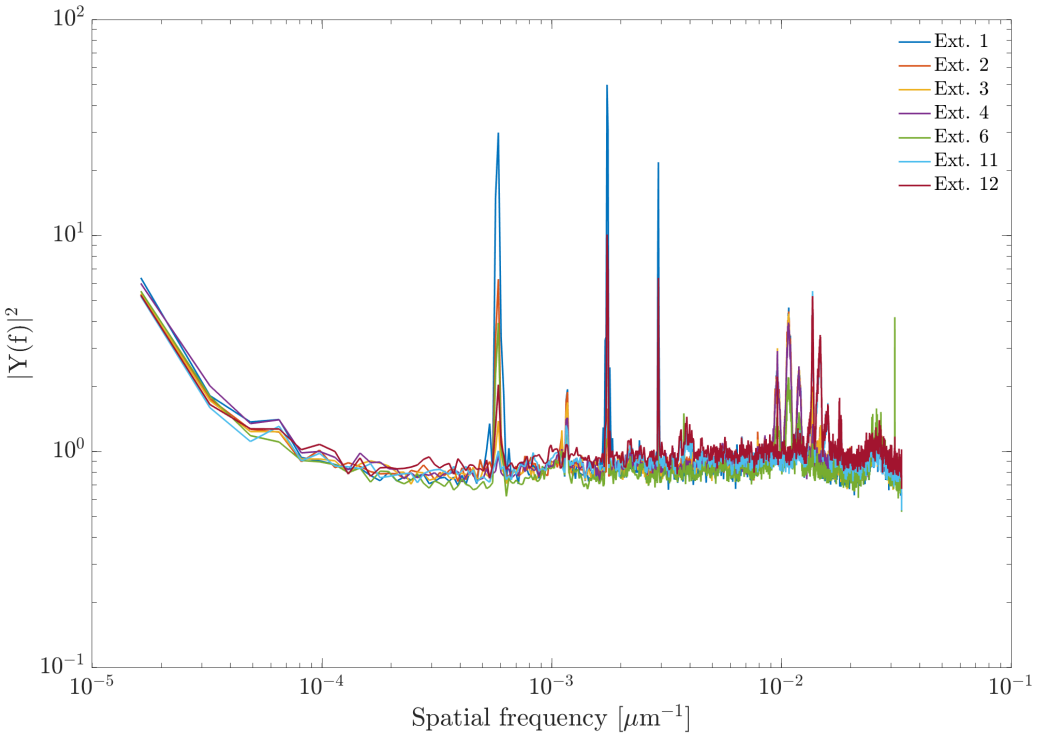

Figure 3.2: Fast Fourier Transform based pixel power spectrum of DAMIC at SNOLAB data for different extension CCDs.

$$\hat{R_i^*} = mL_i + c, \tag{3.1}$$

creating the new pixel value estimator $\hat{R}_i = R_i - R_i^*$. We can explicitly compute the variance of Eq. 3.1 to get:

$$\begin{aligned} \mathrm{Var}(\hat{\mathrm{R}}) &= \mathrm{Var}(\mathrm{R}) + \mathrm{Var}(\mathrm{R}^*) - 2\mathrm{Cov}(\mathrm{R}, \mathrm{R}^*) \\ &= \mathrm{Var}(\mathrm{R}) + \mathrm{m}^2\mathrm{Var}(\mathrm{L}) - 2\mathrm{mCov}(\mathrm{R}, \mathrm{L}) \end{aligned} \tag{3.2}$$

We can solve for the Maximum Likelihood Estimate of the coefficient m analytically as:

$$m = \frac{E[RL] - E[L]E[R]}{\mathrm{Var}(\mathrm{L})} = \frac{\mathrm{Cov}(\mathrm{R}, \mathrm{L})}{\mathrm{Var}(\mathrm{L})} \tag{3.3}$$

Which means we can work out the exact reduction in variance as:

$$\begin{aligned} \mathrm{Var(R)} - \mathrm{Var}(\hat{\mathrm{R}}) &= 2\frac{\mathrm{Cov(R,L)}}{Var(L)}\mathrm{Cov(R,L)} - \frac{\mathrm{Cov}^2\mathrm{(R,L)}}{\mathrm{Var(L)}^2}\mathrm{Var(L)} \\ &= \frac{\mathrm{Cov}^2\mathrm{(R,L)}}{\mathrm{Var(L)}} \end{aligned} \tag{3.4}$$

A more robust method should account for the existence of extra information from all j CCDs in an array being read simultaneously. We explicitly start with reducing the total variance of the new construction. For an image i we can write $\hat{R}^i = R^i - \sum_j a_j L_j$ where a_j is the weight on the corresponding noise-only extension. We can then minimize the variance on $\hat{R}^i$ as:

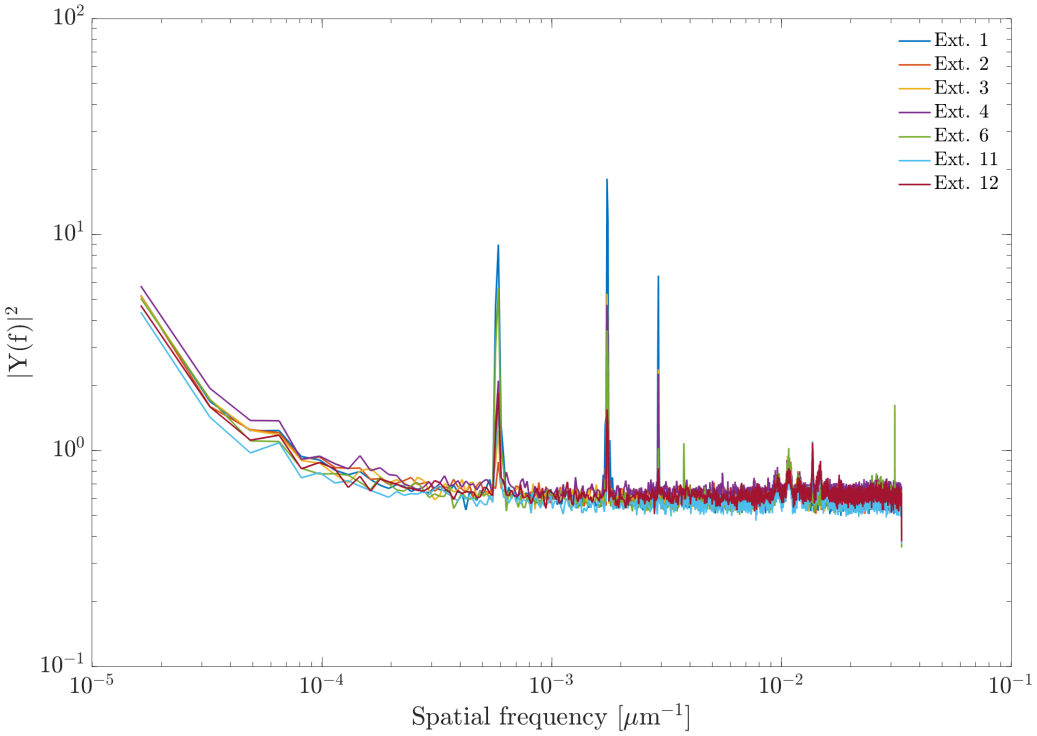

Figure 3.3: Fast Fourier Transform based pixel power spectrum of DAMIC at SNOLAB data for different extension CCDs after applying the correlated noise subtraction procedure outlined in the text.

$$
\begin{aligned}
\mathrm{Var}(\hat{\mathrm{R}}^{\mathrm{i}}) &= \mathrm{Var}(\mathrm{R}^{\mathrm{i}}) + \sum_{\mathrm{j}} \mathrm{a}_{\mathrm{j}}^2 \mathrm{Var}(\mathrm{L}_{\mathrm{j}}) - 2\sum_{\mathrm{j}} \mathrm{a}_{\mathrm{j}} \mathrm{Cov}(\mathrm{R}^{\mathrm{i}}, \mathrm{L}_{\mathrm{j}}) \\
\frac{\partial \mathrm{Var}(\hat{\mathrm{R}}^{\mathrm{i}})}{\partial a_j} &= 0 \equiv 2\sum_{j} a_j \mathrm{Var}(\mathrm{L}_{\mathrm{j}}) - 2\sum_{\mathrm{j}} \mathrm{Cov}(\mathrm{R}^{\mathrm{i}}, \mathrm{L}_{\mathrm{j}}) \\
&\implies \sum_{j} a_j \mathrm{Var}(\mathrm{L}_{\mathrm{j}}) = \sum_{\mathrm{j}} \mathrm{Cov}(\mathrm{R}^{\mathrm{i}}, \mathrm{L}_{\mathrm{j}}) \\
&\implies \mathbf{a} = \mathbf{Cov}(\mathrm{R}, \mathrm{L}) / \mathbf{Var}(\mathrm{L})
\end{aligned}
\tag{3.5}
$$

where we have switched to matrix notation for the last entry. This formulation can be seen as the natural extension of the one-image method outlined previously and further guarantees the largest reduction in variance for *a linear combination* of blank images. We can observe the effect this procedure has on the power spectrum in Fig. 3.3 where we notice a reduction in the higher frequency components. Furthermore, we can see an improvement in the noise of the processed $\hat{R}$ images using multiple images versus a raw image by looking at their pixel distribution, as seen in Fig. 3.4. A 15% improvement in the noise over the raw data is obtained as tabulated in Table 3.1. While this may seem a modest improvement, any reduction in noise is beneficial in DM searches given the exponential rise in the energy spectrum expected at lower energies.

Extension	σ_{raw} [e$^-$]	σ_{linear} [e$^-$]	$\sigma_{\mathrm{analytic}}$ [e$^-$]
1	2.1289	1.82(1)	1.67(1)
2	1.90(1)	1.76(1)	1.57(1)
3	1.95(1)	1.79(1)	1.64(1)
4	1.95(1)	1.79(1)	1.59(1)
6	1.98(1)	1.77(1)	1.62(1)
11	1.97(1)	1.69(1)	1.65(1)
12	2.09(1)	1.79(1)	1.67(1)

Table 3.1: Read noise computed over 105 images 1x100 images taken during 2017-2018, showing consistent correlated noise reduction of roughly 15% over the raw read noise for the multi-image formulation vs. about %9 for the old single image procedure.

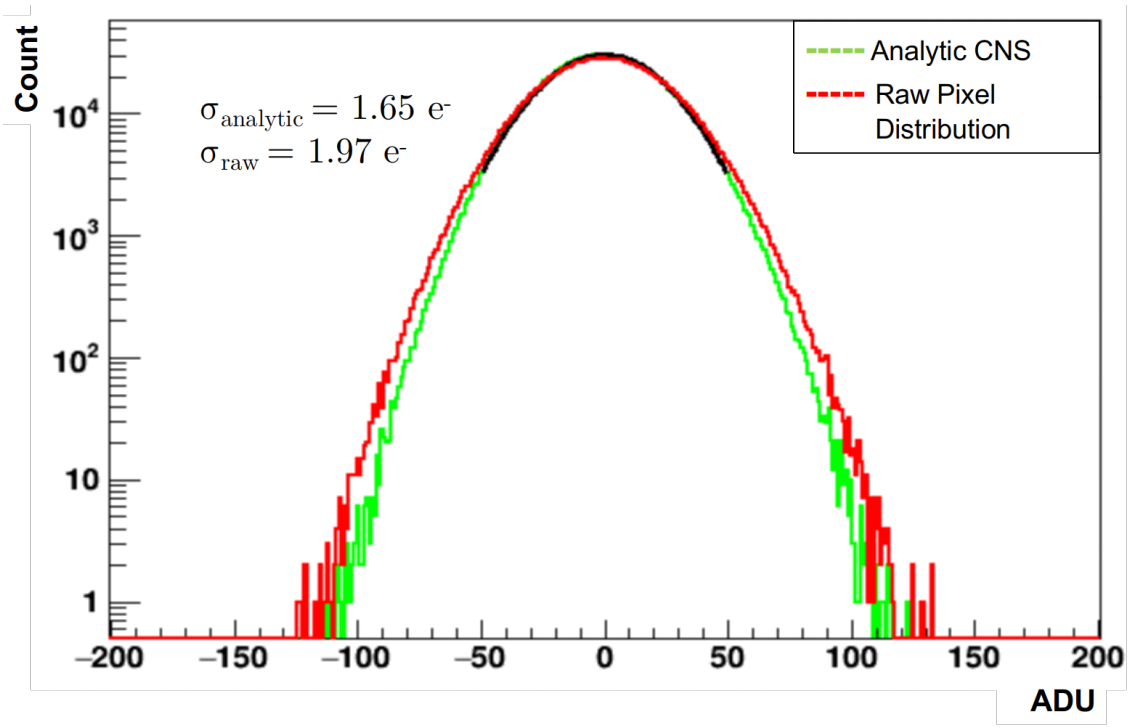

Figure 3.4: Comparison of pixel distribution histograms for Ext. 4 after the application of the dual correlated noise subtraction strategies outlined in the text, showing a 15% improvement in the noise having applied the multi-image correlated noise reduction procedure to the raw-data vs. %9 for the single image fitting approach

3.2 Characterizing leakage current

Leakage Current (LC), the shot noise production of spurious charge unrelated to ionization, is a key limiting factor in the sensitivity of the DAMIC experiment. It is interchangeably called Dark Current (DC) because it is present even with no external or background radiation ionizing the CCD. We can classify DC into *bulk* and *surface* contributions, the former occurring deep within the silicon while the latter is created at interfaces between CCD layers, and both are strongly driven by thermal effects. We use leakage current as a broader term because it can encompass *any* unexpected charge production — perhaps from mechanical stress, light-leaks, or the clocking of the CCD. Identifying the overall leakage, expressed in literature in units of A cm^{-2} or also in e^{-} pix^{-1} d^{-1}, is extremely important for proper operation of these devices. High levels of LC can indicate unforeseen changes in the operating environment, particularly if the CCDs are stressed in some manner.

We will discuss precise measurements and potential sources of LC in Chap. 7 and how to use LC for physics analyses in Chap. 6, but here we will present a simple method

of quantifying the leakage current in a CCD image, talk about the expected dominant "depletion" bulk dark current, and then see how this measurement was used to set optimal exposure times for the Stage II CCDs.

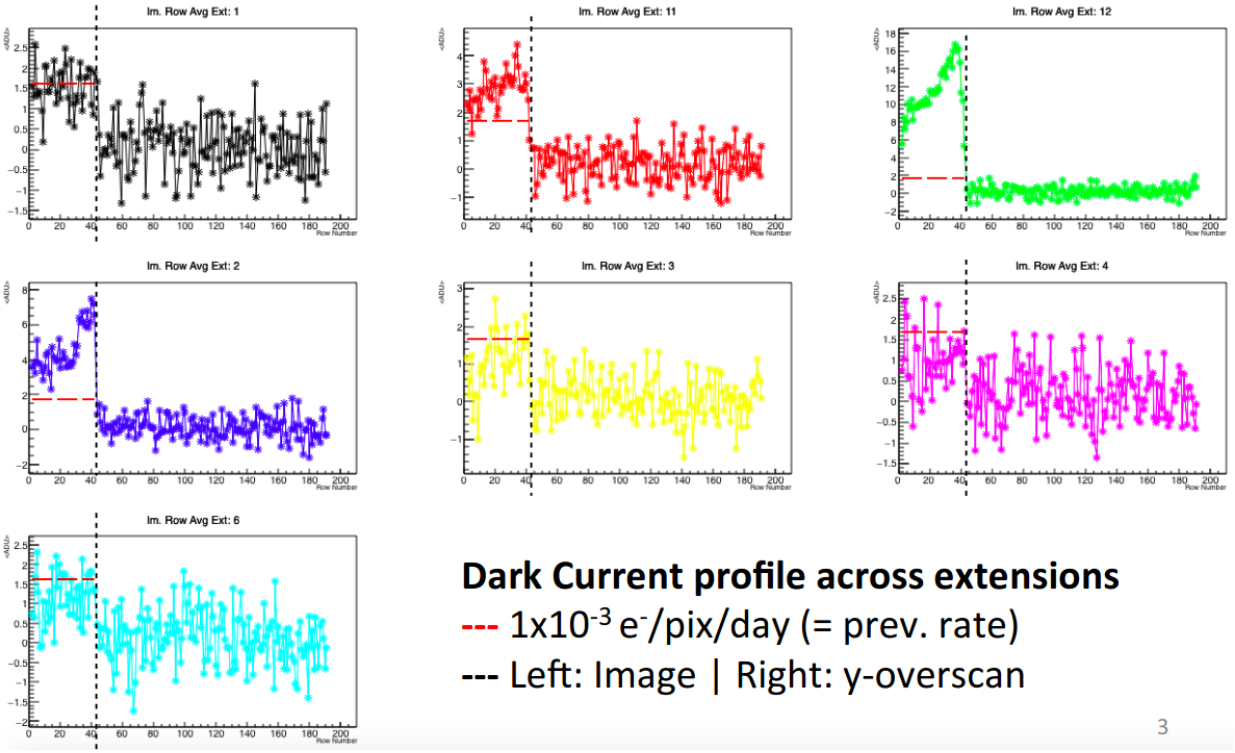

Figure 3.5: Row projection of 140K image data for 7 extensions of Stage II experiment. Previous Stage I demonstrator LC value of approx. $1{\times}10^{-3}$ e^- pix^{-1} d^{-1} are shown in red for comparison. Vertical line denotes boundary of Image region and Overscan region (zero exposure) with expected drop-off.

For a selected image set taken during the Stage II run, as listed in Table. 3.2, we:

1. Select all images for a given extension. Define Image regions X=[500, 3500] and Overscan region X=[4125:4160]. We select Y=[100:4000] (1x1 binned) or Y=[2:39] (1x100 binned)

2. Subtract the Median overscan on a per-row basis from the image to create the Normalized image (pedestal = 0)

3. Mask high energy clusters in the Normalized image, i.e. remove their pixels from consideration, using the clustering algorithm defined in Sec. 2.1.2.

4. Compute the median across all the Normalized images to create the Median image.

5. Scale the Median image using the calibration constants computed in Sec. 3.4, now every pixel is in e^- counts.

6. Fit a Gaussian to the pixel distribution and extract the μ (mean) parameter. This is interpreted as the leakage current per pixel for an image.

7. Scale this LC value to a per day basis by $\tau = T_{\text{exp}} + T_{\text{read}}$ as the images are effectively continuously read out.

We can look at the row-projections from Step 4 in Fig. 3.5 on a per-extension basis to see the elevated charge in an image region that drops off at the start of the Y-Overscan. This charge is the leakage current. We can see some non-linear behaviour for Ext. 2 & 12, indicating an alternate source to the expected spatially uniform Poisson distribution of spurious charge creation, perhaps a light-leak or non-uniform mechanical stress. Note that these 2 CCDs are the top and bottom of the stack (Ext. 1 is sandwiched between 2 lead blocks) and may be preferentially exposed to light leaking in.

Temperature [K]	**# of files**	**Exposure+Read Times** [s]	**Binning**
240	6	1450+510	1x1
220	11	1450+510	1x1
200	18	4130+510	1x1
180	6	4130+510	1x1
170	3	7350+510	1x100
160	3	7350+510	1x100
140	14	100000+510	1x100

Table 3.2: Datasets used for estimating leakage current as a function of temperature, taken during either commissioning or during cool-down phase of experiment restart after operational shutdown, between 2017-2018.

Repeating the enumerated analysis steps for all temperatures and extensions, we can generate the temperature profile seen in Fig. 3.6. There is an approximately log-linear relationship (dashed line) between temperature and leakage current, and we can say that a ΔT=10° change in temperature would result in an approx. 6x change in the leakage.

The dominant portion of this observed leakage is likely from *depletion dark current*. In general, dark current carriers are produced by charges hopping between intermediate bandgap states associated with imperfections or impurities within the semiconductor [4]. These imperfections alter the lattice structure and give rise to a polluted band structure with numerous states lying between the valence and conduction band. The carrier generation-recombination rate, U [carriers per time per volume], through these intermediate centers is

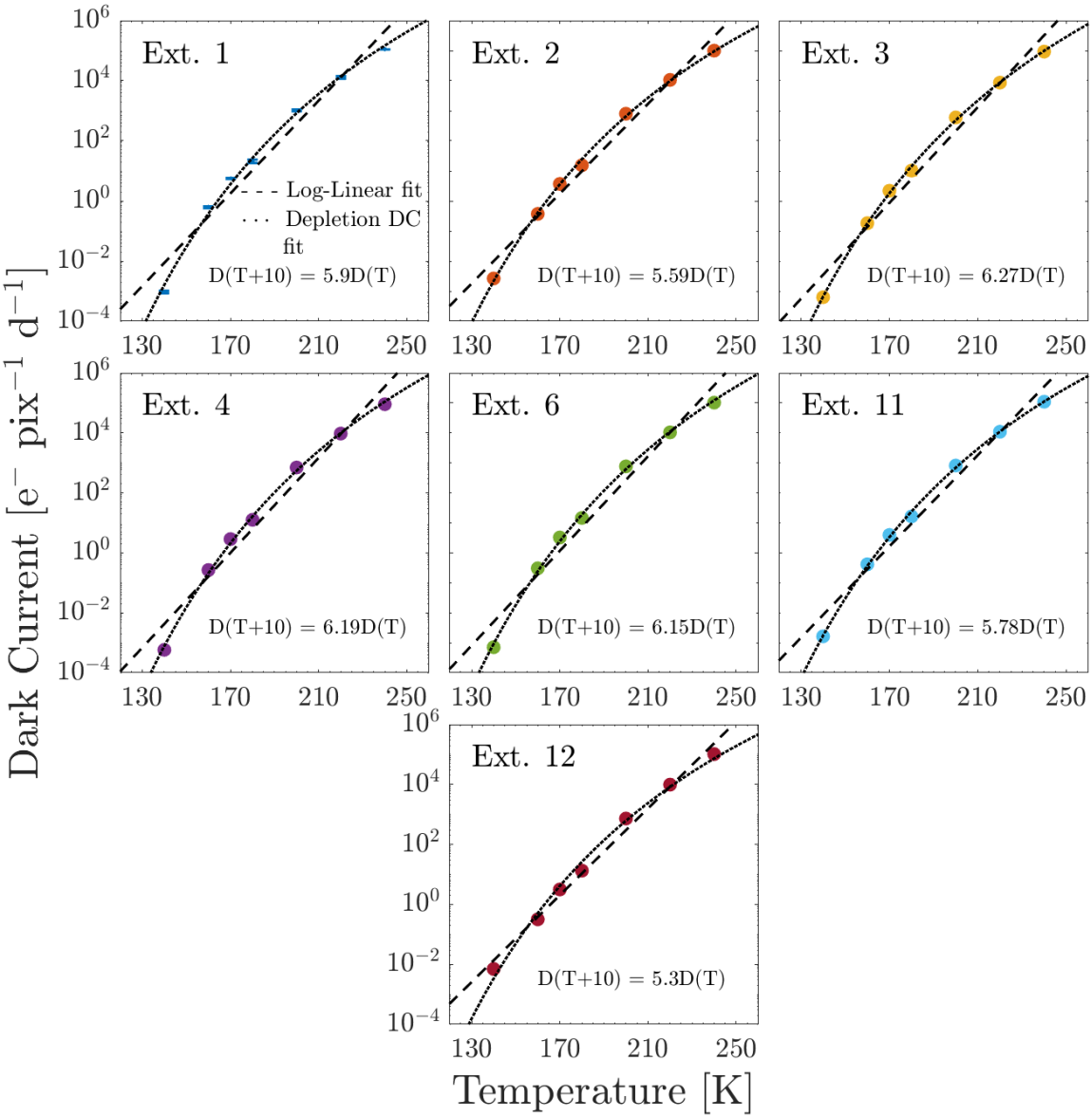

Figure 3.6: Leakage current as a function of temperature for the DAMIC at SNOLAB CCDs taken either during commissioning or during the cool-down phase of restarts after operational shutdowns. One can see a roughly 6x log-linear relationship between 10° shifts in CCD box temperature (dashed lines). A depletion dark current fit (dotted) is also provided, see text for details. Error bars are shown for Ext. 1 but suppressed for remainder figures.

described by the Shockley-Hall-Read equation reproduced below from [5] and using their notation:

$$U = \frac{\sigma_h \sigma_p v_{\rm th}(pn - n_i^2)N_t}{\sigma_h\left[h + n_i exp\left(\frac{E_t - E_i}{kT}\right)\right] + \sigma_p\left[p + n_i exp\left(\frac{E_t - E_i}{kT}\right)\right]} \tag{3.6}$$

where $\sigma_{h,p}$ are the capture cross-sections for holes and electrons respectively, v_{th} is the carrier thermal velocity, (h,p) are the hole and electron concentrations, n_i is the intrinsic carrier concentration, N_t is the concentration of intermediate centers of energy level E_t, E_i is the Fermi level, and k is the Boltzmann constant.

In the depleted region, where $h = n = 0$, and assuming $\sigma_h = \sigma_p$, we can reduce Eq. 3.6 to:

$$U = \frac{\sigma v_{\rm th} n_i N_t}{2{\rm cosh}\left[\frac{\rm E_i - E_t}{\rm kT}\right]} \tag{3.7}$$

Identifying that a certain group of constants above has units of time, we can define the *carrier lifetime* τ — the time it takes to thermally generate an electron-hole pair on average, to get:

$$U = \frac{n_i}{2\tau} \tag{3.8}$$

And then to get the dark current in a pixel volume, scaling by the depletion depth $x_{\rm dep}$ and pixel area $A_{\rm pix}$ we arrive at the dark current rate in e-/pix/[Time] of:

$$\lambda_{\rm dep} = \frac{x_{\rm dep} A_{\rm pix} n_i}{2\tau} \tag{3.9}$$

Ref. [5] then walks us through the relation between temperature dependence and intrinsic carrier concentration (the number density of electrons/holes available in an undoped semiconductor) to finally give us an equation for for $\lambda_{\rm dep}$(T):

$$\lambda_{\rm dep} = \frac{x_{\rm dep} A_{\rm pix} c_n}{2\tau} T^{3/2} {\rm exp}\left(-\frac{\rm E_g(T)}{\rm 2kT}\right) \tag{3.10}$$

where E_g is the band-gap as a function of temperature, while c_n is a carrier density prefactor.

Since the carrier density and carrier lifetime are quantities that either have large associated systematics or are quoted inconsistently in literature, we fit a generic version of Eq. 3.10 with 2 free parameters, $\lambda_{\rm dep} = C_1 A_{\rm pix} x_{\rm dep} T^{3/2} {\rm exp}(-{\rm C_2/kT})$, where $C_{1,2}$ are a prefactor and a temperature independent energy scale in the exponential respectively. The results of

this fit are:

$$\begin{aligned} C_1 &= (1.74 \pm 0.26) \times 10^{14}\ \mathrm{cm}^{-3}\mathrm{K}^{-3/2}\mathrm{s}^{-1} \\ C_2 &= 0.51 \pm 0.03\ \mathrm{eV} \end{aligned} \tag{3.11}$$

This 2 parameter modified depletion dark current expression reproduces the observed data quite well as seen from Fig. 3.6 (dotted lines), suggesting its importance in accounting for the overall leakage current. While we have not included in the fit the energy dependence of the band-gap, the close value of C_2 to the Fermi level E_i of half the band-gap is in agreement with the expected microphysics.

3.3 Low-energy calibration

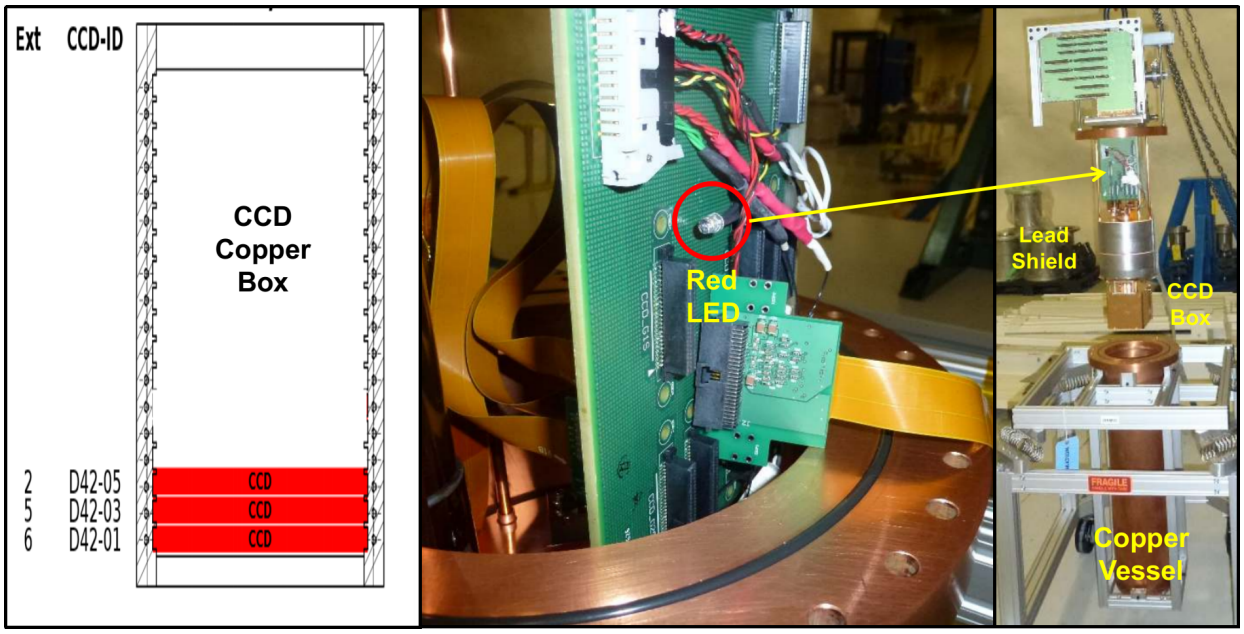

Figure 3.7: Schematic of Stage I DAMIC demonstrator, showing the location of the 3 CCDs and their extension labeling. A red LED was placed above and outside the CCD copper box, within the copper vacuum vessel, to provide the necessary illumination for the analysis presented in the text.

Accurate calibration and proof of its linearity is vital when dealing with a low energy experiment. The DAMIC at SNOLAB experiment uses an analysis threshold of 40 eV (driven by efficiencies and a pixel clustering threshold of $> 5\sigma_{\mathrm{pix}} \approx 5{\times}2\mathrm{e}^- \times 3.77\ \mathrm{eV/e}^-$) where it is tricky to use radioactive sources to calibrate. To determine the calibration constant k [ADU

e^{-1}] of CCDs down to this threshold we used optical photons from a red (≈700 nm) light emitting diode (LED) installed on the Stage I demonstrator setup (Fig. 3.7). These photons predominantly produce single electron-hole pairs via photoelectric absorption. Nine 4k×2k images, binned in 1×100 mode, were taken where the LED was flashed for a 20s exposure. The high-energy X-Ray calibration constants, k_{x}, for the 3 CCDs, from irradiation with an ^{55}Fe source during surface commissioning, are presented in Table 3.3.

Extension	**^{55}Fe Calibration Constant (k)** [ADU e^{-1}] $\epsilon = 3.77$ **eV** $\mathbf{e}^{-1}$
2	12.973(1)
5	13.835(1)
6	14.031(1)

Table 3.3: High-energy calibration constants for Stage I demonstrator from surface commissioning using 5.9 keV x-rays from an ^{55}Fe source, provided for 2 values of the pair creation energy ϵ. Calibration constants in DAMIC literature are always quoted using $\epsilon = 3.77$ eV e^{-1} unless otherwise specified.

A standard method [4, 6] to calibrate CCDs exploits the Poissonian nature of the charge detected in a pixel under constant light illumination. Several images are taken with the CCD exposed to a constant source of light. Then, for a given pixel, the number of charge carriers detected across all images will follow a Poisson distribution $N = \mathrm{Pois}(\lambda = \mathrm{I_l/k})$ with I_l the light intensity. By computing the ADU mean (μ_l) and variance (σ_l) after equalization, one can exploit the following relationship to determine the calibration constant:

$$\frac{E[N]}{\mathrm{Var(N)}} = \frac{I_l k^2}{I_l k} = k \equiv \frac{\mu_l}{\sigma_l^2}, \tag{3.12}$$

However for our dataset the computation is not straightforward due to the presence of varying light intensities complicating the analysis, as seen in Fig. 3.8 Left. One hypothesis is that thermal effects in the LED can lead to fluctuations in the power output (Ref. [7] measures up to 68% change in LED light intensities arising from thermal instability) breaking the inherent assumption in Eq. 3.12 of a constant light source. This leads to a skewed distribution for k, Fig. 3.8 Right. To account for the variation we instead used a Monte-Carlo approach briefly outlined as follows:

1. Select a seed value of the calibration constant k_{seed} within the distribution range shown in Fig. 3.8 Right.

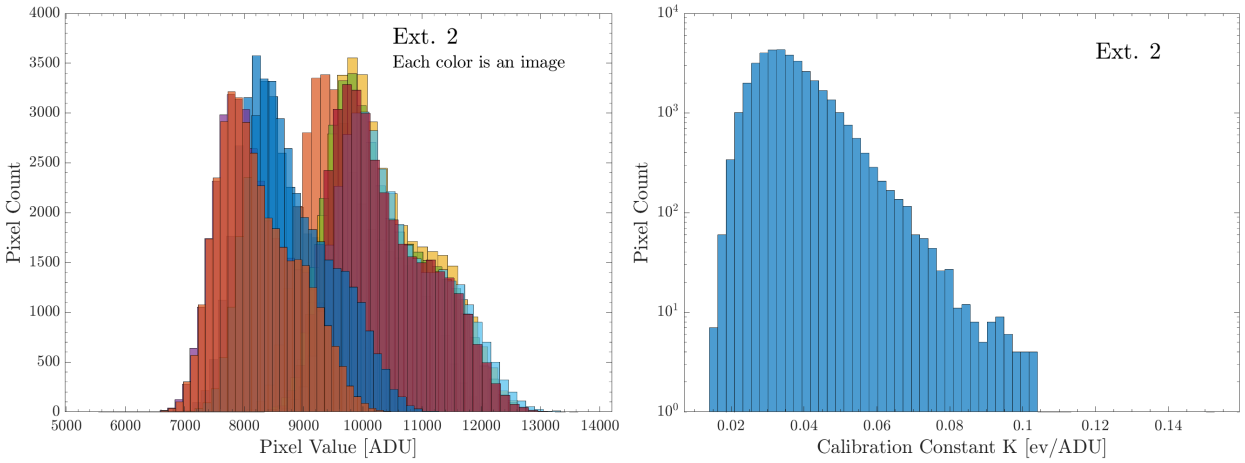

Figure 3.8: Left: Pixel distributions for Ext. 2 following exposure to a red LED. The shifts in the average pixel values are due to variations of LED light intensity. Right: The corresponding distribution of k showing significant deviations from the expected Gaussian distribution.

2. Generate an equivalent set of 9 images similar to the original dataset using this seed and a 2D light intensity profile fitted from each individual image.

3. Compute a new distribution of k_{MC}, and compare these to the original distribution using a Kolmogorov-Smirnov metric for equality.

4. For every seed value repeat from Step 3 $M = 100$ times and average over the resulting metrics, selecting the best seed as k_{final}

Given that the light intensity was a strong function of the row — an effect of the 100 row binning — this Monte-Carlo approach applied on a row-by-row basis allowed the measurement of the calibration constant for a range of energies around the threshold of the experiment, as seen in Fig. 3.9. Ext. 2 receives the most light, being at the top of the stack, and this is reflected by the 2 order of magnitude increase in the absorbed energy compared to the other extensions. We also see that Ext. 2 matches the gain from the ^{55}Fe x-ray unity line (dashed black), confirming the validity of this approach. At lower energies, and above the 40 eV detector threshold (dashed red line), we observe that the gain extracted from Ext. 4 and 6 is within 5% of the higher values. Thus, as the inset figure (using just the Ext. 5 and 6 points and published in Ref. [3]) summarizes, we can see that these CCD devices can be calibrated down to their clustering threshold and are linear within their operating region.

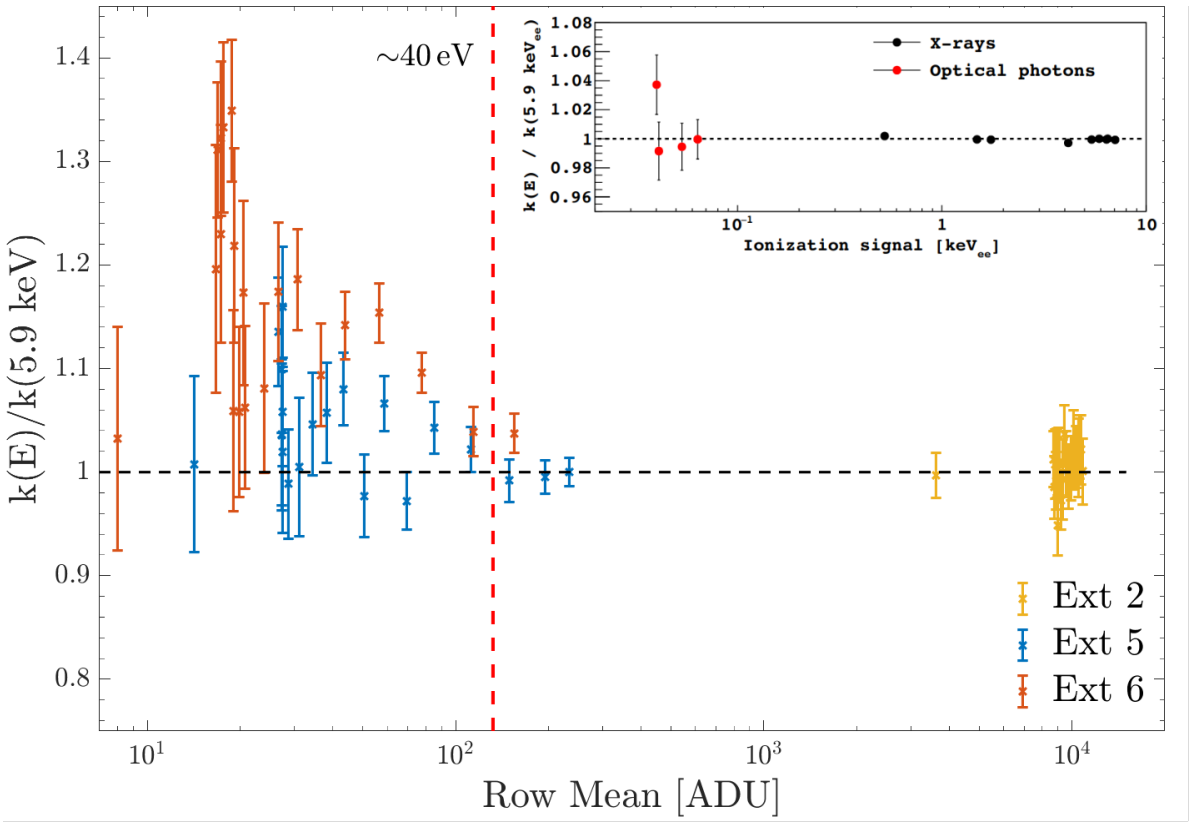

Figure 3.9: Monte-Carlo computed gain values for Ext. 2, 5, 6, scaled to their corresponding high-energy value from Table 3.3. Dashed horizontal line denotes unity while dashed vertical line is the 40 eV threshold. Inset: Published results, summarizing the LED points (red) along other separate x-ray calibration points at higher energies (black), reproduced from Ref. [3]

3.4 In-situ energy calibration of DAMIC at SNOLAB using emission peaks

The upshot of the commissioning problems outlined in Sec. 2.2.1 was that the 7 deployed CCDs for the Stage II experiment were poorly calibrated. This unfortunate situation necessitated a different approach to obtaining the calibration constant in the energy region of interest (0.05–15 keV) once the experiment was live. By searching for emission peaks from atomic species other than Silicon one can more precisely infer the energy scale of the experiment. Based on exploratory analysis, we expect the energy peaks listed in Table 3.4 and shown in Fig. 3.10 (red curve). The Cu lines come from the fluorescence of the surrounding Copper while the Bismuth x-rays are traced to the decay of the ^{210}Pb contaminant in the setup [1, 8]. The data (black points) displayed in that plot are roughly the full 864 1x100 science-run images (13.6 kg days exposure) from 2017-2018 with every extension calibrated

using $K = 2.6 \times 10^{-4}$ keV/ADU $\equiv$ a gain of 14.5 ADU/e- (assuming $\epsilon = 3.77$ eV/e-), a reasonable first estimate. However, fitting to the presumed Cu Kα data points (blue dashed) results in a ~ 4 times wider than expected peak while the overall template fit is poor, as seen by the high reduced χ^2.

Emission Line	**Energy** [keV]
Cu Kα	8.05
Cu Kβ	8.91
Bi Lα	10.84
Bi Lβ_4	12.69
Bi Lβ_2	12.97
Bi Lβ_1	13.02
Bi Lβ_3	13.21

Table 3.4: Relevant emission energies from Ref. [8] for the in-situ calibration template outlined in text.

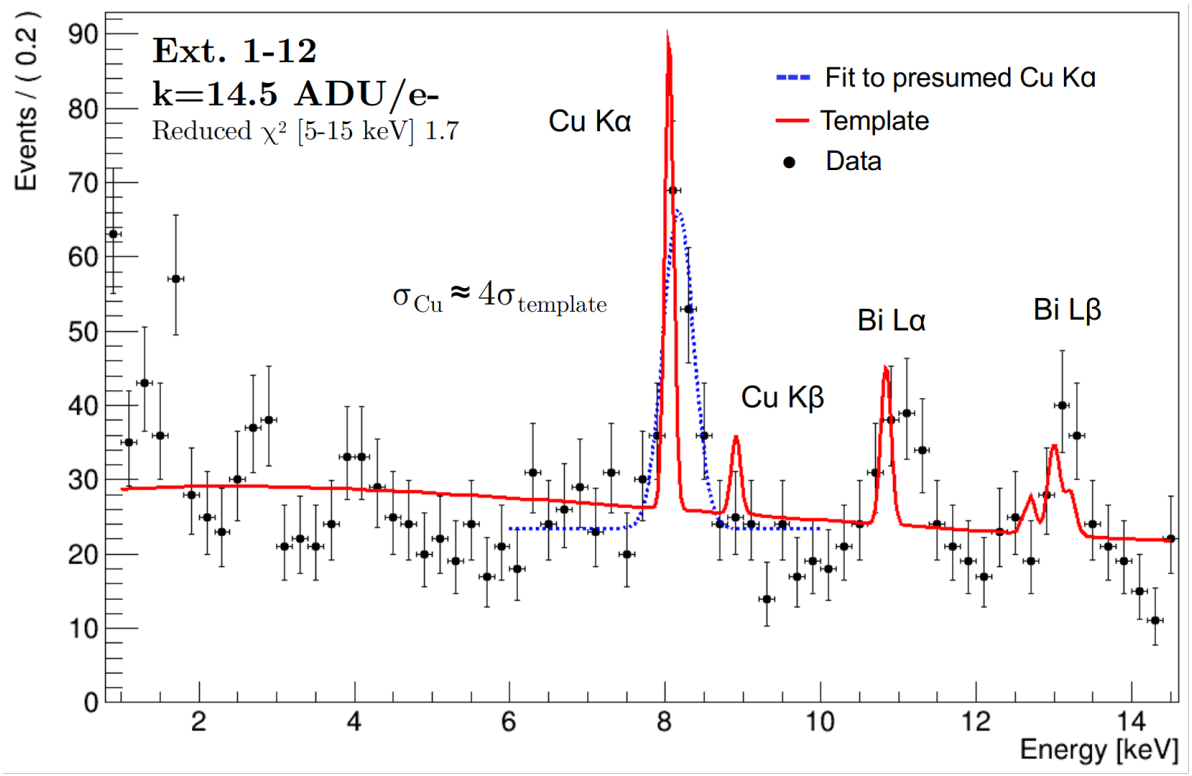

Figure 3.10: Template derived from Table 3.4 (Red). A naive fit to the presumed location of the Cu Kα peak (blue dashed) results in a width estimate much larger than noise and Fano expectations.

To correctly calibrate every extension, we do a binned log-likelihood fit to individual extensions with the aforementioned template model optimized over 4 free parameters:

- P - a multiplicative correction to the calibration constant
- F - a flat background level
- C - amplitude of the Cu fluorescence
- B - amplitude of the ^{210}Pb decay x-rays

An example of this fitting can be seen for Ext. 1 and Ext. 12 in Fig. 3.11 for cases of low and high statistics.

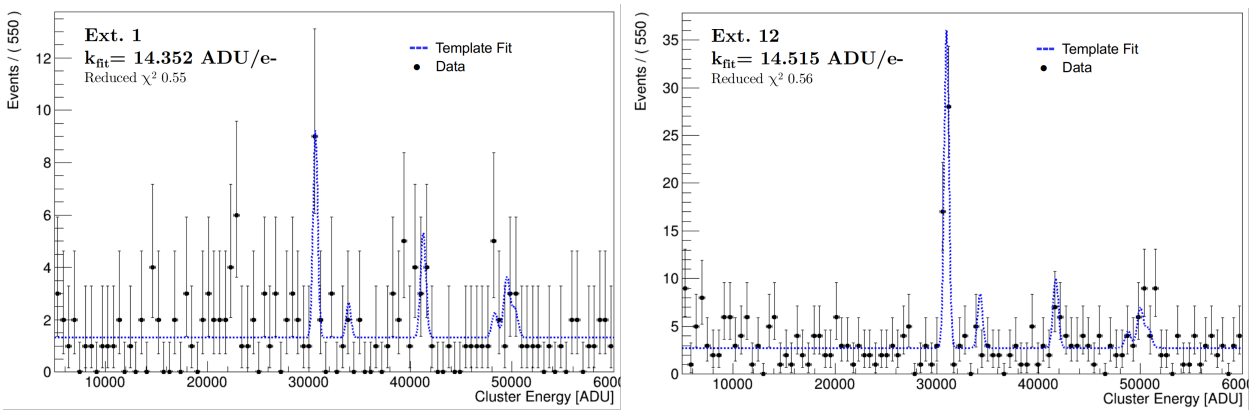

Figure 3.11: Fitting the emission template to individual extensions, shown here Ext. 1 and 12.

Combining the individual extensions, with multiplicative correction results reported in Table 3.5 along with final calibration constants, we end up with the overall energy spectrum shown in Fig. 3.12. We can visually appreciate, and confirm with the χ^2 value, the much improved template match. We do not report F, C, or B (the amplitudes of the individual template components) as they are not useful without the further context of an overall background model with a discussion of radioactive contaminants, selection cuts, and efficiencies — decidedly outside the scope of this work.

3.5 Energy calibration of a CCD using a gaseous source

Calibration methods like those outlined in Sec. 3.4 are last resorts when one is unable to get a commissioning measurement with systematics below a few percent. The preferred

Extension	**F, correction to K=2.6×10^{-4} keV/ADU**	**K$_{new}$** 10^{-4} [keV/ADU]	**gain** ADU/e-
1	1.014(3)	2.636(8)	14.30(4)
2	0.957(2)	2.488(5)	15.15(3)
3	0.979(2)	2.545(5)	14.81(3)
4	0.986(2)	2.564(5)	14.71(3)
6	1.009(5)	2.623(1)	14.37(7)
11	0.975(2)	2.535(5)	14.87(3)
12	0.998(1)	2.595(3)	14.53(2)

Table 3.5: Multiplicative corrections to individual extensions, along with their new calibration constant. We have assumed $\epsilon = 3.77$ eV/e- for computing the gain. The largest systematic uncertainty is likely differences to the x-ray energies reported in Table 3.4 followed by exclusion of non-dominant emissions in the fitting.

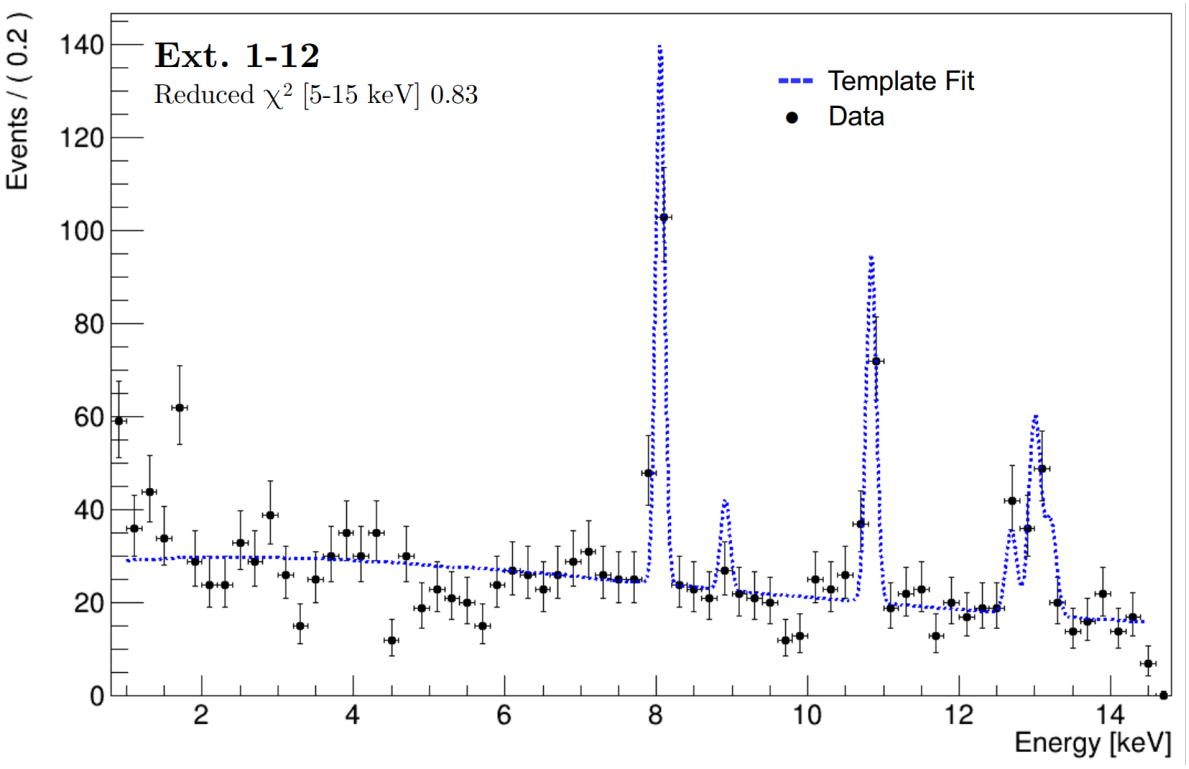

Figure 3.12: Post-calibration energy spectrum from combining individual calibrations performed on Ext. 1-12. The improved template match can be seen vs. the same data in Fig. 3.10. Calibration values per extension are provided in Table 3.5

energy calibration technique is to use either optical or radioactive line sources with fixed energies and reconstruct their interactions with the detector. Gaseous and liquid detectors like the XENON-1T [9] have used dissolved sources (e.g. ^{220}Rn, ^{83m}Kr) which are able to

be circulated within the detector material for a homogeneous calibration signal. Solid-state detectors have relied on static or solid sources (e.g. LEDs, ^{59}Fe) which have the disadvantage of having non-uniform exposure to all parts of the target. In the Stage III DAMIC-M design a tightly packed stack of 50 CCDs will require a calibration solution that can "see" the innermost devices while balancing the competing requirements of $\mathcal{O}$(keV) deposits without being attenuated by the surrounding CCDs.

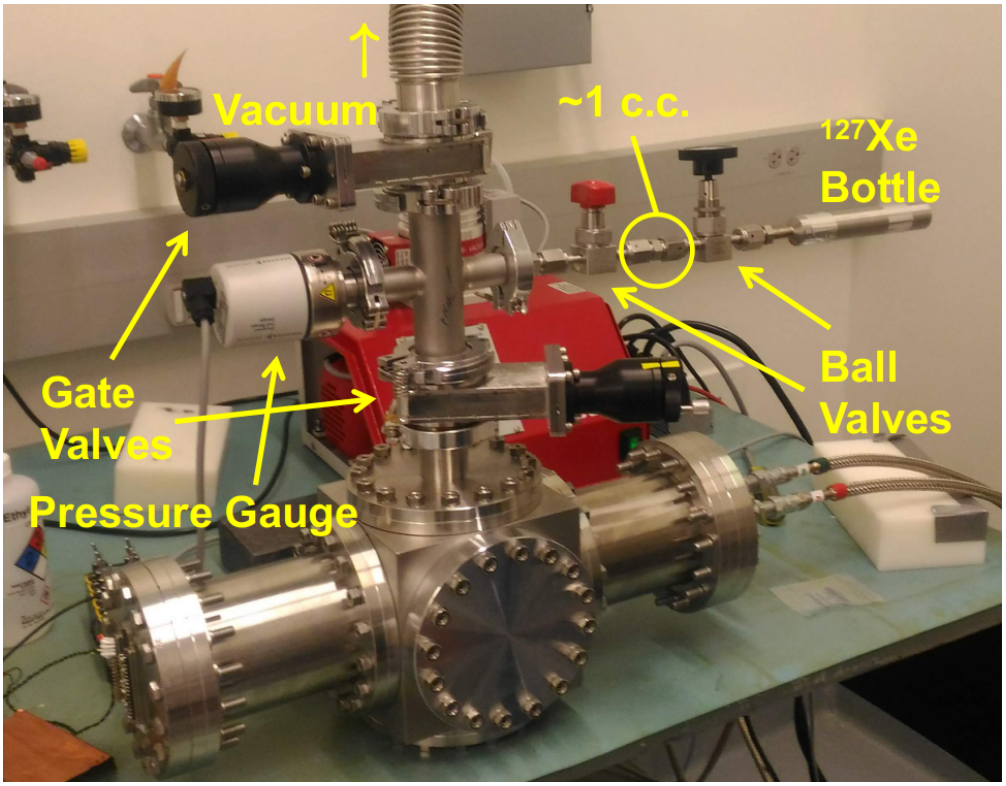

Figure 3.13: Chamber setup for ^{127}Xe gaseous calibration exercise. A 1 c.c. slug of Xenon from the bottle was released into the outlined holding area and then allowed to diffuse into the larger chamber by control of the highlighted ball and gate valves.

To that end, we exposed a a 4k x 4k, 675μm thick CCD in the UChicago calibration chamber to a gaseous ^{127}Xe source that would permeate the vacuum chamber and provide a bath of keV photons. The ^{127}Xe was produced at Fermi National Accelerator Laboratory (Fermilab) by irradiating a container of natural Xenon with a neutron beam. The ^{127}Xe isotope has a half-life of 36.35 days which is $\gg$ than any other isotope produced in this process [8]. A 50 c.c. bottle of this activated Xe, after a cooling period of 4 months to decay away other isotopes, was shipped to UChicago with an estimated activity of 100 nCi. Relevant emissions of ^{127}Xe are listed in Table 3.6. We do not consider electron emissions

due to the majority's inability to pass through the 2μm dead-layer on the surface of the CCD, as computed from the NIST ESTAR stopping power database [10].

Photon Emission	**Energy** [keV]	**# per 100 disintegration**
Lα	3.93	9.6
Lβ	4.22-4.57	
Kα	28.51	71.5
Kβ	32.44	16.42

Table 3.6: A condensed reproduction of the ^{127}Xe decay scheme from Ref. [8]. If the separation between lines is < the total resolution we only report the weighted average of the energy and intensity

A brief outline of the experimental procedure, with reference to Fig. 3.13, is as follows:

1. The vacuum line was gated off, along with closing the chamber.
2. A 1 c.c. slug of Xe was released into a holding volume and the bottle closed off.
3. The second ball valve was opened, allowing the Xe to occupy the cross-junction, with a measured pressure of 1.13 mbar per slug
4. The chamber gate was opened and the Xe allowed to diffuse into contact with the CCD.
5. The process was repeated from Step 1 until the bottle was emptied into the chamber (after $\sim$10 c.c. the entire bottle was directly opened to the chamber)

An immediate problem was that the chamber pressure of 1 slug was approx. 0.5 mbar but subsequent releases, including the final dump, only brought the total pressure up to 1.06 mbar. The melting point of Xe is approx. 161.4K and the CCD frame temperature was recorded to be 130K, with the cryogenic cold-head likely at a lower temperature than that. Thus, the Xenon in the chamber was probably frozen when in contact with the internal cold components, dropping the chamber pressure. This hypothesis was bolstered when attempting to evacuate the Xenon by opening the upper gate value to the vacuum, after which the pressure plateaued at 0.25 mbar with the vacuum under full power draw. The system had to be warmed up to room temperature and once chamber pressure returned to normal, the CCD was cooled down again.

Nevertheless, 639 files of 1040 seconds exposure+read time were obtained with the source in the partially frozen configuration, and 932 images with the same parameters were taken

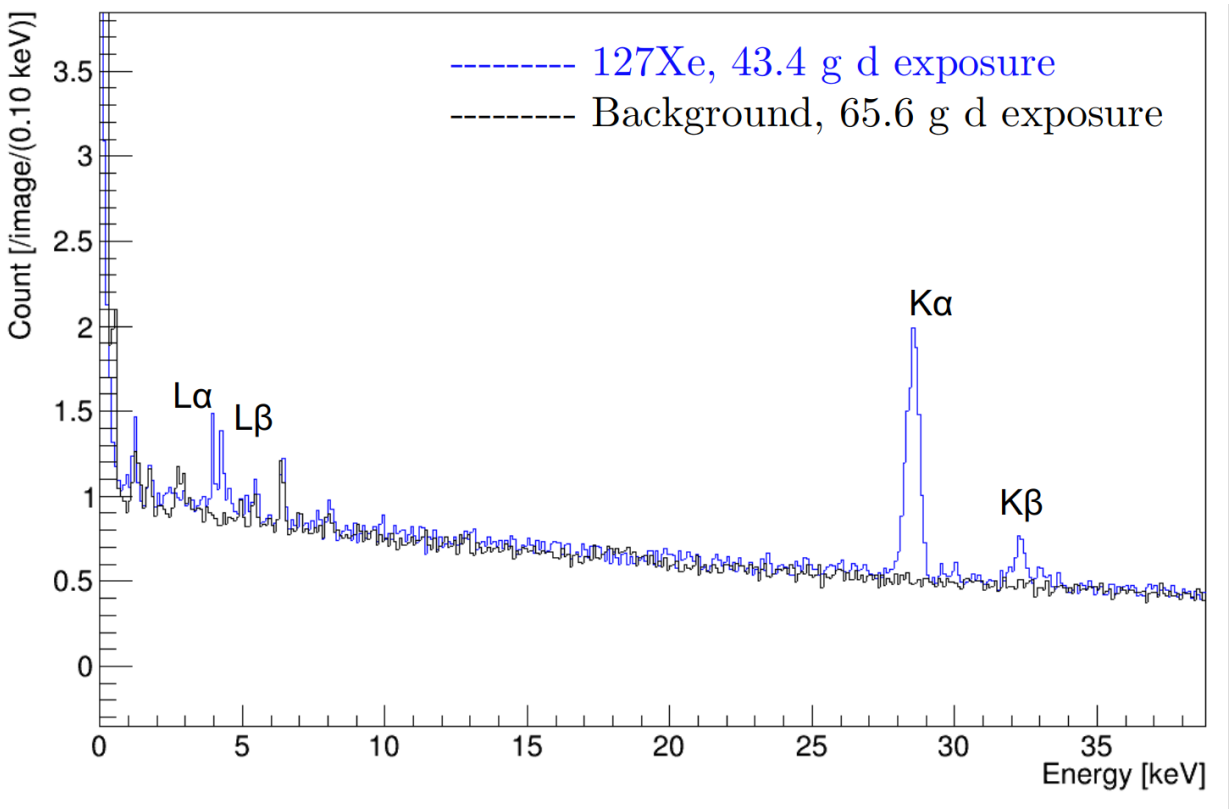

Figure 3.14: Energy spectrum from ^{127}Xe calibration (blue) and background (black), clearly showing the presence of x-ray peaks when the source is in the chamber.

for the background after the warming cycle. The resulting energy spectra of the two runs is presented in Fig. 3.14, clearly indicating the presence of x-ray peaks that can be calibrated to when the source is in the chamber. A more robust experimental setup for a publication quality analysis would require tracking of the irradiation and source production for an accurate measurement of activity and isotopic composition of the Xenon. Further, steps would need to be taken to prevent freezing, perhaps by operating at a higher temperature or with a different gaseous source. However this demonstration confirmed the applicability of gaseous calibration and based on a brief literature review is likely one of the first showing its validity for solid state detectors.

References

[1] Jing Zhou. *Direct dark matter detection with the DAMIC experiment at SNOLAB*. PhD thesis, The University of Chicago, 2015.

[2] Alvaro E Chavarria, Javier Tiffenberg, Alexis Aguilar-Arevalo, Dan Amidei, Xavier

Bertou, Gustavo Cancelo, Juan Carlos DOlivo, Juan Estrada, Guillermo Fernandez Moroni, Federico Izraelevitch, et al. Damic at snolab. *Physics Procedia*, 61:21–33, 2015.

[3] A Aguilar-Arevalo, D Amidei, X Bertou, M Butner, G Cancelo, A Castañeda Vázquez, BA Cervantes Vergara, AE Chavarria, CR Chavez, JRT de Mello Neto, et al. Search for low-mass wimps in a 0.6 kg day exposure of the damic experiment at snolab. *Physical Review D*, 94(8):082006, 2016.

[4] James R Janesick. *Scientific charge-coupled devices*, volume 83. SPIE press, 2001.

[5] Ralf Widenhorn, Morley M Blouke, Alexander Weber, Armin Rest, and Erik Bodegom. Temperature dependence of dark current in a ccd. In *Sensors and Camera Systems for Scientific, Industrial, and Digital Photography Applications III*, volume 4669, pages 193–201. International Society for Optics and Photonics, 2002.

[6] Vincent Lapeyrere, Pernelle Bernardi, J-T Buey, M Auvergne, and D Tiphène. Calibration of flight model ccds for corot mission. *Monthly Notices of the Royal Astronomical Society*, 365(4):1171–1179, 2006.

[7] Selcuk Sakar, Sarah Rönnberg, and Math HJ Bollen. Light intensity behavior of led lamps within the thermal stabilization period. In *2018 18th International Conference on Harmonics and Quality of Power (ICHQP)*, pages 1–6. IEEE, 2018.

[8] M.-M. Be, V. Chiste, C. Dulieu, M.A. Kellett, X. Mougeot, A. Arinc, V.P. Chechev, N.K. Kuzmenko, T. Kibedi, A. Luca, and A.L. Nichols. *Table of Radionuclides*, volume 8 of *Monographie BIPM-5*. Bureau International des Poids et Mesures, Pavillon de Breteuil, F-92310 Sevres, France, 2016. ISBN 978-92-822-2264-5.

[9] E. Aprile et al. Xenon1t dark matter data analysis: Signal reconstruction, calibration, and event selection. *Phys. Rev. D*, 100: 052014, Sep 2019. doi: 10.1103/PhysRevD.100.052014. URL `https://link.aps.org/doi/10.1103/PhysRevD.100.052014`.

[10] Martin J Berger, JS Coursey, MA Zucker, J Chang, et al. *Stopping-power and range tables for electrons, protons, and helium ions*. NIST Physics Laboratory Gaithersburg, MD, 1998.

CHAPTER 4

SILICON AS A TARGET MEDIUM FOR LOW ENERGY DEPOSITS

n.b. This chapter forms the basis of the preprint Ramanathan and Kurinksy [28]. The manuscript has been accepted for publication in Physical Review D at the time of writing and material and text from here will be found therein. Sections IV.D, V, and Appendix A of the paper have been reduced and/or cut appropriately here as they are primarily the work of my co-author. Copyright rests with the American Physical Society.

In Chap. 1 we discussed the idea of looking for types of light DM other than the standard WIMPs, but ran into the issue that the current DAMIC experiment of Chap. 2 would be unable to resolve the $\mathcal{O}$(eV) clusters that such DM candidates would deposit. However recent developments in silicon based particle detectors, in particular 'Skipper' CCDs that we will talk about in Chap. 7 and other technologies like cryogenic calorimeters [15, 31], have demonstrated the ability to count individual charge-pairs.

To use these detectors effectively we need to precisely identify the energy of the external particle. Generically, particle detectors work by measuring the deposited energy in an absorber material by one of three main avenues: charge production (ionization), photon production (e.g. scintillation) or collective excitations (phonons and plasmons), with further down-conversions intermixing these different production modes.

In a semiconductor like Si — where ionization plays a dominant role above the *band gap* E_g ($\sim$1.1 eV) — the deposited *recoil energy* E_r is often inferred from counting the number of electron-hole pairs created, n, by way of the *mean energy-per-pair* ϵ_{eh}. Due to the concurrent emission of phonons during the ionization process, $\epsilon_{eh} > E_g$ and ϵ_{eh} is only reflective of the aggregate response of the material. We can understand this with an example: suppose a particle interaction deposits 25 eV and seven-tenths of it goes to the phonon channel, then only $25-(25\cdot\frac{7}{10}=7.5$eV is left for ionization. Based on the band gap this is an ionization of roughly $7.5/1.1 \approx 7$ e$^-$which works out to $25/7 = 3.6$ eV/e$^-$which is in line with literature values. A linear relationship of this form can be seen for many materials, as illustrated by Fig. 4.1.

The other very important quantity is the *Fano factor*, F, which quantifies the dispersion of n for a given E and is sub-Poissonian (F<1). For deposits $\gg$50 eV and particularly past the K edge ($\sim$1.84 keV) in Si the statistical nature of this ionization process leads to an almost constant behavior in the values for ϵ_{eh} and F and thus provides for a simple relationship between the expected energy and what was counted.

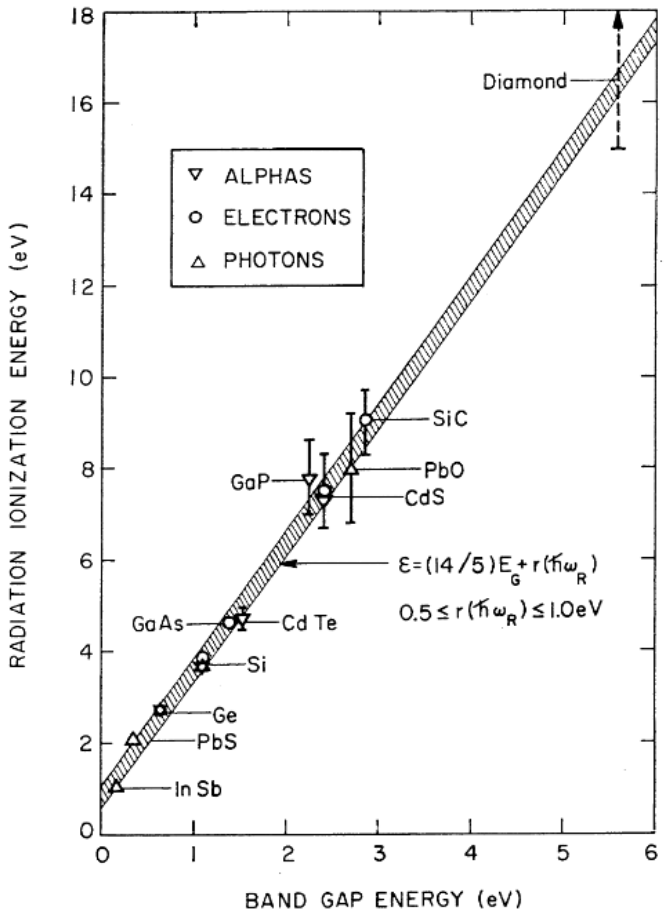

Figure 4.1: Relation between band-gap and charge yield for commonly used semiconductor and detector materials, plot taken from Ref. [18]

In this chapter we demonstrate that this relationship is not straightforward in the low-count regime. The finite band-gap, the complex features of the band-structure of crystalline Si which are not averaged out, and the width of the hole band have an impact on the charge yield in the regime between 12–50 eV. Disentangling the effect of ionization is vital for correctly attributing the response of the detector to the physics of dark matter or some other unmeasured process, such as potential signals from elastic nuclear recoil or the Migdal effect (ionization induced by the sudden shift of a recoiling nucleus) [16].

The existing literature on ionization response is vast and often delves deeply into the condensed matter foundations of this topic which perhaps does not serve well a practitioner from the particle-physics community. And so the goal of this work was to summarize and provide for a simple phenomenological model, well supported by data, allowing experimental collaborations using Si detectors to provide results on an equal footing. Similar work was

done by Refs. [6, 21] with particular focus on incorporating the shell structure of Silicon in the absorption process and in dealing with how the inner-shells (L_1, $L_{2,3}$, K) affect absorption at and above these edge energies. This is not particularly useful for our low energy, low count case and so we seek to refine and further the $\mathcal{O}$(eV) portion of absorption (i.e. where the valence band and M shells play a role).

In Sec. 4.1 we describe the four parts of our model: how to initially partition E_r, how subsequent down-conversion happens, how to fold in micro-physics effects, and finally how to synthesize these parts using a Monte-Carlo simulation approach. Next, Sec. 4.2 collates existing data available in the literature. Finally, Sec. 4.3 discusses how we apply our model to investigate and extract the micro-physics and energy dependence for the parameters in question, leading to the main result: computation of $p_n(E_r, T)$, that is the probability to ionize n charge-pairs at temperature T as a function of any deposited energy E_r.

4.1 Modeling Quantum Yield

The process we attempt to model is energy redistribution from an initial hot carrier (a hot carrier is any charge with momentum much larger than that accessible thermally; for high-purity Si at cryogenic temperatures *all* carriers produced by particle interactions can be considered hot) to the electron and phonon system, in particular the ionization of subsequent electron-hole pairs by the initial carrier, known as impact ionization. All of the initial recoil energy is given to a single electron-hole pair. The number of total electron-hole pairs created after the cascade process is typically calculated as

$$n = \frac{E_r}{\epsilon_{eh}(E_r)} \tag{4.1}$$

where ϵ_{eh} has been shown to be constant in the high-energy limit (see Table 4.1).

At low energy, when $E_r \sim \epsilon_{eh}$ we know that this formula should break down since we expect an integer number of charge-pairs well defined over a continuum of energies. In a perfect lattice, any ionizing interaction below E_g is energetically inaccessible, so this equation is undefined ($\epsilon_{eh} \to \infty$). For energies between E_g and $2E_g$, only one electron-hole pair is allowed by energy conservation, forcing a direct relationship between energy and ϵ_{eh} to ensure the mean is fixed. The uncertainty in this function therefore enters between $E_r = 2E_g$ and the high energy limit $E_r \gg E_g$.

This allows us to summarize the goal of this work as fully characterizing the behavior

Table 4.1: Literature values for the Fano factor F, mean energy per electron-hole pair ϵ_{eh} in the high-energy limit, band-gap energy E_g, the ratio A of phonon-carrier to carrier-carrier scattering, the valence band width W, the optical phonon energies $\hbar\omega_o$, and the plasmon energy $\hbar\omega_{pl}$. An earlier version of this table specific to Fano factor can also be found in Fraser et al. [14]. We summarize the energy gap at a few key temperatures, but all references have many more data points and focus on fitting measurements to the functional form of Varshni [36]; see there for more details. We exclude band-gap data from Macfarlane et al. [20], fit in [36], due to discrepancy with more modern methods which have seen widespread adoption (see for example Canali et al. [7]). For the last four values, these are not from quantum yield measurements. The Chang et al. [10] values come from hot-electron injection measurements.

Parameter	Value	Temperature	Source	Reference
F	0.118	110 – 240 K	5.9 keV γ	Lowe and Sareen [19]
	0.117	180 K	5.9 keV γ	McCarthy et al. [22]
	0.14 – 0.16	180 K	2 – 3.7 keV γ	Owens et al. [24][a]
	0.128	130 K	5 – 8 keV γ	Ramanathan et al. [29]
	0.119	123 K	5.9 keV γ	Rodrigues et al. [30]
ϵ_{eh}	3.66 eV	300 K	1 eV – 1 keV γ	Scholze et al. [34]
	3.66 eV	300 K	115 – 136 keV e,γ	Pehl et al. [25]
	3.63 eV	300 K	1 MeV e^-, 5.5 MeV α	Ryan [32]
	3.62 eV	300 K	5.5 – 6.3 MeV α	[25]
	3.67 eV	180 K	2 – 3.7 keV γ	[24]
	3.749 eV	123 K	5.9 keV γ	[30]
	3.75 eV	110 K	5.9 keV γ	[19]
	3.70 eV	100 K	5.5 MeV α	Canali et al. [7]
	3.72 eV	6 – 70 K	480 keV γ	Dodge et al. [12]
	3.72 eV	5 K	5.5 MeV α	[7]
E_g	$\sim$1.12	300 K	Photoabsorption	Alex et al. [1]
	1.127	290 K		Bludau et al. [4]
	1.164	110 K		[4]
	1.166	90 K		[4]
	1.169	0 K		[1]
	1.170	0 K		[4]
A	5.2 eV[2b]	300 K	2 – 5 eV e^-	Chang et al. [10]
$\hbar\omega_0$	59 meV (TO), 62 meV (LO)	N/A	DFT[c]	Jacoboni and Reggiani [17]
W	12 eV	N/A	DFT	Scholze et al. [33]
$\hbar\omega_{pl}$[d]	16.6 ± 0.1 eV	N/A	EELS[e]	Chen et al. [11]

[a] See also Owens et al. [23]

[b] Data compared to the value obtained by Alig et al. [3]

[c] Calculated from density functional theory (DFT), assumed temperature independent; see [17] for more details.

[d] We did not do an exhaustive survey of plasmon energy measurements as they were not important for the detailed low-energy modeling, but we expect there is some uncertainty in this value beyond the statistical uncertainty on this measurement.

[e] Electron energy-loss spectroscopy

first of ϵ_{eh}:

$$\epsilon_{eh}(E_r) = \begin{cases} \infty & E_r < E_g \\ E_r & E_g \leq E_r < 2E_g \\ \epsilon_{imp}(E_r) & E_r \geq 2E_g \\ \epsilon_{eh,\infty} & E_r \to \infty \end{cases} \tag{4.2}$$

where $\epsilon_{imp}(E_r)$, the mean energy imparted by impact ionization, is the unknown function.

This process also has a variance $\sigma^2(E_r)$, commonly related to the mean energy by the Fano factor [13]:

$$F(E_r) = \frac{\sigma^2(E_r)}{n_{eh}(E_r)} = \frac{\sigma^2(E_r)\epsilon_{eh}(E_r)}{E_r} \tag{4.3}$$

This factor, too, has an energy dependence, and in the high-energy limit some measurements have been made, but this parameter is far less well constrained (see Table 4.1). From energy conservation, $F = 0$ below $2E_g$ and like the mean, has an asymptotic limit. The function is therefore

$$F(E_r) = \begin{cases} 0 & E_r < 2E_g \\ F_{imp}(E_r) & E_r \geq 2E_g \\ F_\infty & E_r \to \infty \end{cases} \tag{4.4}$$

This two-component model has been repeatedly validated for energies >6 keV (see Table 4.1). A straightforward extension to lower energies, a placeholder often used in literature when discussing low energy phenomena, is to modify the piece-wise descriptions above to $\epsilon_{imp} = E_r$ and $F_{imp} = 0$ for $E_g < E_r < \epsilon_{eh}$; we refer to this as the "Simple Model" hereafter. Our goal here however is to explore a phenomenological model which stitches together the near-gap and high-energy limits based on available experimental measurements. This requires a framework for calculating ϵ_{imp} and F_{imp}. We begin by breaking down the calculation into constituent components, and then explore calculations made under different assumptions, as well as implications for Fano factor modeling.

Following Wolf et al. [38], we calculate the number of electron-hole pairs generated as

$$n(E_r) = 1 + \int_{E=0}^{E_r - E_g} dE P(E, E_r) \langle N(E) \rangle \tag{4.5}$$

where $P(E, E_r)$ is the probability distribution of generating a hole or electron of energy E relative to the top or bottom of the respective band, given an energy deposition E_r, and $\langle N(E) \rangle$ is the quantum yield, the average number of charges produced by impact ionization

by a carrier with initial energy E above gap [1], assumed identical for electrons and holes. By definition, if the carriers do not impact ionize any additional electron-hole pairs, $n(E_r) = 1$.

4.1.1 Initial Energy Distribution

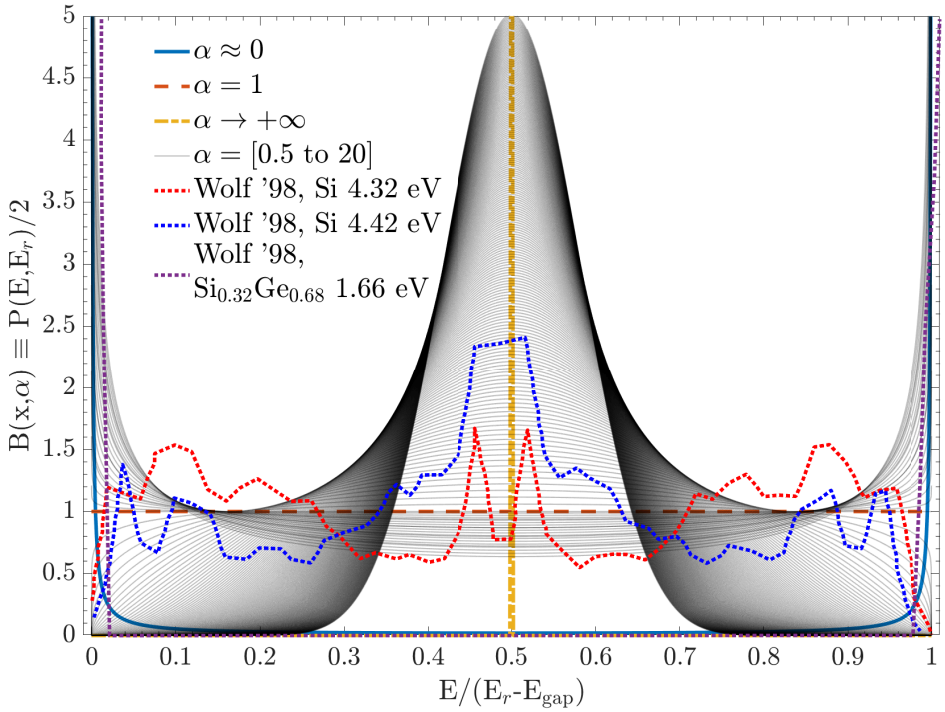

Figure 4.2: Evolution of the finite support Beta distribution, used to model the double probability distribution P(E,E_r), for selected values of shape parameter α. The $\alpha \to 0$ case corresponds to all the deposited energy going to a single carrier. The $\alpha = 1$ scenario is a uniform distribution, while $\alpha \to \infty$ corresponds to an equal energy splitting. Overlaid (dotted lines) is data extracted from Wolf [38] for Si at 4.32 and 4.42 eV (derived from internal quantum efficiency measurements of a Si solar cell) and $Si_{0.32}Ge_{0.68}$ at 1.66 eV (numerical calculations), indicating the general evolution even over a small energy range between the different regimes of energy partitioning between hot carriers.

The role of $P(E, E_r)$ is to describe how energy is distributed between the carriers in the electron-hole pair, and is normalized in E by definition to 2 (one electron and one hole per pair). The full treatment used by Ref [38] is to treat carriers equally, such that this function

1. Note that E_r is the total absorbed energy, measured from the top of the valence band, while E is the energy above the bottom of the conduction band for electrons or below the top of the valence band for holes.

obeys the symmetry relationship

$$P(E, E_r) = P((E_r - E_g) - E, E_r) \tag{4.6}$$

where, for small energies, we find the distribution is highly peaked around $E = 0$ and $E = E_r - E_g$. The robust calculation involves a summation over allowed energy states for the conduction and valence bands given the transition matrix element for photon absorption, and that model will be included in our comparison of calculations. The symmetry of this function, however, allows for three simplifying assumptions to capture the full range of possible outcomes:

1. $P(E, E_r) = \delta(E) + \delta(E_r - E_g - E)$ – A peaked distribution for maximal energy imbalance, approximately true for very low energy transfer (referred to in the following as 'all to one');

2. $P(E, E_r) = 2\left[E_r - E_g\right]^{-1}$ – A flat distribution, approximately true for $E_r >> E_g$ (referred to the following as 'uniform');

3. $P(E, E_r) = 2\delta(E_r - E_g - 2E)$ – A peaked distribution at half of the above-gap energy, which occurs for E_r around resonance features near the ~ 3.4–$4.2\ eV$ direct-gap transitions in Si (referred to in the following as 'equal split'). This is also the case that minimizes overall impact ionization, which is a strong function of energy.

We extend these three cases to the one-component model described by the one-parameter beta distribution

$$P(x|\alpha) = \frac{2}{B(\alpha)} x^{\alpha-1}(1-x)^{\alpha-1} \tag{4.7}$$

where $x = \frac{E}{E_r - E_g}$ and $B(\alpha)$ is the one-parameter Beta function used to normalize the probability distribution. One can see that this function has the same symmetry as $P(E, E_r)$, and each case above has a corresponding α value: case 1 corresponds to $\alpha \to 0$, case 2 to $\alpha = 1$, and case 3 to $\alpha \to \infty$. These cases, and more general cases for a range of α values found in this paper, are shown in Fig. 4.2.

We can qualitatively compare the shape of this distribution to the calculations done by Ref. [38], to set expectations for how α scales with energy. We see that, for $E_r \sim E_g$, the excess energy is given entirely to either the electron or hole, and we expect $\alpha \to 0$ in the low energy limit. Around $E_r = 4.3 - 4.4$ eV, see Fig. 4.2, we observe a transition from equal energy split to more uniform energy sharing, corresponding to a rapid increase in α through

1 to $\alpha > 1$. Ref. [33] notes that the hole valence band width W is only 12 eV wide, and thus we expect in the high-energy limit that the electron takes the majority of the energy; so we expect the applicability of our $P(E, E_r)$ description to lessen due to its inability to capture the narrower allowed space for the hole energy and the asymmetry of the distribution.

4.1.2 Impact Ionization Model

The second leg of the yield model is the quantum yield impact ionization function $\langle N(E)\rangle$, which we recollect describes the mean number of electron-hole pairs produced by a hot carrier with initial energy E. This function is bounded by two extremes; in the limit of maximal impact ionization, up to $\langle N(E)\rangle = E/E_g$, electron-hole pairs can be created (rounding down to the nearest integer), and in the limit of no impact ionization, $\langle N(E)\rangle = 0$. In the second case, energy is largely dissipated by phonon emission, meaning that the true $\langle N(E)\rangle$ is thus determined by a rate balance between impact ionization and phonon emission as a function of energy. Ref. [17] shows that the dominant phonon-scattering mechanism in these energy ranges, both by rate and total energy dissipated, is through the emission of optical phonons, and thus acoustic phonon emission can be neglected in impact ionization modeling.

As in Ref. [38], we adopt the 'Alig' impact ionization model outlined in Ref. [3]. In this model, only two energy dissipation processes are considered: electron-hole pair creation, and emission of a phonon of energy $\hbar\omega_0$. In Si, $\hbar\omega_0 \sim 63$ meV [17], so a charge carrier well above the gap energy can easily create many optical phonons. If the rate of electron-hole pair creation is $\Gamma_{eh}(E)$ and phonon production is $\Gamma_{ph}(E)$, then the probability of generating an electron-hole pair at a given energy is dependent only on the ratio of these rates, found to be

$$\frac{\Gamma_{ph}(E)}{\Gamma_{eh}} = A\frac{105}{2\pi}\frac{(E-\hbar\omega_0)^{1/2}}{\left(E-E_g\right)^{7/2}}. \tag{4.8}$$

Here A is a constant of the system, defined as

$$A = \frac{|M_{ph}|^2}{|M_{eh}|^2}\frac{4\pi^4}{V\Delta}\left(\frac{\hbar^2}{2m}\right)^3 \tag{4.9}$$

where V is the semiconductor volume, Δ is the volume per electronic state, m is the free particle mass, and $|M_{ph}|$ ($|M_{eh}|$) is the phonon (electron) scattering matrix element.

This enables us to calculate the charge production probability of a particle with energy

E_i, using Eq. 4.8, as

$$p_{eh} = \left[1 + \frac{\Gamma_{ph}(E_i)}{\Gamma_{eh}(E_i)}\right]^{-1}. \tag{4.10}$$

The elegance of this model is that it is able to reduce the complex micro-physics of the problem to one phenomenological constant, A, which can be tuned to match experimental values. This is beneficial due to the complex nature of electron-electron interactions at this energy scale.

There are a number of simplifying assumptions made in this model which need to be explicitly stated. The electrons and holes are assumed to be free particles to first approximation, and therefore scattering is isotropic and effective masses are vacuum masses. It assumes all states are equally accessible, and therefore that the matrix element for each transition is identical. We do however constrain the hole energy $E_h \leq W$, where W is the maximum width of the hole band. All these assumptions are akin to assuming interactions are highly athermal and occur far enough above the band-gap that the detailed band structure is negligible. It also simplifies phonon scattering substantially, allowing for a single, quantized phonon energy, ignoring the multiple optical phonons and the continuum of acoustic phonon energies [17].

The latter assumption is justified by the rate difference mentioned earlier; the optical phonons all have comparable energy, so the impact of having multiple distinct energies is small. The former assumption comes from the high density of states for particles far above the band-gap, but nonetheless makes A a non-physical parameter, and requires explicit validation of this model before it can be considered predictive. The benefit is that A can be tuned to produce the correct ϵ_{eh} in the large energy limit, where it is the only degree of freedom since the interplay between parameters like α and W will wash out to a constant ϵ_{eh} and F, meaning that the success of the impact ionization model matching data across many energy scales validates its underpinning assumptions (see e.g. Refs. [9, 10, 38]). Nevertheless, we should keep in mind that, in practice, A may be a function of temperature or substrate purity, among other possible effects. This is likely to be the leading systematic in applying this model to regimes which have not been validated (e.g. $T < 5$ K, or highly-doped substrates).

The last mode of energy dissipation that needs to be accounted for is plasmon production [26]. The 'Alig' model [3] makes the simplifying assumptions that energy redistribution is largely done through conservative creation of plasmons above the plasmon energy $\hbar\omega_{pl}$, and below this value energy redistribution proceeds according to the charge-phonon scattering balance model. This implies that charge production should be linear above this energy, which matches what is measured experimentally (see Table 4.1). In our implementation, we split

the total energy into $n_{pl} = \lfloor (E_r - E_g)/\hbar\omega_{pl} \rfloor$ plasmons of energy $\hbar\omega_{pl}$ with a final electron that has energy $E_r - E_g - n_{pl}\hbar\omega_{pl}$. This implicitly assumes that the total energy is evenly divided among plasmons of a fixed energy, and that those plasmons decay by production of an electron-hole pair with total energy equal to the plasmon energy. We do not observe any impact on the ionization yield by adding or removing this mechanism in agreement with the conclusions of Ref. [3].

4.1.3 Temperature Dependence

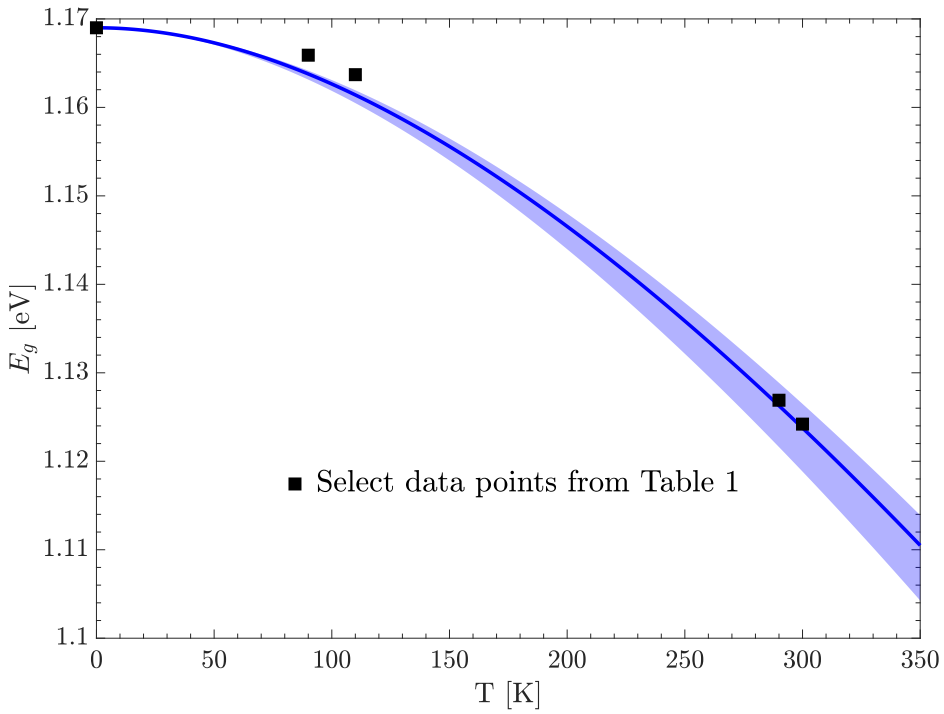

Figure 4.3: Evolution of band gap as a function of Silicon temperature from Eq. 4.11 (solid line) showing $\pm 1\sigma$ bands (shaded region) and a characteristic sample of data points from Table 4.1.

A final, important consideration we make in this paper is the effect of temperature dependence on the ionization yield. Detectors relevant to rare event searches are often operated cryogenically in order to mitigate high dark rates at room temperature, in the temperature range below 120 K down to ∼10 mK. Given the simplified nature of the band structure for the ionization model discussed above, we incorporate temperature dependence purely through the variation of the gap energy, as first described by Varshni [36] and given

by Eq. 4.11:

$$E_g(T) = E_g(0) - \frac{aT^2}{T+b} \tag{4.11}$$

where we take $E_g(0)$=1.1692, $a = (4.9 \pm 0.2) \times 10^{-4}$ eV and $b = 655 \pm 40$ K following the results of Alex et al. [1] who experimentally measure the photoluminescence spectra of crystalline silicon up to 1000 K. The resulting gap energies, plotted in Fig. 4.3, are in general agreement with other values in Table 4.1. It should be noted that this equation is purely phenomenological, but can successfully fit the temperature dependence of the band-gap across many semiconductors [36]. Other forms, such as piece-wise quadratic fits [4], have been used as well, and give similar results.

While one can discuss tuning the gap energy independently without modifying temperature, that is a distinct effect with many potential causes. We recognize the primacy of temperature as an experimental input, and thus argue that any change in T can be seen to first approximation as a change in E_g.

The only other parameters that may show a temperature dependence are A and the phonon energy $\hbar\omega_0$. Because these processes are highly athermal, however, we fix them in our model, and expect that any change in these parameters due to temperature is subdominant to the systematic uncertainties on their nominal values. As we will briefly see in Section 4.3, a change in gap is sufficient to match temperature dependent results from the literature, validating this approach.

4.1.4 Monte-Carlo Simulation

We are now in a position to combine elements of the previous subsections into a cohesive structure. To compute p_n, ϵ_{eh} F, and $\langle N(E) \rangle$ we employ the Monte-Carlo algorithm of Alig [2], following the schematic shown in Fig. 4.4 extracted from Ref. [3]. A single external particle deposits energy E_r, and with selected parameters A, $\hbar\omega_0$ and E_g triggers a cascade briefly outlined as follows:

1. If $E_r > E_g$, we generate an electron and a hole with energies given by $P(E, E_r)$ (with the imposed simulation constraint forcing the hole energy E_h to be less than W); otherwise, if $E_r < E_g$ the chain terminates.

2. We follow each particle as it down-converts. Any electrons with energy $>\hbar\omega_{pl}$ are assumed to create plasmons of quantity $n_{pl} = \lfloor E_i/\hbar\omega_{pl} \rfloor$. These are individually treated as impact ionizations.

3. We calculate the charge production probability p_n of a particle with energy E_i using Eq. 4.10. We select ionization or phonon production according to this probability.

4. If a phonon is produced, then energy $\hbar\omega_0$ is lost in the medium and the process loops back to step 2. with new energy $E_{i+1} = E_i - \hbar\omega_0$.

5. If instead an ionization event occurs then 3 new particles are effectively created — the original plus an electron and a hole, with a total energy of $E_i - E_g$ due to the release of the new electron-hole pair. We assume here that the conduction and valence bands are isotropic and parabolic, and that all states are available to the new scattered products. The split between these 3 particles results in energies $E_{i+1,e,h}$ with values given by integrating over the density of states (see Section II.B. in Ref. [2]) and where E_{i+1} is the new energy of the original particle. Here is where, post-hoc, we set $E_h \leq W$, also applicable to the original particle if it is a hole, and re-split the difference in energies uniformly between remaining carriers.

6. If $E_{i+1} < E_g$then the process terminates and only $E_{e,h}$ are fed back into step 2. otherwise all 3 particles are independently looped back to step 2.

This process continues until all tracked particles have kinetic energy below E_g, including those produced by the plasmons, resulting in the production of n electrons (and holes). Repeating this nested approach a few thousand times per energy, yields a distribution of charge pairs — normalization of which gives the requisite probability of pair-creation p_n. We can from these simulations obtain the quantum yield and Fano factor as:

$$\begin{aligned} \langle N(E) \rangle &= \sum_{n=0}^{\infty} n p_n \\ \langle N(E)^2 \rangle &= \sum_{n=0}^{\infty} n^2 p_n \\ F &= \frac{\langle N(E)^2 \rangle - \langle N(E) \rangle^2}{\langle N(E) \rangle} \end{aligned} \tag{4.12}$$

4.2 Data

The specific data for quantum yield and Fano factor in Si considered in this paper are summarized in Table 4.1. Most of the available measurements of F and ϵ_{eh} are made at high energy, and these measurements are broadly consistent with each other. There are few

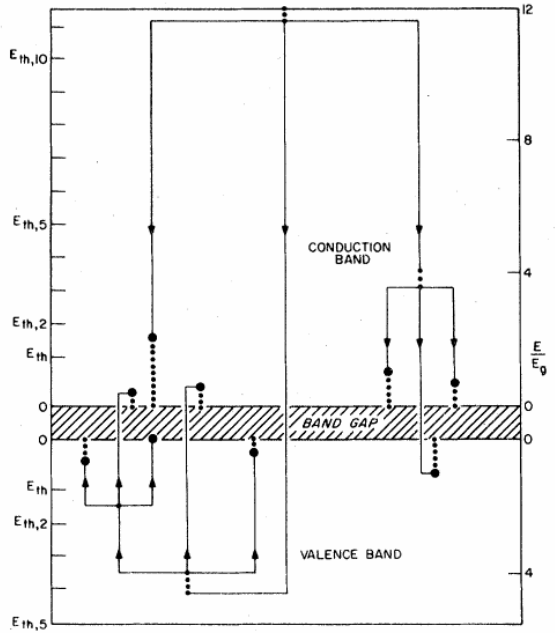

Figure 4.4: Diagram of an impact ionization cascade extracted from [3], implemented in our Monte-Carlo. Kinetic energy of the particles is represented in the vertical axis. Ionizations are indicated by a 3-way branch while phonon emissions are indicated by a dashed line. A particle with $12E_g$ energy starts at the top and the cascade shows all its daughter particles as they undergo similar down conversions until everything thermalizes to below the band gap energy (shaded grey region).

references which make measurements between 2.4 eV and 1 keV, the energy range in which our models show the most variation:

1. Chang et al. [10] measure electron impact ionization via injection of hot electrons of known energy into a Si transistor. Their measurements validate the impact ionization model of Alig et al. [3] up to 5 eV and can visually be seen in Fig. 4.5

2. Wolf et al. [38] measure quantum yield for photon absorption between 2.5 eV and 5 eV, and compare it to the quantum yield predicted by the Alig et al. [3] model and an energy-sharing distribution determined from summing over momentum eigenstates from band structure calculations, but do not directly comment on ϵ_{eh} or F as relevant for Table 4.1.

3. Scholze et al. [34] measure ϵ_{eh} at 300 K between 3 and 1500 eV, with a gap between 8 eV and 50 eV, using a Si photodiode in an X-ray beamline. The span of this data is useful for extracting an α curve as a function of photon energy at room temperature, as we will discuss in Sec. 4.3.2.

4. Canfield et al. [8] and Wilkinson et al. [37] come from spectral irradiation of Si photodiodes at unspecified temperatures, assumed to be ambient.

5. Borders et al. [5] include measurements from averaged surface integration tests of the Hubble Wide Field Camera 3 CCDs at 224 K, under light exposure.

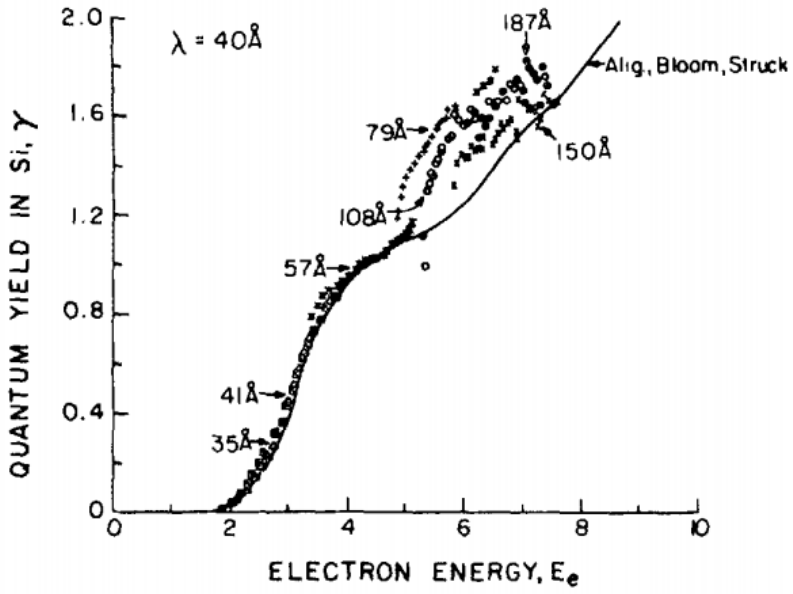

Figure 4.5: Validation of impact ionization of Alig model from hot electron injection into an Si transistor, taken from [10], showing that up to 5 eV the data tracks the theoretical line. The deviation above this energy is attributed by the authors to tunneling effects spreading out carrier energies.

The gap in the Ref [34] data is reflective of a broader "UV-gap" in the region between VUV and X-ray energies caused both by lack of tunable sources and the very short mean free path of photons in this energy range in all materials (see e.g. Ref. [35]). For wavelengths below ∼8 eV, photons from a thermal or athermal source can penetrate through thin windows and coatings, and enough deposition occurs in the Si to be distinguished from quenched surface events. Above 8 eV, very few table-top sources exist, and only specialized windows can transmit light with adequate efficiencies. At 50 eV and above X-ray fluorescence sources become available[2]. At these energies, the photoelectric cross section also begins to drop, and high intensity light can be generated and propagated to the detector through thin metal windows [34]. For these reasons very little data exist over this 40 eV energy gap, and in the

2. The lowest Kα line is found in Lithium at 52 eV

following section we discuss the extrapolations we employ to stitch together the quantum yield across this gap.

4.3 Results

We begin this section by exploring through simulation the effects of the parameters A and E_g at ∼100 eV ($>>E_g$) on ϵ_{eh} and F, allowing us to fold in the effects of temperature. Next, we present the results of fitting our single-parameter model to data to finally produce the pair-creation probabilities $p_n(E,T)$.

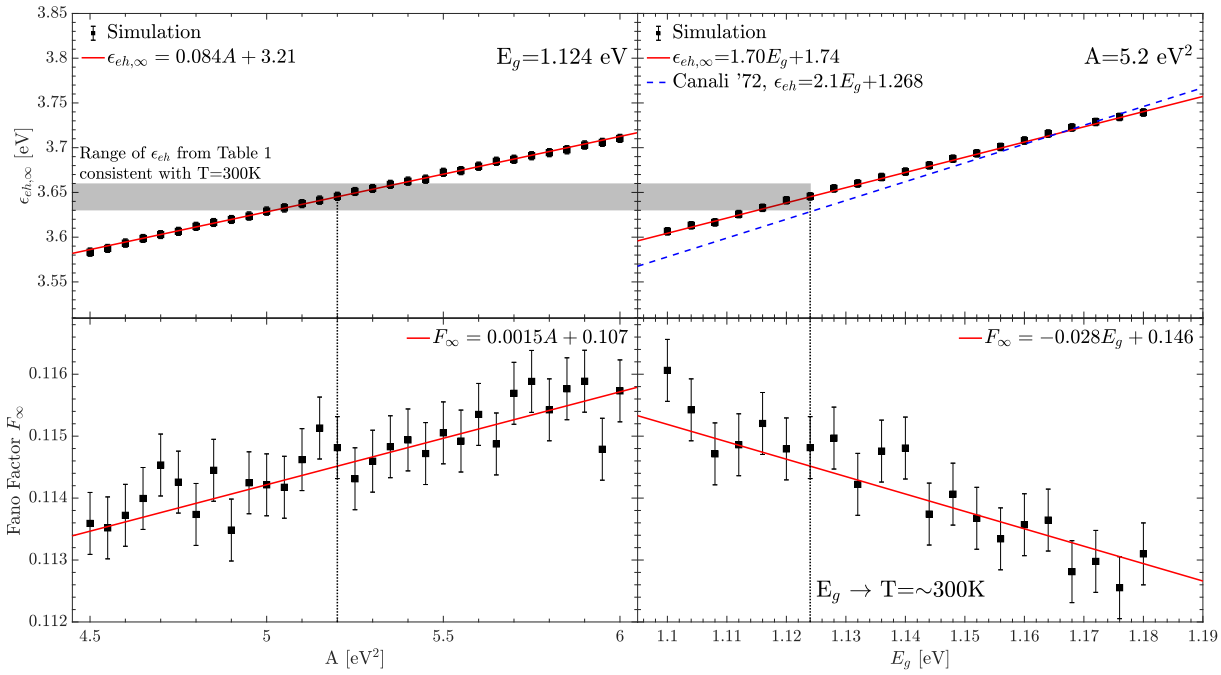

Figure 4.6: Left: Simulation of dependence of both mean energy-per-pair $\epsilon_{eh,\infty}$ (top) and Fano factor F_∞ (bottom) at the 300 K slice (E_g= 1.124) on the A parameter, the propensity for energy loss to occur due to phonon emission (larger A) versus ionization, as represented from Eq. 4.9. Linear fits, and corresponding equations, are also provided (solid red lines). The scatter in data points is due to Monte-Carlo statistics. Right: Simulation of Mean energy-per-pair $\epsilon_{eh,\infty}$ (top) and Fano factor F_∞ (bottom) dependence on band-gap energy $E_g$at the A=5.2 eV^2 slice. The temperature effect is expressed by varying the band-gap energy according to Eq. 4.11. Linear fits, and corresponding equations, are also provided (solid red lines). A fit from Canali *et al.*, Ref. [7], for E_g is also shown (dashed blue) demonstrating the general capture of features seen in data. The scatter in data points is again due to Monte-Carlo statistics.

4.3.1 Micro-physics dependence

To investigate the effects of both temperature, by proxy of gap energy E_g as through Eq. 4.11, and changes in the probability of phonon emission A, we compute the dependence of both ϵ_{eh} and F on these parameters via simulation. Based on linear behavior across both dimensions for both quantities, we identify the global relations at high-energy as:

$$\epsilon_{eh,\infty} = 1.7E_g + 0.084A + 1.3, \tag{4.13}$$

$$F_\infty = -0.028E_g + 0.0015A + 0.14 \tag{4.14}$$

via least-squares regression. We confirm the consistency of both the model and of selecting $A = 5.2$ eV^2, matching the original derivation in Ref. [3] and the empirical validation in Ref. [10], by noting that the resultant ϵ_{eh} values are in agreement with Table 4.1 at 300 K, seen by the confluence of dashed lines in the planar slices of Fig. 4.6.

Fano values, shown in Fig. 4.6 (bottom) are constant at the 2% level, but undershoot literature as per Table 4.1. For example, the most recent measurements of the Fano Factor in Si from Rodrigues *et al.* [30], using a device with single charge resolution, indicate $F = 0.119(2)$ at 123K which at first blush is inconsistent with Figs. 4.3, 4.6. We note that unlike for ϵ_{eh}, our model is not tuned for a specific Fano factor, and thus should be predictive. However the discrepancy observed between Fano measurements, and between the model and measurements, can potentially be attributed to one-sided systematics inherent to the measurements we quote that serve to inflate the measured Fano factor.

An example of such a systematic effect is a degradation of the charge collection efficiency (CCE). In this case, the probability of observing $n - k$ final charges given n initial charges is [27]:

$$P_{n-k} = \frac{n!}{k!(n-k)!}\eta^{n-k}(1-\eta)^k, \tag{4.15}$$

where η is the collection efficiency. For $\eta = 1$, we find that $P_{n-k} = \delta(n-k)$ as expected. If we assume perfect charge resolution, we can calculate the measured mean (n_{meas}) and variance (σ_{CCE}) of the resulting charge distribution, which gives

$$n_{meas} = \eta \cdot n, \tag{4.16}$$

$$\sigma^2_{CCE} = \eta \cdot n(1-\eta) = n_{meas}(1-\eta). \tag{4.17}$$

Given these moments, we thus get the measured Fano factor

$$F_{meas} = \frac{\sigma^2_{meas}}{n_{meas}} \tag{4.18}$$

$$= \frac{\sigma^2_{fano} + \sigma^2_{CCE}}{n_{meas}} \tag{4.19}$$

$$\approx \frac{F \cdot n + \eta \cdot n(1-\eta)}{\eta \cdot n} \tag{4.20}$$

$$= \frac{F}{\eta} + (1-\eta) \tag{4.21}$$

If we plug in numbers, a very small 0.4% degradation in CCE would be sufficient to explain the differences we see ($\frac{0.115}{0.996} + 0.004 = 0.119$). Broadly, any experimental systematic that affects charge production or measurement will result in a higher Fano factor. Furthermore, chronologically speaking, the Silicon measurements in Table. 4.1 have trended closer to our asymptotic value and with Ref. [30] is now within 5%.

Finally, ϵ_{eh} tracks the relationship from the experimental setup of Canali *et al.* [7], to within 0.5%, allowing us to conclude that our single-parameter model, regardless of energy partition, is capable of reproducing measured ϵ_{eh} and F for high-energy depositions.

4.3.2 Energy Dependence

We account for $P(E, E_r)$ by extracting it from Scholze et al. [34], via a likelihood fit to their measured pair creation energy as a function of energy below 100 eV. This fit is performed with the Monte-Carlo set at $A = 5.2$ eV^2 and by setting $T = 300$ K, the temperature at which these data were acquired. The Top panel of Fig. 4.7 shows the mean energy-per-pair ϵ_{eh} as a function of initial energy for the 3 simplified energy distribution scenarios discussed in Section 4.1.1. We note that the assumptions lead to the same behavior below 3 eV, and converge to the same value by the L-shell ($\sim$100 eV), but are largely discrepant in the energies between these points. None of the simplified models accurately reproduce the measured behavior between 3 and 10 eV; by 20 eV, all but the extreme $\alpha = 0$ energy distributions have converged. We turn off the effects of W and plasmon production when discussing the simplified energy distribution scenarios to more precisely disentangle their effects on the overall charge yield.

The lack of experimental data in the region between $\sim$9–50 eV, the aforementioned UV-gap, necessitates the use of an extrapolation, where we have chosen to drive α to 1

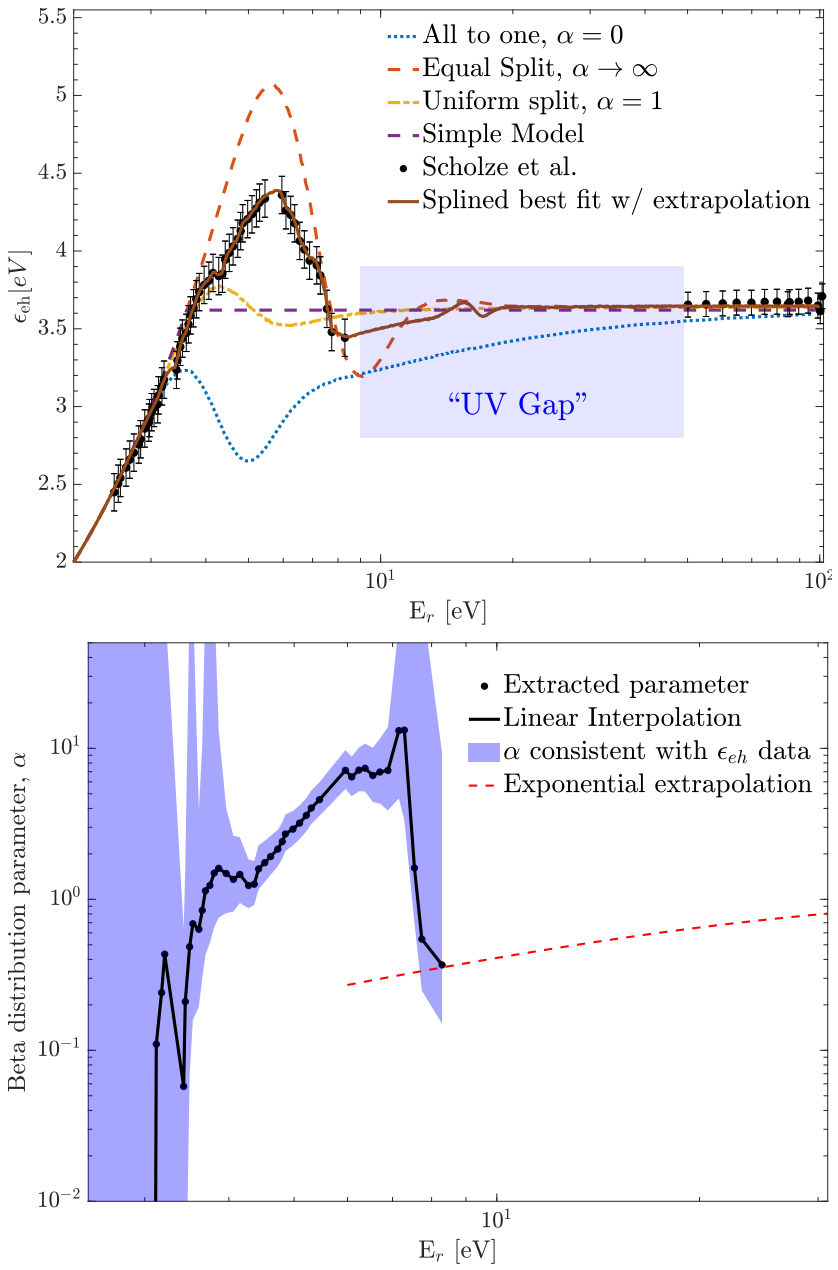

Figure 4.7: Top: Pair creation energy ϵ_{eh} for various energy partitioning schemes outlined in Section 4.1 and 4.3.2. Low-energy data points (black circles) from Scholze *et al.* [34] between 2–8 eV are fit using the model prescribed in this paper to give α values which are then interpolated and simulated back into ϵ_{eh} space (brown solid curve). The feature seen at 15–20 eV is a result of the imposed finite valence band width. Bottom: The extracted Beta distribution parameter, α, with linear interpolation between neighboring points and single parameter exponential extrapolation in UV-gap region as discussed in the text. The shaded bands represents the resultant fit on the $\pm 1\sigma$ from the extracted Scholze points. However, some values of ϵ_{eh} are not recoverable to within a tolerance of 1×10^{-4}, regardless of the α parameter, hence the shaded area encompasses $\alpha = [0, \infty]$ for certain energies.

parsimoniously using a single parameter exponential tied to the location of the last point. In and above this region, we expect a transition to the micro-physics based model of capping the maximum amount of energy transferable to a hole (W)[33].

The Bottom panel of Fig. 4.7 shows the best-fit values for α in the range between 0 and 8 eV, and the Top panel demonstrates that the mean energy inferred from each fit point is an excellent fit to the data. The structure observed implies the following:

1. Up to ∼4 eV, the data is consistent with a uniform energy distribution; there is little enough impact ionization, however, that we can only really conclude that the 'all to one' case is not valid above ∼3.5 eV. For event energies in the range E_g–$2E_g$ (1.2–2.4 eV in Si) only one electron-hole pair is allowed by energy conservation, forcing all charge yields to be insensitive to charge energy distribution and thus all models are identical. Above $2E_g$, impact ionization is possible, but the probability is strongly energy independent, and impact ionization only becomes appreciable when carriers exceed ∼2 eV of energy above gap.

2. Around 4 – 7.5 eV, our best-fit α rises quickly, indicating the distribution trends from an 'uniform split' ($\alpha = 1$) to 'equal split' ($\alpha \to \infty$).

3. At ∼8 eV, where existing data stops, ϵ_{eh} appears to disfavour the charge yield predicted by the 'all to one' model, while still in tension between the 'uniform split' and 'equal split' models. The range of best-fit α parameters implies that $P(E, E_r)$ is perhaps not captured effectively by a one parameter Beta distribution.

4. Above 8 eV ϵ_{eh} trends towards $\epsilon_{eh,\infty}$ with an oscillatory feature spanning between 14-20 eV (a signature of the inclusion and finite value of W).

The conclusions based on this empirical model agree with the energy distributions derived from density functional theory (DFT) of Ref. [38], where a local maximum in the quantum yield curve around 4.5 eV is attributed to a point of maximum energy sharing between electrons and holes, as shown in Fig. 4.2. The large error in α from Fig. 4.7 Bottom for ∼8 eV does not affect the extrapolation past this point since the error is partially an artifact of the similarity in ϵ_{eh} between the $\alpha = 0$ and $\alpha = \infty$ curves near this energy as seen in Fig. 4.7 Top.

It is interesting to note that as we pass the UV-gap, where $W \ll E_r$, one would expect the behavior of ϵ_{eh} to be indistinguishable from the 'all to one' case since the cap on the hole energy mimics all the energy going to the electron in every down-conversion step. Nevertheless the ϵ_{eh} curve more closely tracks $\alpha > 0$ and agrees with the best-fit and energy

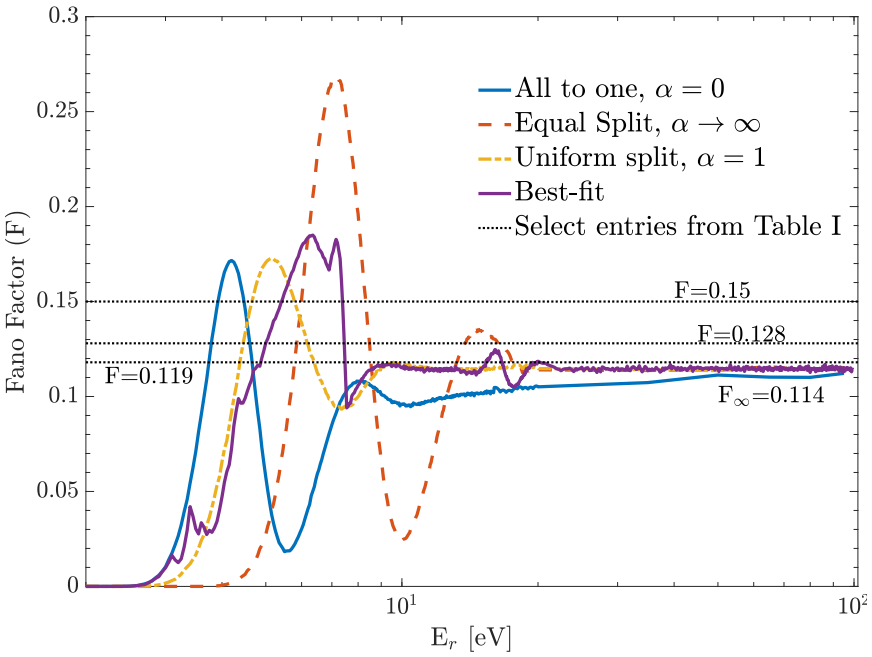

Figure 4.8: Computed Fano factor at 300 K for energy partitioning schemes discussed in text, along with curve (solid purple) from best-fit model. Dashed lines indicate values from literature as compiled in Table 4.1.

sharing models by 20 eV, a result also seen in Ref. [34]. The remaining uncertainty is therefore largely restricted to the 10–20 eV energy range, where our best-fit model shows some non-linear behavior, and the different energy-sharing models are still not in agreement. Our exponential extrapolation largely splits the difference between the uniform and energy sharing distributions, and is only an approximate guess at the behavior here[3]. The full range of possible charge yields is bounded by the three energy sharing models, and does not include potential resonance features near e.g. the plasmon energy. On this point, no choice of $\hbar\omega_{pl}$ (varied from 14–22 eV and $\to \infty$ effectively turning it off) modified the shape of the curves or $\epsilon_{eh,\infty}$ and F_∞. This is likely attributed to the perfect down-conversion efficiency baked into our plasmon model. Suffice to say, experimental data in this energy regime is needed to refine the empirical model further.

Fig. 4.8 demonstrates the non-constant behavior of the Fano factor at energies < 20 eV. We once again note that the presented assumptions all match the observed asymptotic value F_∞ by the $L_{2,3}$ edge but are all individually discrepant from measured behaviour below that, by a factor of $2\times$ in some regimes.

3. The exponential extrapolation is just an ansatz that allows us to connect fits at 8 eV to data at 50 eV, and is a median model within the bounded behavior shown in Fig. 4.7

4.3.3 Pair-creation probabilities

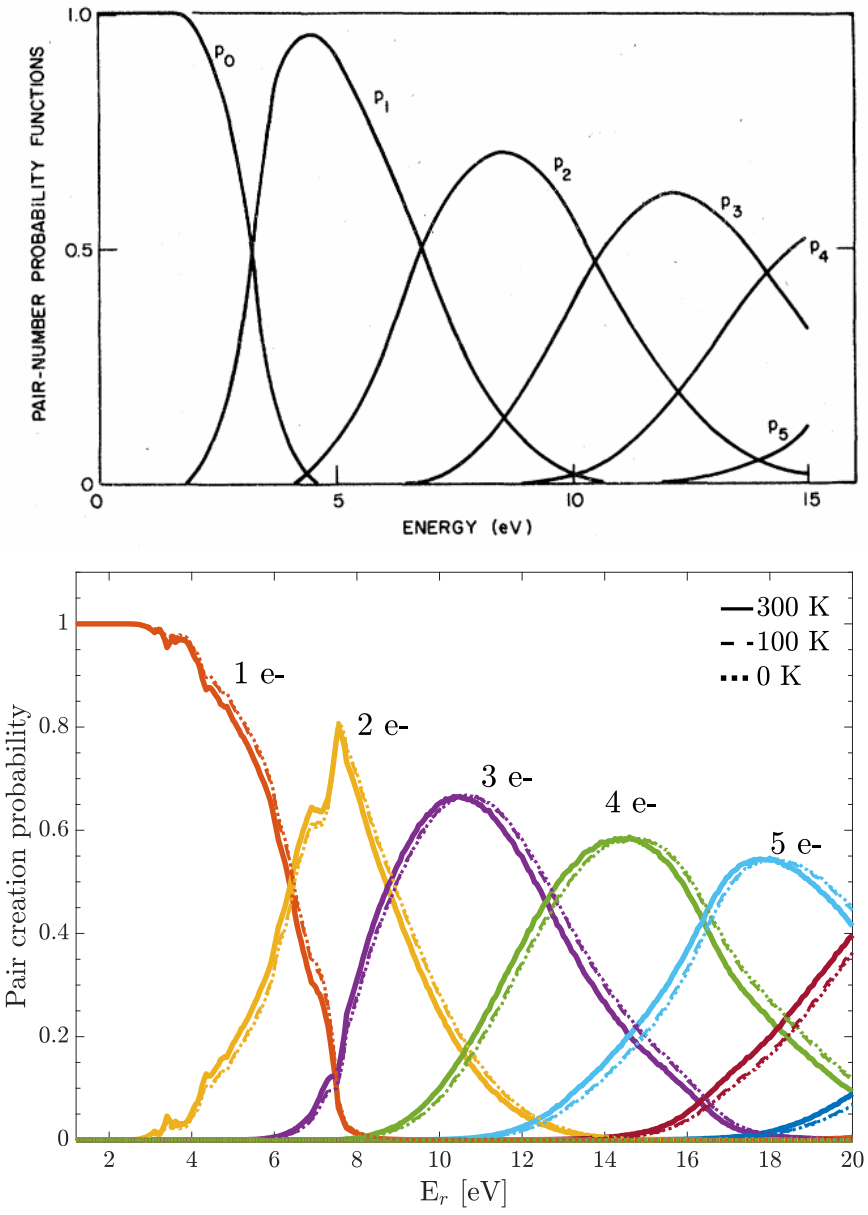

Figure 4.9: Top: Pair-creation probabilities for impact ionization case (no initial splitting of E_r from the pure computation of the Ref. [3] Monte-Carlo, extracted from therein. Bottom: Pair-creation probability distributions for our absorption best-fit model at 0 K, 100 K and 300 K (former curves effectively overlap). These lines are to be interpreted as the probability to ionize the labeled number of charge pairs for a given deposited energy. These are *not* PDFs in that only the sum of curves across a given point in energy is normalized to 1.

Tuning and validating the parameters of the Monte-Carlo model, as discussed in the prior section, enables us to produce the pair-creation probabilities seen in Fig. 4.9 for 3

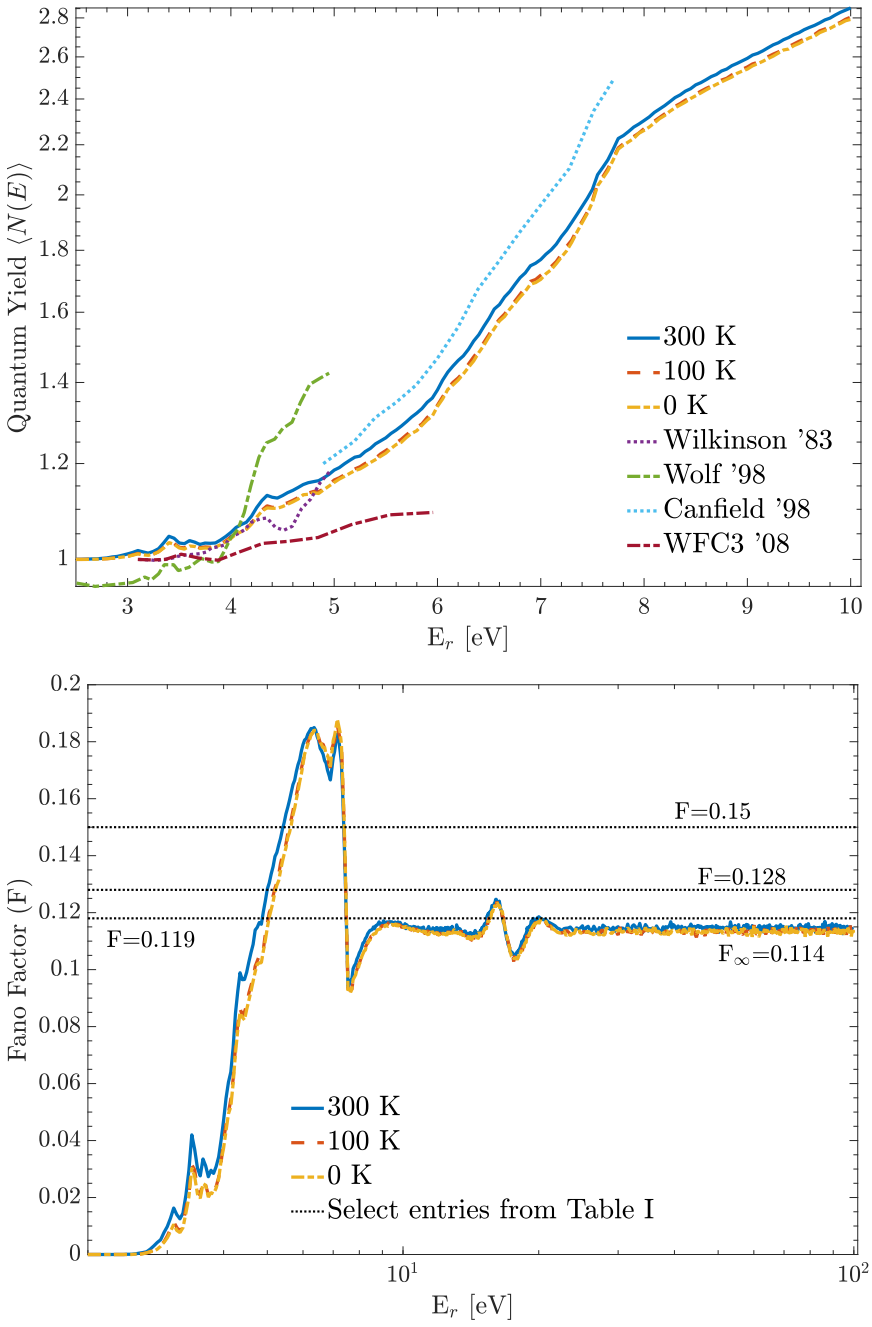

Figure 4.10: Top: The quantum yield, defined as the average number of charge pairs created at a given energy, for the best-fit model at 0K, 100K and 300K. Empirical data from Wolf et al. [38], Wilkinson et al. [37], Canfield et al. [8], and WFC3 tests [5] are provided as points of comparison. Bottom: Variation of the Fano factor $F$for the best-fit model at 0K, 100K and 300K. While the asymptotic values, equivalent to those computed in Fig. 4.6 (bottom right), are within 1% of each other, there can be upwards of a ∼10% difference at specific energy values.

temperature points around which many detectors operate. These can be compared the ones found by Ref. [3] for the case of impact ionization, showing similar behaviour. The empirically derived nature of $p_{1,2,3}$ in our case is clearly visible with smoother curves for $p_{>=4}$ where the model is reflective of the transition to an $\alpha = 1$ regime. Fig. 4.10 illustrates the behavior of the best-fit quantum yield and Fano factor as a function of temperature compared to measurements from the literature, illustrating a significant dispersion of quantum yield measurements at a few eV and with our computed values lying centrally in this range.

We stress here the point that both $\langle N(E)\rangle$ and F are derived quantities, which are arguably only useful at "high" energies where they are a shorthand for packaging the messy dynamics of ionization response with appeals to the central limit theorem. We argue that p_n is the preferential basis to understand charge yield by referring back to Eq. 4.12 from which we recognize that the use of aggregate quantities, and exclusion of higher moments, informationally constrains both parameters. Stated more concretely, if $\sum_n \left[p_n(E) > 0\right] > 2$, as is true for most energies, then there are more terms than constraining equations and multiple solutions of p_n would satisfy the same $\langle N(E)\rangle$ and F curves.

However, due to the well behaved nature of ϵ_{eh} and F for $E_r \gtrsim 50$ eV, where they are effectively constant, we can compute the exact Gaussian functional form,

$$p_n(E) = \frac{1}{\sqrt{2\pi n F_\infty}} \mathrm{Exp}\left[-\frac{1}{2}\left(\frac{\mathrm{n}\epsilon_{\mathrm{eh},\infty} - \mathrm{E}}{\sqrt{\mathrm{nF}_\infty}\epsilon_{\mathrm{eh},\infty}}\right)^2\right] \tag{4.22}$$

to infer p_n in and beyond this region, sufficient for practical applications.

We refer the reader to Ref. [28] for an application of this charge yield model to the scientific case of DM-e$^-$scattering, showing that improper charge yield modeling can lead to differences of 50% in exclusion limits for certain parameter choices.

References

[1] V. Alex, S. Finkbeiner, and J. Weber. Temperature dependence of the indirect energy gap in crystalline silicon. *Journal of Applied Physics*, 79(9):6943–6946, 1996. doi: 10.1063/1.362447.

[2] R. C. Alig. Scattering by ionization and phonon emission in semiconductors. ii. monte carlo calculations. *Phys. Rev. B*, 27:968–977, Jan 1983. doi: 10.1103/PhysRevB.27.968. URL `https://link.aps.org/doi/10.1103/PhysRevB.27.968`.

[3] R. C. Alig, S. Bloom, and C. W. Struck. Scattering by ionization and phonon emis-

sion in semiconductors. *Phys. Rev. B*, 22:5565–5582, Dec 1980. doi: 10.1103/PhysRevB.22.5565.

[4] W. Bludau, A. Onton, and W. Heinke. Temperature dependence of the band gap of silicon. *Journal of Applied Physics*, 45(4):1846–1848, 1974. doi: 10.1063/1.1663501.

[5] T. Borders, P. McCullough, and S. Baggett. Wfc3 tv3 testing: quantum yield of the uvis ccds. *Space Telescope WFC Instrument Science Report*, jul 2010.

[6] M. Brigida, C. Favuzzi, P. Fusco, F. Gargano, N. Giglietto, F. Giordano, F. Loparco, B. Marangelli, M. Mazziotta, N. Mirizzi, et al. A new monte carlo code for full simulation of silicon strip detectors. *Nuclear Instruments and Methods in Physics Research Section A: Accelerators, Spectrometers, Detectors and Associated Equipment*, 533(3):322–343, 2004. doi: 10.1016/j.nima.2004.05.127.

[7] C. Canali, M. Martini, G. Ottaviani, and A. A. Quaranta. Measurements of the average energy per electron-hole pair generation in silicon between 5-320k. *IEEE Transactions on Nuclear Science*, 19(4):9–19, Aug 1972. ISSN 1558-1578. doi: 10.1109/TNS.1972.4326778.

[8] L. R. Canfield, R. E. Vest, R. Korde, H. Schmidtke, and R. Desor. Absolute silicon photodiodes for 160 nm to 254 nm photons. *Metrologia*, 35(4):329–334, aug 1998. doi: 10.1088/0026-1394/35/4/19. URL `https://doi.org/10.1088%2F0026-1394%2F35%2F4%2F19`.

[9] E. Cartier, M. V. Fischetti, E. A. Eklund, and F. R. McFeely. Impact ionization in silicon. *Applied Physics Letters*, 62(25):3339–3341, 1993. doi: 10.1063/1.109064. URL `https://doi.org/10.1063/1.109064`.

[10] C. Chang, C. Hu, and R. W. Brodersen. Quantum yield of electron impact ionization in silicon. *Journal of Applied Physics*, 57(2):302–309, 1985. doi: 10.1063/1.334804.

[11] C. H. Chen, J. Silcox, and R. Vincent. Electron-energy losses in silicon: Bulk and surface plasmons and Čerenkov radiation. *Phys. Rev. B*, 12:64–71, Jul 1975. doi: 10.1103/PhysRevB.12.64.

[12] W. R. Dodge, S. R. Domen, T. F. Leedy, and D. M. Skopik. Measurement of the mean energy required to create an electron-hole pair in silicon between 6 and 77k. *Phys. Rev. Lett.*, 17:653–655, Sep 1966. doi: 10.1103/PhysRevLett.17.653.

[13] U. Fano. Ionization yield of radiations. ii. the fluctuations of the number of ions. *Phys. Rev.*, 72:26–29, Jul 1947. doi: 10.1103/PhysRev.72.26.

[14] G. Fraser, A. Abbey, A. Holland, K. McCarthy, A. Owens, and A. Wells. The x-ray energy response of silicon part a. theory. *Nuclear Instruments and Methods in Physics Research Section A: Accelerators, Spectrometers, Detectors and Associated Equipment*, 350

(1):368 – 378, 1994. ISSN 0168-9002. doi: https://doi.org/10.1016/0168-9002(94)91185-1.

[15] Z. Hong, R. Ren, N. Kurinsky, E. Figueroa-Feliciano, L. Wills, S. Ganjam, R. Mahapatra, N. Mirabolfathi, B. Nebolsky, H. D. Pinckney, and et al. Single electronhole pair sensitive silicon detector with surface event discrimination. *Nuclear Instruments and Methods in Physics Research Section A: Accelerators, Spectrometers, Detectors and Associated Equipment*, 963: 163757, May 2020. ISSN 0168-9002. doi: 10.1016/j.nima.2020.163757. URL http://dx.doi.org/10.1016/j.nima.2020.163757.

[16] M. Ibe, W. Nakano, Y. Shoji, and K. Suzuki. Migdal effect in dark matter direct detection experiments. *Journal of High Energy Physics*, 2018(3): 194, Mar 2018. ISSN 1029-8479. doi: 10.1007/JHEP03(2018)194. URL https://doi.org/10.1007/JHEP03(2018)194.

[17] C. Jacoboni and L. Reggiani. The monte carlo method for the solution of charge transport in semiconductors with applications to covalent materials. *Rev. Mod. Phys.*, 55: 645–705, Jul 1983. doi: 10.1103/RevModPhys.55.645.

[18] C. A. Klein. Bandgap dependence and related features of radiation ionization energies in semiconductors. *Journal of Applied Physics*, 39(4):2029–2038, 1968. doi: 10.1063/1.1656484. URL https://doi.org/10.1063/1.1656484.

[19] B. Lowe and R. Sareen. A measurement of the electronhole pair creation energy and the fano factor in silicon for 5.9kev x-rays and their temperature dependence in the range 80270k. *Nuclear Instruments and Methods in Physics Research Section A: Accelerators, Spectrometers, Detectors and Associated Equipment*, 576(2):367 – 370, 2007. ISSN 0168-9002. doi: https://doi.org/10.1016/j.nima.2007.03.020.

[20] G. G. Macfarlane, T. P. McLean, J. E. Quarrington, and V. Roberts. Fine structure in the absorption-edge spectrum of si. *Phys. Rev.*, 111:1245–1254, Sep 1958. doi: 10.1103/PhysRev.111.1245.

[21] M. Mazziotta. Electron–hole pair creation energy and fano factor temperature dependence in silicon. *Nuclear Instruments and Methods in Physics Research Section A: Accelerators, Spectrometers, Detectors and Associated Equipment*, 584(2-3):436–439, 2008. doi: 10.1016/j.nima.2007.10.043.

[22] K. J. McCarthy, A. Owens, A. Holland, and A. A. Wells. Modelling the x-ray response of charge coupled devices. *Nuclear Instruments and Methods in Physics Research Section A: Accelerators, Spectrometers, Detectors and Associated Equipment*, 362(2):538 – 546, 1995. ISSN 0168-9002. doi: https://doi.org/10.1016/0168-9002(95)00376-2.

[23] A. Owens, G. Fraser, A. Abbey, A. Holland, K. McCarthy, A. Keay, and A. Wells. The x-ray energy response of silicon (b): Measurements. *Nuclear Instruments and Methods in Physics Research Section A: Accelerators, Spectrometers, Detectors and Associated Equipment*, 382(3):503 – 510, 1996. ISSN 0168-9002. doi: https://doi.org/10.1016/S0168-9002(96)00822-4.

[24] A. Owens, G. Fraser, and K. J. McCarthy. On the experimental determination of the fano factor in si at soft x-ray wavelengths. *Nuclear Instruments and Methods in Physics Research Section A: Accelerators, Spectrometers, Detectors and Associated Equipment*, 491(3):437 – 443, 2002. ISSN 0168-9002. doi: https://doi.org/10.1016/S0168-9002(02)01178-6.

[25] R. Pehl, F. Goulding, D. Landis, and M. Lenzlinger. Accurate determination of the ionization energy in semiconductor detectors. *Nuclear Instruments and Methods*, 59(1): 45 – 55, 1968. ISSN 0029-554X. doi: https://doi.org/10.1016/0029-554X(68)90342-X.

[26] D. Pines. Collective energy losses in solids. *Rev. Mod. Phys.*, 28:184–198, Jul 1956. doi: 10.1103/RevModPhys.28.184. URL `https://link.aps.org/doi/10.1103/RevModPhys.28.184`.

[27] F. Ponce et al. Measuring the impact ionization and charge trapping probabilities in supercdms hvev phonon sensing detectors. *Phys. Rev. D*, 101:031101, Feb 2020. doi: 10.1103/PhysRevD.101.031101. URL `https://link.aps.org/doi/10.1103/PhysRevD.101.031101`.

[28] K. Ramanathan and N. Kurinksy. Ionization yield in silicon for ev-scale electron-recoil processes. *arXiv preprint arXiv:2004.10709*, 2020.

[29] K. Ramanathan et al. Measurement of low energy ionization signals from compton scattering in a charge-coupled device dark matter detector. *Phys. Rev. D*, 96:042002, Aug 2017. doi: 10.1103/PhysRevD.96.042002.

[30] D. Rodrigues, K. Andersson, M. Cababie, A. Donadon, G. Cancelo, J. Estrada, G. Fernandez-Moroni, R. Piegaia, M. Senger, M. S. Haro, et al. Absolute measurement of the fano factor using a skipper-ccd. *arXiv preprint arXiv:2004.11499*, 2020. URL `https://arxiv.org/abs/2004.11499`.

[31] R. K. Romani, P. L. Brink, B. Cabrera, M. Cherry, T. Howarth, N. Kurinsky, R. A. Moffatt, R. Partridge, F. Ponce, M. Pyle, A. Tomada, S. Yellin, J. J. Yen, and B. A. Young. Thermal detection of single e-h pairs in a biased silicon crystal detector. *Applied Physics Letters*, 112:043501, Jan. 2018. doi: 10.1063/1.5010699.

[32] R. D. Ryan. Precision measurements of the ionization energy and its temperature variation in high purity silicon radiation detectors. *IEEE Transactions on Nuclear*

Science, 20(1):473–480, Feb 1973. ISSN 1558-1578. doi: 10.1109/TNS.1973.4326950.

[33] F. Scholze, H. Rabus, and G. Ulm. Measurement of the mean electronhole pair creation energy in crystalline silicon for photons in the 501500 ev spectral range. *Applied Physics Letters*, 69(20):2974–2976, 1996. doi: 10.1063/1.117748. URL `https://doi.org/10.1063/1.117748`.

[34] F. Scholze, H. Henneken, P. Kuschnerus, H. Rabus, M. Richter, and G. Ulm. Determination of the electronhole pair creation energy for semiconductors from the spectral responsivity of photodiodes. *Nuclear Instruments and Methods in Physics Research Section A: Accelerators, Spectrometers, Detectors and Associated Equipment*, 439(2):208 – 215, 2000. ISSN 0168-9002. doi: https://doi.org/10.1016/S0168-9002(99)00937-7.

[35] L. Strüder. High-resolution imaging x-ray spectrometers. *Nuclear Instruments and Methods in Physics Research Section A: Accelerators, Spectrometers, Detectors and Associated Equipment*, 454(1):73 – 113, 2000. ISSN 0168-9002. doi: https://doi.org/10.1016/S0168-9002(00)00811-1. Proc. of the 1st Int Symp. on Applications of Particle Detectors in Medicine, Biology and Astrophysics.

[36] Y. Varshni. Temperature dependence of the energy gap in semiconductors. *Physica*, 34 (1):149–154, 1967. ISSN 0031-8914. doi: https://doi.org/10.1016/0031-8914(67)90062-6.

[37] F. J. Wilkinson, A. J. D. Farmer, and J. Geist. The near ultraviolet quantum yield of silicon. *Journal of Applied Physics*, 54(2):1172–1174, 1983. doi: 10.1063/1.332095.

[38] M. Wolf, R. Brendel, J. H. Werner, and H. J. Queisser. Solar cell efficiency and carrier multiplication in sige alloys. *Journal of Applied Physics*, 83(8):4213–4221, 1998. doi: 10.1063/1.367177.

CHAPTER 5

COMPTON SCATTERING MEASUREMENTS

n.b. This chapter formed the basis of Ref. Ramanathan et al. [1], of which I am first author and was responsible for much of the experimental work, analysis, and plots/text — which is reproduced here as appropriate. Copyright rests with the American Physical Society.

In Chapter 1 we laid out the potential for light dark matter (or a light WIMP) depositing from 10 eV to a few keV energy in a dark matter detector. In the DAMIC experiment, at these low energies, signal and backgrounds are morphologically indistinguishable due to the interaction length either being smaller or the same size as a pixel. Hence, signal and background interactions can only be differentiated by their energy spectrum.

A significant component of the background comes from primordially produced radionuclei like ^{232}Th, ^{238}U and ^{40}K which are common contaminants found in nature, and thus can make their way into both the detectors and the surrounding shielding. When these nuclides and their daughters decay, they can emit significant amounts of high-energy radiation that are then registered by the detector. α emissions can be identified by their distinct shape (see Fig. 2.11) and $\mathcal{O}$(MeV) energy deposit, while βs can often also be identified by their morphology. However the signature of incident high energy γ-rays, particularly through processes like Compton scattering, will mimic a signal deposit. These irreducible electron-recoil external backgrounds can comprise a significant fraction of the overall background, generally orders of magnitude higher than the backgrounds resulting from fast neutrons (another external source of background events). An example of photon production is the decay of ^{210}Pb as follows:

$$^{210}\mathrm{Pb} \rightarrow \beta\,(15\,\mathrm{keV}) + \gamma\,(46.6\,\mathrm{keV})$$

within the copper box holding the CCDs. These keV photons would have sufficient energy to penetrate well past the approx. 2 μm dead-layer on the surface and back of a CCD, and then any interaction would register as a bulk event. A forthcoming background analysis of the DAMIC Stage II detector indicates that inelastic photon backgrounds comprise around 5 dru out of the approx. 12 dru background per CCD [2]. To disentangle this sizeable background fraction, we require a complete understanding of the low-energy spectral features of Compton scattering in a CCD.

As such, in this chapter we describe a successful measurement campaign to determine the spectra of Compton scattering of γ rays above an energy of 60 eV, corresponding to a

signal of $\sim 15\, e^-$, obtained by exposing a DAMIC style CCD at the University of Chicago to γ-rays from ^{57}Co and ^{241}Am radioactive sources. The experimental observation of these low energy spectral features had never previously before been reported in the literature. We then provide a phenomenological parametrization of these features to accurately describe the Compton spectra in the atomic binding regime, as a tool for future experimental efforts to quantify any similar background arising from these interactions.

5.1 Compton Scattering

Compton scattering [3] is an electromagnetic process where an incident photon transfers some of its energy to an electron, and is then deflected from its original direction. For an interaction with a free electron at rest, the energy of a scattered photon (E_s) depends on the energy of the incident photon (E_γ), the mass of the electron (m) and the scattering angle (θ) as

$$\begin{aligned} E_s &= \frac{E_\gamma}{1 + x_\gamma(1 - \cos\theta)} \\ x_\gamma &= \frac{E_\gamma}{mc^2}, \end{aligned} \tag{5.1}$$

with the differential cross section given by the well-known Klein-Nishina formula [4]:

$$\begin{aligned} \frac{d\sigma_{\mathrm{KN}}}{d\Omega} &= \frac{1}{2} r_0^2 \left(\frac{x_s}{x_\gamma}\right)^2 \left(\frac{x_s}{x_\gamma} + \frac{x_\gamma}{x_s} - \sin^2\theta\right) \\ x_s &= \frac{E_s}{mc^2}, \end{aligned} \tag{5.2}$$

where r_0 is the classical electron radius.

The maximum energy transferred to the electron $E = E_\gamma - E_s$ occurs when the γ ray backscatters, i.e., when $\theta{=}\pi$, giving rise to a spectral feature known as the Compton edge. Hence in an energy spectrum from a target exposed to γ-rays, we expect features (see cartoon Figure 5.1 Top) that correspond to the absorption peaks and a Compton *edge* due to a limit on maximal energy loss. Usually this is the end of the discussion in the literature as detectors may not have resolution compatible with the binding energies of their target. However Compton scattering should also have a signature at this precise low end of the spectrum — a series of steps that roughly correspond to the x-ray transition energies of the target medium (see table 5.1 for Silicon). If an incoming γ-ray has just enough energy to knock out a shell electron and no more, we expect some relaxation process to kick in (e.g. fluorescence photons, Auger electrons, Coster-Kronig transition etc. [5]) that put out the

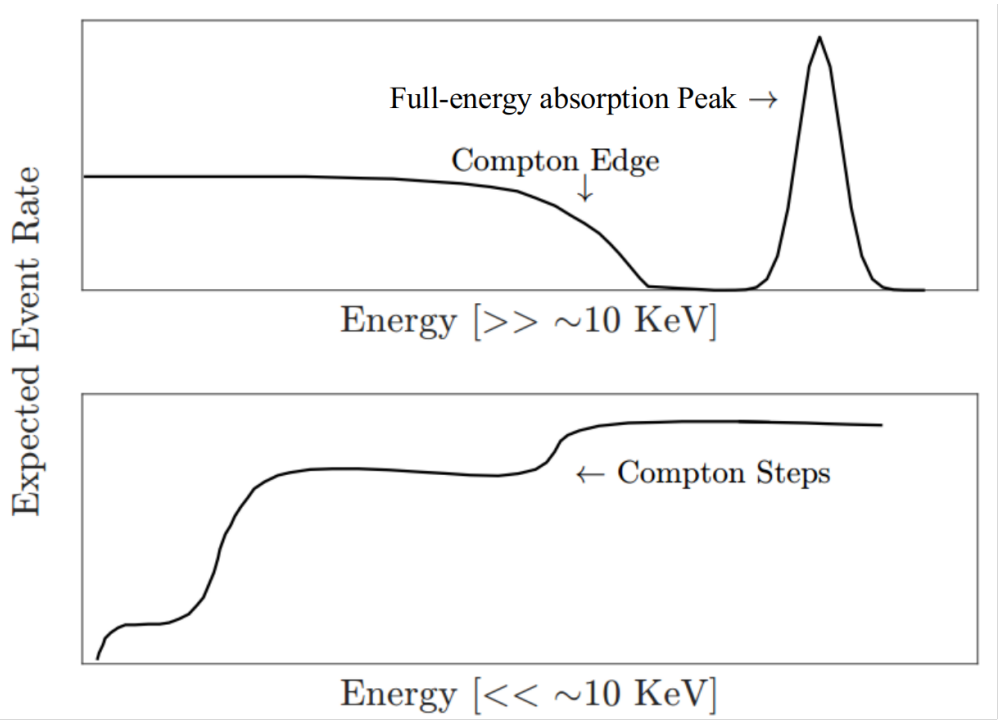

Figure 5.1: Top: Cartoon of Compton edge and Full-energy absorption peak as is usually discussed in detector literature. Bottom: Compton *steps* expected to be resolved at low energies around the binding energies of target material.

difference in shell energy. Since the γ is likely to escape after a single scatter, especially in a thin CCD detector, the only local deposition of energy will be due to this relaxation process. In aggregate these should add up to give step profiles (see cartoon Figure 5.1 Bottom).

5.1.1 Impulse Approximation

Strictly speaking the Klein-Nishina formula mentioned earlier breaks down both when the electrons in a target are bound in atomic shells with non-zero momentum, and when the incoming photon energy becomes comparable with the inner-shell electron binding energy [8] further giving rise to observable distortions in the spectrum. These also include the well-known softening or "Doppler broadening" of the Compton edge [9].

In these regimes one can apply a semi-analytic scattering function correction S($\vec{q}$,Z) to the differential cross section, where $\vec{q}$ is the momentum transfer during collision and Z is the atomic number of the target. The correction, applied in the form $\frac{d\sigma}{d\Omega} = S(\vec{q}, Z)\frac{d\sigma_{\mathrm{KN}}}{d\Omega}$ for example in Waller-Hartree theory [10], is widely used in computational photon transport calculations, resulting in a 'Modified Klein-Nishina' formulation. Alternatively, a straight-

Transition edge	Ref.	Experimental Energy [eV]
K	[6]	1839.13(37)
L_1		149.80(50)
L_2		99.20(10)
L_3		99.340(61)
M_1	[7]	11.3572 (unk.)
M_2		5.08305 (unk.)

Table 5.1: Silicon binding energies, taken from either NIST X-Ray Transition Energies Database [6] or NIST X-Ray Form Factor, Attenuation, and Scattering Tables [7] with unspecified uncertainties.

forward modification for bound electrons is the Relativistic Impulse Approximation (IA) of Ribberfors and Berggren [8], where each electron in an atomic shell is treated as a free electron with a constrained momentum distribution derived from the bound-state wave function. For low momentum and energy transfer (i.e. less than the electron mass mc^2), and following the work of Ribberfors, we can write the differential cross section for a photon scattering with an atomic electron with quantum numbers n and l as:

$$\begin{aligned} \left.\frac{d\sigma}{dE}\right|_{nl} &= \mathcal{C}\int_{-1}^{1}\frac{(1-\delta)(1+\cos^2\theta)+\delta^2}{|\vec{q}|}J_{nl}(p_z)\,d\cos\theta \\ p_z &= \frac{(E_\gamma/c)(1-\delta)(1-\cos\theta)-\delta mc}{|\vec{q}|} \\ |\vec{q}| &= \sqrt{2(1-\delta)(1-\cos\theta)+\delta^2}. \end{aligned} \tag{5.3}$$

The expression above is only valid for $E \geq E_{nl}$, the target electron's binding energy. Otherwise, $d\sigma/dE|_{nl} = 0$, as the minimum energy that the photon can lose in an interaction is that required to free the target electron from the atom. We have introduced $\delta = E/E_\gamma$, which is $\ll 1$ for the energies of interest, and grouped the constant terms in front of the expression as $\mathcal{C} = \pi r_0^2 mc/E_\gamma$. The functions $J_{nl}(p_z)$ are the Compton profiles, which encode the momentum distribution of the target electron before the collision, and p_z is the projection of the momentum of the electron on the scattering vector $\vec{q}$. The advantage of this simple approach is the breakdown of the cross section into the contribution from individual shells, which allows us to discuss Compton scattering in the different energy regimes between shell edge energies. The integral in Eq. 5.3 can only be evaluated numerically. Tabulated data for $J_{nl}(p_z)$ in units of $1/(\alpha mc)$ for different elements can be found in Ref. [11].

Working out the total contribution of all shells, Fig. 5.2 shows the computed spectrum

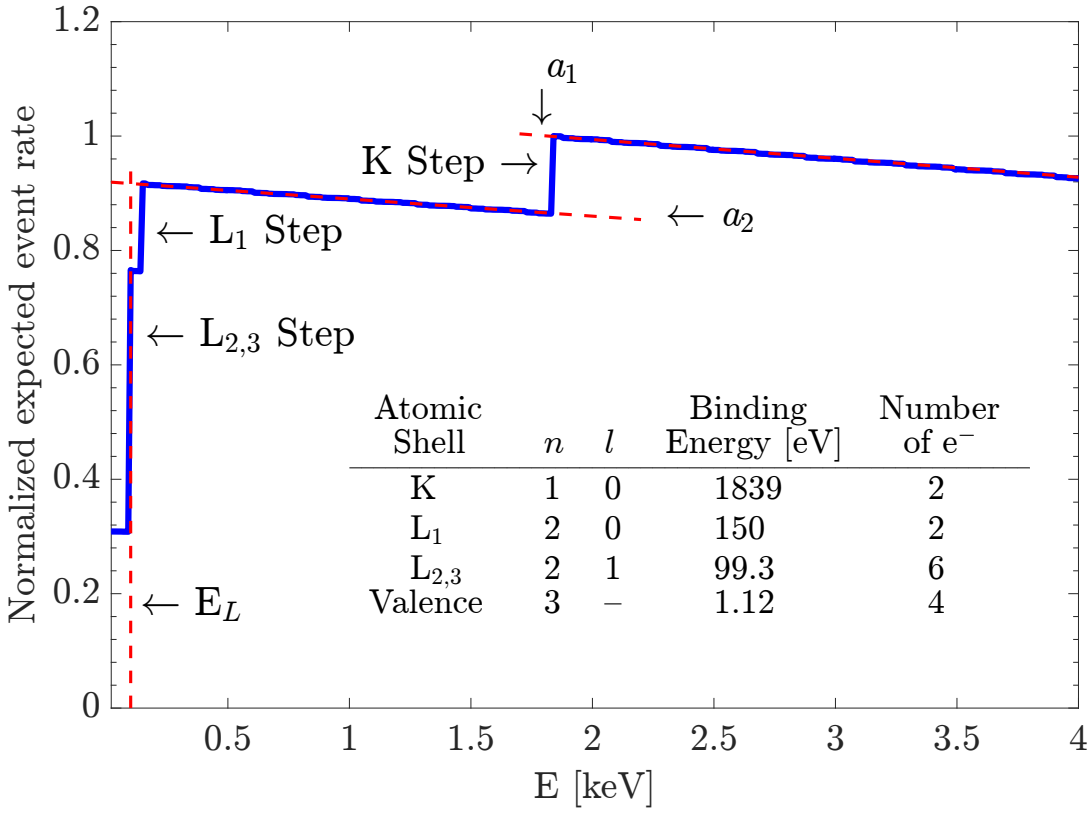

Figure 5.2: Computed low-energy spectrum from Compton scattering of 122 keV γ-rays in silicon. The observed steps occur at the binding energies of the different atomic shells, as given in the inset [6]. The spectrum was normalized so that its value is one on the right-hand side of the K step. Parameters a_1, a_2 and E_L of the general model to be presented in Section 5.9 are labeled.

for a silicon target exposed to 122 keV γ rays, where we added $d\sigma/dE|_{nl}$ over all atomic electrons. A series of steps are observed at low energies, corresponding to the atomic shells of the target, which arise from the condition that $d\sigma/dE|_{nl} = 0$ for $E<E_{nl}$. The height of these steps is directly proportional to the number of electrons present in the shell (i.e. the combined L step 'unlocks' 8 e^- while the K step is only 2 e^- high).

As discussed previously, at the threshold of the steps the freed electron has negligible kinetic energy and the deposited energy comes from the refilling of the atomic vacancy by the emission of secondary products like Auger electrons and fluorescence x rays. The continuum of freed electron energies is what gives rise to the slope structure between steps. We will

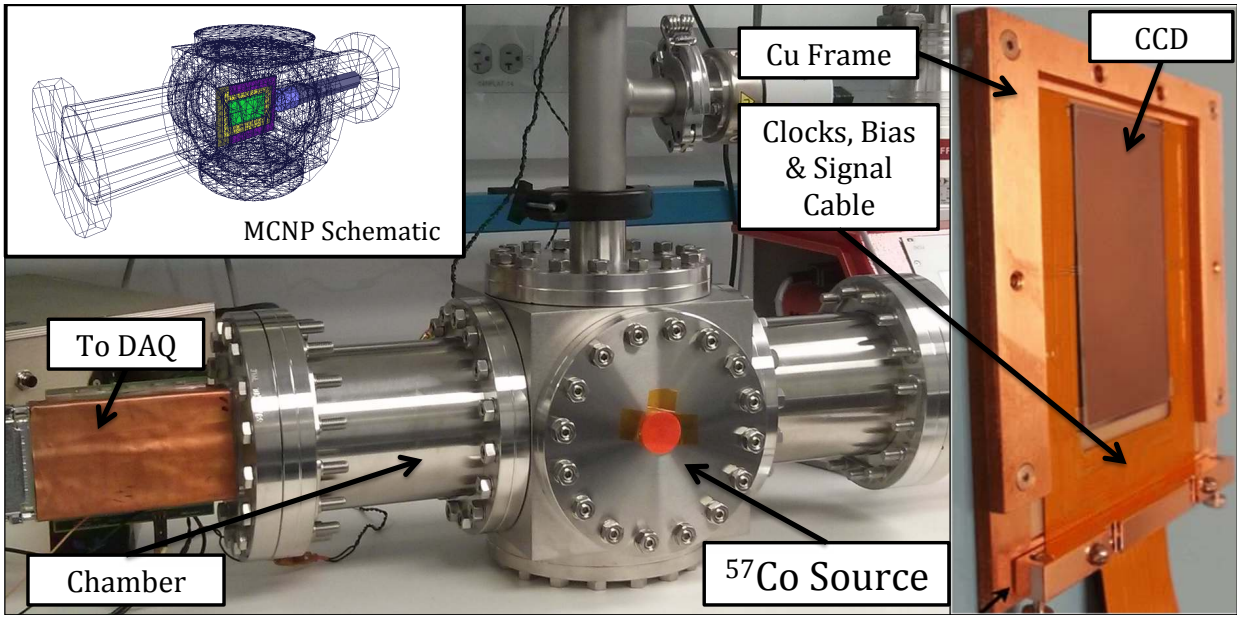

Figure 5.3: Left: Experimental setup at The University of Chicago, showing the ^{57}Co radioactive source installed on the front flange of the stainless steel vacuum chamber. Inset: MCNP simulation model of the experimental setup with the CCD location inside the vacuum chamber shown in green, discussed in Sec. 5.7. Right: Packaged 8 Mpixel CCD in its copper module.

investigate the shape and values of these parameters in Sec. 5.9.

5.2 Experimental Setup

The experimental setup was almost identical to that outlined in Chap. 2.2.2, and can be seen in Fig. 5.3. At the time of the measurement we employed an 8 Mpixel CCD (pixel size $15\times15\,\mu\text{m}^2$) with an active area of $18.8\,\text{cm}^2$, a thickness of $500\,\mu$m and a mass of 2.2 g, cooled to a nominal operating temperature of 130 K. The pixel noise achieved with this system was $1.86\pm0.02\,e^-$, equivalent to around 7.0 ± 0.1 eV.

Data for this analysis were acquired in two modes: i) standard 1×1 binning, where each pixel was read out individually for maximum spatial resolution, and ii) 4×4 binning, where by the appropriate clocking of the device the charge collected in groups of 4×4 pixels was read out in a single measurement.

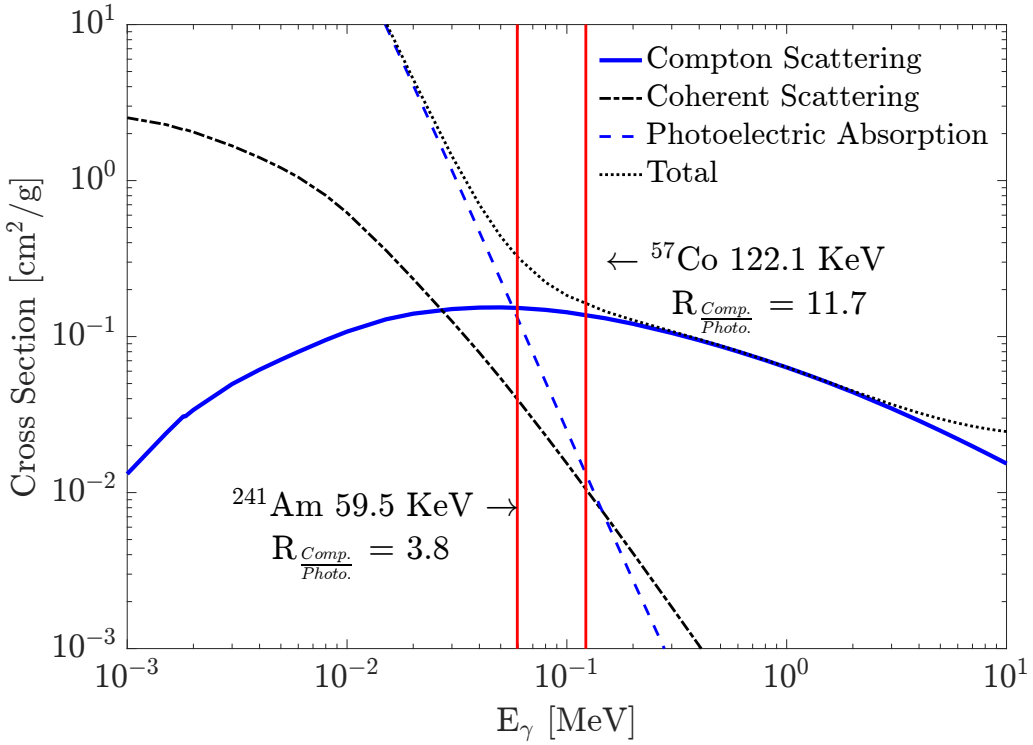

Figure 5.4: Cross sections of silicon interaction processes taken from NIST XCOM database [6], with red lines indicating the energy of primary decay γ-rays for the two sources used in the measurement. Sources were selected with an eye to maximizing the ratio between Compton and Photoelectric cross-sections to allow efficient collection of data in the relevant energy range of Compton features.

Source	Activity [μCi]	Half-Life [y]	E_γ [keV]	Intensity [per 100 decays]
^{57}Co	8.7	0.745 (1)	14.4130 (3)	9.2 (2)
			122.0607 (1)	85.51 (6)
			136.4736 (3)	10.7 (2)
^{241}Am	22	432.6 (6)	26.3446 (2)	2.31 (8)
			59.5409 (1)	35.9 (2)

Table 5.2: Summary of the radioactive sources used in this experiment including the energies (E_γ) and intensities of the relevant γ-ray lines, values from Refs. [12, 13].

5.3 Source Selection

The selection of ^{241}Am and ^{57}Co was driven by a few considerations. Primarily, they provide clean decay lines of intense γ-rays (60 keV, 122 keV and 136 keV) of relatively low energy for which Compton scattering is the dominant interaction in the silicon target, as shown in Fig. 5.4. If the γ-ray energy is too low (e.g. 14 keV and 26 keV in Table 5.2) then photoelectric absorption dominates with no observable Compton spectrum, thus optimizing the ratio of the two processes was paramount. This is balanced by statistical considerations as the Compton spectrum is favorably compressed toward lower energies for lower γ-ray energies with a larger fraction of interactions occurring close to atomic binding energies. Furthermore, lower-energy γ rays lead to shorter-range electron recoils, mitigating surface effects by minimizing both the number of electrons that escape the CCD without depositing their full energy and the flux of degraded-energy electrons arising from the surfaces of materials surrounding the device. Finally, the half-lives of both sources $\gg \mathcal{O}$(weeks) which allowed for continuous data taking without significant losses in intensity.

5.4 Data Sets

The eight sets of images used for this analysis are summarized in Table 5.3. For each radioactive source, we acquired data with 1×1 and 4×4 binning (Section 5.2), each followed by a background run with the source removed. The 1×1 data were used to confirm the presence of a dominant bulk signal from Compton scattering relative to surface backgrounds. Thus, these data were acquired at low substrate bias ($V_{\rm sub}$) to increase lateral charge diffusion, and offer maximum spatial resolution for the precise reconstruction of the 3D location of electron recoils. The 4×4 data were used to perform spectroscopy at the lowest energies. Hence, the data were acquired with a high $V_{\rm sub}$ so that most of the charge from an interaction

was collected in a single 4×4 pixel group, minimizing the contribution from readout noise in the charge measurement. Finally, the background data were acquired to characterize and monitor the contribution from electronic noise and environmental backgrounds to the source runs.

5.5 Image Processing & Event Reconstruction

Image processing broadly followed the methodology outlined in Chap. 2.1.2. Once the initial processing was completed we accounted for the detector effects described over the next few sub-sections.

5.5.1 Diffusion, Efficiency & CTI

As outlined in Sec. 2.1.2, diffusion of charge occurs when ionization signals in the bulk, drifted towards the CCD surface by the applied V_{sub}, are subject to thermal motion. This results in a smearing of charge across multiple pixels which, for point like depositions at vertical position z, can be modeled by a 2-D Gaussian with $\sigma_{xy} = -A \ln|1 - bz|$. To verify our understanding of A, b, and other detector settings, we simulated the production of charge carriers and their diffusion as they drift to the CCD pixel array with a dedicated Monte Carlo code. For each energy deposit, we "injected" a given number of charge carriers at a specific z depth within a model of a CCD, and then computationally drifted them to the surface of the CCD. The number and arrangement of pixels where charge is collected was then determined

Binning	Source	V_{sub} [V]	N images	σ_{pix} [e^-]	Exposure [s]	Event density [keV^{-1}]	CTI
1×1	^{57}Co	45	1898	1.92(2)	986	3.5×10^4	
	None	45	1326	1.92(2)	986	4.3×10^3	
	^{241}Am	45	971	1.98(2)	490	4.7×10^4	
	None	45	1235	1.94(3)	490	2.4×10^3	
4×4	^{57}Co	127	1815	1.83(1)	39.8	2.3×10^5	1.0×10^{-5}
	None	127	2060	1.83(1)	39.8	2.6×10^2	
	^{241}Am	127	9828	1.88(2)	39.8	2.5×10^5	3.1×10^{-5}
	None	127	10267	1.86(2)	39.8	1.1×10^3	

Table 5.3: Summary of the data sets used in the analysis. The event density was estimated in the 1–5 keV range after masking pixels excluded from final analysis, see Sec. 5.5.2 for details of the masking procedure.

by the above diffusion model. These simulated events were then pasted onto blank FITS files and analyzed by the same procedure as real data.

We ran 2 consecutive batches of simulations to tune these parameters. The first batch of "high-energy" sets varied A and b for a flat energy spectrum of events between 4–7 keV populated uniformly within the CCD bulk, and compared the charge widths σ_{xy} to selected ^{57}Co data of similarly energetic events, resulting in tuned values of A = 215 ± 15 μm^2 and b = $5.6 \pm 1{\times}10^{-4}$ μm^{-1}. The choice of a spatially uniform distribution in depth is valid because the scattering length of γ-rays in Silicon with energies above 50 keV is >1 cm, much larger than the thickness of the CCD. These empirically derived parameters were in good agreement with those determined from muon energy depositions in prior work within the DAMIC collaboration. [14].

Next we accounted for Charge Transfer Inefficiency (CTI). This is the phenomena in CCD operation wherein charge is effectively smeared or lost when transferred between pixels during the read process. CTI is quantified as the dimensionless ratio of charge lost per pixel transfer and is quoted in the literature as being $\leq 10^{-5}$ during optimal operating conditions [15]. During the intervening year between ^{57}Co and ^{241}Am data acquisition, significant unexplained degradation occurred in the CCD leading to an asymmetric increase in σ_{xy} in the x-direction as is interpreted from Fig. 5.5, a signature of worsening CTI. We accounted for the progressive degradation (observed for increasing column number) in two ways: i) by removing the region x >720 from the analysis, and ii) using our second batch of simulations, now between 0–1 keV, to account for this effect. By tuning the threshold value of CTI, we matched σ_{xy} of selected clusters with energies <1 keV and results are shown in Fig. 5.6. CTI values can be found in the last column of Table 5.3.

The close match between both distributions demonstrates that the recorded spatial distribution of low-energy clusters is consistent with the signal from Compton scattering, with a negligible contamination from surface events or other non-uniform sources of charge.

Finally we accounted for detector and reconstruction efficiency. Efficiency can be qualitatively described as both a measure of the proportion of events at given pixel size for a given energy and how accurately specific energies are reconstructed. The efficiency was computed by comparing the number of clusters for a given pixel size vs the known number of injections. We utilized a bespoke batch of simulations flat in energy between 0–2 keV, and spatially uniform, to perform this analysis. We quantified the efficiency as:

$$\varepsilon_{total}(E) = \sum_{\#\text{pix.}} \varepsilon_i(E) = \sum_{\#\text{pix.}} \left. \frac{N^i_{reconstructed}}{N_{injected}} \right|_E \tag{5.4}$$

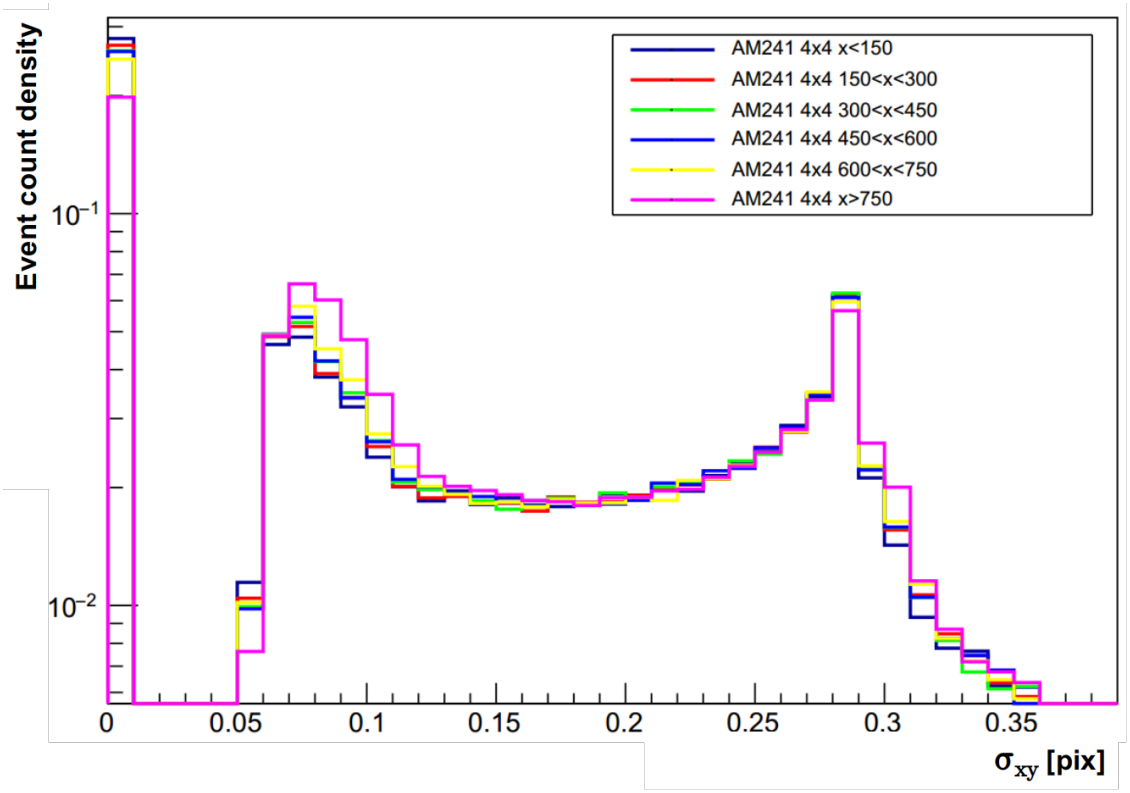

Figure 5.5: Cluster width estimator, σ_{xy}, for ^{241}Am data run as a function of the x-position of the cluster. For larger x, the 1 pix peak is progressively shifted towards the many-pixel bulk, indicative of CCD degradation and charge transfer inefficiency.

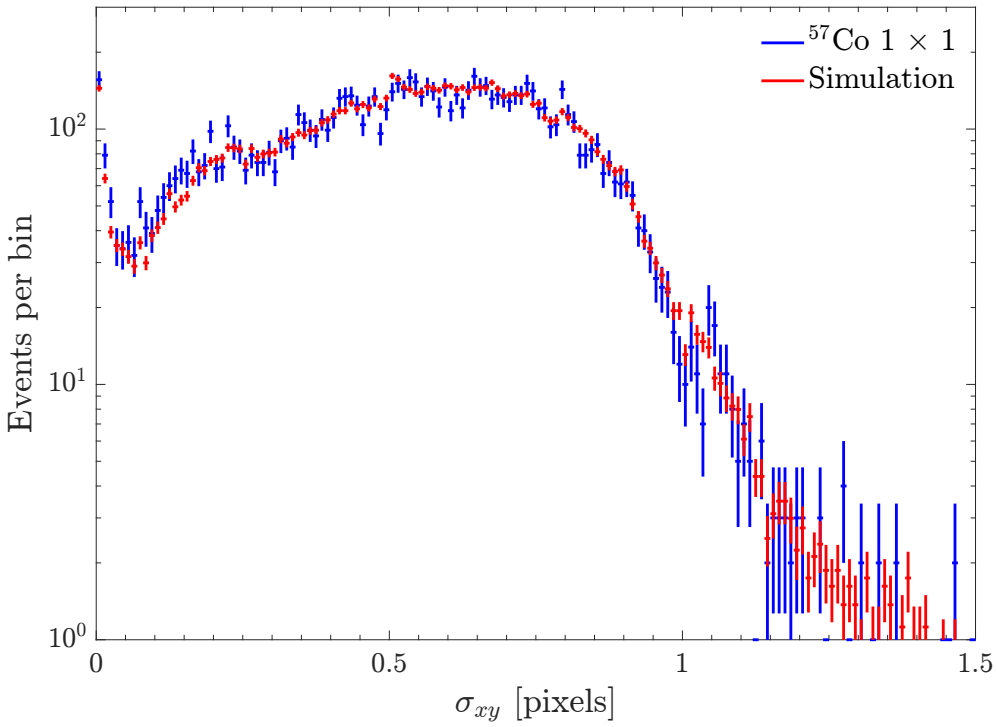

Figure 5.6: Lateral spread (σ_{xy}) of clusters in the ^{57}Co 1×1 data with energies <1 keV excluding readout noise. The result obtained by applying the same procedure to simulated events with a uniform distribution across the thickness of the device is shown for comparison.

where the individual ε_i are the extraction efficiencies for clusters comprised of i pixels. Results of this process can be seen in Fig. 5.7, indicative of a fully efficient procedure from 40 eV upwards. Values less than unity indicate incomplete extraction in the relevant portion of the energy spectrum, while those above 1 are an artifact of the differences in reconstructed vs. injected energy.

We further confirmed that the energy reconstruction procedure and response was indeed linear at energies down to threshold, as seen from Fig. 5.8.

5.5.2 Masking

Within images, pixels are removed before analysis by the process of "masking". *Hot pixels* and *hot columns* occur due to defects in the Silicon lattice that lead to trapped charge and hence result in consistently high read-values. Across an entire dataset we generically

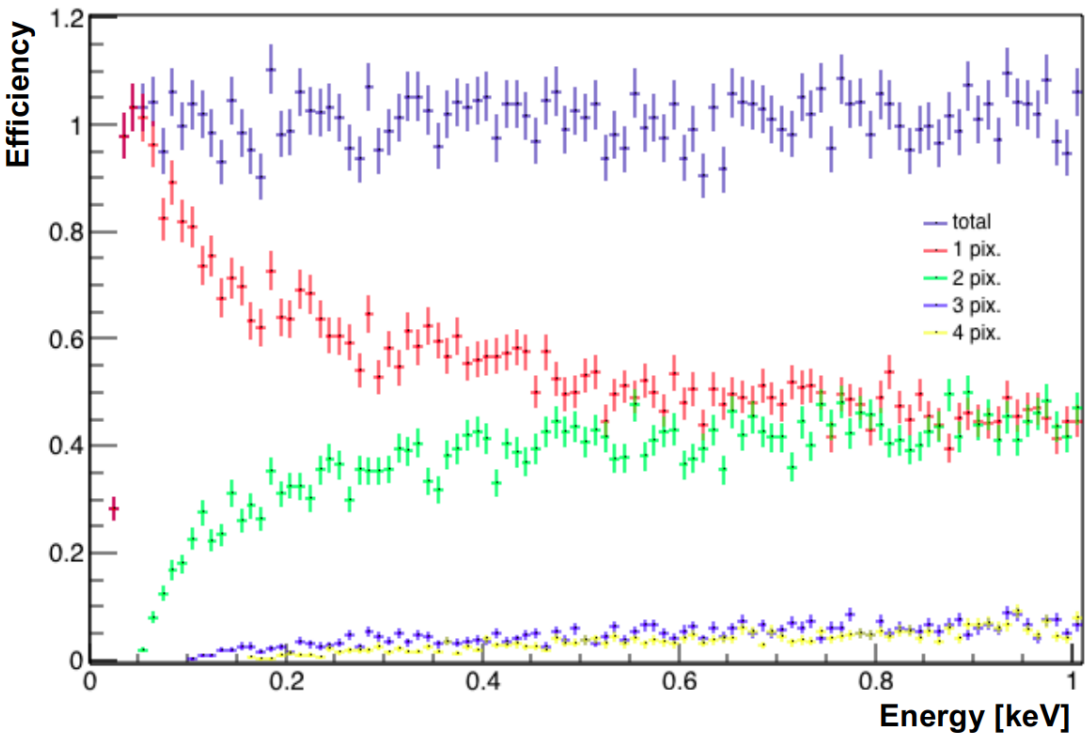

Figure 5.7: Detector efficiency for simulated events with energy between 0–1 keV and cluster sizes between 1 and 4 pixels

expect that the average value of any pixel should be equal to the mean pedestal value within uncertainty. We specifically calculate the median and median absolute deviation (MAD) of all pixels in each of the runs outlined in Table 5.3. We exclude pixels which are more than 3 MAD from the median in at least 50% of the images or those that are distributional outliers when compared to all pixels. Additionally we mask entire columns that have $> 30\%$ of pixels masked and discard any cluster neighboring a masked pixel.

Saturated pixels occur when the local deposition of energy within a pixel exceeds the dynamic range of the Analogue to Digital Converter (ADC). When combined with CTI, pixel to amplifier transfer leads to charge leaking to neighboring pixels in the same horizontal row as the saturated pixel. If there is a coincidental occurrence of a pixel with below pedestal read-value (i.e. a *negative pixel*) between these trailing pixels and the saturated pixel, then the clustering algorithm will spuriously identify two separate clusters. This process artificially increases image noise and to counteract this we discarded clusters that were bordered by negative pixels.

Finally in the ^{241}Am data, due to the increase in x-direction CTI as discussed in Sec. 5.5.1 we identify an artificial effect, see Fig. 5.9, of a sharp spatial drop off in the number

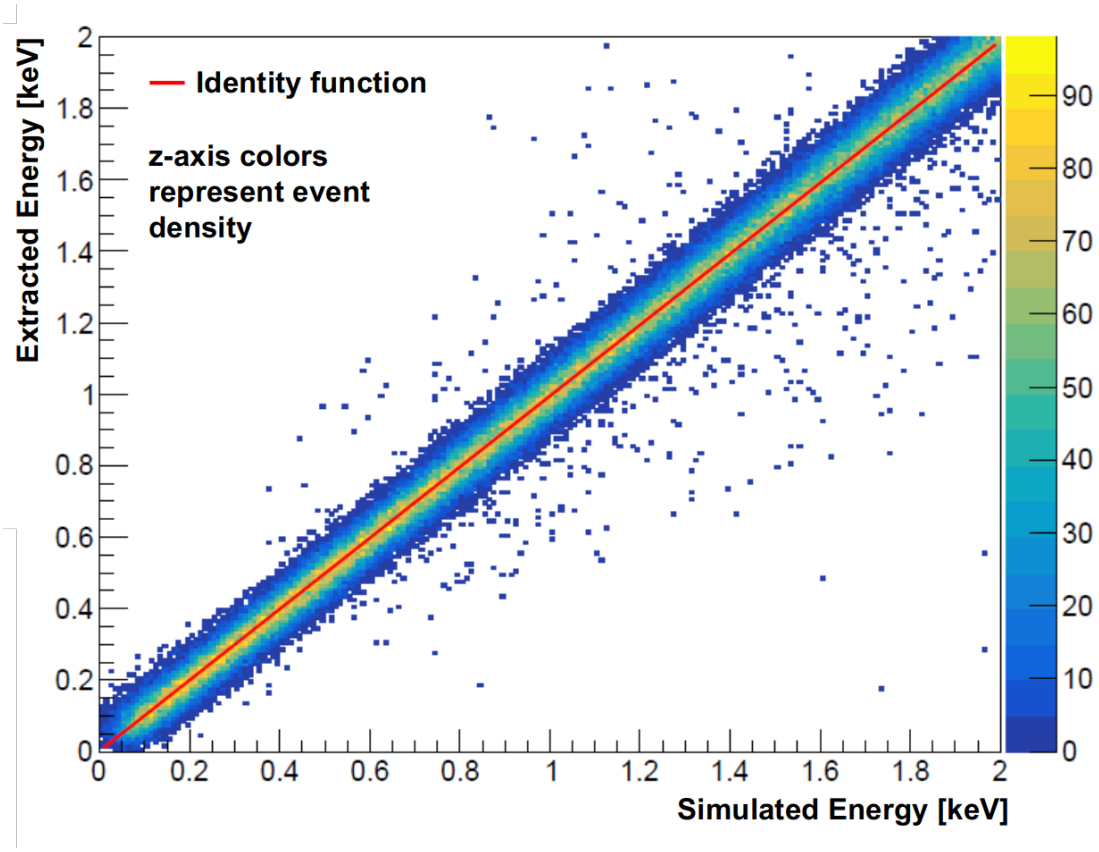

Figure 5.8: Validation of energy reconstruction through simulation. Injected charge is accurately reconstructed as seen by the unity slope of the reconstruction.

of pixel events above column ∼720. These events are sufficiently far away from the output node such that the high CTI causes the clustering algorithm to continually identify point depositions as multiple pixel events. Hence as previously mentioned we discard all pixels with spatial x-value >720. All told the entire masking process typically removed <10% of the pixels in an image.

5.5.3 Background Subtraction

After application of the masking procedure outlined above, noise reduction and background subtraction proceed in three successive steps. As a first pass, images were selected by roughly matching the first and second moments (mean and variance) of the noise distributions between source and background datasets. This was done to prevent over-correction in the background subtraction process. An example of the noise distribution for ^{241}Am pre and post selection cut can be seen in Fig. 5.11.

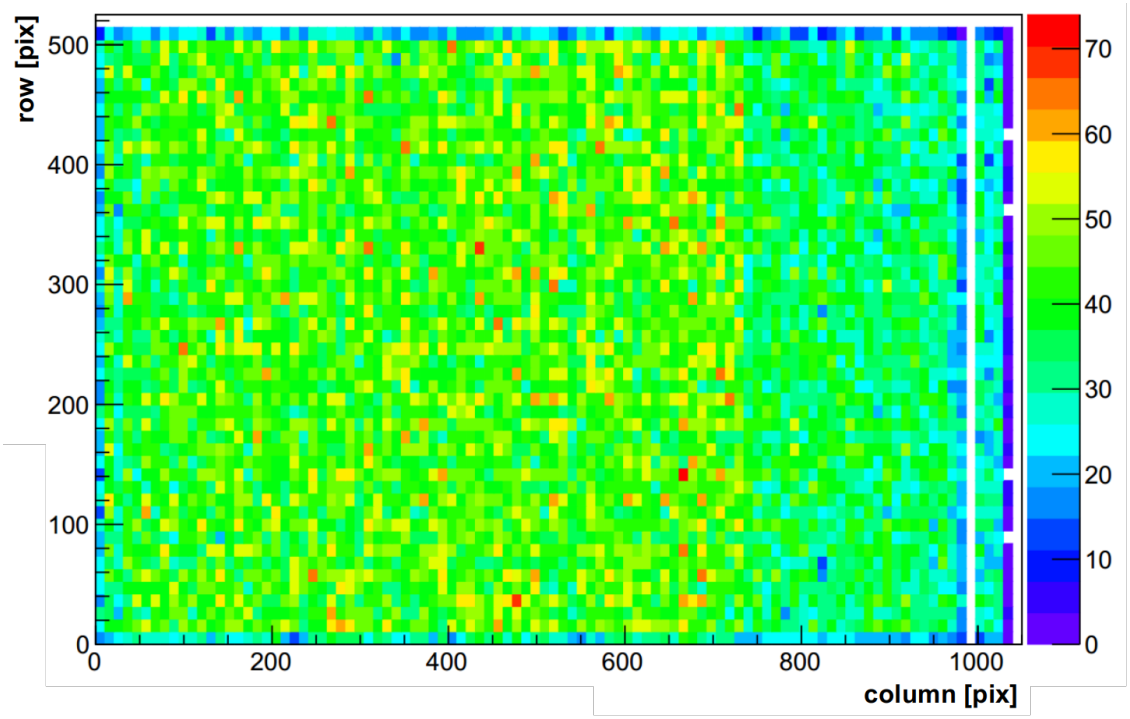

Figure 5.9: Artificial 1-pixel boundary in ^{241}Am 4x4 data

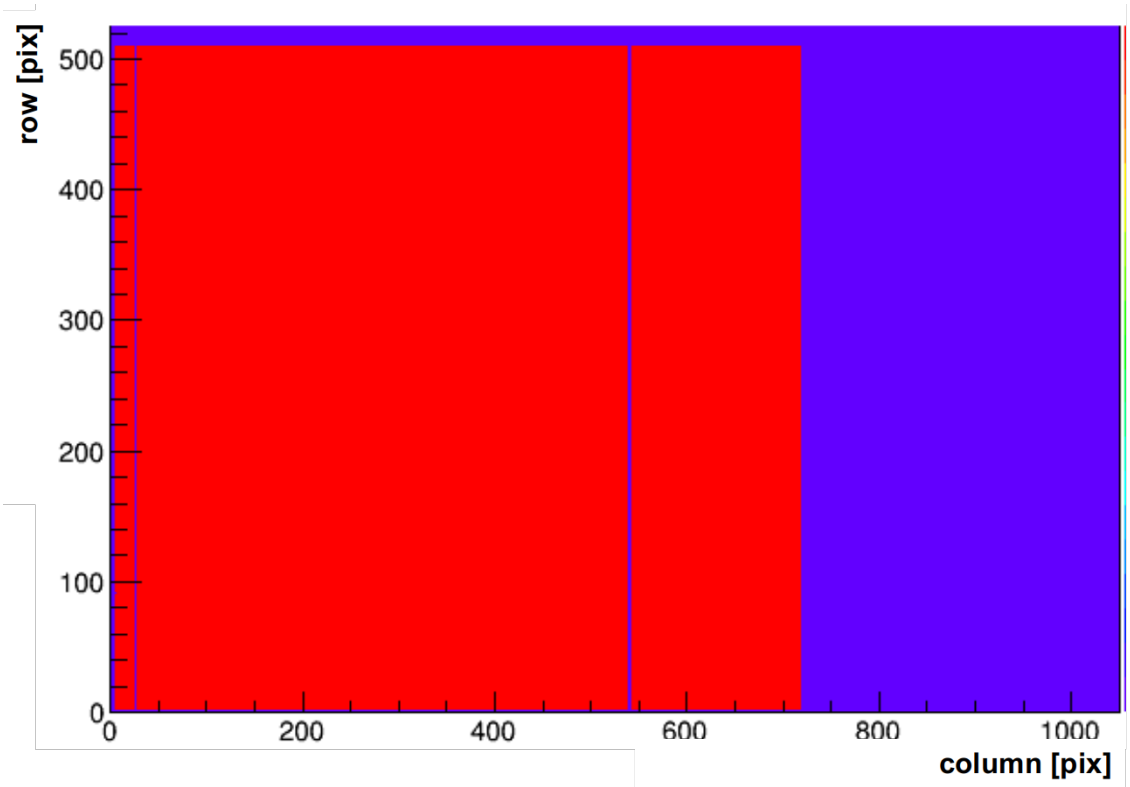

Figure 5.10: Masked (blue) pixels for ^{241}Am data

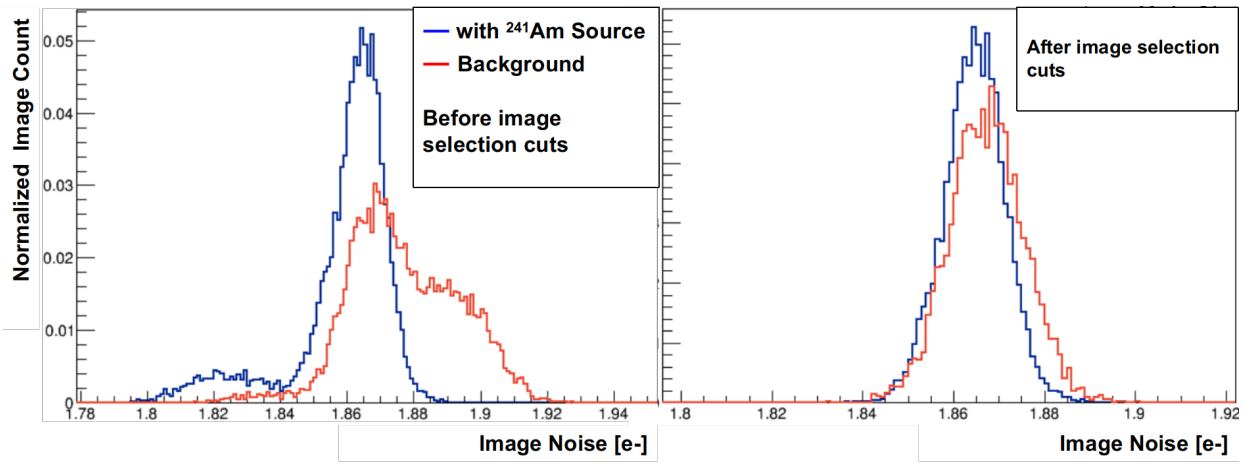

Figure 5.11: Matching mean and variance of ^{241}Am dataset normalized noise distribution

Next, the background data was corrected for pixel occupancy. Effectively the background images have a larger number of noise pixels because there was no source present. We scaled the maximum of normalized pixel distribution of pedestal subtracted background images (i.e. the 0th bin) to match with the source dataset. This translated to a downward correction of $\sim 4\%$ to the background energy spectrum.

The final step in the background subtraction process was the choice of energy threshold to exclude readout noise. Figure 5.12 presents the spectrum of selected clusters with different number of pixels in all background data. The dashed line shows the result of a Gaussian fit to the single-pixel white noise, which demonstrates a negligible contribution of readout noise for single-pixel clusters above 60 eV. Readout noise is still important for clusters with a larger number of pixels up to 80 eV, becoming negligible beyond this point. Hence, to construct the final spectra, we considered only single-pixel events in the 60–80 eV range and corrected for the 95%–90% efficiency of this selection (see 5.5.1). For energies >80 eV, we considered all clusters without any correction, as the efficiency of clustering an event at these energies was already >99 %.

5.6 Fano Factors & Resolution

The functional form of the total energy resolution in the energy spectrum is:

$$\begin{aligned} \sigma_E^2 &= \sigma_C^2 + \sigma_F^2 \\ \sigma_F &= \sqrt{FE\epsilon_i} \\ \sigma_C &= \sqrt{N}\sigma_{pix}, \end{aligned} \tag{5.5}$$

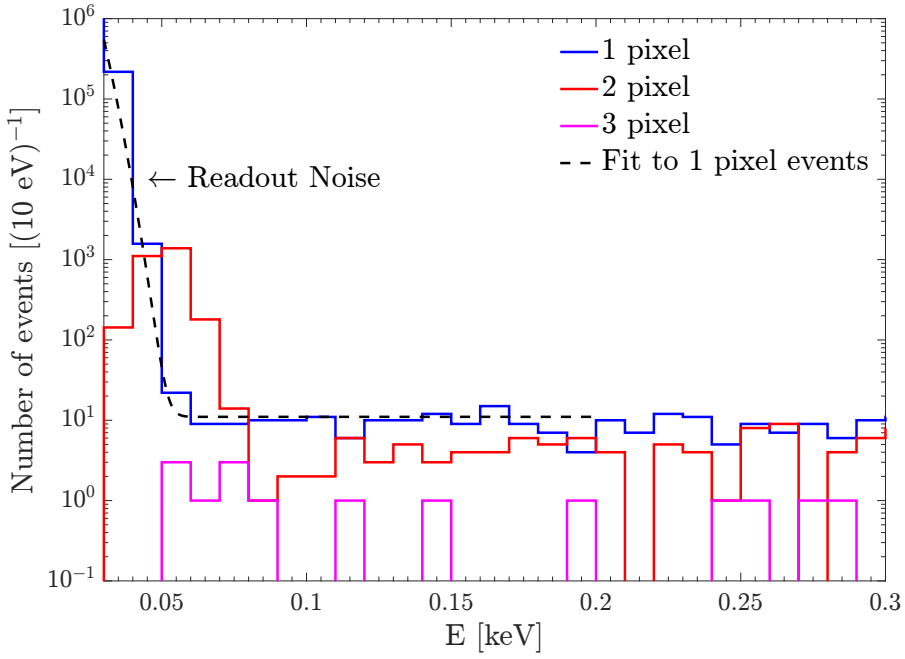

Figure 5.12: Energy spectra from the 4×4 background data for clusters of different sizes. A Gaussian fit was performed to estimate the contribution of readout noise to the single-pixel spectrum.

with the respective contributions of the read noise of a cluster σ_C and the Fano factor F as a function of energy E. ϵ is the charge pair ionization energy from Chap. 4, N is the number of pixels in a cluster and σ_{pix} is the per-pixel read noise tabulated in Table 5.3. We measured the Fano factor to be $F = 0.128 \pm 0.002$ from fitting x-ray fluorescence peaks from the ^{57}Co source 4×4 binned data, as shown in Fig. 5.13. These peaks occur when the emission γs impinge on the chamber or copper frame and cause atomic excitations in their constituent atoms (e.g. Cr, Mn, Fe, and Ni) resulting in characteristic x-rays.

We find the best fit relation of $\sigma_{tot}^2 = (12\text{eV})^2 + (3.8\text{eV})\text{FE}$ and take this as input for the simulations discussed in Sec. 5.5.1.

5.7 MCNP Simulation

A simulation of the experiment was conducted using MCNPX (Monte Carlo N-Particle eXtended; v. 2.7.0 (2011)) particle transport code [16]. Full photon and electron transport is enabled using the corrected MCPLIB84 library to properly account for Doppler broadening

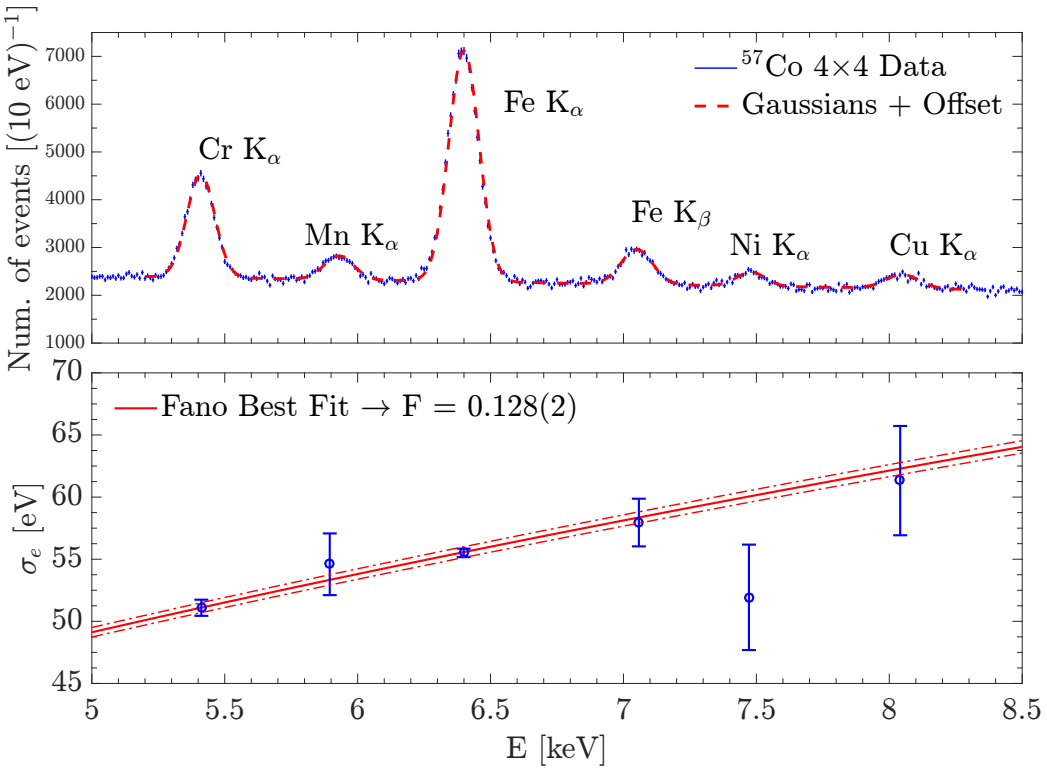

Figure 5.13: Top: Energy spectrum from the ^{57}Co source with Gaussian fits to the fluorescence lines used for calibration. Bottom: Energy dependence of the line width; the Fano factor was obtained from a fit with the energy resolution model of Eq. 5.5

[17]. The geometry and material specification of the setup was reconstructed to high-fidelity and the reproduced 3D model can be seen in the inset of Figure 5.3.

Figure 5.14 shows the observed electron-recoil spectrum in the 1×1 data with the ^{57}Co source, with overall gross features labeled. Because of the high spatial resolution of the CCD, each event arises from a single γ-ray interaction. In addition to the spectral continuum from zero up to the Compton edges, other characteristic spectral features are evident, including the mono-energetic peaks from photoelectric absorption of the primary 122 keV and 136 keV γ rays, and secondary x-ray fluorescence lines from the surrounding materials. The simulated spectrum with MCNP is shown for comparison, presenting a good agreement to the data, with some underestimation of the fluorescence yields.

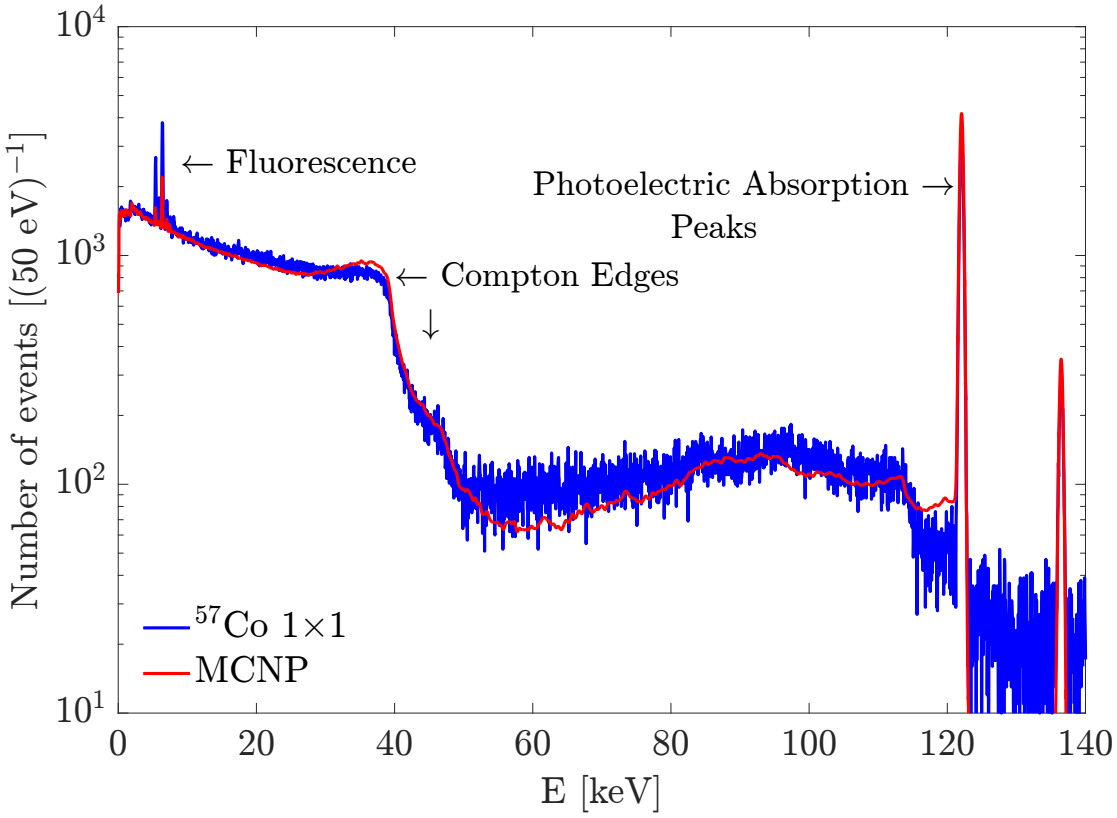

Figure 5.14: Spectrum observed in the 1×1 data from the ^{57}Co source. The expectation from MCNP, with its amplitude normalized to the photoelectric absorption lines, is shown for reference. Characteristic spectral features are labeled.

5.8 Low Energy Spectra

After the entire data processing chain, we show the final Compton spectra in the 60 eV–4 keV range in Figures 5.15 and 5.16 for ^{57}Co and ^{241}Am respectively. The data are compared to the predictions from IA and the MCNP model, scaled to match the right-hand side of the K step in the data.

Both the IA and MCNP are able to correctly match the gross features of the Compton spectra at low energies, implying a satisfactory implementation of the underlying physics. Overall, IA provides a better match to the data than MCNP, but it fails to accurately reproduce the shape of the L-step feature (insets of Fig. 5.15 and 5.16). This is unexpected, as the energy, amplitude and shape of the K step is consistent with the IA prediction. It

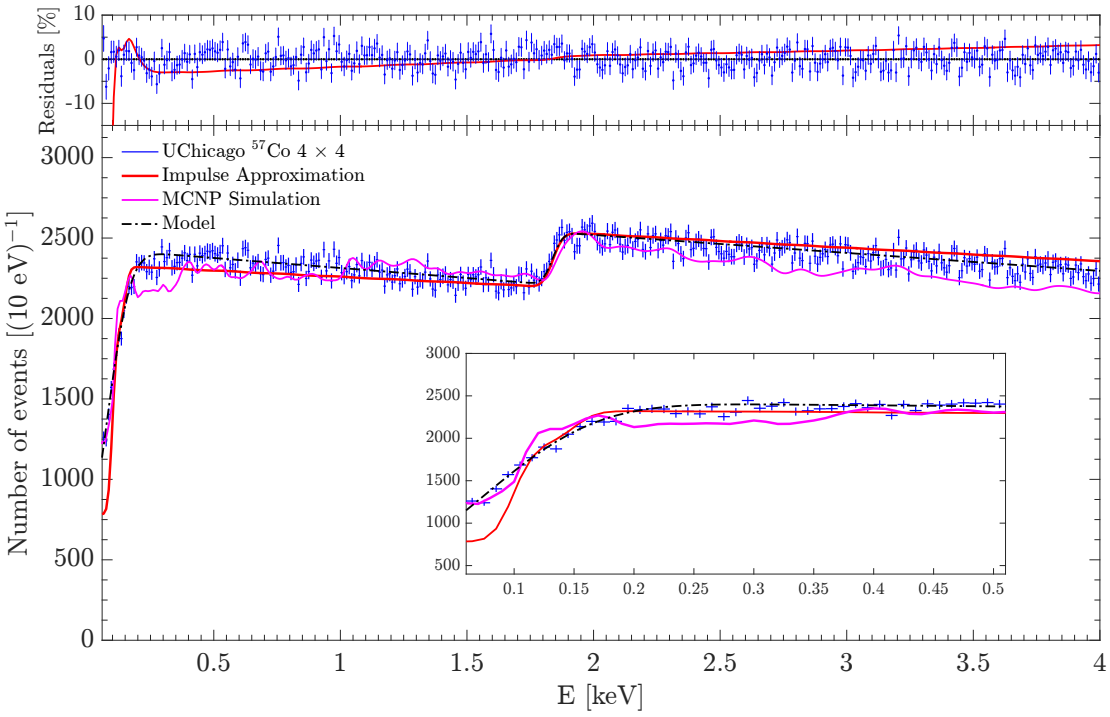

Figure 5.15: Bottom: Low-energy Compton spectrum from the ^{57}Co source. The predictions from the Impulse Approximation (IA) and MCNP are shown for comparison. The best fit to the model described in Sec. 5.9 is presented by the dashed black line. Inset: Detail of the L step in the 60–500 eV range. Top: Residuals after subtraction of the best-fit model from the data.

is unlikely that the apparent decrease in resolution at the L step is due to the response of the detector. Prior work by Ref. [18] in measuring the resolution of CCD detectors, see Fig. 5.17, shows the expected plateauing at low energies, consistent with the noise model proposed in Sec. 5.6. In particular, Oxygen and Calcium $K\alpha$ fluorescence x-ray calibration gives a resolution of approx ∼30 eV at $E_\gamma \leq 525$ eV — *lower* than the measured ∼65 eV at the L step. Thus, we interpret the apparent decreased resolution as genuinely originating from a softened L step in the electron recoil spectrum, which may occur if the theoretical assumption adopted by IA that each atomic shell may be treated independently does not strictly hold beyond the K shell.

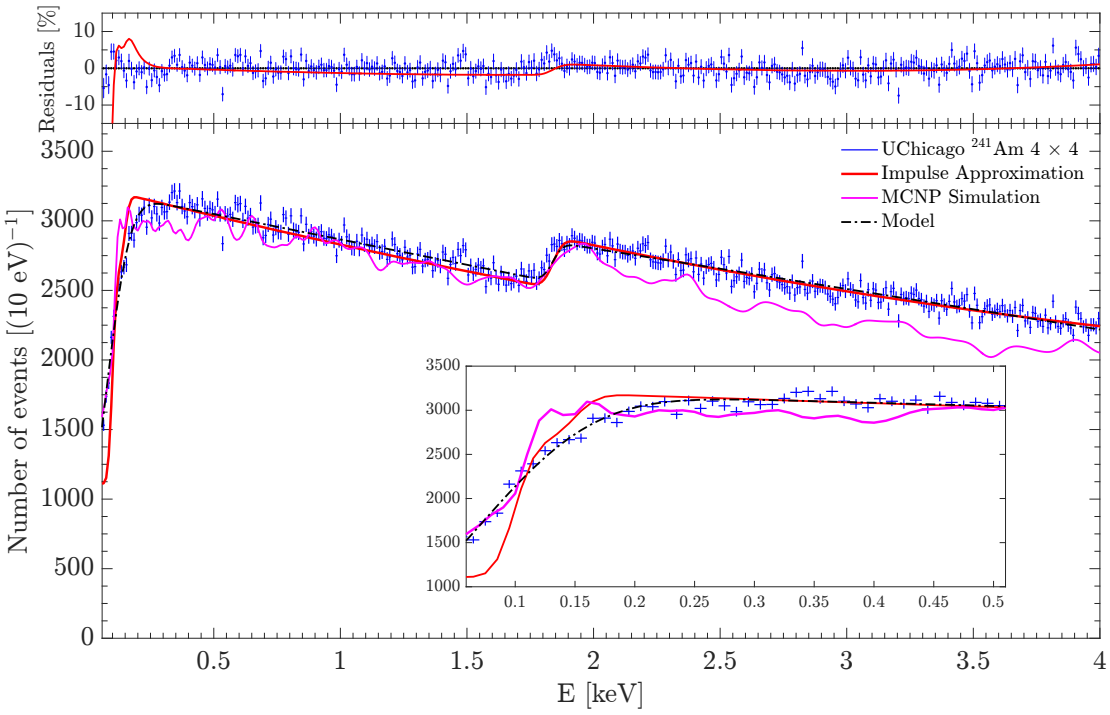

Figure 5.16: Bottom: Low-energy Compton spectrum from the ^{241}Am source. The predictions from the Impulse Approximation (IA) and MCNP are shown for comparison. The best fit to the model described in Sec. 5.9 is presented by the dashed black line. Inset: Detail of the L step in the 60–500 eV range. Top: Residuals after subtraction of the best-fit model from the data.

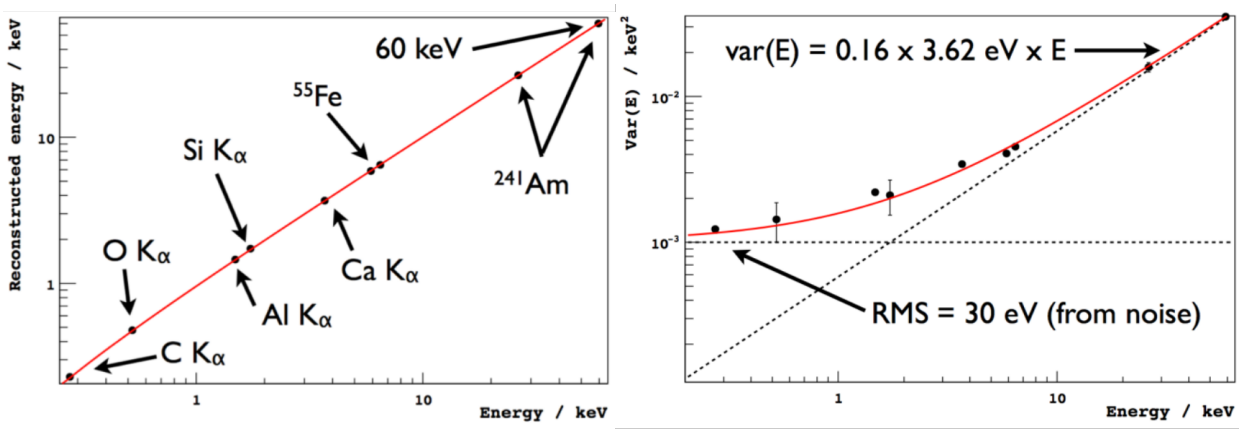

Figure 5.17: Prior work done by Zhou [18] and reproduced from there, showing the energy response of a DAMIC CCD. Left: Reconstructed energy points were extracted from x-ray fluorescence peaks. Right: Energy resolution associated to those features (right).See paper for experimental details.

5.9 Model of Compton spectra at low energies

As is evident from Fig. 5.15 and 5.16, and expected from IA (Fig. 5.2), the Compton spectra at low energies is rather generic, with the position of the steps determined by the atomic shells of the target and the slope of the spectrum between the steps being approximately constant. To get a sense of this slope (referring back to $a_{1,2}$ in Fig. 5.2), we can work with the standard Klein-Nishina formula to solve for the total cross section by substituting Eq. 5.1 into Eq. 5.2 and integrating over the full solid angle ($d\Omega = \sin\theta \mathrm{d}\theta \mathrm{d}\phi$), as in Ref. [5], to get:

$$\sigma_{KN} = 2\pi r_0^2 \left[\frac{1+x_\gamma}{x_\gamma^2} \left(\frac{2(1+x_\gamma)}{1+2x_\gamma} - \frac{\ln(1+2\mathrm{x}_\gamma)}{x_\gamma} \right) + \frac{\ln(1+2\mathrm{x}_\gamma)}{2x_\gamma} - \frac{1+3x_\gamma}{(1+2x_\gamma)^2)} \right] \tag{5.6}$$

We then differentiate the expression above, and recast it in terms of the deposited energy E to get the KN differential spectrum in deposited energy:

$$\frac{d\sigma_{KN}}{dE} = \frac{2\pi r_0^2}{x_\gamma^2 mc^2} \left[1 + \left(\frac{E}{E_s} \right)^2 \left(\frac{1}{2x_\gamma^2} \frac{E_s}{E_\gamma} - \frac{1}{x_\gamma} \frac{E_s}{E} \right) \right], \tag{5.7}$$

Next, we linearize this expression for $E \approx 0$ (i.e. strictly speaking $\delta \ll 1$) with a Taylor expansion to get:

$$\begin{aligned} \frac{d\sigma_{KN}}{dE} &\approx \frac{2\pi r_0^2}{x_\gamma^2 mc^2} \left(1 - \frac{E}{E_\gamma x_\gamma} \right) \\ \implies a_{1,2} &\approx -\frac{2\pi r_0^2}{x_\gamma^3 E_\gamma mc^2} \end{aligned} \tag{5.8}$$

While Eq. 5.8 is a good rule of thumb we can deploy the full machinery of the IA prediction for energies <4 keV and fit them with a piecewise function constructed from first-order polynomials bounded by the atomic binding energies. With the appropriate choice of parameters, the function agrees to better than 0.5% with IA for a wide range of γ-ray energies for which the Compton scattering cross section is significant. Motivated by this result, we proposed a parametrization of the Compton spectra in the energy range 60 eV–4 keV with an expression of the form:

$$f(E) = A \times \begin{cases} a_1(E - E_K) + 1 & E \geq E_K \equiv E_{10} \\ a_2(E - E_K) + b_2 & E_L \leq E < E_K \\ b_3 & E < E_L, \end{cases} \tag{5.9}$$

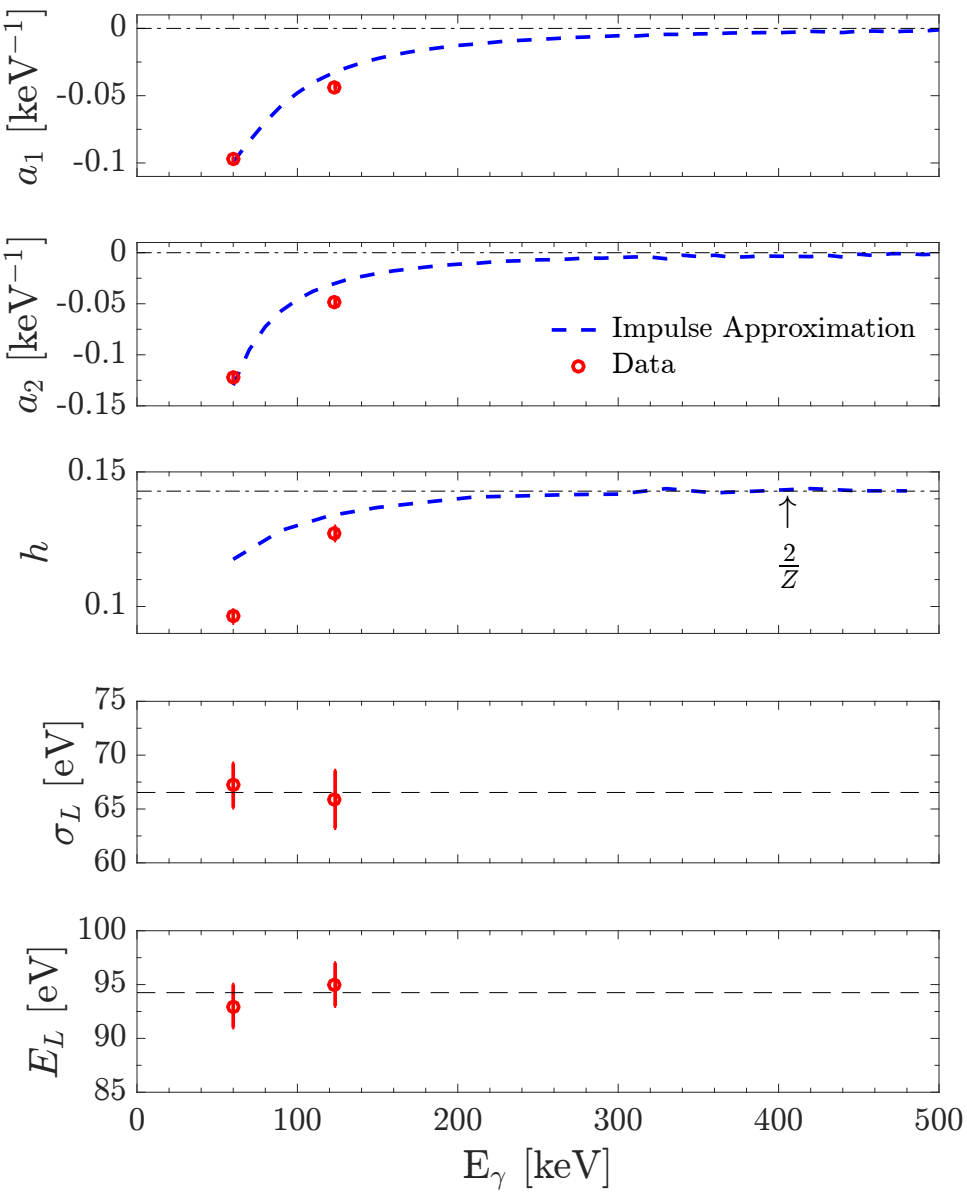

Figure 5.18: Dependence of the five model parameters that determine the Compton spectrum at low energies, i.e, a_1, a_2, h, σ_L and E_L, on the incident γ-ray energy. The dashed blue line in the top three panels shows the prediction from IA, while the dashed black line of the bottom two panels is the mean value of both measurements.

with an additional Gaussian resolution term σ_L that applies only for E <0.5 keV to smooth the L-step feature. Although the IA predicts two distinct L_1 and $L_{2,3}$ steps, we include a single step at an effective energy E_L. With the appropriate choice of σ_L and E_L, this definition significantly improves the description of the data by the model over the result from IA presented in Section 5.8.

To simplify the model further, we introduce the following approximation:

$$b_3 = \frac{Z-10}{Z-2}[b_2 + a_2(E_L - E_K)],$$

which defines the relative amplitude of the spectrum before and after the L step as the ratio of the number of target electrons that contribute to the signal below and above E_L. After imposing this constraint, the number of free parameters of the proposed parametrization decreases to six: the amplitude of the K step ($h = 1 - b_2$), the slopes to the right and left of the K step (a_1 and a_2), the parameters defining the shape of the L step (σ_L and E_L), and the overall normalization of the spectrum (A).

The best fit to the data with our model (including the detector response presented in Section 5.6) is shown by the dashed black line in Fig. 5.15 and 5.16 with the residuals in the top panel, which demonstrate an agreement to better than 5% throughout the full energy range. Figure 5.18 shows the best-fit values as a function of γ-ray energy for the five parameters that determine the shape of the spectrum. For a_1, a_2 and h, we included the prediction by IA. Our observations are consistent with the expectations from IA: i) the magnitude of the slope of the spectrum is inversely proportional to E_γ, and ii) the value of h asymptotically approaches the fraction of electrons in the K shell, i.e., $2/Z$. The best-fit values of σ_L∼65 eV and E_L∼95 eV are consistent between the ^{57}Co and ^{241}Am data, with no dependence on E_γ.

5.9.1 Application to a continuous spectrum

Because of the linear nature of Eq. 5.9 and the constant values of σ_L and E_L, the addition of multiple functions corresponding to incident γ rays of different energies would also be accurately described by the same function with the appropriate choice of average values for the parameters. Therefore, the proposed parametrization should be a good description for the Compton background at low energies for any energy distribution of the incident γ-ray flux. We can test this by applying the parametrization to the case of a continuous photon

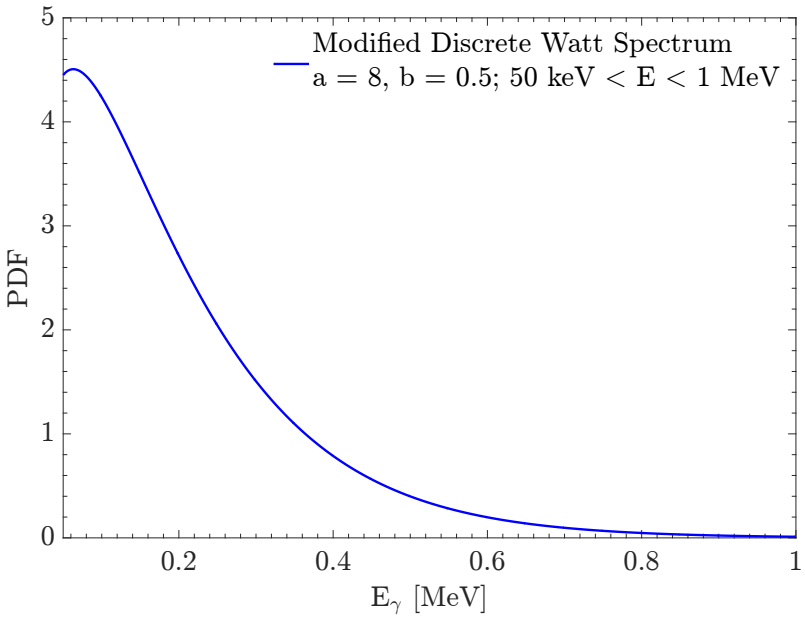

Figure 5.19: Truncated Watt distribution, tuned to simulate continuous low-energy background with peak at 60 keV.

spectrum (e.g. Bremsstrahlung) simulated in MCNP. We tune an in-built Watt Spectrum:

$$W(E) = \left(\left(\frac{\pi}{4a\alpha}\right)^{\frac{1}{2}} e^{\frac{\beta}{4\alpha}}\right)^{-1} e^{-\alpha E} sinh\left((\beta E)^{\frac{1}{2}}\right), \tag{5.10}$$

with scale parameters a and b (Eq. 5.10) and truncate the energy to between 0.05 MeV and 1 MeV and normalize the resultant distribution, PDF of which can be seen in Fig. 5.19

We then compute the expected Compton spectrum ($S(E^i_{1,2})$ for bin i in Region 1 or Region 2) for this incident γ-spectrum by integrating the parametrization presented previously:

$$S(E^i_{1,2}) = \frac{1}{C}\int_{50keV}^{1MeV} dE_\gamma W(E_\gamma)[a_{1,2}E^i_{1,2} + b_{1,2}] \tag{5.11}$$

The resulting overlay of the simulated spectrum and the computed parametrization can be seen in Fig. 5.20 with accompanying residuals. Using either the MCNP or the IA based parametrization as a benchmark, we can see that both approaches are within 10% and importantly get equivalent slopes before and after the K-shell. The adequate fit indicates that

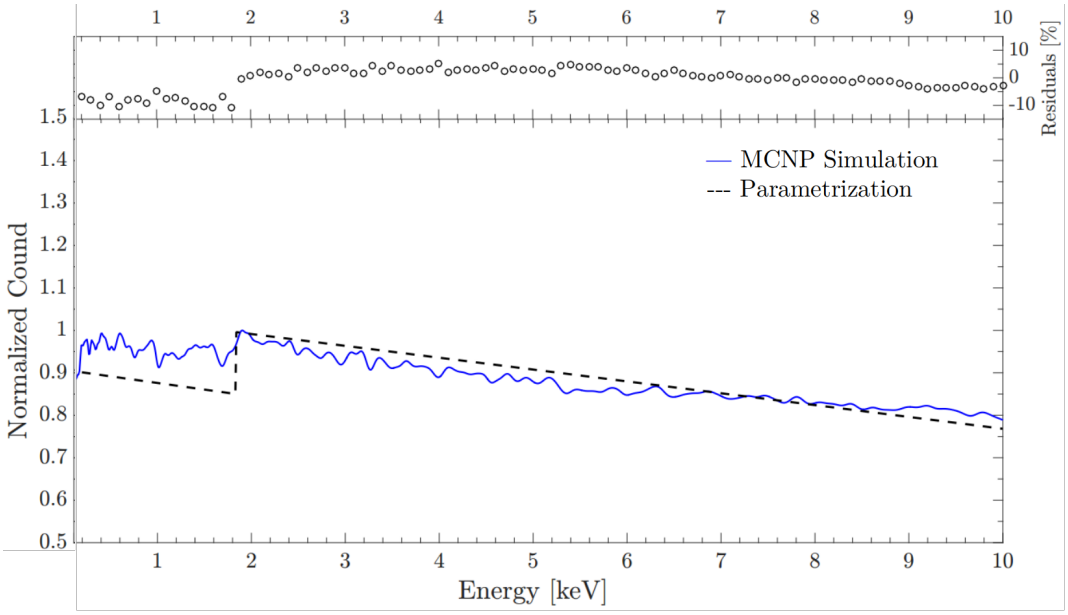

Figure 5.20: Parametrization described in Sec. 5.9 fit to the MCNP simulated continuous spectrum of Eq. 5.10, with residuals plotted above.

the simplified approach used in this chapter should be applicable for computing background estimates in dark matter experiments with significant and spectrally realistic Compton scattering contributions.

References

[1] K. Ramanathan et al. Measurement of low energy ionization signals from compton scattering in a charge-coupled device dark matter detector. *Phys. Rev. D*, 96:042002, Aug 2017. doi: 10.1103/PhysRevD.96.042002.

[2] A Aguilar-Arevalo et al. Results on low-mass weakly interacting massive particles from a 11 kg d target exposure of damic at snolab. 2020. unpublished.

[3] Arthur H. Compton. A quantum theory of the scattering of x-rays by light elements. *Phys. Rev.*, 21:483–502, May 1923. doi: 10.1103/PhysRev.21.483. URL `https://link.aps.org/doi/10.1103/PhysRev.21.483`.

[4] O. Klein and Y. Nishina. Über die streuung von strahlung durch freie elektronen nach der neuen relativistischen quantendynamik von dirac. *Zeitschrift für Physik*, 52(11):853–868, 1929. ISSN 0044-3328. doi: 10.1007/BF01366453. URL `http://dx.doi.org/10.1007/BF01366453`.

[5] Hideo Hirayama. Lecture note on photon interactions and cross sections. *KEK, High*

Energy Accelerator Research Organization, Oho, Tsukuba, Ibaraki, Japan, 2000.

[6] RD Deslattes et al. X-ray Transition Energies. URL `http://physics.nist.gov/XrayTrans`. version 1.2 [Online], National Institute of Standards and Technology (2005).

[7] CT Chantler, K Olsen, RA Dragoset, J Chang, AR Kishore, SA Kotochigova, and DS Zucker. NIST x-ray form factor, attenuation and scattering tables (version 2.1). http://physics.nist.gov/ffast, October 2005.

[8] R. Ribberfors and K. F. Berggren. Incoherent-x-ray-scattering functions and cross sections $(\frac{d\sigma}{d\Omega'})_{\text{incoh}}$ by means of a pocket calculator. *Phys. Rev.*, A26:3325–3333, Dec 1982. doi: 10.1103/PhysRevA.26.3325. URL `https://link.aps.org/doi/10.1103/PhysRevA.26.3325`.

[9] Jesse W. M. Du Mond. Compton modified line structure and its relation to the electron theory of solid bodies. *Phys. Rev.*, 33:643–658, May 1929. doi: 10.1103/PhysRev.33.643. URL `https://link.aps.org/doi/10.1103/PhysRev.33.643`.

[10] I. Waller and D. R. Hartree. On the intensity of total scattering of x-rays. *Proceedings of the Royal Society of London A: Mathematical, Physical and Engineering Sciences*, 124(793):119–142, 1929. ISSN 0950-1207. doi: 10.1098/rspa.1929.0101.

[11] F. Biggs, L.B. Mendelsohn, and J.B. Mann. Hartree-fock compton profiles for the elements. *Atomic Data and Nuclear Data Tables*, 16(3):201 – 309, 1975. ISSN 0092-640X. doi: https://doi.org/10.1016/0092-640X(75)90030-3. URL `http://www.sciencedirect.com/science/article/pii/0092640X75900303`.

[12] M M Bé et al. *Table of Radionuclides*, volume 1–A = 1 to 150. Monographie BIPM-5, Sèvres, 2004.

[13] M M Bé et al. *Table of Radionuclides*, volume 5–A = 22 to 244. Monographie BIPM-5, Sèvres, 2010.

[14] A. Aguilar-Arevalo et al. Search for low-mass WIMPs in a 0.6 kg day exposure of the DAMIC experiment at SNOLAB. *Phys. Rev.*, D94(8):082006, 2016. doi: 10.1103/PhysRevD.94.082006.

[15] J.R. Janesick. *Scientific Charge-Coupled Devices*. The International Society for Optical Engineering, Bellingham, WA, 2001. ISBN 9780819436986. URL `http://books.google.com/books?id=rkgBkbDie7kC`.

[16] X-5 Monte Carlo Team. MCNPX 2011. Los Alamos National Laboratory Report No. LA-UR-03-1987, unpublished (2008).

[17] M. White. Further Notes on MCPLIB03/04 and New MCPLIB63/84 Compton Broadening Data For All Versions of MCNP5. Los Alamos National Laboratory Report No.

LA-UR-12-00018, unpublished (2012).

[18] Jing Zhou. *Direct dark matter detection with the DAMIC experiment at SNOLAB*. PhD thesis, The University of Chicago, 2015.

CHAPTER 6

LIGHT DARK MATTER SEARCHES

n.b. This chapter formed the basis of Aguilar-Arevalo et al. [3] and Aguilar-Arevalo et al. [4], for each of which I am considered first author within the collaboration (the publications listed authorship alphabetically according to collaboration rules) as I was responsible for the analyses and plots/text for both works — sections of which are reproduced here. Copyright rests with the American Physical Society.

In Chap. 1 we discussed Light Dark Matter candidates (LDM) in the context of a natural evolution of community interest in alternative DM candidates. However if we take one of these candidates, such as for DM recoiling off electrons as in Sec. 1.4.3, and look at its ionization spectrum in a Silicon detector, we get a plot like Fig. 6.1. We see that the ionization spectrum cuts off below approx. 45 eV ($12\,e^-$) which is on par with the DAMIC threshold, for conventional CCDs, established in Chap. 2.

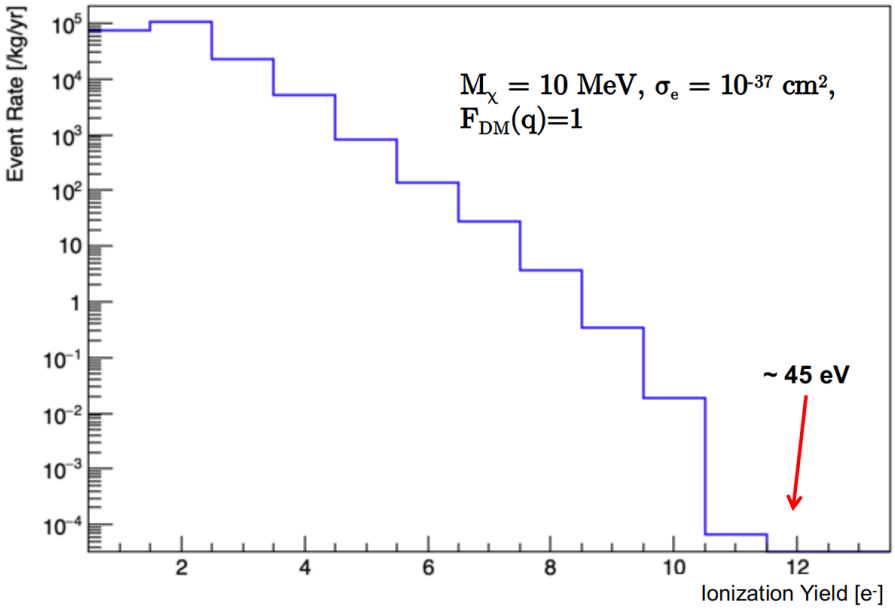

Figure 6.1: Example ionization spectrum for a 10 MeV DM candidate recoiling off electrons in Silicon, for given parameters (see Sec. 1.4.3) for explanations). Note how all events deposit less than approx. 45 eV ($12\,e^-$)

At first glance this obstacle seems insurmountable since clustering will not work efficiently below threshold so accurately picking out any interaction that arises from such an LDM will be a challenge. However, if we are not concerned with discovery potential, we can exploit the statistical nature of Leakage Current (LC) accumulation in the device as a way around

the problem. We remind ourselves from Chap. 2 that LC is the shot noise production of spurious charge unrelated to ionization. This can come from a multitude of sources like thermal effects, stress in the CCDs, light leaking into the vacuum vessel, blackbody radiation etc.

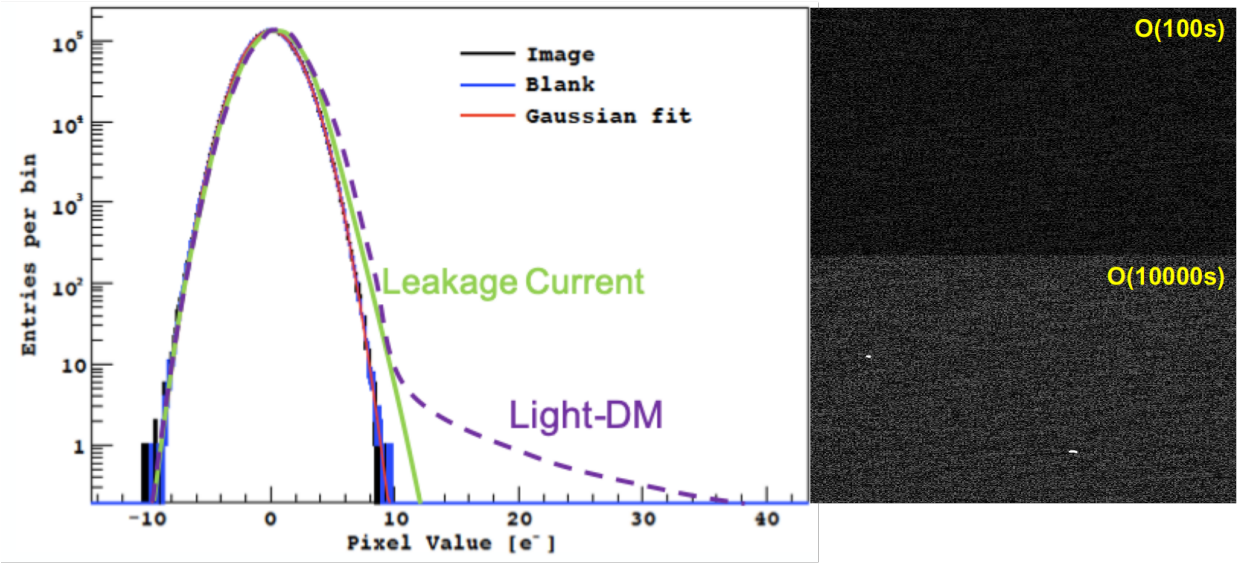

Figure 6.2: Left: Example pixel distribution of a short exposure Image and Blank file, with overlaid drawings suggestive of the modifications caused by leakage current (green) and light DM (purple). Right: Small sections of images with different exposures (bottom: long and top: short) taken with same parameter settings, where brightness is a proxy for charge contained within the pixel. A noticeable difference is seen in the bottom image even if only two clusters (bright dots) can be visually identified, suggestive of leakage current.

We illustrate the limit setting idea in Fig. 6.2. On the Right we show portions of two images taken with the same parameters but different exposures. Brightness is correlated with charge content so we can clearly see that the longer exposure image has a much higher baseline even if only two clusters (the bright dots) can be visually confirmed. We show a pixel distribution on the Left from a real image (black histogram, with Gaussian fit in red) with overlaid distributions corresponding to a LC (green) and to a flux of LDM (purple). Generically then, if we interpret the dark current that exists in our setup as *being produced by a LDM* that will allow us to set a limit on that flux *below our clustering threshold*. To be specific, if the LDM deposit sub-threshold energy stochastically on the pixel array, we can trade off between a model of this DM and a model of our LC to determine the relative contributions of both. This will be a competitive method to traditional DM searches if our LC is low, which we have already demonstrated in Chap. 3.2. To reiterate, while this will not allow us to *claim* discovery of DM, meaningful limits may be placed.

In the following sections, we will show how we applied this simple idea to set leading limits on Hidden Photons and sub-GeV DM recoiling off electrons, for certain regions of their respective parameter spaces. Our initial limits on HPs were done with the Stage I detector in 2017, while both DM-e$^-$ and improved HP limits were set in the follow-up publication in 2020.

6.1 Charge distribution models

6.1.1 Hidden Photons & the Optical properties of Silicon

To compute the ionization yield for hidden photons, we refer back to Chap. 1.4.2 to understand the physics of these DM candidates and their interaction rate in our CCD through Eq. 1.20. Fundamental quantities like the *polarization tensor* $\Pi(\omega)$ (in the case of natural units with E = ω) and the photon mass absorption cross section σ_γ must be extracted from the experimental literature.

The polarization tensor quantifies the dielectric properties of a medium and defines the anisotropy in polarizability of the material by electric fields. We also introduced the complex index of refraction $\hat{n} = n + ik$ and relate it to the complex conductivity $\bar{\kappa} = \kappa_1 + i\kappa_2$ through the relation $\hat{n}^2 = 1 + \frac{i\hat{\kappa}}{\omega}$. All these quantities define how electromagnetic waves interact, propagate, and refract through a medium.

For low momentum transfers $|\vec{q}| \ll \omega$, we make the simplification that the transverse and longitudinal components of the polarization tensor are equivalent (following Ref. [16]) and we reduce it from a tensor to a complex quantity:

$$\begin{aligned} \Pi(\omega) &\equiv \omega^2(1 - \hat{n}^2) \\ &= \omega(-i\hat{\kappa}) \\ &= \omega(\kappa_2 - i\kappa_1) \end{aligned} \tag{6.1}$$

Now we use Refs. [8, 17] to state the relation between the photon mass absorption coefficient and the polarization tensor, through the optical theorem, as:

$$\begin{aligned} \sigma_\gamma &= -\frac{\mathrm{Im}(\omega)}{\omega} \\ \text{Eq.6.1} \implies \sigma_\gamma &\equiv \kappa_1 \end{aligned} \tag{6.2}$$

Now by expressing the refractivity $\hat{n}^2$ in terms of n and k, and independently κ_1 and κ_2, and then matching the real and imaginary components, we finally solve for the photon mass absorption cross section as:

$$\sigma_\gamma = \frac{2nkE}{\rho\hbar c} \tag{6.3}$$

The optical constants tables of Palik [22] are our source of $\hat{n}$ at 300K. As the values for the mass absorption cross section are temperature independent for energies $\gtrsim$ 3.5 eV ($\lambda \lesssim$ 350 nm, see Ref. [18]), we adopt the table unchanged for this regime. Below 3.5 eV we must correct for the lower DAMIC Stage I operating temperature of ∼100K. We turn to Rajkanan et al. [23] for a semi-analytic parametrization of the absorption coefficient (in cm^{-1}) $\alpha(T) = \frac{\rho N_A}{m_a}\sigma_\gamma$ (for molar mass m_a, density ρ, Avogadro constant N_A) as a function of temperature, valid in this region of interest between ∼1–4 eV, which we reproduce below, with coefficients given in Table 6.1.

$$\begin{aligned}
\alpha(T) &= \sum_{i,j=1,2} C_i A_i \left[\frac{\{\hbar\omega - E_{gj}(T) + E_{pi}\}^2}{\{e^{E_{pi}/kT} - 1\}} + \frac{\{\hbar\omega - E_{gj}(T) - E_{pi}\}^2}{\{1 - e^{-E_{pi}/kT}\}} \right] \\
&\quad + A_d[\hbar\omega - E_{gd}(T)]^{1/2} \\
E_g(T) &= E_g(0) - [\beta T^2/(T+\gamma)]
\end{aligned} \tag{6.4}$$

Parameter	**Value**	**Parameter**	**Value**
E_{g1}(0K)	1.1557 eV	A_1	3.231×10^2 $\mathrm{cm}^{-1}\,\mathrm{K}^{-1}$
E_{g2}(0K)	2.5 eV	A_2	7.237×10^3 $\mathrm{cm}^{-1}\,\mathrm{K}^{-1}$
E_{gd}(0K)	3.2 eV	A_d	1.052×10^6 $\mathrm{cm}^{-1}\,\mathrm{K}^{-1}$
E_{p1}	1.827×10^{-2} eV	E_{p2}	5.773×10^{-2} eV
C_1	5.5	C_2	4.0
β	7.021×10^{-4} eV K^{-1}	γ	1108 K
k	8.617×10^{-5} eV K^{-1}		

Table 6.1: Absorption coefficient parametrization values from Ref. [23] for Eq. 6.4

We calculate the ratio α(100K)/α(300K) and apply it as a multiplicative factor to correct the values from Palik [22] for low energies. A further small, constant multiplicative correction of q=1.1 is applied below 3.5 eV to match the value of σ_γ at the boundary, with the overall linear attenuation coefficients and scaling relations shown in Fig. 6.3. The resulting mass attenuation ($\sigma_\gamma \equiv \frac{\alpha}{\rho}$) for the full energy range is finally shown in Fig. 6.4.

We can now derive (referring again to Chap. 1.4.2 for notation) the interaction rate of a

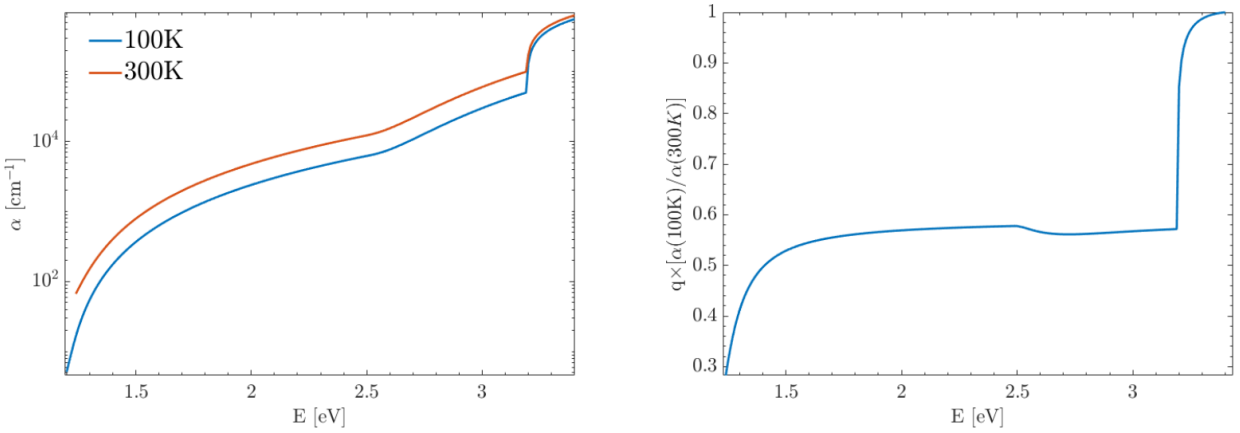

Figure 6.3: Left: α(T) computed from Eq. 6.4 for operating and room temperatures. Right: Multiplicative factors q and α-ratio applied to 300 K optical constants data.

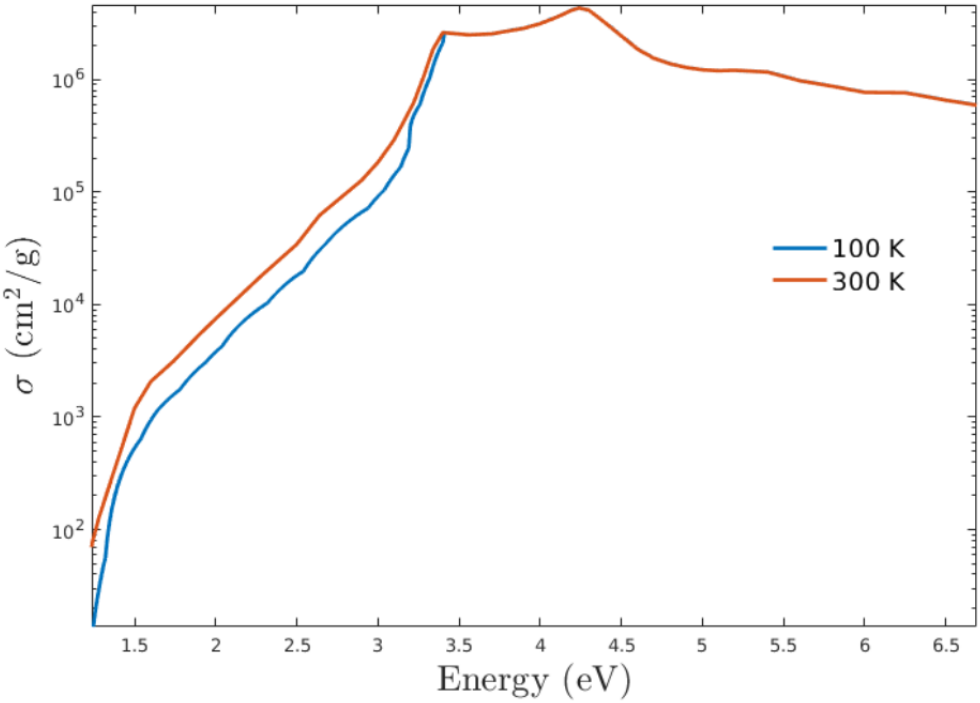

Figure 6.4: Photon mass absorption coefficient σ_γ for DAMIC Stage I operating temperature of approx. 100K, derived from optical constants data at 300K

HP mass of m_V hitting our detector per unit time and per unit mass to be:

$$\Gamma_{\text{int}} = \frac{\rho_{DM}}{\tau m_V} \kappa_{eff}^2 \sigma_\gamma(m_V) c \tag{6.5}$$

Our strategy is to use our detector to determine a limit on $\Gamma_{\rm int}$, extract $\kappa^2_{\rm eff}$ from the above equation and then convert it to a universal limit on the kinetic mixing parameter κ after factoring out the Silicon dependent in-medium effects through:

$$\kappa^2_{eff} = \frac{\kappa^2 m_V^4}{[m_V^2 - Re(\Pi(\omega))]^2 + [Im(\Pi(\omega))]^2} \tag{6.6}$$

The raw ionization spectrum dR/dn_e for a given mass m_V (i.e. the spectrum of charge pairs n_e created for a given flux of particles) is now nothing more than the direct application of the charge yield machinery discussed in Chap. 4 through the ionization probability curves of Fig. 4.9. Since this analysis was written well before these updated set of curves, we actually used the semi-analytic terms found in Alig et al. [6]. We treat the HPs as having almost perfect absorption efficiency since in our mass range of interest of approx. 1.5 eV to 30 eV the absorption length (Fig. 6.3) is $\ll$ the thickness of a CCD.

6.1.2 DM-e$^-$ Scattering & the Crystal Form Factor

To recap the physics of DM-e$^-$interactions, we refer the reader to Chap. 1.4.3. The brief upshot is that modelling DM-e$^-$ interactions presents challenges due to the bound nature of the electrons and crystalline band structure of the target, implying one cannot treat electrons as free unlike nuclei. Thus we follow the work of [13] who parametrize the event rate in the detector with the help of two form-factors, for DM mass m_χ energy E_e, and transferred momentum q, as

$$\frac{dR}{d\ \ln\ E_e} \propto \bar{\sigma_e} \int d\ \ln\ q\ J(m_\chi, q, E_e)|F_{DM}(q)|^2 |f_{\rm c}(q, E_e)|^2 \tag{6.7}$$

where $\bar{\sigma_e}$ is a reference cross section for free electron scattering, J includes the dependence on astrophysical parameters, F_{DM} is the dark matter form factor, and $f_{\rm c}(q, E_e)$ quantifies the atomic transitions of bound state electrons.

The dark matter form factor expresses the model dependent momentum transference in an interaction, generically as $F_{DM} = (\alpha m_e)/q^n$ $\{n = 0, 1, 2\}$. The $n = 0$ case corresponds to pointlike interactions with heavy mediators or a magnetic dipole coupling, the $n = 1$ case to an electric dipole coupling, and $n = 2$ for massless or ultra-light mediators. The crystal form factor encodes target material properties for Silicon and is numerically derived from DFT (density functional theory) via a bespoke code (QEDark) written by the authors of

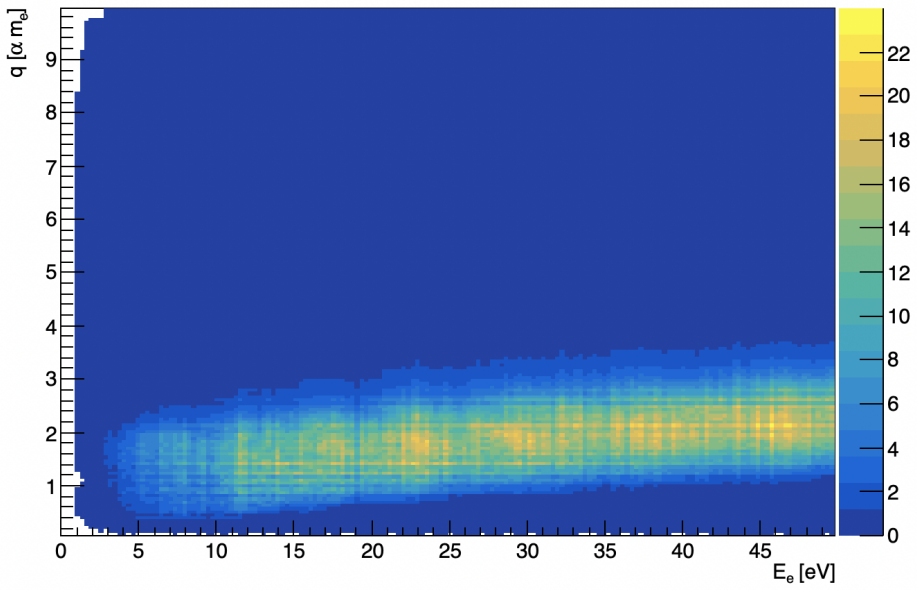

Figure 6.5: Dimensionless crystal form factor computed by Ref. [13], shown in deposited energy and momentum space.

Essig et al. [13] for the simulation package QuantumEspresso [15]. This crystal form factor is shown in Fig. 6.5.

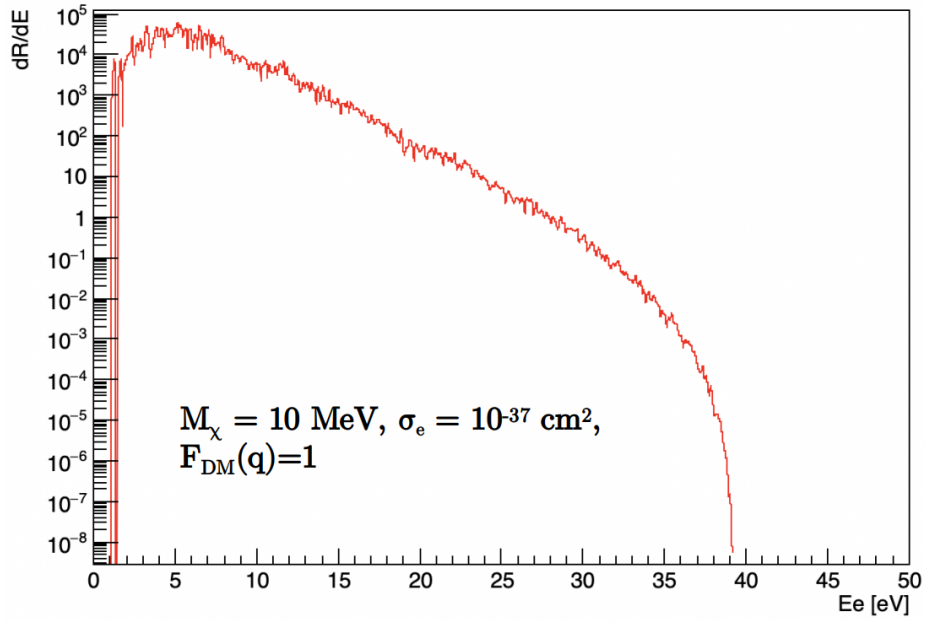

Figure 6.6: Differential event rate for 10 MeV c^{-2} unity momentum coupled DM-e$^-$ scattering process.

The DM signal was computed using Eq. 6.7. To compute J we assumed halo parameters of dark matter density $\rho_{DM} = 0.3$ GeV c^{-2} cm^{-3}, isothermal Maxwellian velocity distribution with escape velocity $v_{esc} = 544$ km s^{-1} and mean $v_0 = 220$ km s^{-1}, and periodic Earth motion with mean velocity $v_E = 232$ km s^{-1} [20]. The resulting ionization rate dR/dE_e (see Fig. 6.6) was then discretized into dR/dn_e, where n_e is the number of ionization charges, once again using the pair-creation probability prescription laid out in Chap. 4. The differential ionization rate was then obtained from $dR/dn_e = \int dE_e p_n (dR/dE_e)$, an example of which we saw previously in Fig. 6.1

6.1.3 Signal Model

Regardless of whether it was the Stage I or Stage II experiment we next construct our signal charge model $S \equiv S(j|\theta)$, which specifies the probability to produce j charges in a pixel given a DM parameter set θ — where $\theta = \{\Gamma, m_V\}$ or $\theta = \{\bar{\sigma_e}, m_\chi\}$ for the respective cases of HPs or DM-e$^-$ scattering.

To construct these signal charge models we rely on Monte Carlo simulations, under the following generic methodology:

1. Pick a parameter set θ and calculate dR/dn_e.

2. Generate a number of interactions drawn from a Poisson distribution that would be seen in an exposure identical to the dataset, following the cross-section or flux parameter. We expect these events to be evenly distributed in $\{x, y, z\}$ on the CCD and to be pointlike interactions.

3. Each of these interactions produces a selected j number of charges. Diffuse each of the charges using Eq. 2.2 until it arrives at the surface. The effect of diffusion on the resultant charge distribution can be seen in Fig. 6.7

4. Collate the final charge distribution into our $S(j|\theta)$ signal function.

6.2 Datasets

Since we require a good handle on the LC of these devices, we need datasets where we can measure the current accurately above the read noise background. Since LC scales with time, we require datasets from long exposure. Further, since we are interested in the pixel

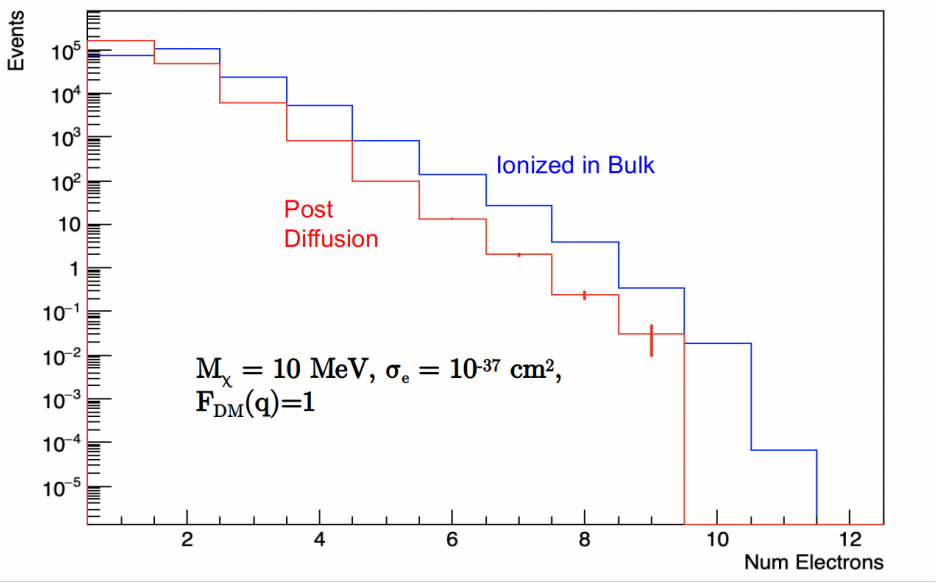

Figure 6.7: Example event rate distribution pre and post diffusion for M_χ=10 MeV c^{-2} unity momentum coupled DM-e$^-$ scattering process.

distribution and not any spillover from high-energy clusters we will apply a cluster and hot pixel mask.

6.2.1 Stage I data for Hidden Photons analysis

The dataset for this analysis was taken with extension 2 from the Stage I experiment detailed in Chap. 2. Extension 2 was selected as it demonstrated the lowest dark current, based on a first pass analysis, along with being the most physically shielded CCD from the primary background of the experiment — radiogenic γ-rays. Nine exposures of 0.695 d each were acquired with images 4622×60 pixels in size. The reduced y-axis is due to the data being acquired with a 1×100 binning meaning each pixel in the image is effectively $15 \times 1500\,\mu\text{m}^2$ in size. Before each exposure, the CCD was cleared of charge by doing an 'erase' procedure bringing it into inversion so as to suppress surface dark current [19]. The actual CCD data was contained in a 4116×42-pixel segment of the image, corresponding to the physical size of the device, with the remaining regions considered the overscan where either the serial register alone or a much reduced exposure row was read out. The CCDs had been previously calibrated on the surface with x-ray from known energy sources to give a $k \approx 13.76\,\text{ADU/e}^-$.

The image processing followed the broadly standard process laid out in Chapters 2 and 3 as:

1. Noise reduction by way of correlated noise subtraction, via the simultaneous empty image taken from the opposite amplifier on the same serial register. To recap, from every pixel we subtracted a linear combination of the pixel values in the corresponding three noise images, with the coefficients determined as to minimize the variance of the pixel noise. Following this procedure, the noise in the images was estimated from the pixel values of the y overscan to be σ_{pix}=1.9 e^-.

2. Subtraction of the pedestal, the constant offset of the pixel values introduced during readout, estimated independently for each row as the mean value of the pixels in the x overscan.

3. To exclude a slight pedestal transient at the beginning of every row, the analysis was limited to 2500 columns of the image, for which the pixel values along rows in the y overscan were found to be constant within statistical uncertainty.

4. Figure 6.8 shows the mean value of pixels in each row, $\langle p \rangle$, over the nine images after the image processing and pixel selection described above. Rows $\geq$43 correspond to the y overscan, for which $\langle p \rangle$ is consistent with zero. The first 42 rows of the image contain the CCD data, for which an offset is clearly visible due to charge collected by the pixels. Hidden-photon absorption would produce charge uniformly distributed throughout the pixel array. The higher values of collected charge in rows 30–40 indicate the presence of nonuniform sources of leakage current, e.g., optical or near-infrared photons inside the vessel or dark current exacerbated by mechanical stress of the silicon lattice. The same pattern is more clearly observed in the other CCDs, with higher leakage current,

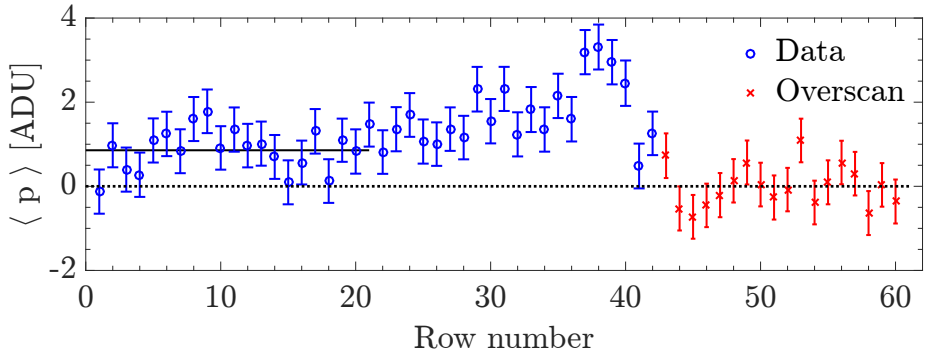

Figure 6.8: Mean of the pixel values in each row over the nine images $\langle p \rangle$, as a function of row number. The first 42 rows contain the CCD data, while the remaining 18 rows constitute the y overscan. The dotted line shows $\langle p \rangle$=0, while the solid line presents the level of leakage charge that corresponds to λ=4.0 e^- mm^{-2} d^{-1}.

installed in the DAMIC box, for which the increase is evident starting at row 22, suggesting that the charge distribution is spatially uniform only in the bottom half of the devices, i.e., rows 1–21.

5. We calculated the median and median absolute deviation (MAD) of every pixel over 114 images from a previous higher-temperature data set dedicated to background studies. These quantities were used to construct a mask, which excludes localized dark current spikes due to defects in the silicon lattice [19]. These were identified as pixels that either deviate more than 3 MAD from the median in at least 50% of the images or have a median or MAD that is an outlier when compared to the distributions of these variables for all pixels. This selection removed 0.17% of the pixels.

6. We considered as clusters any contiguous pixels with signals larger than $6\sigma_{\rm pix}$=11.4e$^-$.

7. Further, pixels that were less than 4 pixels to the right or less than 200 pixels to the left of every cluster, i.e., within the 200 subsequent pixel readouts, were also masked. This requirement rejected pixels with stray charge due to CCD charge transfer inefficiencies, which may happen when a high energy interaction results in a large number of charge carriers in the serial register. Because of the low event rate from radioactive backgrounds ($\sim$1 g^{-1} d^{-1}), only 0.95% of the pixels were removed by this procedure.

An example image after masking can been seen in Fig. 6.9. The black bars represent areas that have been masked as outlined above while the red stars are single pixels with values greater than $4\,\sigma_{\rm pix}$which would in a traditional analysis be considered as a cluster. Since there is no spatial correlation with other clusters apparent with these points, they are not discarded from the final analysis.

All told, after the outlined cuts and masking procedure we are left with N=4.68$\times$10^5 unmasked pixels over the nine images, equivalent to an exposure of 11.5 g d. We can see the final Ext. 2 pixel distribution as the black data points in Fig. 6.12 Top.

6.2.2 Stage II data for DM-e$^-$ scattering

The dataset for this analysis came from the Stage II experiment detailed once more in Chap. 2. Prior to the exposures for this dataset, the CCDs were individually calibrated in-situ by a red LED, with calibration constants $k \approx 14.5$ ADU/e$^-$. The analysis was performed on a special data set consisting of 38 exposures, each 100 ks ($\approx$ 1.16 days) long, collected in late

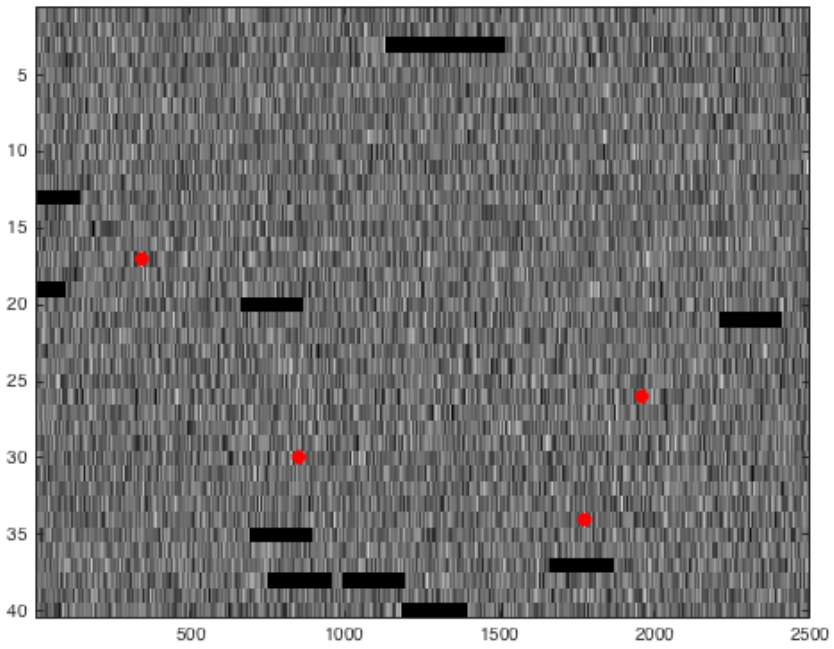

Figure 6.9: Example of processed image read out by detector. Black bars represent areas that have been masked, as outlined in the text, in the analysis due to presence of high-energy clusters (defined to be >6 σ of background noise). Red stars indicate pixels with values of $\geq$ 120 ADC ($\sim$ 30 eV). There is no spatial correlation with other clusters apparent in these points, so they are not discarded in the final analysis.

2017. "Blank" images with a much shorter 30 s exposure are also taken immediately after each long exposure as a systematic check of the device operation. All data were acquired with 1×100 binning. Each image contained 4272×193 pixels, with a subset of 4116×42 pixels corresponding to the actual active area of the CCD with the rest being the overscans.

Again the image processing roughly followed the standard process laid out in Chap. 2:

1. To remove correlated readout noise, we subtracted from every pixel an appropriate linear combination of corresponding pixel values in the noise images acquired with the aforementioned second readout node. The subtraction coefficients are calculated to minimize the variance of the pixel noise. The resulting image noise is found to be σ_{pix} = 1.57–1.62 e^-.

2. Subtraction of the pedestal, estimated on a per-row basis as the mean value of pixels in the x-overscan. To exclude an instrumental increase in transient noise at the boundaries of the CCDs, the analysis is restricted to 2500 columns in a central portion

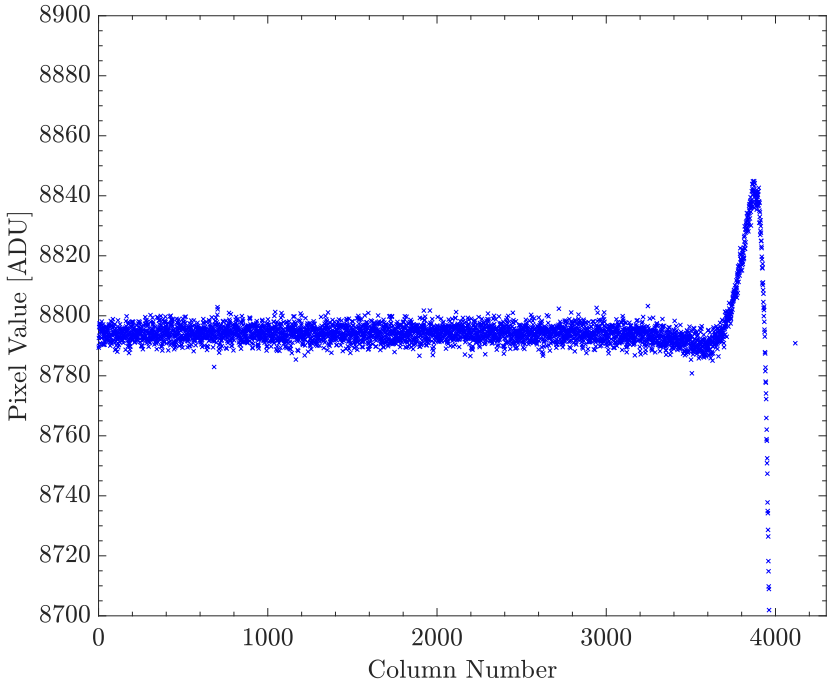

Figure 6.10: Sample image, averaged column-wise after excluding charge clusters. A non-uniform structure is clearly visible in the last third likely caused by electronic artifacts introduced during the read process.

of the image, see Fig. 6.10.

3. We applied a mask from the median and MAD of 864 images of the full-science data set, once again pruning pixels that either deviated more than 3 MAD from the median in at least 50% of the images or have an outlier median or MAD, resulting in the removal of ≈0.25% of pixels.

4. Clusters of pixels with signal larger than $8\,\sigma_{\rm pix}$, arising from deposits of more than 50 eV, were also excluded as to limit the analysis to leakage current and signals from light dark matter. To mitigate the effect of charge trailing along rows from charge transfer inefficiency in the serial register, 200 pixels to the left of every cluster are masked along with 4 pixels to the right. Each pixel above and below these clusters is also masked to account for charge splitting across rows due to diffusion. This procedure removed between 1.4% (Ext. 3) to 3.0% (Ext. 6) of pixels. We increased the threshold to $8\sigma_{\rm pix}$ from $6\sigma_{\rm pix}$ (as in the previous analysis) to confirm a systematic check that the results were insensitive to changes in the threshold cut.

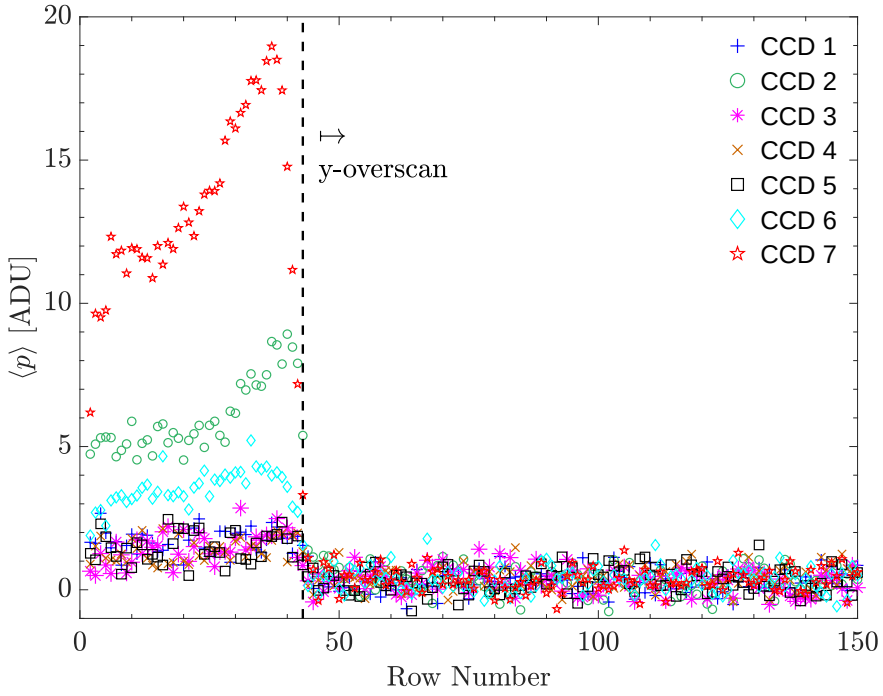

Figure 6.11: Mean pixel ADU values, after the processing described in the text, as a function of row in the CCD. The first 42 rows correspond to the active region of the CCD, while rows $\geq$ 43 correspond to the y overscan. The offset observed in rows $\leq$ 42 is due to charge accumulated in the pixels.

5. Ext. 2, 11 and 12 were discarded from the analysis due to a row-correlated increase in collected charge indicative of the presence of nonuniform sources of leakage current as seen in the pixel average $\langle p \rangle$ in Fig. 6.11, inconsistent with a DM explanation that would produce charge uniformly throughout the pixel array. In addition, because of sharp drop-off in pedestal values in the last few rows, strongly visible in Ext. 12, the analysis was further restricted to rows 1-36. For the four remaining CCDs, the analysis is restricted to rows 1-36 where $\langle p \rangle$ is found to be constant within uncertainty.

The final selected region includes $\approx 3.2\times10^6$ pixels for each of the four CCDs, with their corresponding pixel value distributions shown in Fig. 6.12. The total equivalent exposure of the search was 200 g d. We can see the final pixel distributions for the different extensions as the different color histogram points in Fig. 6.12 Bottom.

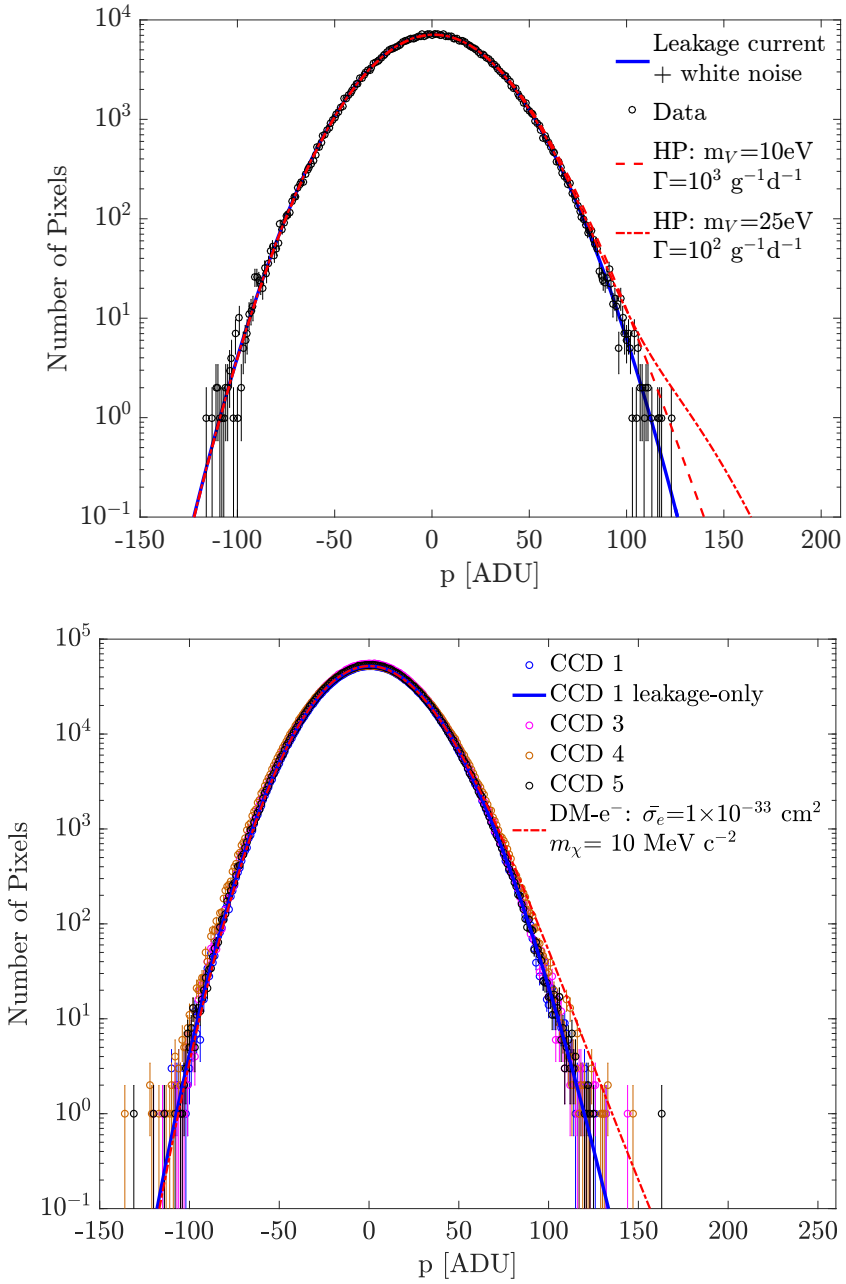

Figure 6.12: Top: Distribution of the pixel values p considered for Stage I analysis (markers). The solid line shows the best-fit result with the null hypothesis, i.e., only pixel white noise and a constant leakage current source across the device. The p value is 0.78. The dashed (dot-dashed) line shows the result after including a fixed contribution from hidden photons with masses m_V=10 eV (25 eV) and an absorption rate of Γ=10^3 g^{-1} d^{-1} (10^2 g^{-1} d^{-1}). Bottom: Distribution of pixel values (with conversion constants $k \approx 14.5$ ADU/e$^-$) for the four CCD Stage II analysis. An example of best fit result for the leakage-only model (no DM-e$^-$) is given for CCD n. 1 (blue line); the dashed red line is the expectation for a DM-e$^-$ model with $\bar{\sigma}_e = 1 \times 10^{-33}$ cm^2, $m_\chi = 10$ MeV $c^{-2}$and $F_{DM} = 1$

6.3 Modelling leakage current and shot noise

We previously discussed how to obtain the signal model $S(j|\theta)$. Our goal now is to include a noise model to fully represent features of the pixel distribution. The natural approach is that of Gaussian white noise which we can model with 2 parameters — an offset μ_0 from pedestal subtraction and a width $\sigma_{\rm pix}$. We incorporate leakage current as a Poisson shot-noise term with rate parameter λ. The pixel value distribution for a given CCD is then given by:

$$\Pi(p) = N \sum_{n=0}^{\infty} \left(\left[\sum_{j=0}^{n} S(j \mid \theta) \mathrm{Pois}(n-j \mid \lambda) \right] \mathrm{Gaus}(p \mid \alpha\left[n_{\rm tot} + \mu_0\right], \alpha\sigma_{\rm pix}) \right), \tag{6.8}$$

where n is the number of charges in a pixel, N is the fixed total number of pixels which serves as a normalization factor, and $\alpha \equiv 1/k$ as the e$^-$to ADU calibration constant.

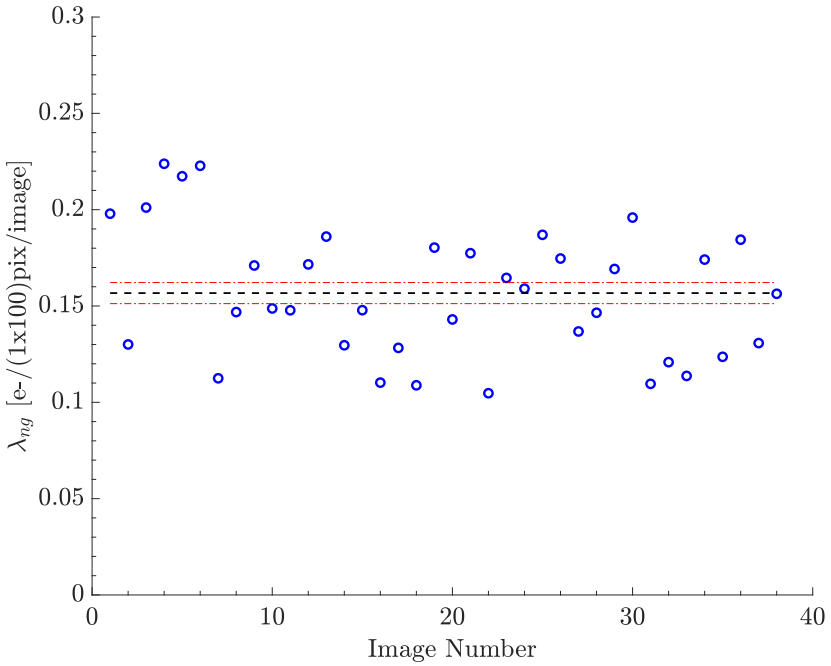

Figure 6.13: Poisson shot noise parameter λ extracted from corresponding blank images for Ext. 1, with estimate of mean and error on the mean, showing the relative stability of parameter

We explore the validity of this model by performing maximum likelihood fits to the blank and overscan pixel distributions, where due to the null exposure we should have no signal ($S_0 \equiv \{S(0) = 1, S(j \geq 1) = 0\}$) by construction but also no shot-noise component (λ=0)

meaning only the Gaussian term should survive.

As a brief aside, we expand on likelihood fitting but urge the reader to turn to pedagogical sources like Ref. [21] for a more complete explanation. Basically, we can construct a *likelihood function* $\mathcal{L}(\theta_k \mid x)$ which is interpreted as the probability of observing the outcome x given a parameter set θ of size k. Since probabilities are often multiplied and due to the product rule of logarithms, it is often easier use the *log-likelihood* function which is just the logarithm of the likelihood function. So in the case of a binned histogram like we have, we can compare some model Π to a binned dataset D by constructing the total log-likelihood as:

$$\mathcal{LL} = -\sum_k \frac{(\theta_k - \theta_k^{\text{pref}})^2}{2\sigma_{\theta_k}^2} - \frac{1}{2}\log(2\pi\sigma_{\theta_k}^2) + \sum_{i=1}^{\text{bins}} D_i \log(\Pi_i) - \Pi_i - \log(\Gamma(D_i + 1)) \quad (6.9)$$

The first summation terms in Eq. 6.9 are Gaussian "penalty" terms in the fit if there are preferred parameter values θ_k^{pref} that require enforcement, with its leniency set by σ_{θ_k}. Furthermore, we have assumed that the bin contents are Poisson distributed to arrive at the second summation term. Note also that for practical purposes we minimize the negative $\mathcal{LL}$ as function minimization is the default technical operation of most optimization algorithms.

Turning our attention back to the blank and overscan pixel distribution, we likelihood fit Eq. 6.8 under the no signal condition and find $\lambda = 0$ within error for the Stage-I data but *not* for the Stage-II data where λ is a positive non-zero value $\gg$ statistical error, as seen in Fig. 6.13.

This unexpected deviation can be further quantified by looking at the goodness of fit, via Monte Carlo for the two cases shown in Fig. 6.14. To produce the Top plot, we fit a Gaussian to the Stage-I background data and record its $\mathcal{LL}$ value. We then use the best fit parameters to generate a few hundred Monte-Carlo background datasets which are then refit with the same model. Since the Gaussian is a good model, we get the data $\mathcal{LL}$ to lie within the M.C. distribution with a p-value $\gg 0$. In the Bottom plot, for the Stage-II data the 2 parameter Gaussian is a significantly worse description of the data than the 3 parameter model with shot noise.

We also investigated whether the background data can be better described by a different multi-parameter model. One choice was a Gaussian with energy dependent terms where $\{\sigma = \sigma(E) \mid \sigma(E_1) > \sigma(E_2) \quad \text{if} \quad \mathrm{E}_1 > \mathrm{E}_2\}$; another model is the sum of multiple Gaussians with offset μ. In both cases, our goodness of fit test suggested no difference vs. a shot noise. More importantly, one can imagine a charge injection process (behaving as a shot noise) either in the amplifier or in the downstream electronics that might result in the observed

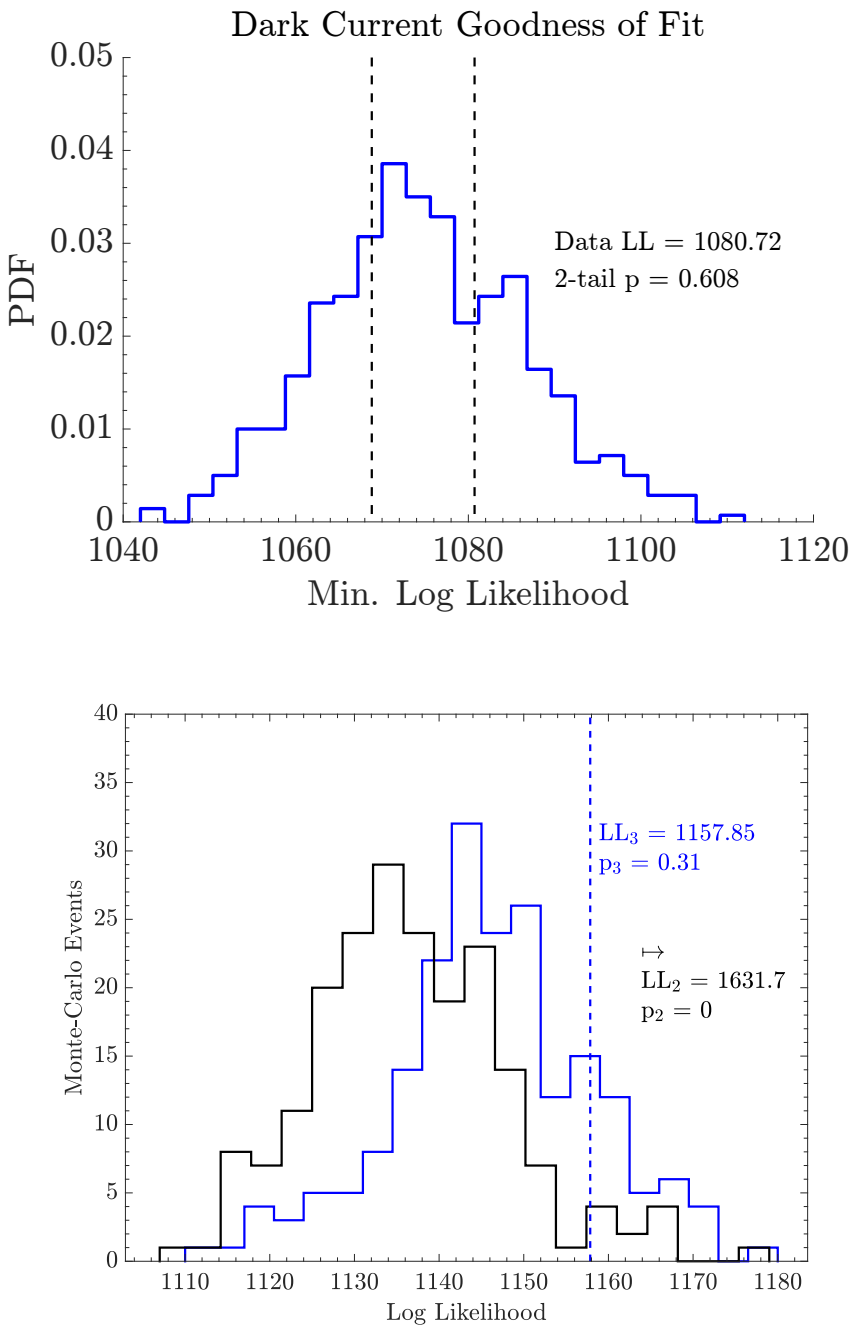

Figure 6.14: $\mathcal{LL}$ distribution showing goodness of fit for noise model cases of 2 parameters (Gaussian) and 3 parameter model if applicable. 300 Monte-Carlo distributions were simulated using parameters obtained from best fit to total blanks+y-overscan distribution and then refit to determine min-$\mathcal{LL}$. Best fit $\mathcal{LL}$ and 2-tail p-values indicated by subscript. Top: Stage-I data set showing that the Gaussian noise model is an appropriate choice for the data pixel distribution. Bottom: Stage-II dataset showing that the Gaussian noise model is incomplete, as indicated by its fit to data lying well outside the MC distribution.

distribution while similarly intuitive explanations for the other proposed distributions are harder to come by. One justification for a multi-Gaussian background is if different areas of the CCD had different baselines, but we tested this hypothesis by looking at the column projections of the blank and overscan data, as in Fig. 6.15. We see no difference between regions by performing a Kolmogorov-Smirnov test between N sub-segments (N = 2 to 10). We find that the hypothesis of multiple baselines is rejected at the 10% level.

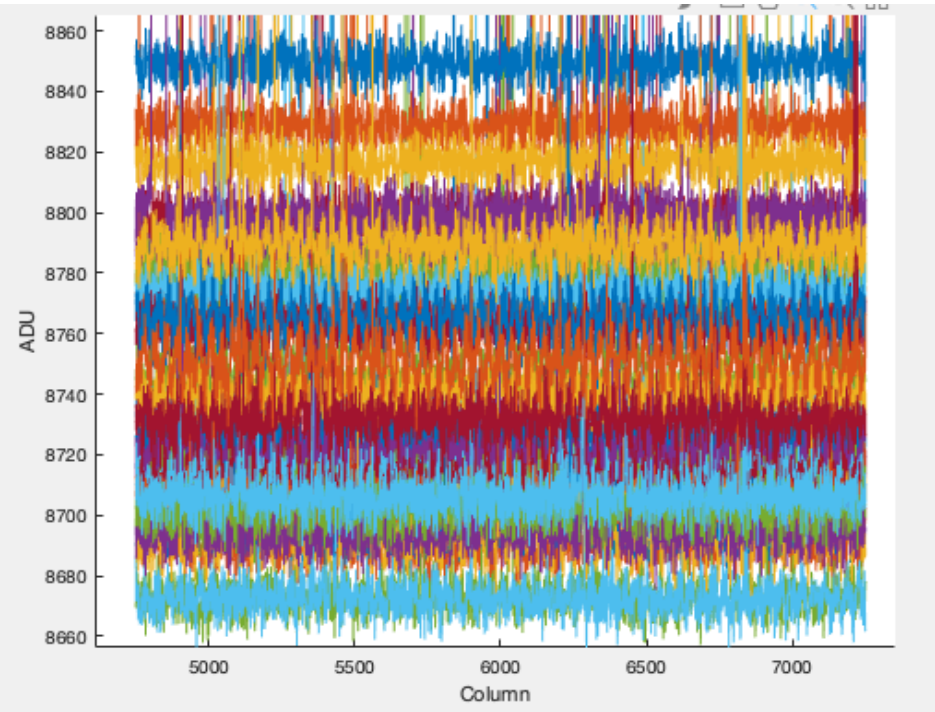

Figure 6.15: Column projection of 38 Ext. 1 images, each shown by different color. No difference or trend is seen in each of the baselines nor any difference in $\sigma_{\rm pix}$ within each image.

Now that we have developed a 2 parameter and 3 parameter background model for the Stage-I and Stage-II datasets we can re-fit Eq. 6.8, this time to the data pixel value distributions discussed in the previous section, to infer the pure leakage current by again enforcing the S_0 condition, with penalty terms that come from the fit to the blank and overscan data. The caveat with the 3-parameter model is that we need to rethink Eq. 6.8 slightly and explicitly decompose the shot-noise contribution from the background vs. the

leakage current as:

$$\Pi(p) = N \sum_{n_c=0}^{\infty} \sum_{n_l=0}^{\infty} \Bigg(\quad \Big[\sum_{j=0}^{n_c} S(j \mid \theta) \mathrm{Pois}(n_c - j \mid \lambda) \Big] \\ \mathrm{Pois}(n_l \mid \lambda_d) \mathrm{Gaus}(p \mid \Omega\big[(n_c + n_l) + \mu_0\big], \Omega\sigma_{\mathrm{pix}}) \Bigg) \tag{6.10}$$

$$= N \sum_{n_{\mathrm{tot}}=0}^{\infty} \Bigg(\Big[\sum_{j=0}^{n_{\mathrm{tot}}} S(j \mid \theta) \mathrm{Pois}(n_{\mathrm{tot}} - j \mid \lambda_{\mathrm{tot}}) \Big] \mathrm{Gaus}(p \mid \Omega\big[n_{\mathrm{tot}} + \mu_0\big], \Omega\sigma_{\mathrm{pix}}) \Bigg)$$

$$\text{with} \quad n_{\mathrm{tot}} = n_c + n_l \; ; \quad \lambda_{\mathrm{tot}} = \lambda_{\mathrm{d}} + \lambda \, , \tag{6.11}$$

where now n_c (the number of charges in a pixel from the DM signal and leakage current, n_l is the number of charges in a pixel from readout shot noise, λ_d is the shot-noise excess, λ_{tot} is the total fit value, and λ is purely the leakage portion.

The dark current results for the Stage-I setup are given in Table 6.2 along with visualization of the leakage only component in Fig. 4.7 Top (blue line).

Pixel Value Distribution	N [pix]	μ_0 [ADU]	σ [ADU]	λ [$\mathrm{e^- \, mm^{-2} \, d^{-1}}$]
Blanks + Overscan	4.05×10^5	0.21±0.04	26.03±0.03	≈0
Image	8.92×10^5	0.25±0.04	25.94±0.02	4.8±0.1

Table 6.2: Leakage current and fit parameters for Ext. 2 data pixel value distribution for Stage I detector

Similar results for the Stage-II experiment, on a per extension basis are reported in Table 6.3; σ_{pix} and μ_0 from the constrained fit were found to be consistent with the blank and y-overscan values. Notice that λ represents an upper limit to the leakage current, with $\lambda = 1.0 \, \mathrm{e^- mm^{-2} \, d^{-1}}$ ($\approx 2\times10^{-22} \, \mathrm{A \, cm^{-2}}$) for CCD 4, the lowest ever measured in a silicon device.

6.4 Analysis

Now that we have a pixel value distribution model Π along with a data pixel value distribution D our next step is to perform a likelihood ratio test to quantify how good a given model is and determine some constraints on our parameter set. Referring to Eqs. 6.8 and Eq. 6.11 we generically have 5 parameters — a mass m, a Poisson rate λ, a signal parameter S (either

CCD n.	σ_{pix} [e^-]	λ_d [$e^-\,mm^{-2}\,img^{-1}$]	μ_0 [e^-]	$\lambda = \lambda_{tot} - \lambda_d$ [$e^-\,mm^{-2}\,d^{-1}$]
1	1.628(1)	8.2(2)	-0.185(3)	2.8(2)
3	1.572(1)	7.8(2)	-0.160(4)	1.7(2)
4	1.594(1)	10.0(2)	-0.219(4)	1.0(2)
5	1.621(1)	8.5(2)	-0.183(4)	2.0(2)

Table 6.3: Relevant parameters used in modeling the pixel value distribution for the Stage II data, with statistical uncertainty in parentheses. The first three columns correspond to the fit of blanks and overscans, while the last column to the leakage-only fit to data. Where appropriate, units were converted from $e^-\,pix^{-1}\,img^{-1}$, as for Eq. 6.11, to $e^-\,mm^{-2}\,d^{-1}$.

the cross-section $\bar{\sigma_e}$ or interaction rate Γ for the different DM cases), and the 2 Gaussian noise terms which we will call G. For each value in a *discrete set of masses*, we constructed the test statistic:

$$\begin{aligned}\mathcal{T}_m(S) &= -2\log\frac{\mathcal{L}_{\rm m}(\hat{\lambda},\hat{\rm S},\hat{\rm G})}{\mathcal{L}_{\rm m}(\hat{\lambda},{\rm S},\hat{\rm G})} \\ &= -2(\mathcal{LL}_m[\hat{\lambda},\hat{S},\hat{G}) - \mathcal{LL}_m(\hat{\lambda},S,\hat{G})] \equiv -2\Delta_{LL}\end{aligned} \tag{6.12}$$

where $\mathcal{LL}$ is defined in Eq. 6.9.

To concretely demonstrate this process we can look at the DM-e^-case as an example. For a given m_χ, we increased the value of $\bar{\sigma_e}$ in discrete steps starting from cross-sections $\ll$ than the expected sensitivity. At every step and for every CCD i we minimized the log-likelihood $\mathcal{LL}_i$ leaving λ and μ_0 as free parameters in the fit while constraining σ_{pix} and λ_d within their uncertainty as in Table 6.3. Next, we constructed a profile likelihood of the total log-likelihood value $\mathcal{LL} = \sum_{i=1\text{ to }4}\mathcal{LL}_i$. A scan of the test statistic is shown in Fig. 6.16.

To obtain a 90% C.L upper limit on our signal variable for each mass, our analysis relies on *Wilks theorem* — a statement that the distribution of the likelihood ratio test is well approximated by a χ^2 distribution. Since we have one degree of freedom (the signal rate) that we scan over, the 90% CL upper limit is the value of S given by an increase of approx. 1.35 from the minimum value of -Δ_{LL} for our 1-parameter varying alternative, since $\chi^2_{df=1,\alpha=0.1} \approx 2.7$. We urge the reader to refer to pedagogical sources on Wilks theorem like Ref. [5] in addition to general statistical likelihood fitting as in Ref. [21]. A check of the applicability of this procedure can be seen in Fig. 6.17 wherein we simulated j=200 pixel value distributions using the assumed 90% C.L limit $\bar{\sigma}^\star_e$ for DM-e^- m_χ=10 MeV and

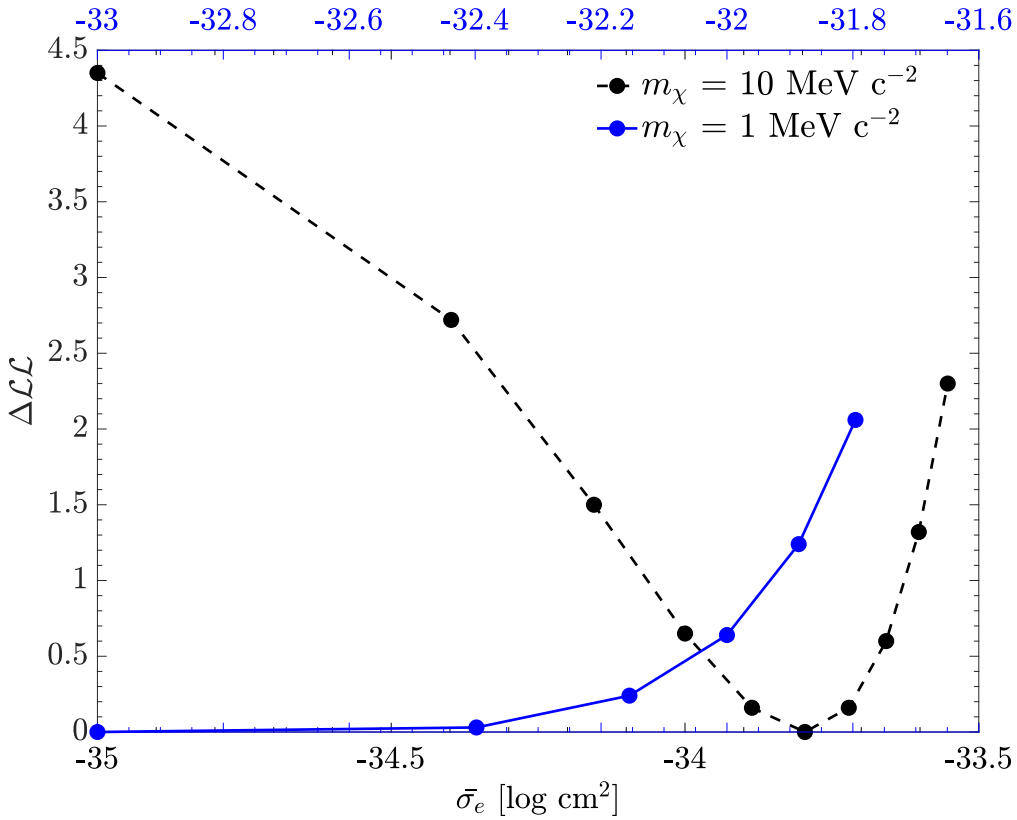

Figure 6.16: Scan of the test-statistic component $\Delta\mathcal{LL} = \mathcal{LL} - \min(\mathcal{LL})$ as a function of $\bar{\sigma}_e$ for $F_{DM} \sim q^{-2}$ and $m_\chi = 1$, 10 MeV c^{-2}

then re-fit them using the profile likelihood process and we report Δ_{LL} as the minimum of the refit minus the original 90% CL limit. Intuitively this tells us that if the DM were to exist with the 90% C.L. parameters and we were to run a whole bunch of experiments, we would observe our given test-statistic value fewer than 10% of the time. We see that this asymptotically follows a 1 degree of freedom χ^2 distribution.

6.4.1 Results

For the Stage I data where we only considered Hidden Photons, we can see the 90% C.L. Γ values in Fig. 6.18 Top. Below m_V=5 eV c^{-2}, HP absorption produces only one charge carrier, meaning that it would indistinguishable from leakage current. At higher masses, the multiplicity in the number of carriers produced per absorption increases, leading to pixels that collect significantly more carriers than would be expected from leakage current, which leads to a long tail on the right-hand side of the pixel distribution and thus a stronger limit. We can see this effect in Fig. 6.12 Top. which shows the best-fit results with fixed parameters

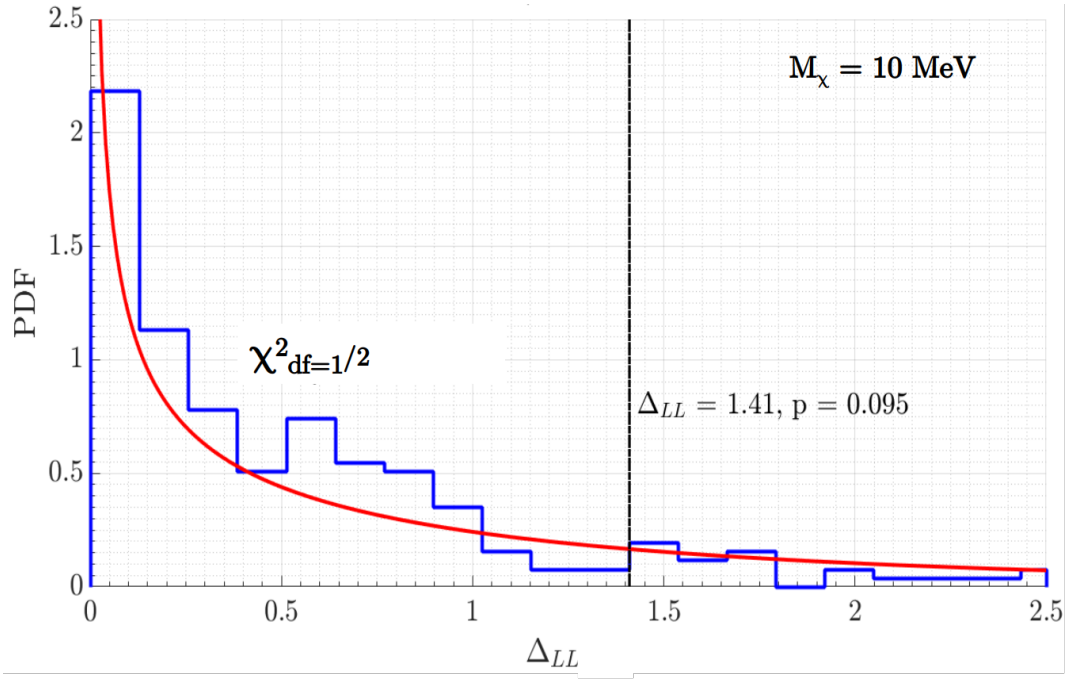

Figure 6.17: Applicability of Wilks theorem demonstrated by the distribution of Δ_{LL} which is seen to follow a 1 degree of freedom χ^2 variable, shown here for the case of $m_\chi = 10\,\mathrm{MeV}\,c^{-2}$. The indicated p-value is consistent with our statement that over the course of many trials, the $\mathcal{LL}_{\min} + 1.35$ value will only occur fewer than 10% of the time.

m_V=10 eV and 25 eV with their pronounced tails.

The HP DM constraints are reported in Fig. 6.18 Bottom, along with other experimental and astrophysical limits. We note that our measurements are the most stringent direct detection constraints on HP dark matter with masses $<12\,\mathrm{eV}\,c^{-2}$and we comment that since our current sensitivity is in line with current Solar constraints, the future DAMIC-M experiment should exceed these constraints comfortably.

Turning our attention to DM-e$^-$ scattering we find that non-zero values of $\bar{\sigma_e}$ are preferred for DM masses above a few MeV c^{-2}. This is due to the presence of a few pixels with values $> 6\,\sigma_{pix}$ in the positive tail of the p distribution (Fig. 6.12), consistent with the higher charge multiplicity expected for larger m_χ. However, the presence of a similar tail in the negative side of the p distribution and of similar features in the blank images suggest a noise origin. Furthermore the change in noise behaviour between Stage I and Stage II of the detector, requiring an extra shot noise parameter as discussed, is suggestive of unexplained detector effects that are potentially contaminating the pixel distribution. In Table 6.4.1, we report the number of pixels found in the negative and positive tails of the p distribution. The thresholds for the tails were chosen appropriately to obtain an expectation of two pixels from the fit with

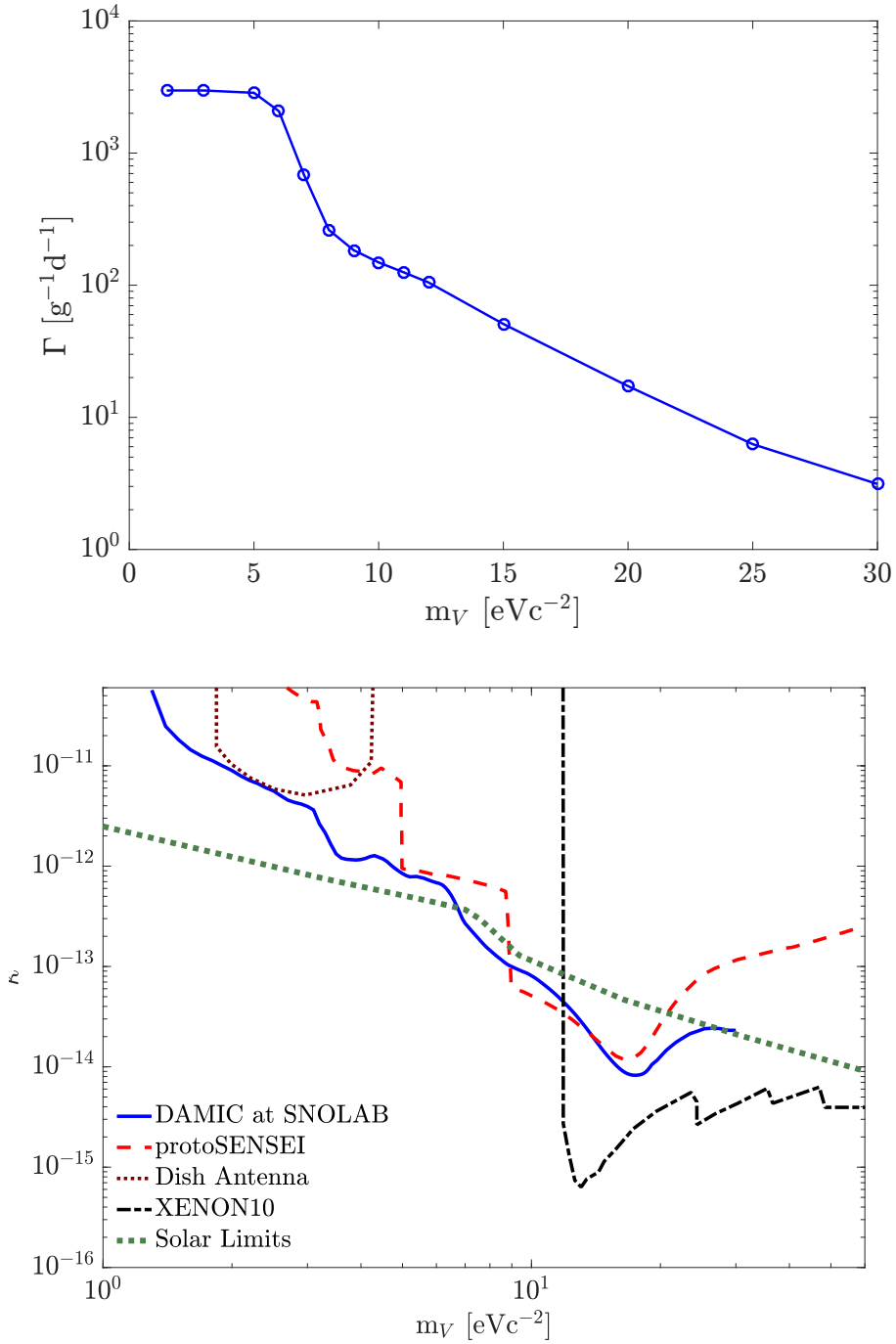

Figure 6.18: Top: Upper limits (90% C.L.) on the hidden-photon absorption rate Γ as a function of hidden-photon mass m_V obtained from the likelihood fit described in the text for Stage I data. Bottom: 90% C.L. constraints on the hidden-photon DM kinetic mixing parameter κ as a function of the hidden-photon mass m_V from the Stage II data. Current best direct-detection limits from protoSENSEI at MINOS [1], an analysis of the XENON10 data [10], a dish antenna [24], and astrophysical solar limits [7, 10] are also shown for comparison.

the leakage-only model. There is evidence for an overall excess with comparable numbers on both sides of the distribution and between blank and exposure images. We conclude that the preference for non-zero values of $\bar{\sigma_e}$ in the fit is due to an imperfect modeling of the extreme tails of the noise distribution. We do not attempt to parametrize these tails further, and our test statistic of Eq. 6.12 naturally places more conservative limits when the minimum of the total log-likelihood, $\mathcal{LL}_{\rm min}$, is found at a non-zero value of $\bar{\sigma_e}$.

CCD no.	1	3	4	5
	(negative p tail) / (positive p tail)			
Exposures	1 / 3	2 / 4	5 / 5	3 / 2
Blanks	3 / 5	4 / 1	2 / 1	2 / 3

Table 6.4: Number of pixels in the negative and positive tails of the p distribution of Stage II data, chosen such that there is an expectation of two pixels from the leakage-only fit.

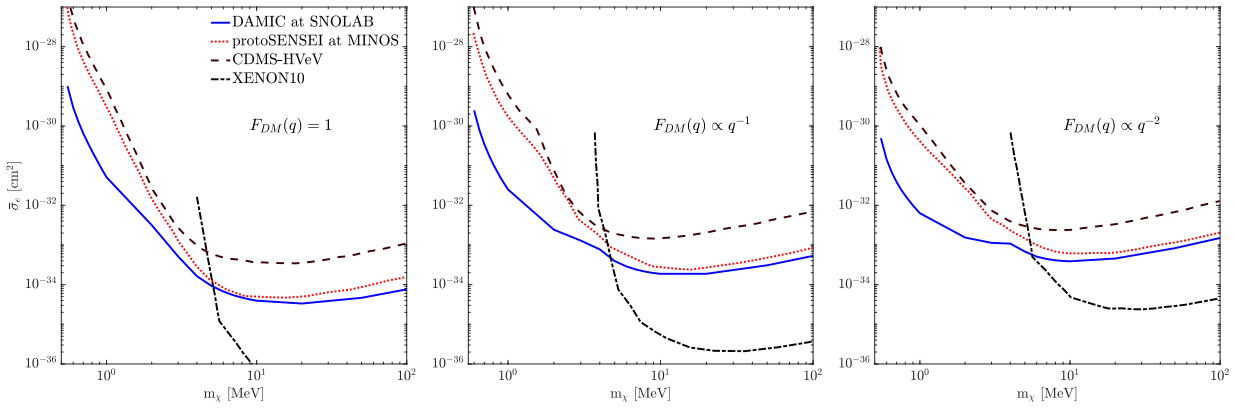

Figure 6.19: 90 % C.L upper limits on the DM-electron free scattering cross section $\bar{\sigma_e}$ as a function of DM mass m_χ for $F_{DM} \propto q^{-n}$ $(n = 0, 1, 2)$ obtained by DAMIC at SNOLAB (solid line). Current best limits from protoSENSEI at MINOS (dotted line) [1, 12], CDMS-HVeV surface run (dashed line) [2], and an analysis of the XENON10 data (dashed-dotted line) [14] are also shown for comparison.

The 90% C.L. constraints on the DM-e$^-$ cross section from this analysis are compared in Fig. 6.19 to the current best direct-detection limits in Refs. [1, 2, 12, 14]. Complementary limits for heavier DM masses from noble liquid experiments can be found in Ref. [9]. Note that for a high enough DM-e$^-$ cross section the DM flux at SNOLAB would be drastically reduced by interactions in the rock overburden [12]. However, this region has already been excluded by experiments at shallower sites [12]. Other constraints from analyses based on

astrophysical modifications to the dark matter speed distribution can be found in Ref. [11].

To complete the analysis we considered several sources of systematic uncertainty:

1. The largest effect is from the uncertainty in the linearity of the CCD output signal. We changed the calibration constant k by $\pm 10\%$ and noticed a change in the HP interaction rate Γ ranging from 10% for $m_V < 5\,\mathrm{eV}\,c^{-2}$up to a factor of 2 for $m_V = 30\,\mathrm{eV}\,c^{-2}$. Similarly for $\bar{\sigma_e}$ we noticed a change in the limits by $\mp 20\%$ for m_χ below few $\mathrm{MeV}\,c^{-2}$.

2. We confirmed the absence of pixels with values from 6 to 8 $\sigma_{\mathrm{pix}}$for the Stage I data; thus, the result is insensitive to the upper bound on the pixel values. However the Stage II data was only clear for pixels with values from 8 to 10 σ_{pix}. The limits would have dramatically improved with a $6\sigma_{\mathrm{pix}}$ cut due to the presence of 6 to 8 σ_{pix} positive tail pixels as referenced in Table 6.4.1.

3. Varying the temperature by $\pm 10\,\mathrm{K}$ had a $<5\%$ impact on the upper limits of κ.

4. Lastly, performing the analysis with different portions of the CCD images changed limits by $< 10\%$

In sum, the results were fairly robust to the studied systematic changes when viewed from a logarithmic exclusion plot.

References

[1] O. Abramoff et al. Sensei: Direct-detection constraints on sub-gev dark matter from a shallow underground run using a prototype skipper ccd. *Phys. Rev. Lett.*, 122:161801, Apr 2019. doi: 10.1103/PhysRevLett.122.161801. URL `https://link.aps.org/doi/10.1103/PhysRevLett.122.161801`.

[2] R. Agnese et al. First dark matter constraints from a supercdms single-charge sensitive detector. *Phys. Rev. Lett.*, 121: 051301, Aug 2018. doi: 10.1103/PhysRevLett.121.051301. URL `https://link.aps.org/doi/10.1103/PhysRevLett.121.051301`.

[3] A. Aguilar-Arevalo, D. Amidei, D. Baxter, G. Cancelo, B. C. Vergara, A. Chavarria, E. Darragh-Ford, J. de Mello Neto, J. DOlivo, J. Estrada, et al. Constraints on light dark matter particles interacting with electrons from damic at snolab. *Physical review letters*, 123(18):181802, 2019.

[4] A. Aguilar-Arevalo et al. First direct-detection constraints on ev-scale hidden-photon dark matter with damic at snolab. *Phys. Rev. Lett.*, 118(14):141803, 2017. doi: 10.1103/PhysRevLett.118.141803.

[5] S. Algeri, J. Aalbers, K. D. Morå, and J. Conrad. Searching for new phenomena with profile likelihood ratio tests. *Nature Reviews Physics*, pages 1–8, 2020.

[6] R. Alig, S. Bloom, and C. Struck. Scattering by ionization and phonon emission in semiconductors. *Phys. Rev. B*, 22(12):5565, 1980. doi: 10.1103/PhysRevB.22.5565.

[7] H. An, M. Pospelov, and J. Pradler. New stellar constraints on dark photons. *Phys. Lett.*, B725:190–195, 2013. doi: 10.1016/j.physletb.2013.07.008.

[8] H. An, M. Pospelov, J. Pradler, and A. Ritz. Direct detection constraints on dark photon dark matter. *Physics Letters B*, 747:331–338, 2015.

[9] E. Aprile et al. Light dark matter search with ionization signals in xenon1t. *arXiv:1907.11485 [hep-ex]*, 2019. URL `http://arxiv.org/abs/1907.11485`.

[10] I. M. Bloch, R. Essig, K. Tobioka, T. Volansky, and T.-T. Yu. Searching for dark absorption with direct detection experiments. *Journal of High Energy Physics*, 2017(6): 87, 2017. doi: 10.1007/JHEP06(2017)087.

[11] Y. Ema, F. Sala, and R. Sato. Light dark matter at neutrino experiments. *Phys. Rev. Lett.*, 122(18):181802, 2019. doi: 10.1103/PhysRevLett.122.181802. URL `https://link.aps.org/doi/10.1103/PhysRevLett.122.181802`.

[12] T. Emken, R. Essig, C. Kouvaris, and M. Sholapurkar. Direct detection of strongly interacting sub-gev dark matter via electron recoils. *arXiv:1905.06348 [hep-ph]*, 2019. URL `http://arxiv.org/abs/1905.06348`.

[13] R. Essig, M. Fernández-Serra, J. Mardon, A. Soto, T. Volansky, and T.-T. Yu. Direct detection of sub-gev dark matter with semiconductor targets. *Journal of High Energy Physics*, 2016(5):46, 2016. doi: 10.1007/JHEP05(2016)046.

[14] R. Essig, T. Volansky, and T.-T. Yu. New constraints and prospects for sub-gev dark matter scattering off electrons in xenon. *Phys. Rev. D*, 96:043017, Aug 2017. doi: 10.1103/PhysRevD.96.043017. URL `https://link.aps.org/doi/10.1103/PhysRevD.96.043017`.

[15] P. Giannozzi, S. Baroni, N. Bonini, M. Calandra, R. Car, C. Cavazzoni, D. Ceresoli, G. L. Chiarotti, M. Cococcioni, I. Dabo, et al. Quantum espresso: a modular and open-source software project for quantum simulations of materials. *Journal of physics: Condensed matter*, 21(39):395502, 2009.

[16] Y. Hochberg, T. Lin, and K. M. Zurek. Detecting ultralight bosonic dark matter via absorption in superconductors. *Physical Review D*, 94(1):015019, 2016.

[17] Y. Hochberg, T. Lin, and K. M. Zurek. Absorption of light dark matter in semiconductors. *Phys. Rev. D*, 95:023013, Jan 2017. doi: 10.1103/PhysRevD.95.023013. URL `https://link.aps.org/doi/10.1103/PhysRevD.95.023013`.

[18] S. E. Holland, D. E. Groom, N. P. Palaio, R. J. Stover, and M. Wei. Fully depleted, back-illuminated charge-coupled devices fabricated on high-resistivity silicon. *IEEE Transactions on Electron Devices*, 50(1):225–238, 2003.

[19] J. R. Janesick. *Scientific charge-coupled devices*, volume 83. SPIE press, 2001.

[20] J. Lewin and P. Smith. Review of mathematics, numerical factors, and corrections for dark matter experiments based on elastic nuclear recoil. *Astroparticle Physics*, 6(1): 87–112, 1996. doi: 10.1016/S0927-6505(96)00047-3.

[21] I. J. Myung. Tutorial on maximum likelihood estimation. *Journal of mathematical Psychology*, 47(1):90–100, 2003.

[22] E. D. Palik. *Handbook of optical constants of solids*, volume 3. Academic press, 1998.

[23] K. Rajkanan, R. Singh, and J. Shewchun. Absorption coefficient of silicon for solar cell calculations. *Solid-State Electronics*, 22(9):793–795, 1979.

[24] J. Suzuki, T. Horie, Y. Inoue, and M. Minowa. Experimental Search for Hidden Photon CDM in the eV mass range with a Dish Antenna. *JCAP*, 1509(09):042, 2015. doi: 10.1088/1475-7516/2015/09/042.

CHAPTER 7

SKIPPER CCDS

Back in Chap. 2 we described the operation of a conventional CCD and the destructive nature of the readout stage. However, Janesick et al. [1] and Chandler et al. [2] realized in the early 90s that one could fabricate a non-destructive readout stage by exploiting the same principles inherent to clocking charge in the rest of the CCD. This 'Skipper' concept CCD works by repeated measurement of the same pixel, interchangeably referred to as 'Skipping' or Non-Destructive Charge Measurements (NDCMS). We remind ourselves that the i'th time a pixel is read its contents are generically distributed as the sum of the true charge C plus a read noise component (modeled by Gaussian white noise):

$$\begin{aligned} P_i &= C + \mathrm{Gaus}(0, \sigma_{\mathrm{pix}}) = \mathrm{Gaus}(\mathrm{C}, \sigma_{\mathrm{pix}}) \\ &\implies \mathrm{Var}(\mathrm{P_i}) = {\sigma_{\mathrm{pix}}}^2 \end{aligned} \tag{7.1}$$

meaning that repeatedly measuring the same pixel N times and then averaging the readings, under the assumption that the readings are *independent*, nets us:

$$\begin{aligned} \bar{P} &= \frac{1}{N}\sum_{i=1}^{N} P_i \\ \mathrm{Var}(\bar{\mathrm{P}}) &= \mathrm{Var}\left(\frac{1}{\mathrm{N}}\sum_{\mathrm{i=1}}^{\mathrm{N}} \mathrm{P_i}\right) = \frac{1}{\mathrm{N}^2}\sum_{\mathrm{i=1}}^{\mathrm{N}} \mathrm{Var}(\mathrm{P_i}) = \frac{{\sigma_{\mathrm{pix}}}^2}{\mathrm{N}} \\ \implies \sigma_P &\equiv \boxed{\frac{\sigma_{\mathrm{pix}}}{\sqrt{N}}}, \end{aligned} \tag{7.2}$$

a reduction in the read noise by the root number of readings, with the potential to achieve *sub-electron* noise levels.

The key idea here is the ability to do readings independently at a frequency where we are 'quieter' as previously seen in Fig. 3.2 power spectrum (i.e. high frequency). This enables us to overcome the low frequency ($1/f$) component of a long integration period that we argued limited conventional readout CCDs as shown by the sketch previously in Fig. 2.7. We can visualize this new readout process as Fig. 7.1

The tradeoff for this multi-measurement precision is of course the time it takes to make a reading. Suppose we wanted to achieve a reduction from $2 \rightarrow 0.2$ e^- in read noise. That would require $(2/0.2)^2 = 100$ skips. A SNOLAB style 4k×4k can be efficiently read in just over 12 mins for a 2 e^- noise level. That would now jump linearly to 1200 mins = 20 hours

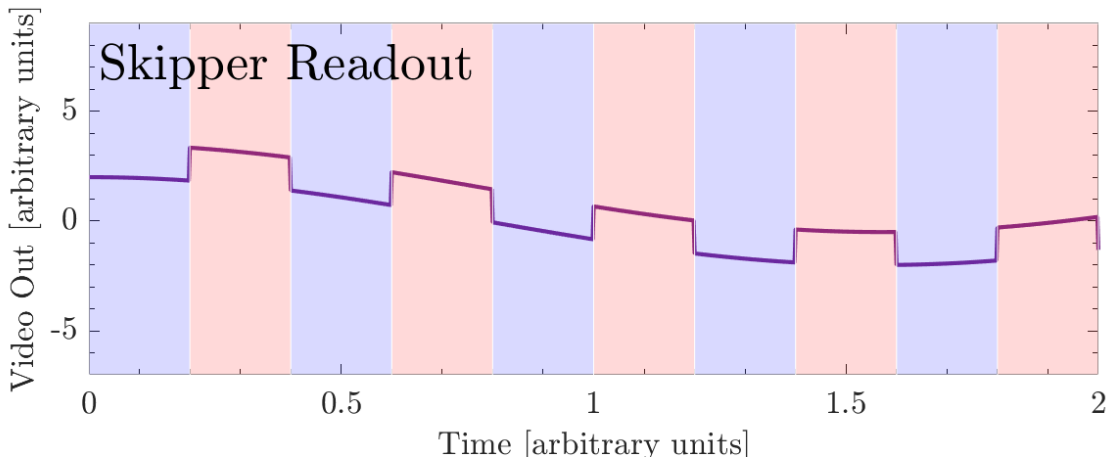

Figure 7.1: Video signal for the Correlated Double Sampling method as applied to Skipper readout, with pedestal readout occurring in the blue shaded region and signal readout in the red shaded region.

(!) to read out a single image. Optimal use of a Skipper CCD requires investigating these tradeoffs in using them for a science case. In this chapter, as we lay the groundwork for using these devices going forward in DAMIC, we will primarily take images of 1100×800 pixel size with 500 skips for an overall read time of just under 3 hrs. We will also only focus on walking through how Skipper CCDs work, our efforts to realize them operationally at the University of Chicago to demonstrate their sub-electron resolution, and discuss current dark current bottlenecks.

7.1 Output stage modification

The majority of a Skipper CCD, particularly everything other than the amplifier stage, remains identical to a conventional CCD discussed in Chap. 2.1.1 and the reader is encouraged to refer to that chapter for discussion of how CCDs function and their terminology. The difference in a Skipper lies in the design of the output stage, when the charge is dropped off from the serial register. A conventional CCD uses a *floating diffusion gate* structure while a Skipper CCD switches to a *floating gate*. The 'floating' commonality simply refers to the fact that the region the charges are stored/measured in are electrically isolated, meaning that they are surrounded by highly resistive material, and any charge within them can usefully remain unchanged for a long time (i.e. $\gg 10^5$ s in modern data retention technology [3]).

The working of the diffusion gate can be described by referencing the micrograph of a conventional CCD in Fig. 7.2 (which is a zoom in of the earlier Fig. 2.4). The charge that

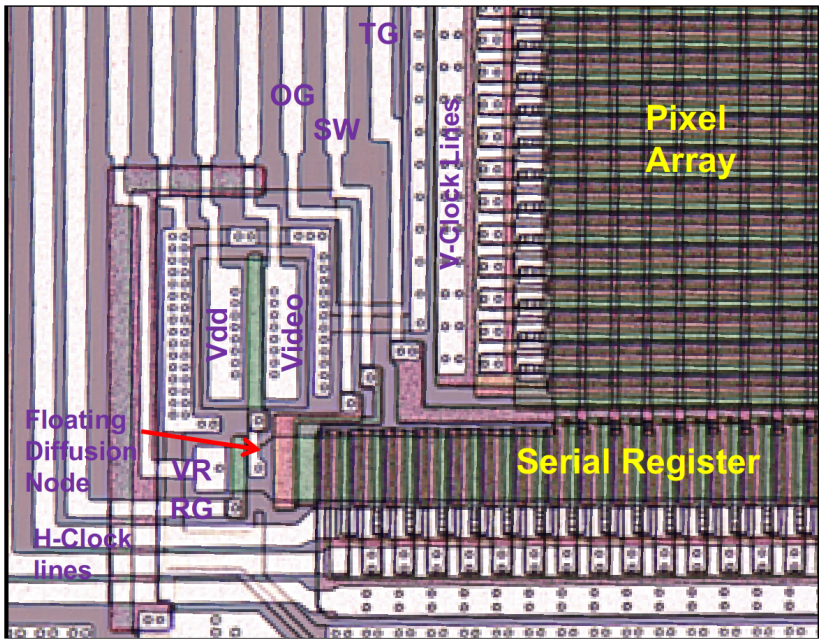

Figure 7.2: Labeled micrograph of a conventional CCD near the output stage.

leaves the serial register finds its way to the diffusion gate region, which is formed by heavily implanting and diffusing a p-type dopant into the n-type bulk substrate, separate from the buried channel. This diffusion region is directly connected, usually through a metal contact, as the gate of the output amplifier MOSFET. Further, the diffusion region is also one of the terminals of the reset transistor. The isolated diffusion region acts like a capacitor and any charge present changes the voltage V_c of the node by way of Eq. 2.1. When the reset gate (RG) is triggered the node is set to V_R, destructively flushing out the charge, and then allowed to float ready and awaiting the next charge dump.

If however we convert the readout node to a floating gate, as represented in Fig. 7.3, we can treat the Sense Node (SN) as basically another gate. Charge is clocked into the region underlying an implanted metal gate in the oxide. The charge electrostatically induces a potential on the floating gate structure which modulates the behaviour of the output amplifier. The key here is that since the charge never makes contact with the measurement apparatus, one can change the previously fixed surrounding gate potentials to drive charge back out from under the floating gate to repeat the cycle. To clear out the charge requires introduction of a new *Dump Gate* (DG) and a new *Drain* potential V_{drain} to flush charge, with Fig. 7.4 labelling all the new components (contrast the otherwise similar layout to Fig. 7.2). The floating gate is reset to a nominal potential V_{R} by triggering the Reset Gate (RG).

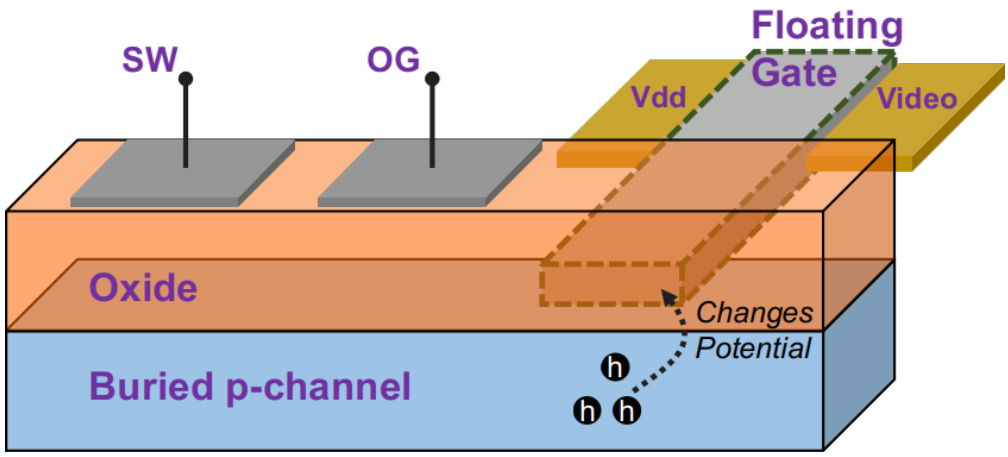

Figure 7.3: Representation of a Skipper floating gate with buried metal contact inside the oxide structure. Holes clocked into the sense node region electrostatically change the potential of the floating gate which then modulates the output amplifier.

7.2 1k x 6k CCDs and Test Setup

The initial batch of Skipper CCDs constructed and used in DAMIC R&D efforts are 1024×6176 pixels diced from the larger circular wafer as shown in Fig. 7.5 and inset. The devices were installed by screwing them into a thin cutout within a large copper box, roughly 4 cm thick and weighing 12 kg. This holder was deigned to strongly shield incident blackbody IR and other radiogenic backgrounds. We calculated a background rate of 29500 dru in the energy range <10 keV, versus a usual surface rate of 225000 dru from prior background exposures [5], suggesting close to an order of magnitude improvement in background events. The setup otherwise remains identical to the Test Chamber setup discussed in Chap. 2.

These CCDs also have pads for the installation of a unity gain JFET on the output (see Fig. 7.5 again). The on-chip amplifier has an output impedance of ≈4 kΩ and thus we can use the JFET to adapt and enforce a 50Ω output impedance, to avoid the potentially lossy nature of transmitting the high frequency output signals over $\mathcal{O}$(ft) cabling (both Kapton and shielded/braided copper) to the external amplification circuits. We noticed a reduction in CCD noise from about 70 ADU → 40 ADU (roughly translated to 6 e^- to 4 e^-) with and without JFETs.

The devices are instrumented with 4 amplifiers, split across 2 serial registers. The 'L2' and 'U2' amplifiers have the same physical geometry as a conventional array, termed '47/6' after specific linear dimensions in the literature', even if they are Skipper nodes, while the 'L1' and 'U1' ('20/6') are a physically smaller node (see Fig. 7.6) in the hopes of lowering the

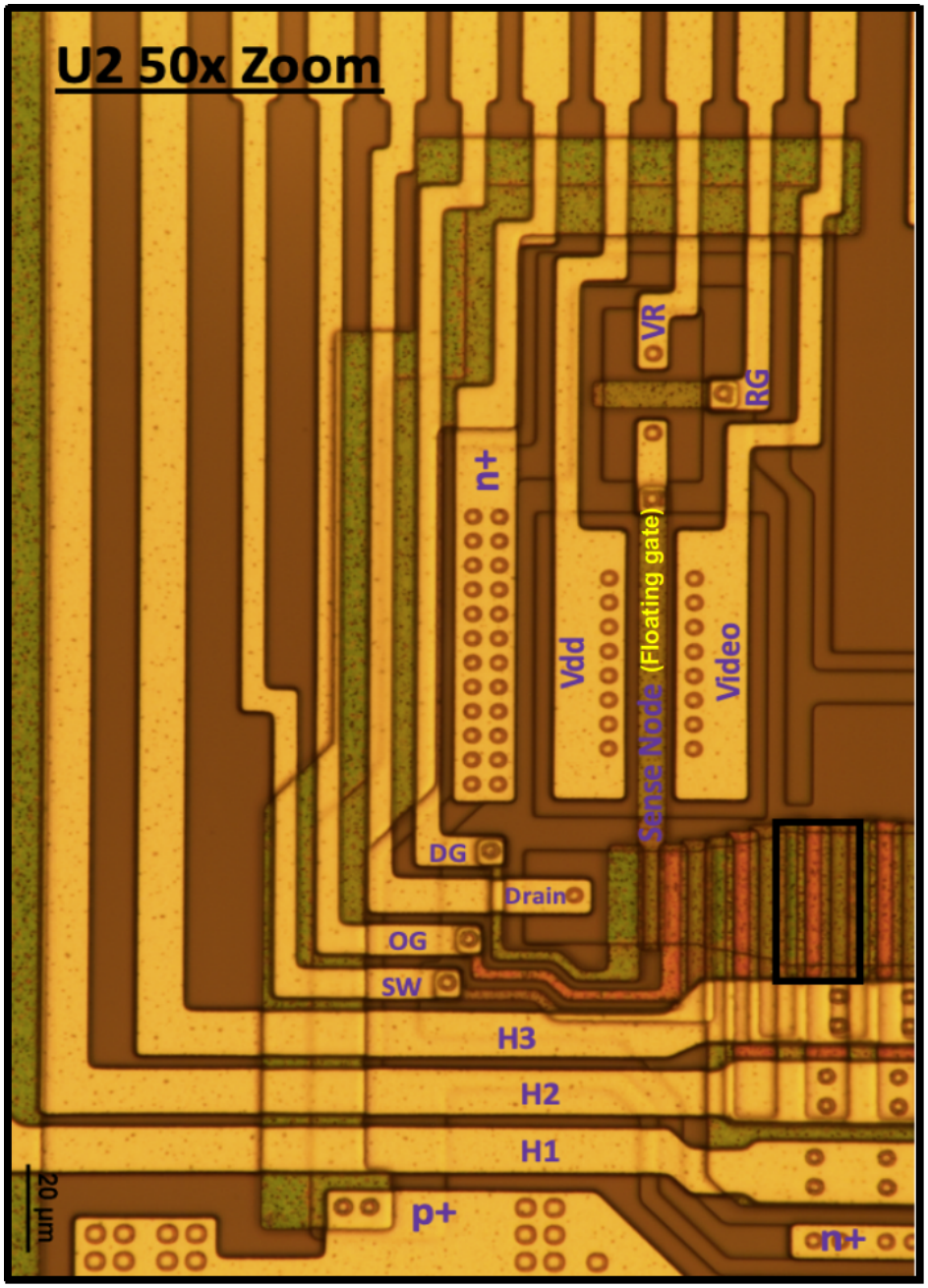

Figure 7.4: Labeled micrograph of a Skipper CCD near the output stage. The labeled p+ and n+ are grounding related considerations not discussed here, see Haque et al. [4] for details. The Serial Register (SR) is akin to another row of the CCD, except about 3x taller.

sense node capacitance C_s, based on the design and calculations of Haque et al. [4]. However, operating these amplifiers in conventional mode (i.e. 1 skip) does not show the expected 20% improvement in noise, as seen from Fig. 7.7, even when our selection of parameters, seen in the figure inset, mimic the choices from Ref. [4]. In fact, the gains seem identical while

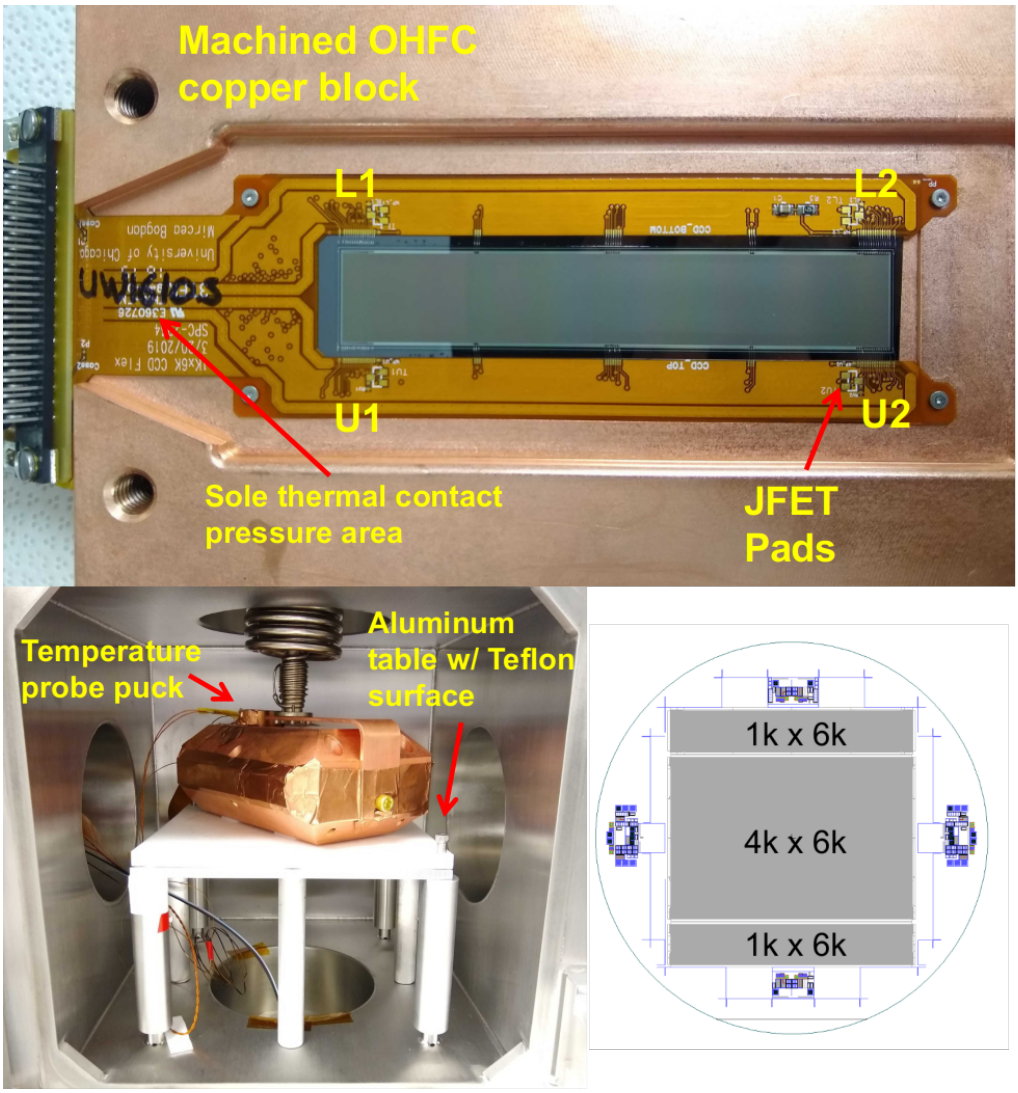

Figure 7.5: Top: Labeled 1k × 6k CCD showing amplifier and JFET locations. Bottom Left: CCD mounted in chamber within a machined ∼12 kg copper block to provide IR and background shielding. Note the displaced location of the temperature sensor. Bottom Right: Schematic of large Silicon wafer on which CCDs are fabricated and then cut out from.

one would expect the decreased capacitance would natively amplify the μV output from the readout node. All results presented in this Chapter are from operating with Register 2 amplifiers.

The basic signal chain remains the same. The LEACH electronics box [6], is responsible for providing all clock and bias voltage signals to the CCD. These signals pass through an external board (designed at the University of Washington, see Fig. 7.8) with the caveat that certain clock signals are shaped using independent RC circuits to modulate their rise and

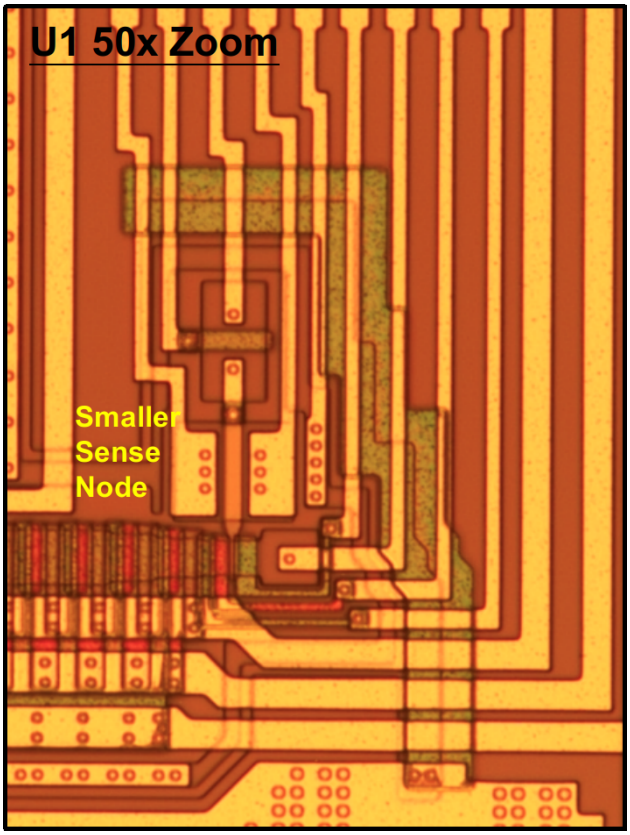

Figure 7.6: Micrograph of the smaller '20/6' Skipper amplifier present on the register 1 side, see Haque et al. [4] for details.

fall times. The return CCD video signal is sent back through the same PCB and passed through independent external amplification circuits for each output amplifier. At their core, these circuits are simply pairs of op-amps with a ∼31x gain.

7.3 Clocks, Voltages & Sequencer Timings

To figure out how exactly Skipping works we can look at a snapshot of a 2 NDCMS sequence of gate potentials, as seen sequentially in Figs. 7.9, 7.10, and 7.11 to better understand the sequence of clocks and gates that are required to accomplish skipping. Charge that is dumped into the Summing Well has to make its way into the Sense Node to be measured before returning back to the Summing Well for a repeat, before being flushed. The applied gate voltages are shown in purple while the V_{eff} (see 'Reference Voltage' explanation further along this section) adjusted values actually felt by the charge in the p-channel are labeled in brown . The Right plots are the waveform representations of the process, with green dots

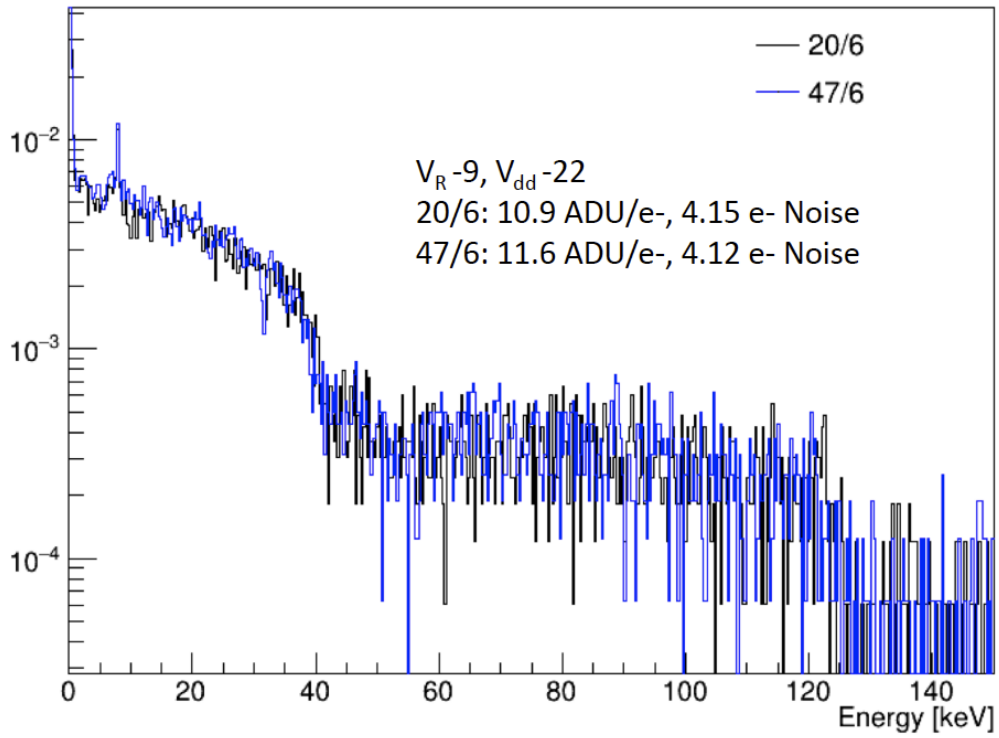

Figure 7.7: '47/6' vs. '20/6' amplifier reconstructed energy spectrum from exposure to a radioactive source, operated at the specified voltage parameters.

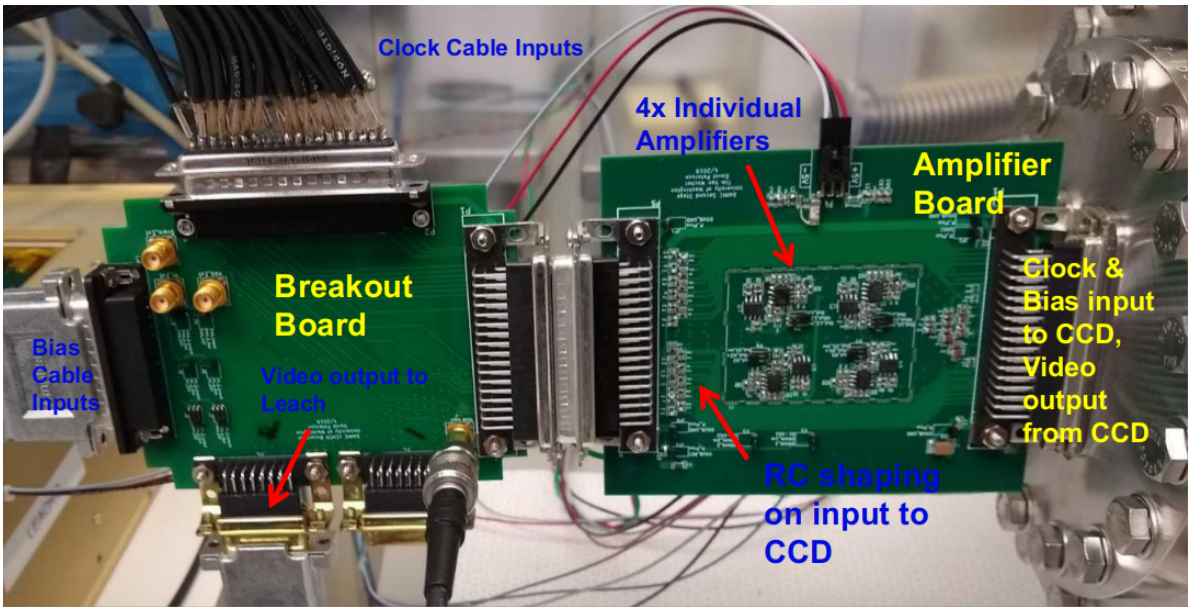

Figure 7.8: External amplifier board that shapes input clocks and amplifies output signal from CCD.

for the current state. A quick sketch of a Skip process is:

1. Charge is dropped into the Summing Well sitting Low.
2. The Reset Gate (RG) is triggered to zero out the SN.
3. The SN is read to get the integrated **pedestal value**.
4. The SW moves up High and cascades charge into the Output Gate (OG) and then into the SN, while the SW moves back down Low. See Fig. 7.10 Top.
5. The SN is read to get the integrated **signal value**.
6. The OG is triggered to move Low, allowing charge to cascade back into the SW and then goes back up High. Refer to Fig. 7.10 Bottom.
7. The RG can optionally be triggered here to zero out the S.N. as in Fig. 7.11 Top.
8. The process from Step 2 is repeated N skip times.
9. The Dump Gate (DG) is triggered Low along with the SW High, now creating a path for all the charge to sweep to the Drain, visualized in Fig. 7.11 Bottom, freshly awaiting a new charge packet to be passed in by the Horizontal Clocks of the Serial Register.

A thorough cataloguing of the sequencer of clock steps is compiled in Table 7.1, beginning after the CCD has been exposed and a readout command triggered, distilled from the relevant Motorola 8600 assembly code. We assume we are only reading out of one amplifier and pushing all the charge to it but there is a shift symmetry to all the clock steps for other amplifiers. We now turn to discussing all these clocks and biases in greater detail.

Vertical Clocks (VC) & Horizontal Clocks (HC): It would seem easy enough to port these operating parameters from a conventional CCD here since their functionality does not change. And while mostly true in that their low values (L) can span from [-2,5] and their high values (H) from [5,12], we did notice some worthwhile points:

- A ΔV of $<$2 V was insufficient to successfully transfer charge and would often result in streaks, indicative of CTI.
- A ΔV of $> \sim$5 V was correlated with charge loss between skips, interesting because one would not expect a clock voltage to affect the output measurement process.

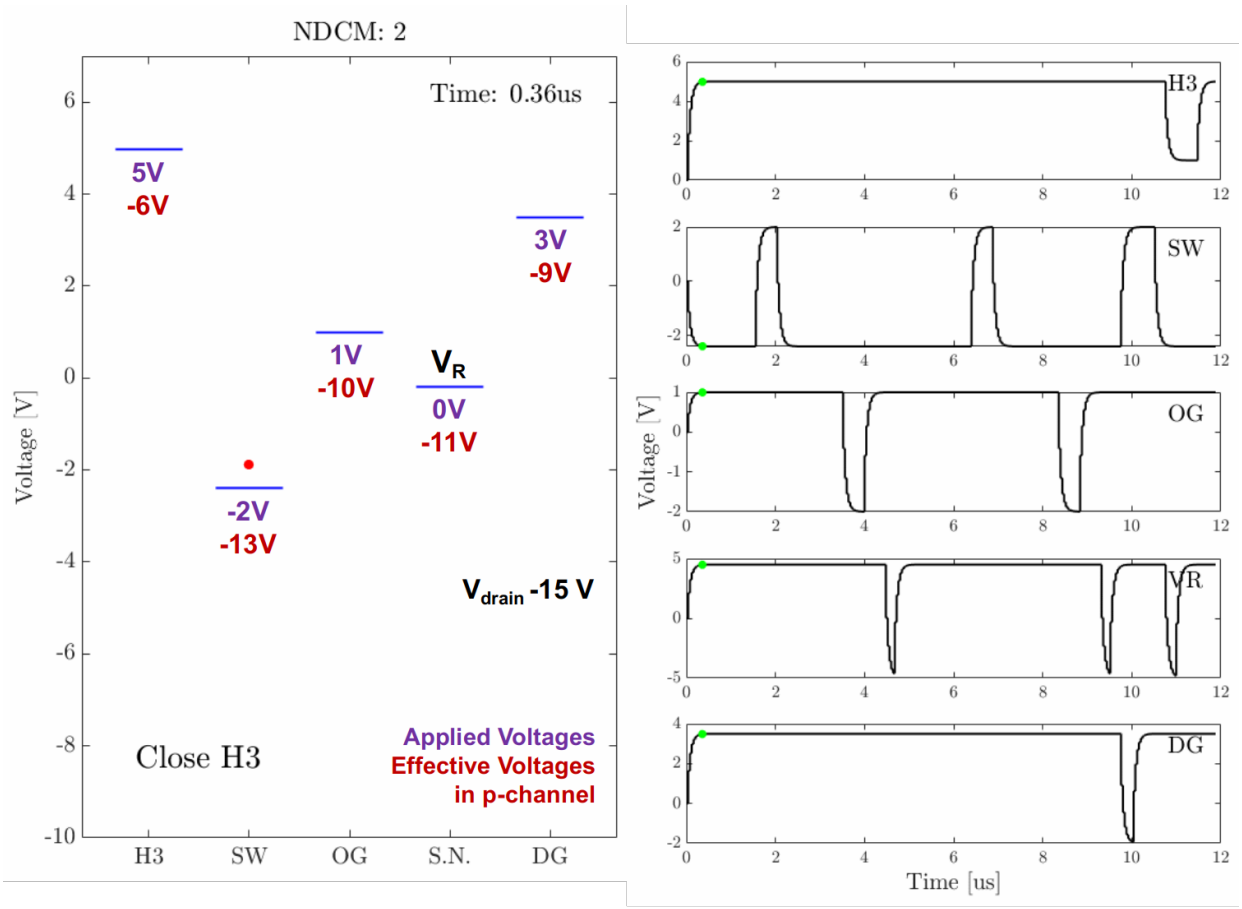

Figure 7.9: Snapshot of 2 NDCMS sequence of gate potentials to achieve Skipper readout. Left: Physical representation of gate potentials moving up and down to move contained charge (red blob). The applied voltages differ from the actual potentials experienced inside the p-channel (see Sec. 7.3 for discussion). Right: Representation of traces for each potential, showing current position (green dot) in sequence.

Transfer Gate (TG): The TG prevents charge in the main array from leaking over to the Serial Register. It is not a physical gate that can store charge but is akin to a 2 state potential barrier that opens (Low) and closes (High). From Stage I of Table 7.1 we can infer that TG should behave like V1 since charge is moved from V3 of the previous pixel into it. Permuting when TG is low for the 7 different steps, assuming it is a valid configuration that allows charge to move through (i.e. HHHLLHH), does not seem to affect the performance characteristics of the CCD — with the exception that if the TG is low for only one step then we notice some CTI, likely due to insufficient time for charge to be moved across.

Summing Well (SW): The Summing Well stores charge when it is not being actively read at the Sense Node. The SW has the largest ΔV since it has to be the lowest potential

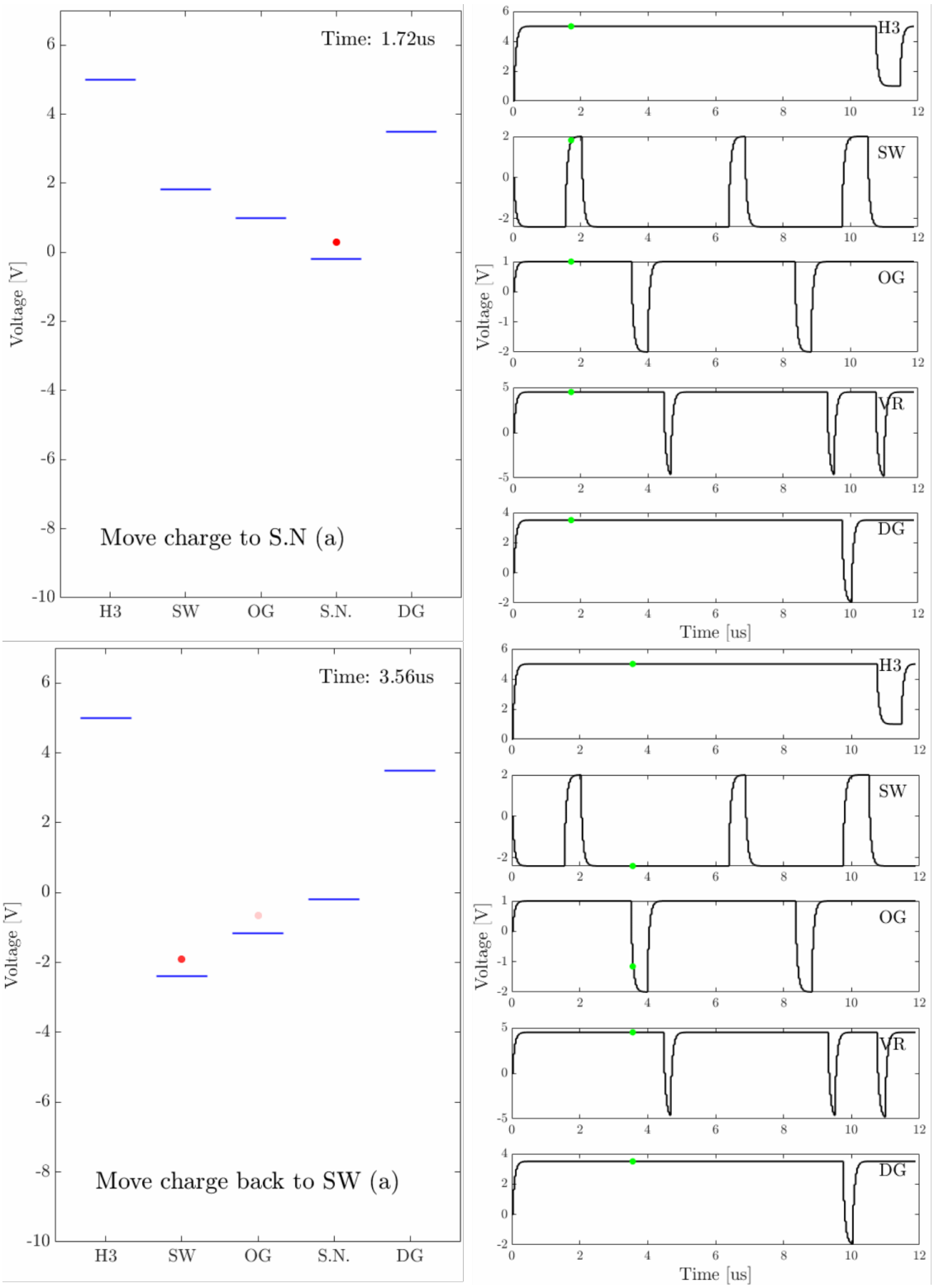

Figure 7.10: Continuation of Fig. 7.9, showing 2 snapshots during charge movement into and out of SW

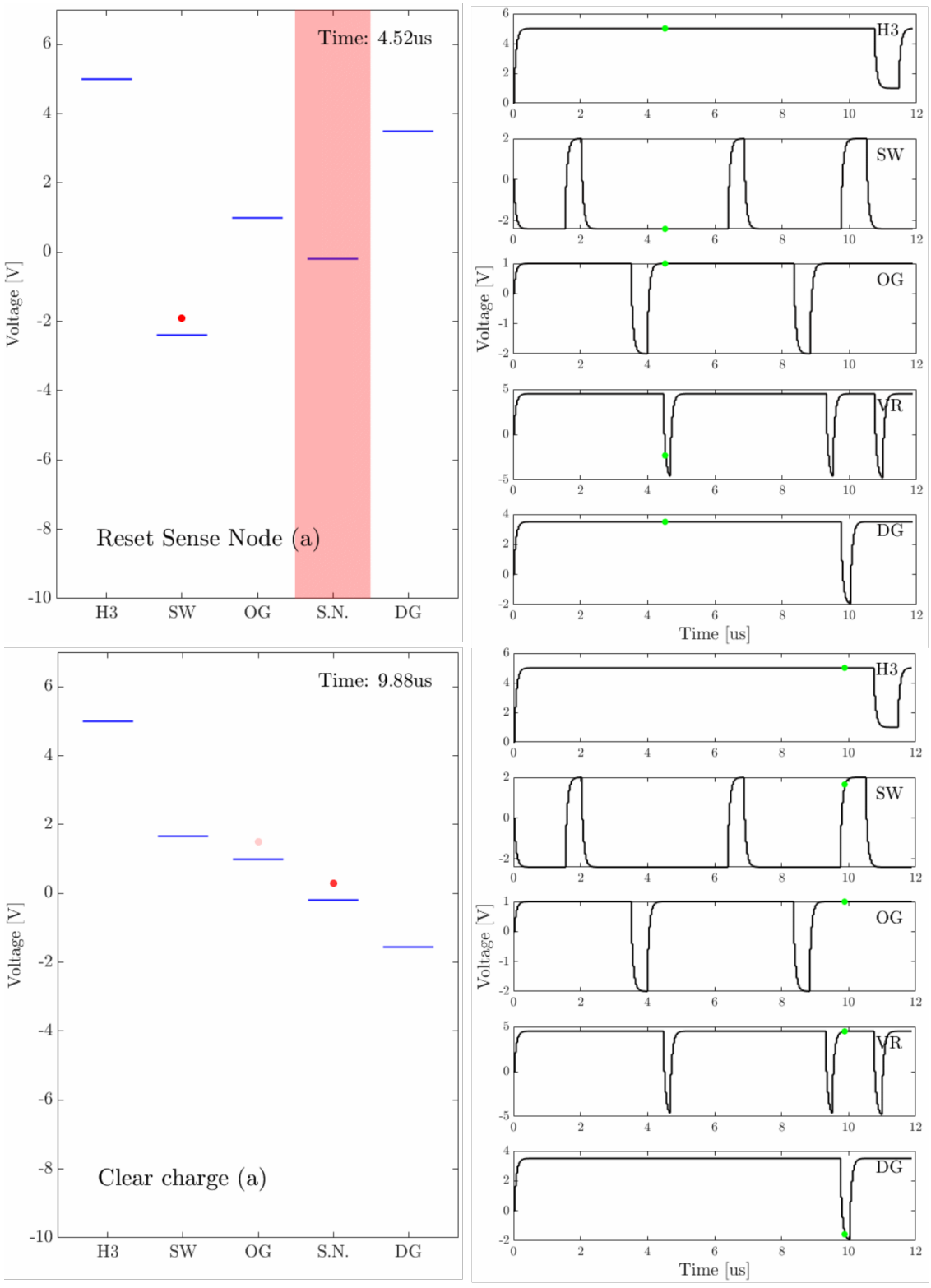

Figure 7.11: Continuation of Fig. 7.10, showing 2 snapshots during Reset of the SN and the charge clearing process.

Stage I **Vertical Transfer**	Hold Time [μs]	V1	V2	V3	TG	Notes
1	30	H	L	H	H	Charge starts under gate 2
2	30	H	L	L	L	
3	30	H	H	L	L	
4	30	L	H	L	L	
5	30	L	H	H	L	
6	30	L	L	H	L	
7	30	H	L	H	H	Charge moved into SR
Stage II **Horizontal Transfer**	Hold Time [μs]	H1	H2	H3		Notes
1	1	H	L	H		Charge starts under gate 2
2	1	H	L	L		
3	1	H	H	L		
4	1	L	H	L		
5	1	L	H	H		
6	1	L	L	H		
7	1	H	L	H		Charged moved to SW
Go back to Stage I if row complete						
Stage III **Skipper**	Hold Time [μs]	SW	OG	RG	DG	Notes
1	0.16	L	H	L	H	Trigger Reset
2	0.48	L	H	H	H	
3	0.5	L	H	H	H	Pedestal Delay
4	τ_{int}					Pedestal integration
5	0.16	H	H	H	H	Summing Well trigger
6	0.5	L	H	H	H	Signal Delay
4	τ_{int}					Signal integration
8	0.16	L	L	H	H	Output gate low trigger
9	0.08	L	H	H	H	Charged moved back to SW
Repeat Stage III N skips						
Stage IV **Clear Charge**	Hold Time [μs]	SW	OG	RG	DG	Notes
1	0.08	H	L	H	L	Dump gate trigger
2	0.48	L	L	H	H	
Go back to Stage II until row complete						

Table 7.1: Sequencer steps for N Skip (NDCMS) CCD operation. H & L refer to the respective high and low potential values for those clocks.

to allow charge to flow back from the SN after a skip read and it also needs to be the highest

potential (though short of the Horizontal Clock high) to allow charge to flow into the SN when triggered up. This Δ is concerning because the effective SW Low cannot be in line with V_{drain} otherwise the complicated fringing fields of the μm scale output area can create a path for charge injection, requiring a SW High - $V_{\text{drain}} > \sim$2 V. Also large voltage swings might put us at risk of clock induced charge (see Sec. 7.6.1).

Output Gate (OG): The OG is the key to skipper operation, its high and low values sandwich V_{R} of the Sense Node. If OG is low, charge can move 'backwards' to the SW while if it is high it opens a path 'forward' to be measured. In a conventional DAMIC CCD this value was fixed to -2.2V but is now allowed to float with a ΔV of 3V around V_{R}.

Reset Gate (RG): The RG triggers a reset of the floating gate potential. We refer to the circuit diagram in Fig. 7.12 to understand the mechanics of what happens and when triggering occurs. Since the reset transistor is a pMOS, it is off if the gate-to source voltage is >0 and on (resetting) otherwise. So to reset, we require $V_{GS} < 0$.

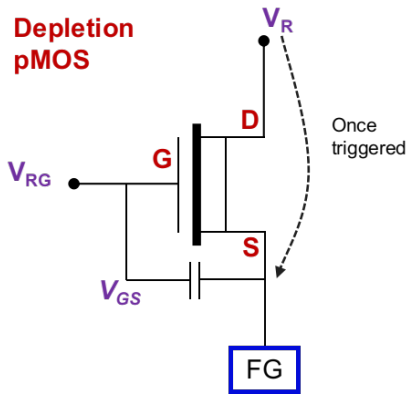

Figure 7.12: Circuit schematic for depletion p-type MOSFET for resetting floating gate Sense Node.

From applying the Kirchoff Voltage Law to the gate to FG loop in the amplifier region, we can work out this condition:

$$\begin{aligned} & & V_R &= V_{RG}^{\text{eff}} - V_{GS} \\ V_{RG}^{\text{eff}} \equiv V_{RG}^{\text{app}} + V_{\text{eff}} & \implies & V_{GS} &= V_{RG}^{\text{app}} - V_R + V_{\text{eff}} \\ V_{GS} = 0 & \implies & V_{RG}^{\text{app}} &= V_R - V_{\text{eff}} \\ & \therefore & \boxed{V_{RG}^{\text{app,L}} < V_R - V_{\text{eff}} < V_{RG}^{\text{app,H}}} & \end{aligned} \tag{7.3}$$

where V_{RG}^{app} is the applied voltage at the user selected/LEACH level while V_{RG}^{eff} is the V_{RG} actually felt by the device.

The V_{eff} indicated in Eq. 7.3 comes from the displacement of the minimum in the potential junction from the actual applied value. We can see this by referring back to the potential diagram of Fig. 2.2 in Chap. 2, where the potential the charges actually feel when they are 'stored' in the p-channel under a gate is close to V_{min}. The difference between the gate potential and this minimum is V_{eff} and knowledge of this value is of paramount importance to understanding if charges can physically move between gates, as represented in Fig. 7.9. A quick way of determining this value is to scan the high values of RG downwards until the reset gate is permanently on (i.e. $V_{GS} < 0$) — one will not see any charge in an image under this condition — from which V_{eff} can be backed out and we arrive at value of approx. **11V** for our current operation.

Reference Voltage (V_{R}) & Drain Voltage (V_{drain}): The Reference voltage is actually different between a Skipper CCD and a conventional device. In a conventional CCD, V_{R} sets the minimum potential and defines the extent of the depleted region at the p-n interface, in conjunction with the gate voltages applied which also affect the depletion. However this role is taken by V_{drain} in a Skipper CCD, while V_{R} is only responsible for setting the potential of the floating gate Sense Node. In comparing these values from both types of CCDs we note that V_{R} was optimally suggested to be -12 V in a conventional device [7], while V_{drain} in a Skipper is unable to be pushed that high due to charge injection concerns (i.e. when there is a path for holes to travel back up into the output stage because potentials are too close). Too low a V_{drain} runs the risk of overextending the depletion region too much towards the Silicon-Oxide interface and careful parameter selection is required to prevent either extreme of charge injection or excess leakage current. An additional complication is that a Skipper V_{R} cannot go above 0V due to LEACH electronics limitations, squeezing the acceptable parameter space.

Dump Gate (DG): The DG blocks charge from escaping from the Sense Node. We have found that mirroring this to the Output Gate, due to the inherent symmetry of their placement w.r.t. the measurement node, is a good rule of thumb. The high value is not overly relevant though any gate voltage change will change the shape of the depletion region near the p-n junction and may cause unwanted behaviour.

Amplifier voltage (V_{DD}): As the amplifier voltage, V_{DD} is one of the key parameters responsible for the gain of the system. The caution here is that too low a value of V_{DD} can result in the amplifiers drawing a lot of power, warming up, and then emitting IR photons that can cause an increased leakage current as will be seen in Sec. 7.6.1.

We have over 40 parameters that can be adjusted in a Skipper CCD, meaning this is a very high dimensional space for optimization that is unfortunately also strongly correlated.

Input	External Shaping RC [μs]	High Value	Low Value	Width [μs]
Horizontal Clocks	33 ns	6.5V	4V	1
Vertical Clocks	2.4 μs	8V	6V	30
Pedestal wait time		0.5 μs		
Signal wait time		0.5 μs		
Integration time		10 μs		
Transfer Gate	2.4 μs	8V	6V	30
Summing Well	100 ns	3V	-2V	0.16
Output Gate	100 ns	2V	-1V	0.08
Dump Gate	33 ns	2V	-5V	0.08
Reset Gate	100 ns	12V	10	0.16
V_{R}		0V		
V_{DD}		-16V		
V_{drain}		-17V		
V_{sub}		45V		

Table 7.2: Set of values for voltages and timings used with the 1k x 6k CCDs

In Table. 7.2 we report a set of parameters which result in proper operation of the Skipper CCD with good noise performance. We have also successfully operated with values of V_R down to -9V by shifting the other voltages levels accordingly.

7.4 A brief interlude into analyzing Skipper Images

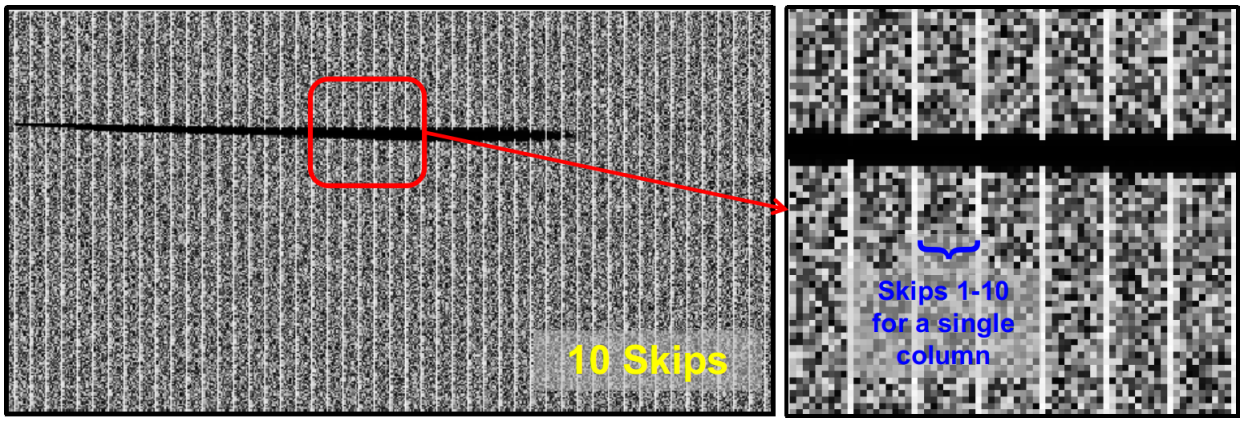

Figure 7.13: 10 Skip raw image. Each vertical band is a collection of Skipper columns, in this case Skips 1-10.

Having discussed parameter selection, we can run the CCD and command the LEACH to take an exposure. The data is returned as a FITS image file, with a visual example seen

in Fig. 7.13. Each vertical band is a collection of Skipper columns. We can construct the k-th sub-image $I^k(i,j)$ (i columns, j rows) by collating the columns of N skip Skipper image S by:

$$I^k(i,j) = S(i \times N + k, j) \tag{7.4}$$

We can get the *average image* by applying Eq. 7.2 as:

$$I^{\text{avg}}_{ij} = \frac{1}{N} \sum_{k=1}^{N} I^k_{ij} \tag{7.5}$$

We can histogram the pixels of the average image to get the familiar raw pixel value distribution, with the caveat that we now have multiple peaks (discussed in the next section), as seen in Fig. 7.14 Left.

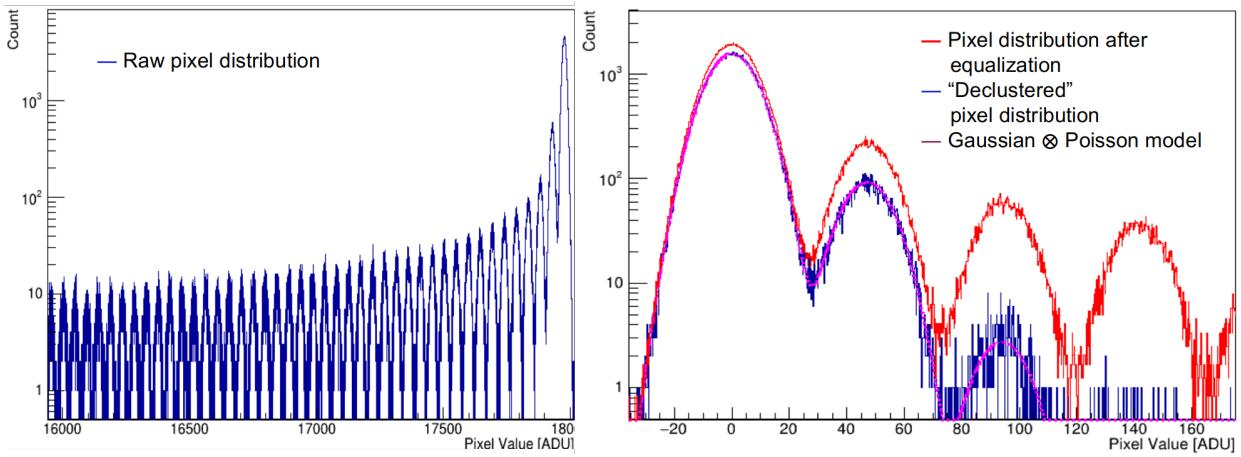

Figure 7.14: Left: Raw pixel distribution from a .fits file. Right: After equalization procedure (red histogram). After clustering and halo masking process (blue histogram). Finally, the leakage current is extracted from a log-likelihood fit using a Gaussian and Poisson convolved model.

The algorithmic analysis of a Skipper image is then quite similar to the method outlined for conventional images in Sec. 2.1.2. The few key differences lie with the existence of discrete peaks. The process is very briefly summarized as follows:

1. Equalization is done on this average image I^{avg} by searching for the 0 e^- peak, defined as the last peak (in a non-inverted pixel distribution, as seen in Fig. 7.14 Left). A Gaussian fit ($\mu_s.\sigma_s$) is performed and pixel values are set to be $p_{ij} = \mu_s - p_{ij}$, which re-orients the distribution, see Fig. 7.14 Right (red curve)

2. The calibration constant k is found by searching for and fitting a Gaussian for the mean to the $1e^-$ peak, defined as the first peak to the right of the $0e^-$ peak, with sigma comparable to σ_s.

3. All pixels are re-scaled by this calibration constant and the image is now in units of e^-.

4. Next a clustering threshold (taken to be $5\,e^-$ initially) is defined. A systematic search of the image is performed where every pixel above this cut is considered as a seed for a cluster. A recursive search then looks for all contiguous pixels touching the seed with contents $\geq 1\,e^-$and all these pixels are counted as belonging to a cluster.

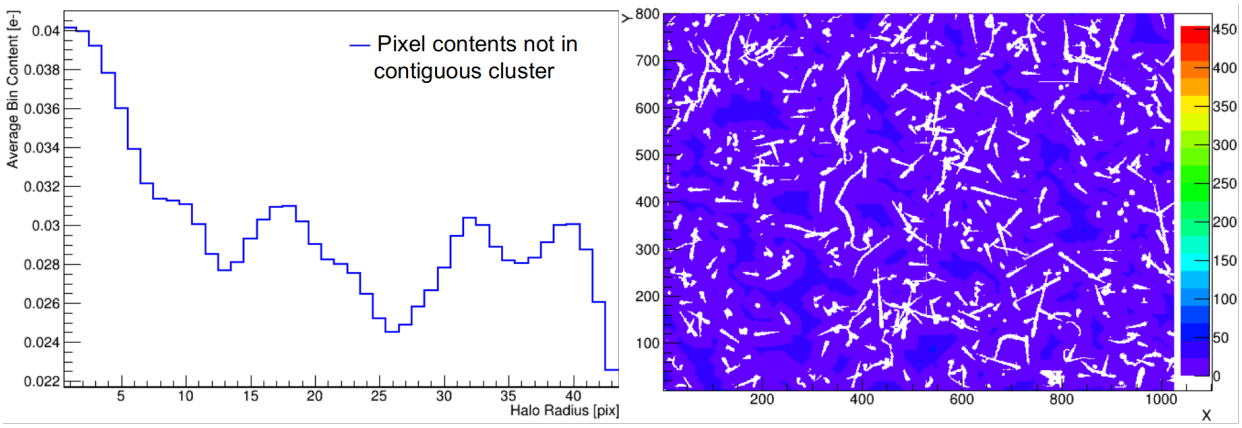

Figure 7.15: Data from an 800x1100, 500 skip image taken using standard parameters. Left: Average charge content of pixels a certain pixel distance away ('halo') from a contiguous cluster. Right: 2D image of this halo computation process. White pixels are contiguous clusters and colors indicate distance a pixel is from closest cluster.

This simplistic clustering algorithm does not take into account charge that may have diffused away from the bulk of a cluster. Further refinements are possible and the subject of ongoing study. In the meantime, we can quantify the strength of this diffusion effect by looking at the pixel distribution of all pixels a given distance away from cluster in an image, see Fig. 7.15 Right. The halo is defined to be all pixels of a certain l_1-norm distance away from the closest cluster, visually represented by the colors in Fig. 7.15 Right. We find an increase charge count up to about a 5 pixel halo, implying that clusters are preferentially surrounded by pixels with elevated charge that are not touching it, a sign that these pixels were caused by charge carriers laterally drifting away from the impact point.

7.5 Achieving single electron resolution

To demonstrate the single electron resolution we have with these devices, we can look at the evolution of the pixel distribution by averaging over an increasing number of sub-images of the same Skipper image. This process can more easily be seen in Fig. 7.16 Left where we show the pixel distribution of the first skip, after averaging over 25 skips, 100 skips, and 1000 skips. We additionally focus our attention on a small patch of the image to see how it evolves (Fig. 7.16 Right). A 1 skip image is basically a conventional CCD and the pixel distribution is almost Gaussian, and the image patch shows a wide variation in pixel contents. After 25 skips, we see the distribution tighten up and the image patch quieten down. After 100 skips we notice a bump forming in the pixel distribution — this is the signature of measuring 1 e^- within those specific pixels (we will use e^- to generically refer to a single unit of charge even if it is technically a hole). With 1000 skips complete, we notice a discrete peak structure for 1, 2, and 3 e^-. The noisy image patch we started with has almost no noise now and we can clearly see the existence of only 3 pixels with non-zero charge that were lurking within. In addition, this automatically reveals the calibration constant since we know the 2nd peak will be the pixels that contain $1\,e^-$ from which we can read-off that the calibration constant $k \sim 18\,\mathrm{ADU/e^-}$.

We can continue this process indefinitely, with the only limitation being PC memory constraints in storing images during readout along with eventual hard drive space[1]. We can see a pixel distribution after 3000 skips in Fig. 7.17. , where the read noise is an impressively low σ_{pix}=0.07 e^-.

7.5.1 Noise reduction and linearity

We recall from Eq. 7.2 that noise reduction goes as $\sqrt{N}$. We can plot σ_{pix} as a function of N, as in Fig. 7.18, and confirm the expected behaviour out to 3000 skips. We further confirm this behaviour for all valid Skipper parameter choices, across Register 1 and Register 2.

Each skip image is however not identical. While the differences between any pair of skips is Gaussian distributed with variance equal to the squared sum of 1 skip noise, as expected if there is no charge loss or other systematic defect and confirmed in Fig. 7.19, the image baselines themselves seem to have step-like features as shown in Fig. 7.20. Particularly interesting is the step down at around 460 skips. This pattern is manifest *regardless of the*

1. a 1k x 6k CCD contains 6 million pixels, and with 16 bit pixels that is 12 MB per image. After a few hundred skips one needs GBs of working memory to store a complete image

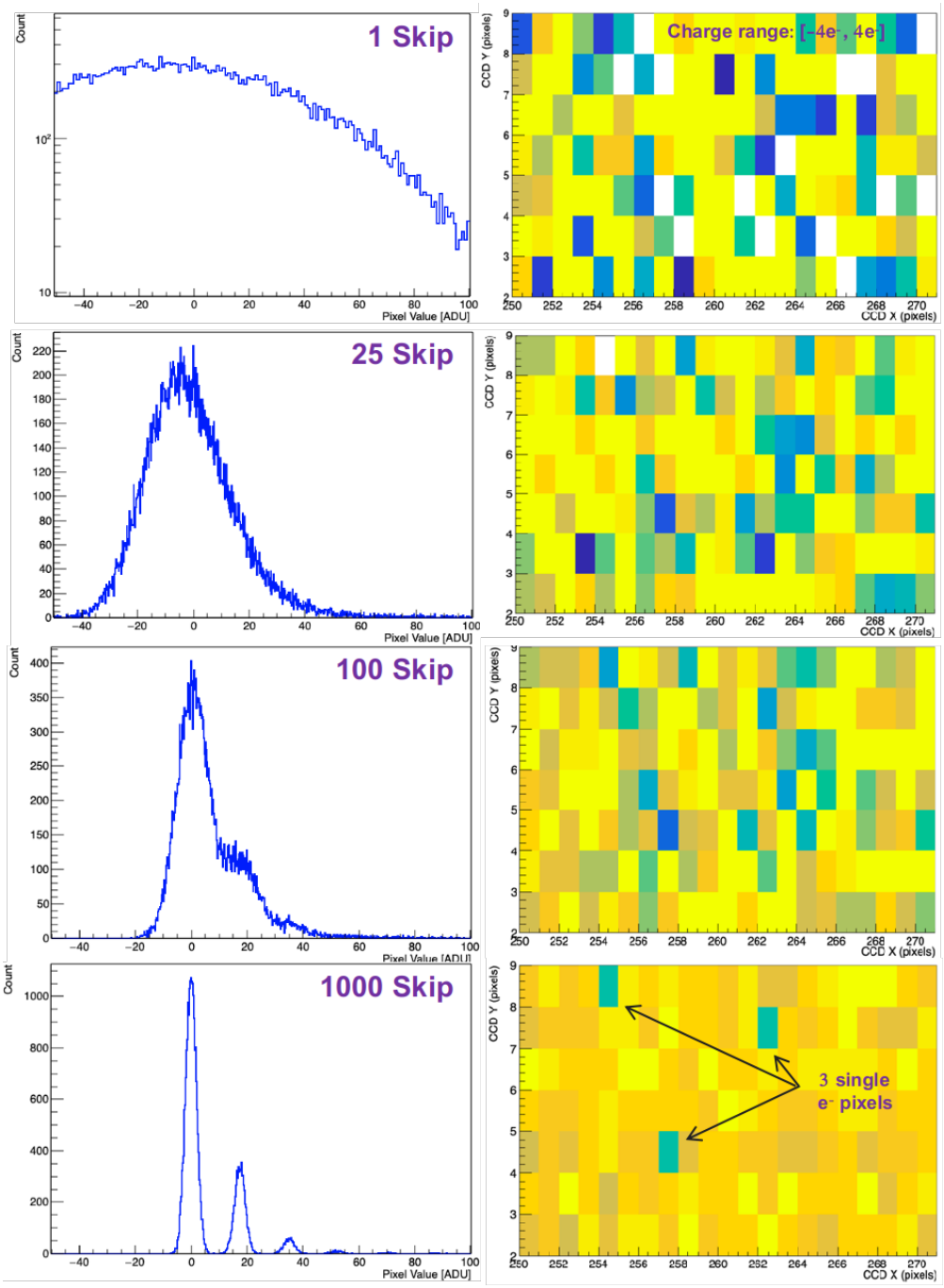

Figure 7.16: Evolution of same pixel distribution and selected image region with increasing skips. As the number of skips increases one can see a tightening of the pixel distribution (Left) and the emergence of discrete peak structure, which is reflected in the reduction of the per pixel noise (right). An image region that had a broad distribution of potential charge values (colors restricted to -4e− to 4e−) is shown to only contain 3 1e− events after 1000 skips. A fit to the 1 e^-peak would reveal the self-calibration nature of these devices, with the mean of the peak by definition being the calibration constant k

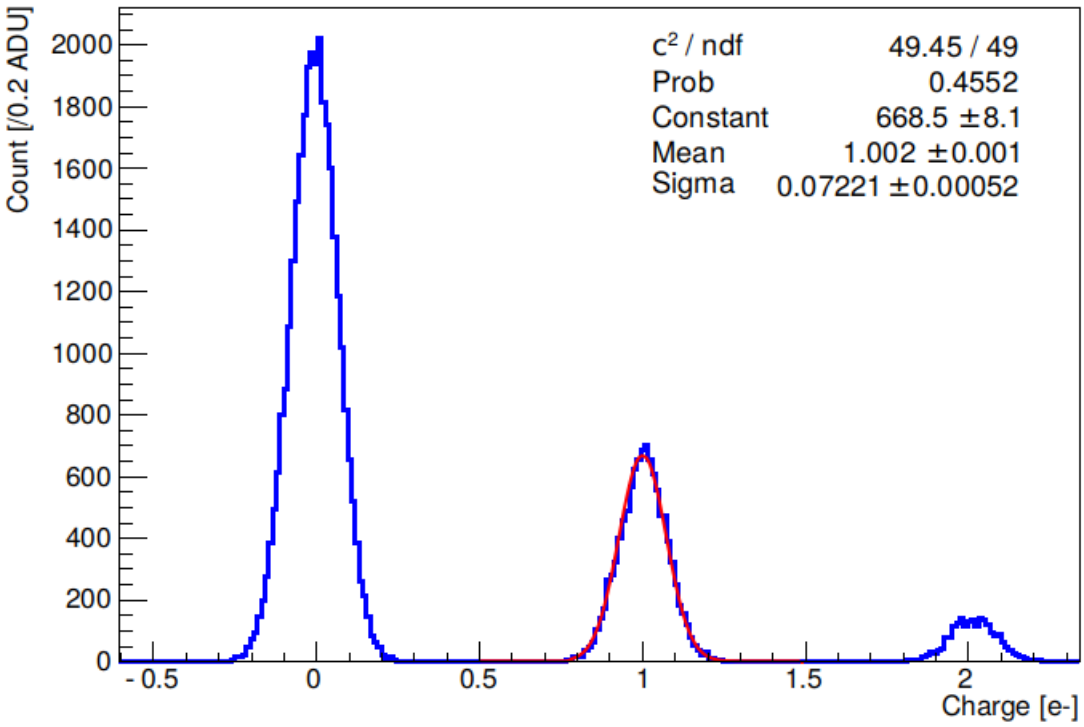

Figure 7.17: Pixel distribution after 3000 skips. Note the clearly defined 0 e^-, 1 e^-, and 2 e^-pixel peaks, and an σ_{pix} of about 0.07 e^-after calibration discussed in text.

number of skips, with this step down feature occurring for the last 40 skips of *every pixel*. The current hypothesis is a yet untraced bug in the LEACH electronics. The sharp increase at the beginning can be attributed to large gate pulses activated when clearing and resetting a pixel that bleed into the first few measurements of the subsequent pixel. For every data set discussed in this chapter, we drop the first few skips and the last ∼40 skips, in the event these spurious features affect pixel charge contents.

The linearity and response of the CCD is a different story though. At first glance, the predicted and actual location for each successive e^- peak appears to be correct, as shown in Fig. 7.21 Top, up to 1 keV. For the selected parameter set, we get a calibration constant of approx. k=45 ADU/e^-. However the sigma of each peak grows linearly, as seen in Fig. 7.21 Bottom, which is unexpected as we expect no difference in measurement precision for varying Sense Node contents.

Digging a little deeper into the gain we can look at the difference in each peak location (Δ_{mn}=Peak$_n$-Peak$_m$ for n=m+1), itself the measure of the calibration constant, allowing us to factor out the growth in uncertainty from using a single calibration constant tied to the 1 e^- peak. We find, as in Fig. 7.22 Bottom, a lurking issue. There is an unexpected

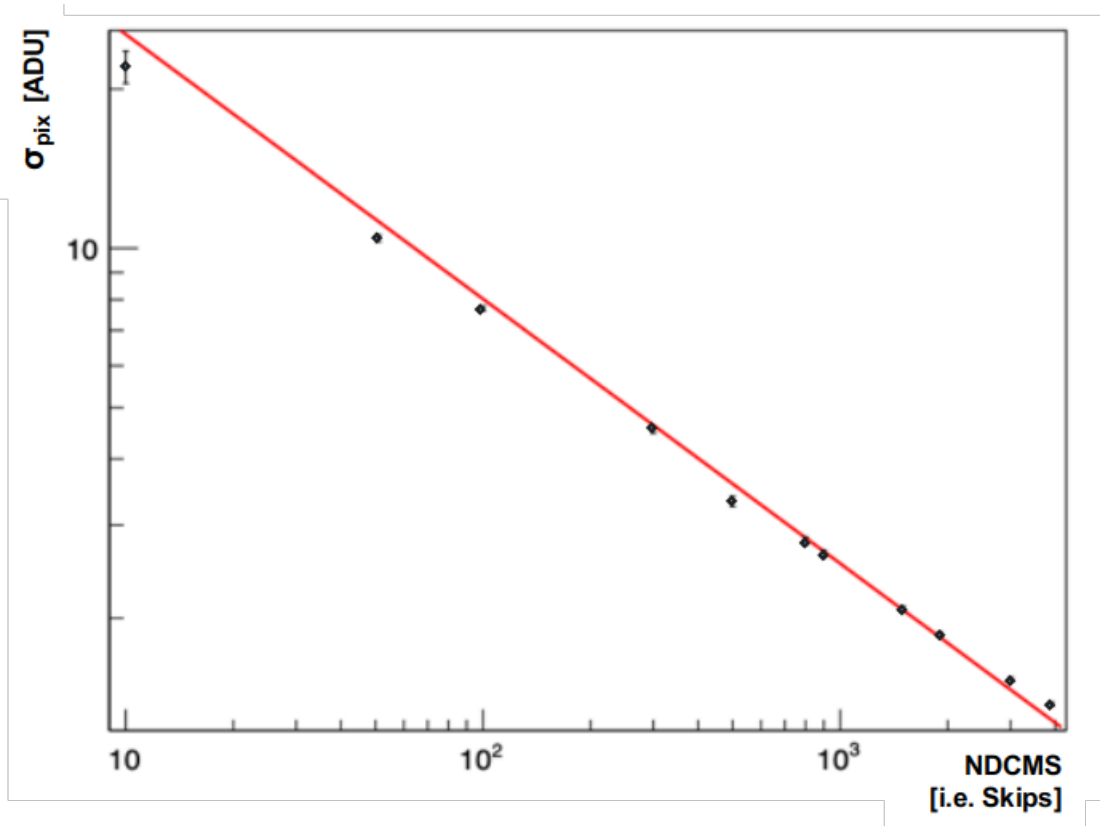

Figure 7.18: Confirmation of $\sqrt{N}$ (red line) reduction in σ_{pix} read noise as a function of NDCMS for a Skipper image.

deviation from a constant value at low counts, plateauing at $\sim 15e^-$. These 2 discrepancies are perhaps indicative of on-chip amplifier issues that need to be resolved with more study.

7.6 Dark Current

In the previous section we briefly outlined how to extract λ_{dc}. We now turn our attention to actually measuring the DC and reducing it to levels suitable for science activities. We remind ourselves that the conventional SNOLAB devices exhibited a DC of roughly 10^{-3} e^-/pix/d.

Removing clusters, along with cutting out the halo, is useful for accurately determining the leakage current in the CCD. Referring back to Fig. 7.14 Right, we see the 'de-clustered' distribution in blue which contains far fewer events, as these are the pixels remaining after not being consolidated with a cluster. The height of the $0e^-$ peak is consistent with the raw distribution as we do not expect empty pixels to be swept up with the clustering process.

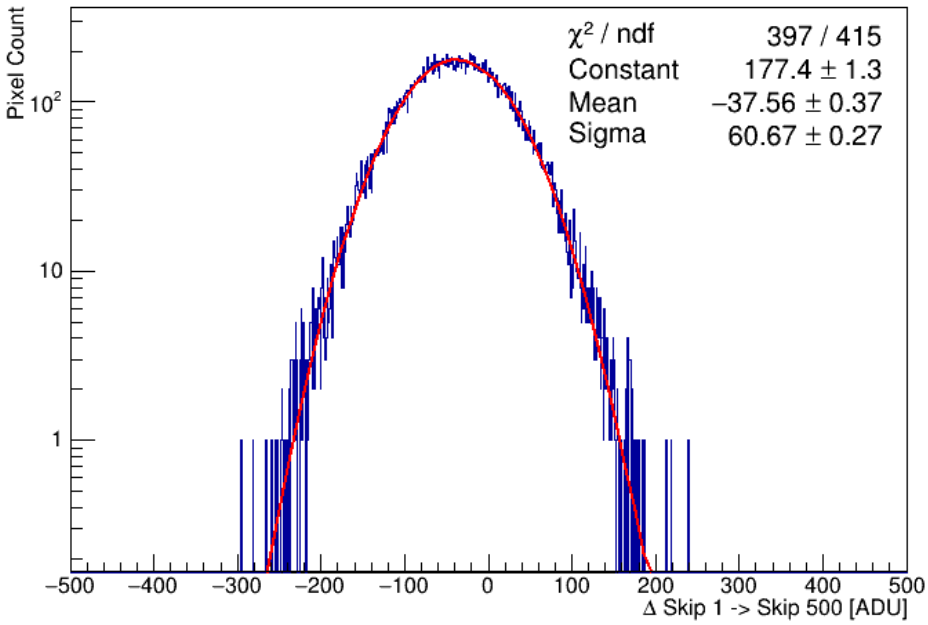

Figure 7.19: Difference between pixel values of 1st and 500th sub-image of a crowded Skipper image with $> 50\%$ pixel occupancy, with overlaid Gaussian fit in red. Both the goodness of fit metric and that the $\sigma \sim 60$ADU is consistent with the squared sum of individual sub-images (having a confirmed σ of approx. 42 ADU), validates the hypothesis that there is no loss of charge.

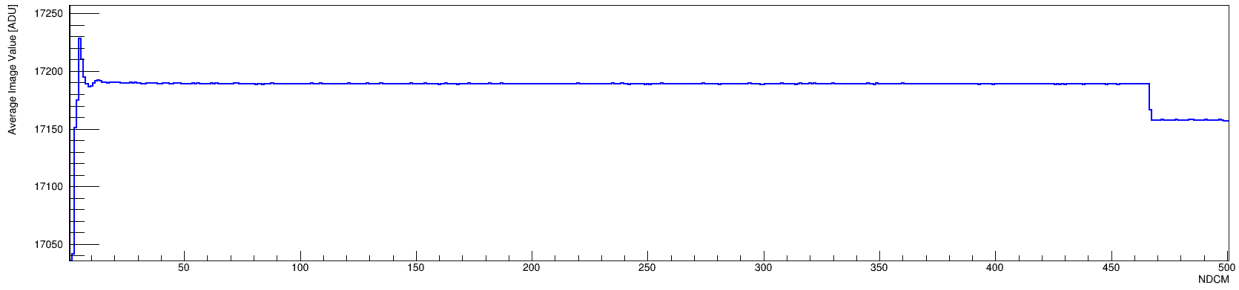

Figure 7.20: Average of each skipper sub-image vs. skip number. Note the constant plateau in the middle section, indicative of regular operation and likely no charge loss. The sharp rise at the beginning can be attributed to the reset gate of the prior pixel changing the image baseline. The step down near the end is thought to be due to an electronics bug.

The pink line is the log-likelihood fitted pixel distribution model:

$$f_p = A \sum_{n=0}^{n=\infty} \mathrm{Pois}(\mathrm{n}|\lambda_{\mathrm{dc}}) \int_{\mathrm{p}-\frac{1}{2}}^{\mathrm{p}+\frac{1}{2}} \mathrm{Gaus}(\mathrm{x}-\mathrm{nk}|0,\sigma_{\mathrm{pix}})\,\mathrm{dx}, \tag{7.6}$$

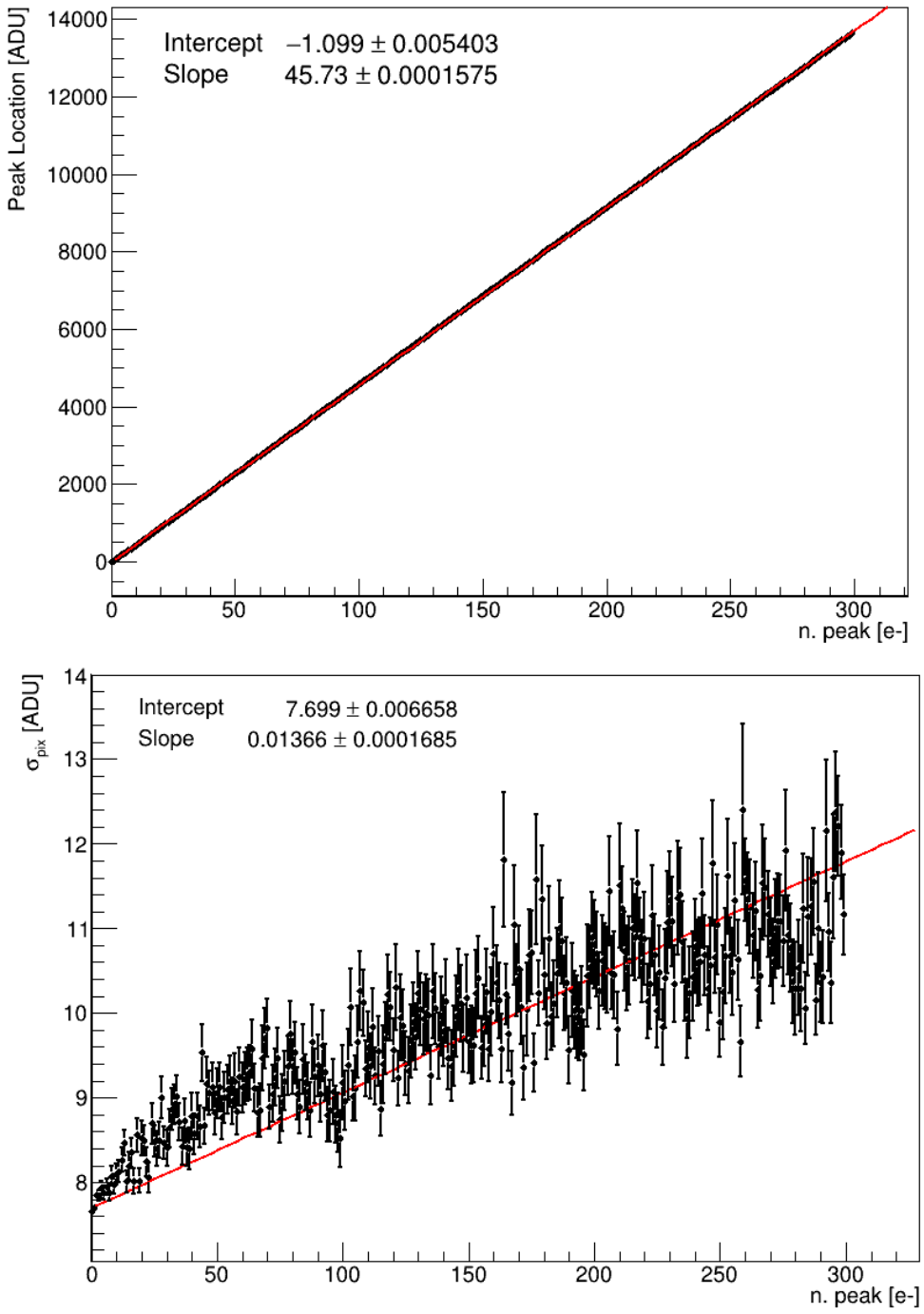

Figure 7.21: Upper: The mean value of each e^- peak up to approx. 1 keV, showing a strongly linear fitted relationship. Bottom: The σ of each peak fit, with best linear fit, indicating an unexplained increase as function of e^- content.

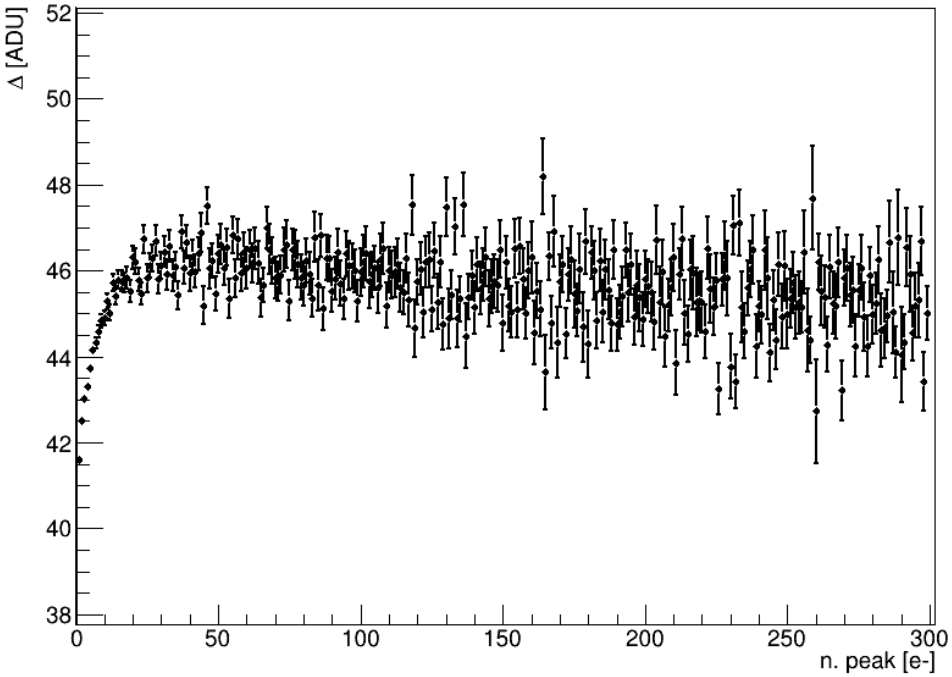

Figure 7.22: Δ between successive peaks in a pixel distribution up to approx. 1 keV, expressed as a function of e^-. One can see the lurking unexpected deviation from a constant value at low counts, plateauing at $\sim$15 e^-.

where f_p is the pixel distribution value for a binned pixel value p in [ADU], A is the number of pixels in the sample, $\lambda_{dc}$is the extracted leakage current, and k is the aforementioned calibration constant.

We continuously took 3h long exposure images of 1100×800 pixels, with 500 skips each, using the parameters outlined in Sec. 7.3. The selection of these parameters, as mentioned, was driven by exhaustive searches for stable parameter settings that showed good linearity, low CTI, and the lowest measured DC. The evolution of the Dark Current can be seen in Fig. 7.23. Each colored set of data points represents a single image, that has been subdivided into chunks of 100 rows. Since we have 800 rows, it takes approx. 7.5 images to fully readout the CCD, which means that during each readout, the unread portion of the CCD above that specific image *will continue to be exposed*, hence the linear growth in exposure over both the subdivisions and the sequential images. The increase will stop after the maximum exposure time for continuous readout of 0.94 days since this is roughly how long it will take to completely read all 6176 rows. The expected linear growth is consistent with a value of 0.06 e^-/pix/day, but artificially plateaus earlier than the expected 0.94 day full exposure. This is likely because pixel occupancy rises dramatically with increasing cluster count —

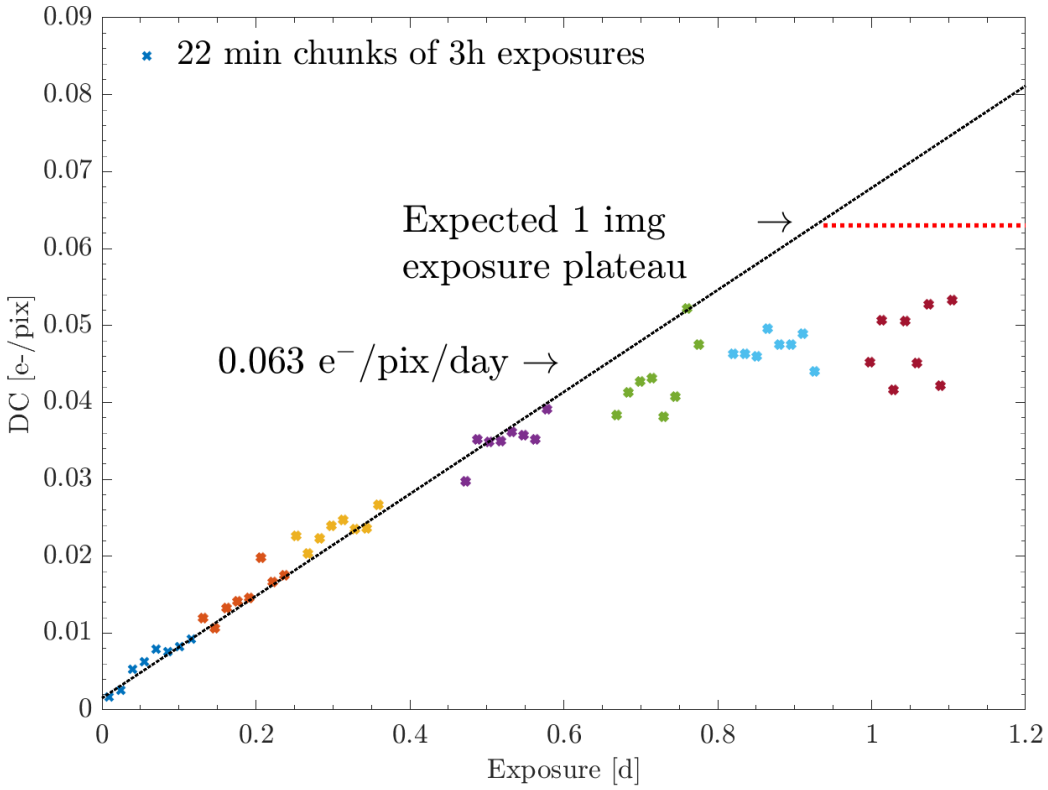

Figure 7.23: Dark current profile vs. image time from last CCD clean for settings discussed in text. Times below 0.94 d correspond directly to image exposure which is the maximum exposure possible for continuous readout under these settings. 3h long exposures of 1100x800 pixels (500 skips) were taken and subdivided into 22.5 min chunks and the dark current was extracted using a Poisson fit. The expected linear growth in DC plateaus before the full image exposure limit is reached. This is likely due to the necessary cut removing clusters $>10e^-$ from the pixel distribution for computation of the DC, dramatically reducing the remaining pixel population for long exposure images with many clusters. Regardless, we extract a DC value of approx. 0.06 e^-/pix/day, roughly 2 orders of magnitude higher than the corresponding value at SNOLAB discussed in Chap. 2.

with a background rate of 30k dru, and a average track length of approx. 20 pix., we are left with just under 5% non-clustered pixels after a day of exposure. This extracted value of λ_{dc} is 2 orders of magnitude higher than that measured at SNOLAB for a comparable temperature.

This discrepancy can plausibly arise from the temperature related depletion dark current discussed in Chap 3.2. The temperature at the CCD could be higher than that returned by the probe measuring a baseline of 130K at the location seen in Fig. 7.5, due either to a strong thermal differential across the massive copper block or very poor thermal contact from the single point of pressure contact to the CCD. We investigated this possibility by

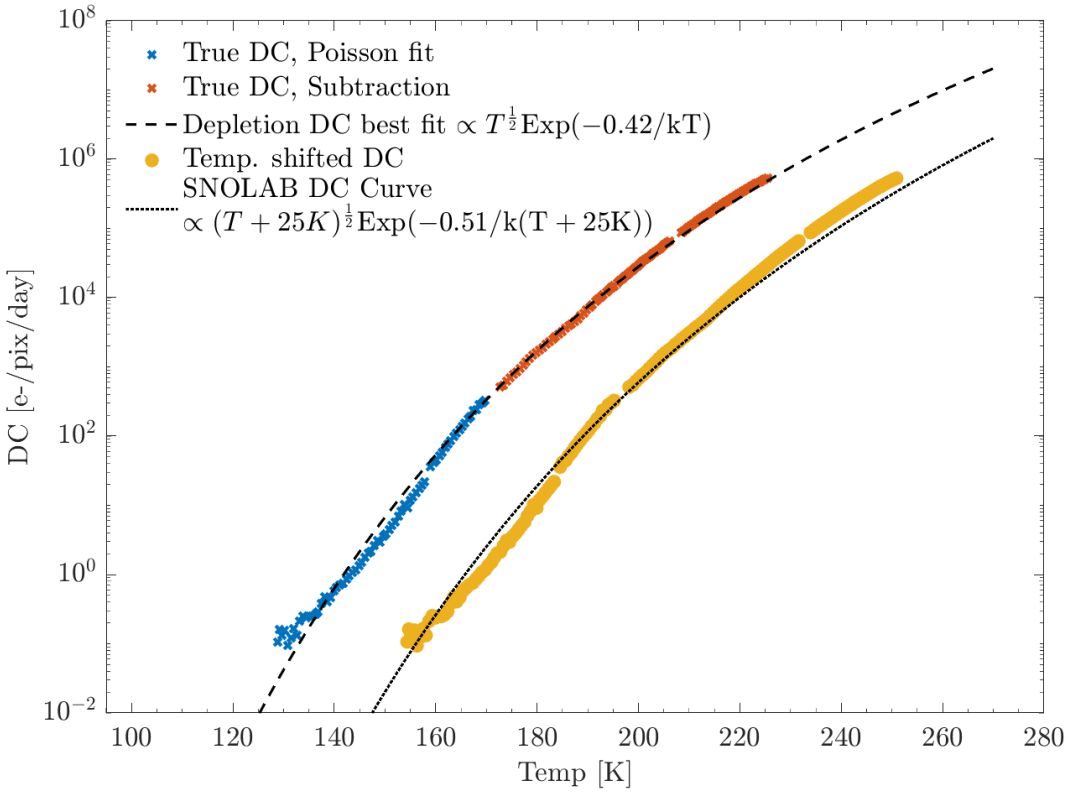

Figure 7.24: The dark current profile measured in a CCD mounted in the Copper box setup shown in Fig. 7.5, with the temperature probe on the outside of the box. The star points (blue and orange) indicate DC values measured either through a Poisson likelihood fit (see Fig. 7.14) or by the subtraction process outlined in Chap. 3.2 respectively. An overlaid depletion dark current fit is provided (dashed line). Additionally, the data points were allowed to float with an offset temperature, fitted to the SNOLAB curve from Chap. 3.2, indicating that a ∼25 K shift could explain the shape of the DC curves too.

warming up the CCD to room temperature and taking 1100×800 pixel 500 skip images, until a temperature of 170K at which point, due to the large dark current, we took 1100×6200 pixel 1 skip images. We then extracted λ_{dc} either through the convolution outlined previously or by the subtraction process discussed in 3.2. The results of this analysis are shown in Fig. 7.24. The dashed line indicates a depletion dark current fit to the data (refer to Eq. 3.10 and the discussion surrounding it for physics details) which indicates an exponential factor of 0.42 eV, inconsistent at the 20% level to the expected $E_g/2$ (=0.56 eV) value. We then allowed the temperature axis to float via an offset term and redid the fit, this time with the coefficients of the fit set to the values extracted from SNOLAB (i.e. C_2=0.51) and work out that the data can also be explained by that prescription if the true CCD temperature were approx. 25K higher. Measurements are currently being undertaken with a temperature

probe directly connected to a CCD to validate this hypothesis.

7.6.1 Alternative sources of spurious charge

While the temperature explanation is a reasonable conclusion, there are other sources of spurious charge generation that have been observed and are worth discussing in greater detail.

Clock induced charge (CIC): CIC is the phenomenon where the movement of any clock voltage, e.g. the rise and fall of the horizontal clock, accelerates charges within the potential. These charges can themselves impact ionize to generate extra spurious charges themselves. 'Electron Multiplying' CCDs (EMCCDs) explicitly exploit this behaviour for a stochastic non-linear output gain e.g. see Ref. [8]. We can get a simple handle on this behaviour by thinking about a hole shunted by a change in potential ΔV, over linear dimension L, akin to what happens in say a horizontal clock. The drift velocity will be $v_d = \mu \Delta V/L$, where μ is the hole mobility in Si of approx. 450 $cm^2\mathrm{V}^{-1}\mathrm{s}^{-1}$. If we say ΔV=5 V and L=15 μm, $v_d \approx 1.5 \times 10^6$ cm/s which is effectively the saturation velocity of holes in lightly doped Silicon, and thus it will take $\sim$1 ns to traverse a distance L. The mean time between collisions will be $\tau_c = \mu m_h/q \approx 0.1$ ps which implies 10000 collisions. The kinetic energy of the hole is small ($\ll$eV) and the dominant loss mechanism will be optical phonon emission, but as it is a stochastic process we can expect that with many clock cycles we run the risk of generating spurious electrons. We can perhaps see the signature of this phenomenon in Fig. 7.25 where we look at the x-overscan pixel distribution across 2 images. Since this is the overscan, we should have 0 charge since the exposure is $\sim$0 in the serial register. However in the inset, we clearly see a $1e^-$ peak that can plausibly be attributed to clock induced charge.

Drain voltage: As previously discussed, the drain is the potential where charges are cleaned out to. Of the many parameters listed in Table 7.2 we found that only V_{drain} has a significant effect on the leakage current. We had started operation with V_{drain} at -24.5V, mimicking a conventional DAMIC CCD, but reducing this value to -15V appears to cut the dark current by approximately half, as seen in Fig. 7.26.

As discussed previously in Sec. 7.3 we reconcile this by arguing that since V_{drain} in a Skipper actually plays the role of V_{R} in a conventional CCD, perhaps a large V_{drain} accounts for over-depleting the p-n junction area thereby allowing charge to accumulate. We remind ourselves that a V_{R} in a conventional device is -12V. We cannot decrease V_{drain} further to this value due to 2 issues: i) charge injection as the drain voltage gets closer to the other

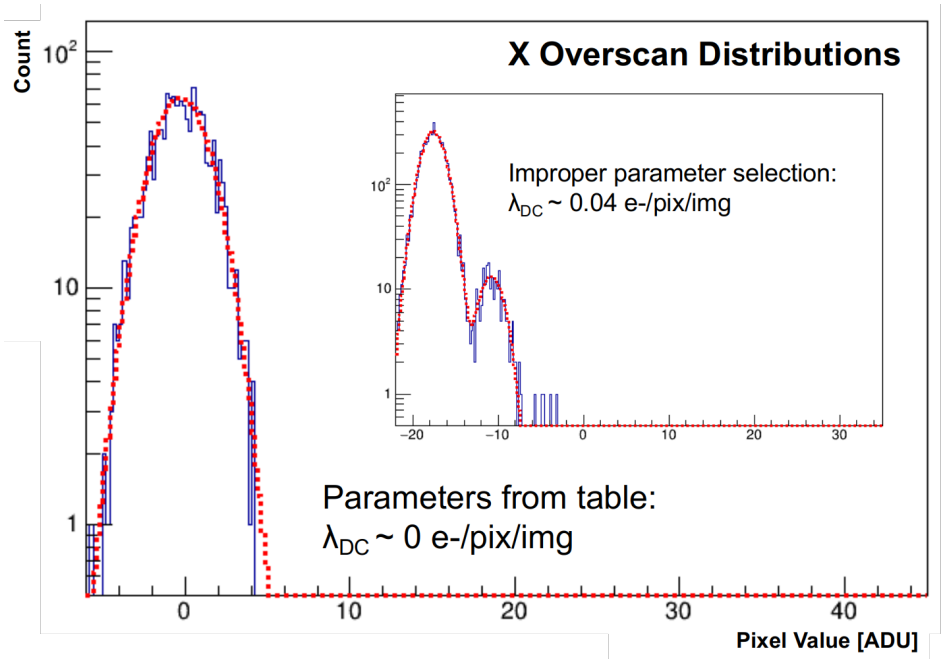

Figure 7.25: Improper parameter selection can lead to spurious charge being observed in regions that should contain ∼0 charge, like in the x-overscan. The pixel distribution for an image taken with parameters from Table. 7.2 is seen indicating expected behaviour, while the inset is an image with large clock voltage swings, where a clear $1e^-$ peak is seen, reflective of CIC or charge injection.

gates, allowing charges to flow *backwards* up the drain (potentially also seen in Fig. 7.25), and ii) the constraints of the other voltages needing to be set amounts apart and that bias potentials like V_R cannot be >0 V in the current LEACH electronics. Our bespoke clocking electronics for DAMIC-M will enable all our parameters to span a larger range including positive bias values, allowing us to move V_{drain} upwards and hopefully further improving the DC.

Surface dark current: Surface dark current is caused by the pollution of the band gap by low lying intermediate energy states, due to interface effects between different materials like the Silicon and Silicon Oxide layers. The canonical way to remove this charge is to operate the CCD in *inversion* [9]. This refers to operating the gate voltages at sufficiently high voltages with respect to V_{sub} to make it favorable for opposite charge carriers (electrons in our case) to collect near the upper interface layers and negate any build up of holes. As Holland et al. [10] discuss however, our high voltage devices do not operate in inversion during collection mode when V_{sub} is high, as this would require our clock voltages to be greater than the substrate bias.

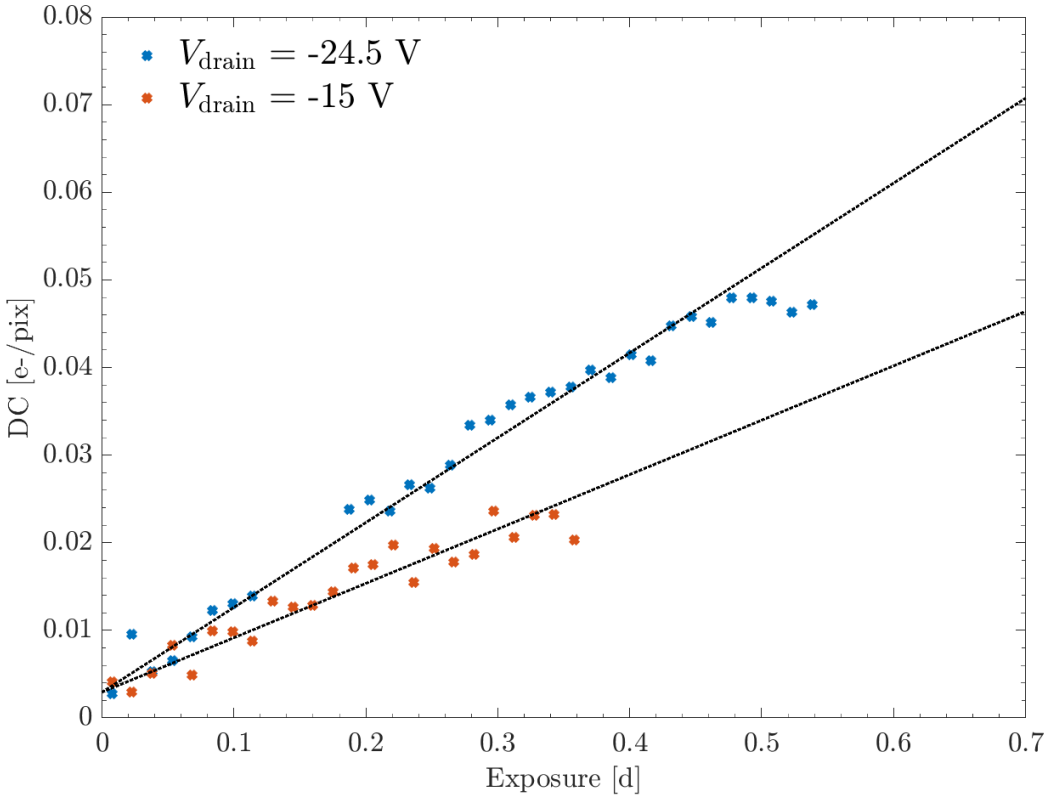

Figure 7.26: Reducing the absolute V_{drain} from -24.5V (the maximum Leach allowable value) to -15V appears to cut the dark current by approximately half.

As such we implement an *erase* procedure that clears the CCD either during startup or when manually commanded, and its methodology is documented in the LBNL CCD operation manual [7]. An erase is accomplished by setting all the clocks to a high positive value and then switching off V_{sub} for a few seconds. This brings the surface to inversion and electrons from the channel stops sweep in and neutralize any built up charge. Then V_{sub} is ramped on again and all the clocks are turned back on. While this procedure has been implemented in all CCDs to date we modified the erase parameters, particularly the high clock voltage values, the ramp up and ramp down times, and the offset to when clocks are restarted, so as to achieve full clear during an erase. The erase procedure can be seen in Fig. 7.27.

Since V_{sub} plays a role in drifting charge, it is natural to assume it might have an effect on the LC. A systematic scan of V_{sub} from 30V — when the CCD is underdepleted — to 60V revealed no change or decrease in the leakage current. However we did notice in 1 CCD the appearance of a charge 'blob' for V_{sub}>40 V as shown in Fig. 7.28. Perhaps the high V_{sub} values were over-depleting into the backside gettering layers and creating a strong

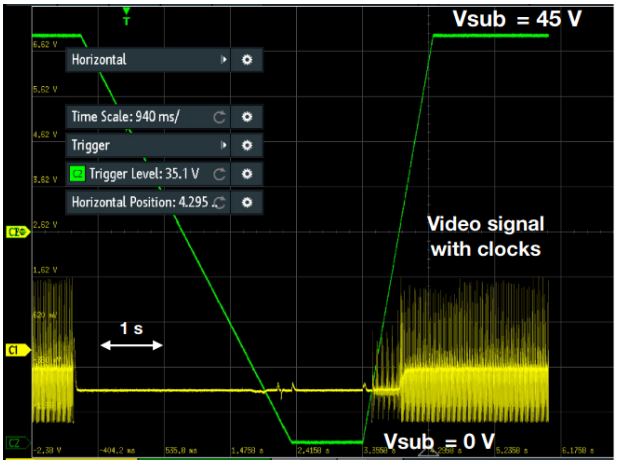

Figure 7.27: Labeled erase procedure implemented in setup. V_{sub} is ramped down at less than 15V/s and held off for 5s (not shown in image), before being ramped up again at less than 15V/s. Clocks are restarted only after V_{sub} exceeds 10V.

gradient therein, which could allow spurious charge generated and otherwise trapped there from mechanical or other defects to leak out and be pushed towards the gates for collection. In the DAMIC Stage II experiment we ran with V_{sub} of 72V and hence that was our original setpoint. After our experience with these spurious charge blobs, we now operate closer to the depletion edge at 42-45V and continue to investigate if these features are universal across our new batch of CCDs or if they can be traced to specific CCD defects.

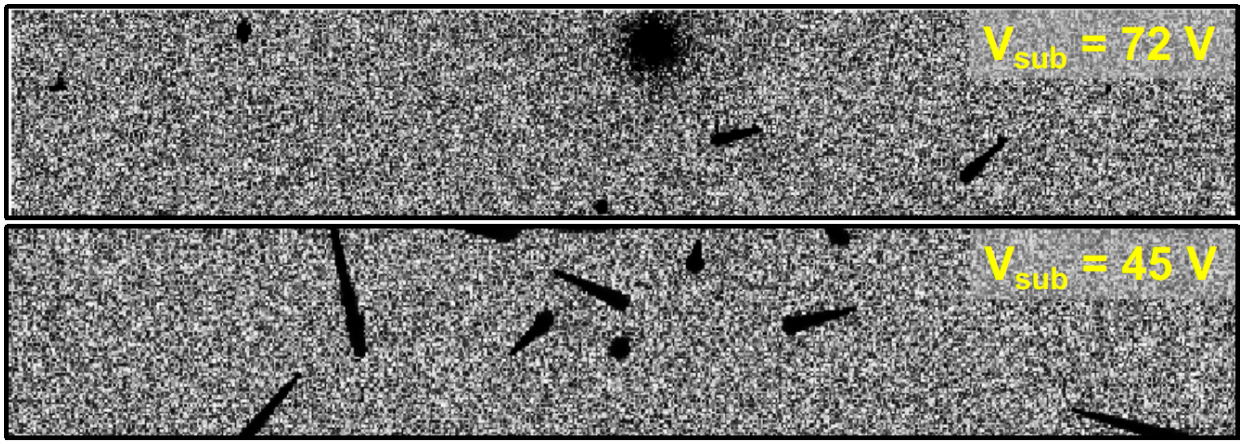

Figure 7.28: charge blob feature (upper center), not identifiable as a standard particle deposition, appeared to decrease significantly with a reduction in V_{sub}. This is plausibly explained by high V_{sub} over-depleting into the backside and creating a strong potential gradient in the rear gettering layers for example, allowing spurious charge generated on the backside (e.g. by defects) to be pushed towards the gates for collection.

Amplifier glowing: The output amplifiers on a CCD are 'powered' by V_{DD}. The behaviour of these MOSFETs is that a higher voltage induces the production of IR photons as the amplifier warms up. These emitted low energy photons can then be absorbed in the detector, preferentially near the sides due to the geometry, leading to excess charge near the amplifier edges and thus contributing to an elevated leakage current.

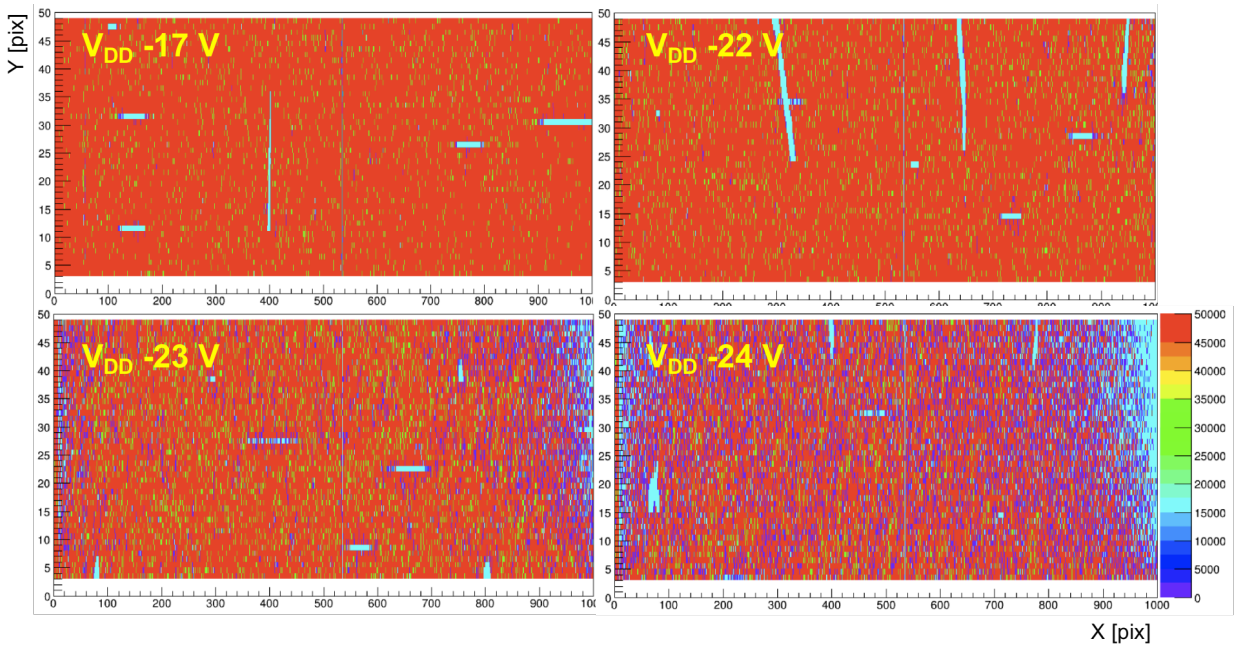

Figure 7.29: Voltage applied to the output amplifier V_{DD} appears to strongly affect the leakage current present in an image, seen by the blue patches appearing as $|V_{DD}|$ is increased.

We tested this hypothesis by taking 500 skip images with V_{DD}between -10 V and -24 V and then measured the dark current. Above -17V (i.e. -10V to -16V) we do not observe a relationship between V_{DD} and λ_{dc} or any other parameter other than obvious reduction in the gain, since this is the output amplifier. Below this threshold value we notice a dramatic rise in elevated charge pixels, best illustrated by Fig. 7.29 which shows an increase in both cluster and cluster density along the side of the image. As such, we operate with V_{DD} at -16V which benefits from good gain without this glowing.

Residual charge: A final possible origin for the DC could be a surface or bulk 'residual image' i.e. persistent images on the CCD due to the potential wells becoming fully saturated and then the overfill becoming trapped charge in the Si-Oxide interface. In our case the mechanism could be induced by charged tracks, which can ionize 10s of thousands of charge pairs and flood the pixels in their immediate vicinity. Charges trapped in the interface layers are then released from their traps with long decay times of hours or more.

We investigated this phenomena by clocking the CCD at 500 skips for around half a day. Then we immediately 'cleaned' the CCD by reading it out rapidly, thereby theoretically removing all charge in the pixel wells. Finally we took a set of images of our usual 1100x800, 500 skip size over the course of a few hours. If there was indeed residual image trapping where traps release charges with a long time constant, we would observe a level of dark current which is in line with the 0.5 day that the CCD was effectively exposed for. We however do not see that and discovered a $\lambda_{\rm dc}$ consistent with our 0.06 e^-/pix/day measurements. The residual charge might be more subtle in that the steady state trap release rate, since the CCD is constantly being bombarded by external charge tracks thus replenishing these traps, is consistent with this upper bound on $\lambda_{\rm dc}$. Nevertheless, we presently disfavour this explanation.

7.7 Minimum Ionizing Particles as a low energy background

Having wrapped up our discussion of Skipper operation and our current work, we turn to more speculative considerations for our elevated dark current levels. In this section we provide brief calculations and simulations for possible mechanisms of a measurable background in Skipper devices by external relativistic particles.

Relativistic particles traversing through a medium lose energy through various channels. The overall contribution is often expressed as a single stopping power ($-dE/dx$, energy loss per distance travelled), an example of which is shown in Fig. 7.30 Left for copper. Of interest in this section is the valley at $\beta\gamma \approx 1 - 100$ where the stopping power is at a minimum, meaning particles at these energies can traverse relatively unimpeded through thick media with minimal energy loss, leading to the term "Minimum Ionizing Particles" (MIPs). In silicon, over the thickness of a CCD we expect about 1 MeV cm^2 g^{-1} $\times$ 2.324 g cm^{-3} $\times$ 0.0675 cm $\approx$ 150 keV of energy deposited at a minimum.

Perhaps the most canonical example of MIPs are muons produced in the upper atmosphere by cosmic ray interactions. These particles impinge on the Earth's surface at intensities of $I_0 \sim$70 m^{-2} s^{-1} sr^{-1}, or in more intuitive terms about 1 cm^{-2} s^{-1} for a horizontal detector. These relativistic particles have mean energies of approx. 4 GeV, with an energy spectrum that displays strong zenith angle (θ, angle from normal of the Earth's surface) dependence as seen in Fig. 7.30 Right. The differential flux is expressed as:

$$\frac{dN}{dAd\Omega dt} \propto I_0 cos^2(\theta) \tag{7.7}$$

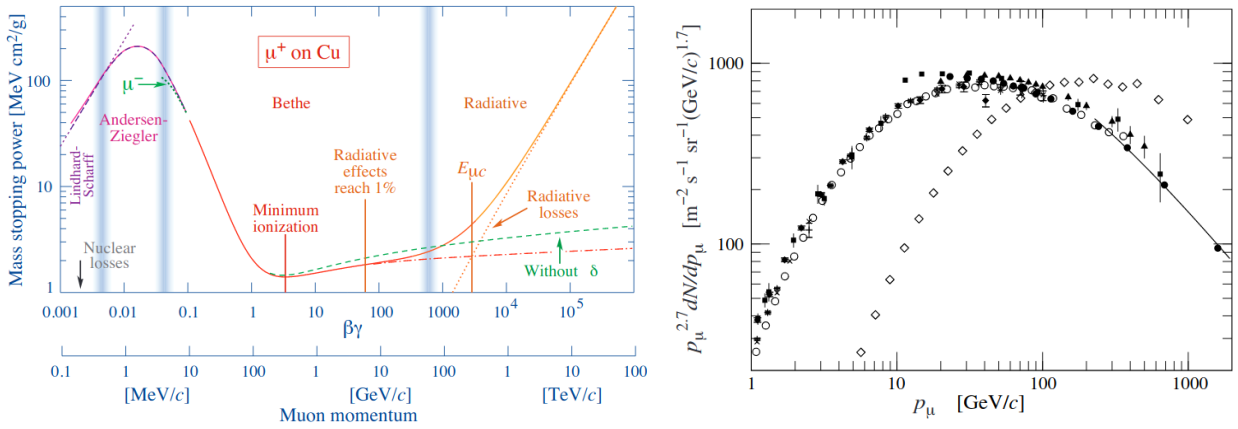

Figure 7.30: Left: Mass stopping power of a μ^+ muon traversing through copper expressed as a function of $\beta\gamma$, showing location of "Minimum Ionizing" valley. Right: Energy spectrum of muons at sea-level at zenith angles of 0° (filled) and 75° (open). Both plots are taken from Ref. [11]

where the $cos^2(\theta)$ is an experimentally measured term that is attributed to:

- The increase in path length of the muon $\propto 1/cos(\theta)$, under the assumption of a flat atmosphere, leading to an attenuation of muons through either their energy deposition or absorptive processes.
- The increased path length again $\propto 1/cos(\theta)$, leading to an increase in decays that exceed any relativistic compensation of their $\approx$2.2 μs lifetime.

There are other zenith angle dependencies that need to be baked in when dealing with a finite sized detector. The aperture, the amount of CCD visible to a muon, is dependent on angle and reduces with increasing zenith, meaning the area element should be more properly expressed as $dA = dA_0 cos(\theta)$. In addition, we assume isotropic azimuthal flux (ϕ, sweeping the cardinal directions), meaning we can recast the solid angle dependence into a pure zenith effect. In combination this leads to:

$$\frac{dN}{dA_0 d\theta dt} = \frac{dN}{dA d\Omega dt}\frac{dA}{dA_0}\frac{d\Omega}{d\theta} \propto I_0 cos^3(\theta) sin(\theta), \tag{7.8}$$

a relation that is seen to match well with surface measured data (100 images, $\tau_{\text{int}} = 2.5$ μs 1 skip, 1k×6k CCD, 14.25 hr cumulative exposure) in Fig. 7.31 Left.

At first blush, energy deposits from these muons in CCDs (or any MIP) are $\gg \mathcal{O}$(eV) and they are intuitively long and narrow, thus very easily identifiable in device images, as clearly seen in Fig. 7.31 Right. These MIPs should not contribute to an elevated $\mathcal{O}$(eV)

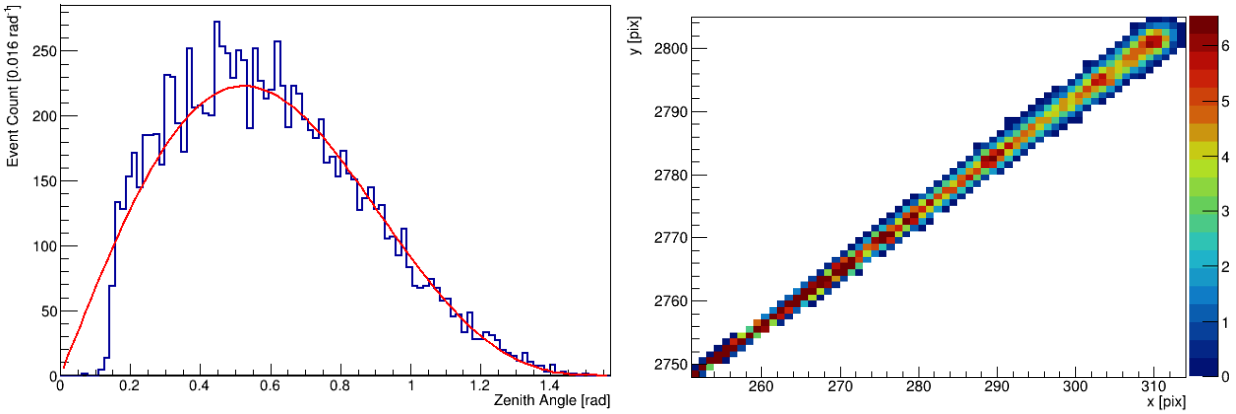

Figure 7.31: Left: Zenith angle distribution of CCD events above 150 keV (blue), with selection cuts for tracks with MIP morphology, showing the applicability of Eq. 7.8 (red) in describing the flux of atmospheric muons. Right: Reconstructed muon track in a 1-skip CCD image, with z-axis corresponding to energy content of a pixel in keV, indicating a deposit of ∼1 MeV.

scale dark current background if properly identified, particularly when including a mask of a few pixels around a track to account for electron diffusion outside the bulk of the track.

However, there are other radiative energy loss processes that occur at the sub-percent level which may be sufficient to introduce a macroscopic low energy background in CCD images. Two processes of interest we discuss here are Cherenkov radiation, and transition radiation. We also briefly touch on thermal emission arising from localized heating, and show that it is likely incapable of accounting for the observed DC.

7.7.1 Cherenkov Radiation

Cherenkov radiation is electromagnetic radiation emitted by a particle if it traverses a medium faster than the phase velocity of light in said medium, under the condition that:

$$\beta n(\lambda) > 1 \tag{7.9}$$

where β is the particle's relative velocity to the speed of light and n is the index of refraction, explicitly written as a function of the wavelength of the emitted radiation. For Silicon, $n \sim 3.6$ which sets the surprisingly low floor of $\beta \sim 0.28 \equiv \gamma \sim 1.041$. An electron traveling through Silicon with just $(1.041 - 1) \times m_e \approx 21$ keV would be sufficient to release Cherenkov photons while the lower bound for a muon is ≈ 4.3 MeV. Radiogenic backgrounds can certainly excite electrons of sufficient energy, but quantifying their presence is

an involved process while muonic background contributions (∼20000 tracks d^{-1} CCD^{-1}) are both significant and easily modeled, providing a natural floor for these background estimates.

We begin this discussion by modeling Cherenkov radiation, expressing the Frank-Tamm formula for the differential rate of photon production, N, first in terms of photon wavelength, λ, and then in photon energy, ω, as:

$$\begin{aligned} \frac{d^2N}{d\lambda dx} &= 2\pi\frac{\alpha}{\lambda^2}\left(1-\frac{1}{\beta^2 n^2(\lambda)}\right) \\ \frac{d^2N}{d\omega dx} &= \frac{d^2N}{d\lambda dx}\frac{d\lambda}{d\omega} = \frac{\alpha}{\hbar}\left(1-\frac{1}{\beta^2 n^2(\omega)}\right) \end{aligned} \tag{7.10}$$

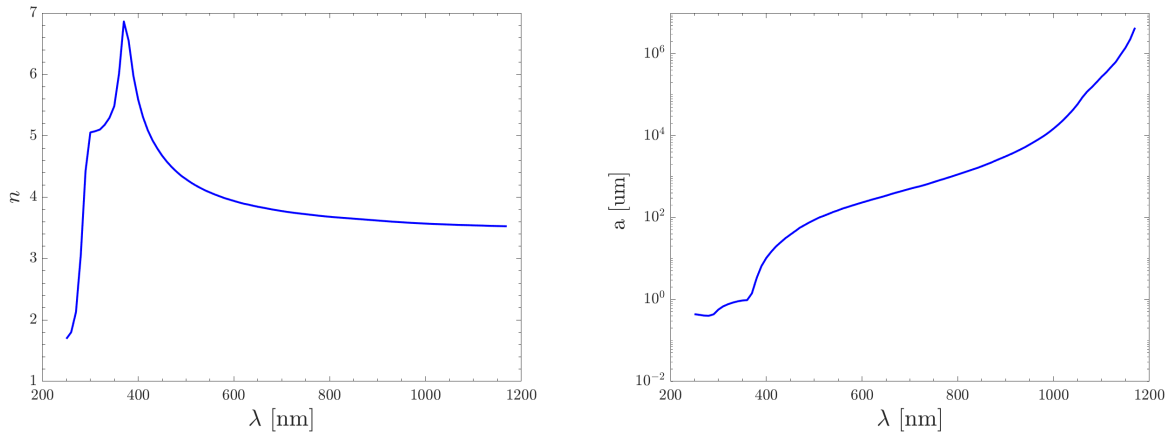

Figure 7.32: Evaluated Silicon optical for index of refraction (Left) and photon absorption length (Right), extracted from Ref. [12]. Note the dramatic increase in absorption length for photon wavelengths close to the band gap of Silicon, ∼1100 nm

We obtain experimentally evaluated optical data for Silicon from Ref. [12], with refraction index and photon absorption lengths shown in Fig 7.32. The key idea, when looking at the latter curve, is that low energy photons (long wavelengths) can travel a distance away from their origin and be absorbed *such that they would be spatially independent from the track that produced them.* Further, due to the high refractive index, Silicon has a small θ_{crit} ($= \sin^{-1}(1/n) \approx 16°$) for Total Internal Reflection whereby photons inside reflect off boundaries if their incidence angle is $> \theta_{crit}$, implying that photons can accumulate very long travel distances without escaping.

We first perform a back of the envelope calculation by looking at the output of Eq. 7.10, as seen in Fig. 7.33 Left. By integrating the differential spectrum for absorption lengths $>\sim$ 5 pix to ∼macroscopic dimension of a CCD, and then multiplying by the thickness of the

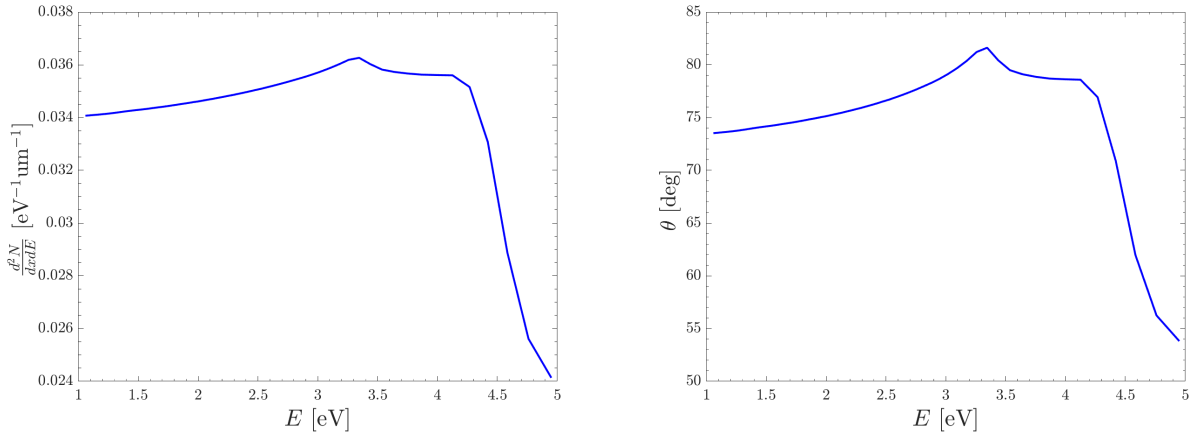

Figure 7.33: Right: Differential photon production Cherenkov radiation, computed using Eq. 7.10. Left: Emission angle of Cherenkov photons, θ_c with respect to travel direction of source muon, as a function of emitted photon energy.

device for path length, we get approx. 5 photons per muon track. This works out to a DC rate of $5{\times}20000/6000000 = 1.6 \times 10^{-2}$ e$^-$ pix^{-1} d^{-1}, which is in line with observed values from Sec. 7.6. To firm up this intuition and more robustly account for internal reflection we develop a toy Monte-Carlo to simulate muon and Cherenkov photon transport in a CCD, with an eye to characterizing the spread of events in the device.

Toy Monte-Carlo:

- We simulate a distribution of incident muons on the surface of a CCD detector with angular distribution given by Eq. 7.8, where we simplify the problem by assuming a constant energy profile ($\gamma = 40$), an assumption that is valid for atmospheric energies at better than a 1% level because of the β^{-2} scaling in Eq. 7.10.

- We transport the muon inside the Silicon via random draws from an exponential distribution with interaction rate parameter $l = \int_0^\infty d\omega \frac{d^2N}{d\omega dx} \mu\text{m}^{-1}$

- Thus at every transport step we create a Cherenkov photon with energy drawn from a PDF constructed from Fig. 7.33 Left, with corresponding emission angle from Fig. 7.33 Right, and a travel length drawn from an exponential distribution with absorption length parameter from Fig. 7.32 Right.

- We transport said photon in sub-micron steps until it is absorbed, reflected, or it escapes — depending on its interaction angle w.r.t θ_{crit}

- If the photon is able to travel its full length, we record the terminal pixel location (x_p,y_p) and its energy.

This process is succinctly represented in Fig. 7.34.

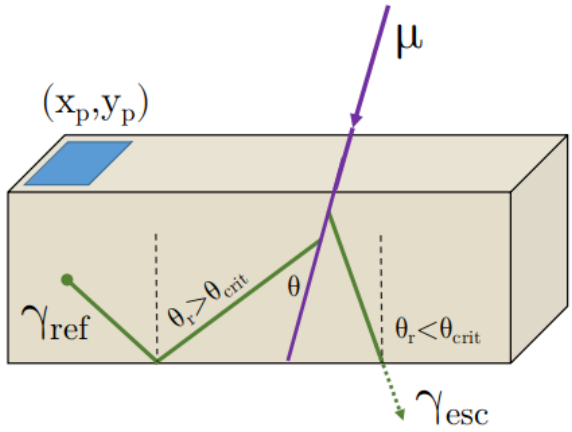

Figure 7.34: Representation of muon (purple) transport in the toy Monte-Carlo outlined in text. At selected intervals a photon (green) is released and either escapes or is reflected at the Silicon-vacuum interface. Upon absorption the pixel location (x_p,y_p) is recorded along with the deposited energy.

We can see what an example simulated track and the Cherenkov absorption of photons nearby in Fig. 7.35. The red pixels are those that contain charge from the photons that were radiatively released and potentially bounced around within the device. The simulation indicates that only about 8% of the photons produced are able to leave the CCD, strongly supporting the hypothesis that these might contribute towards an elevated background. Converting the absorbed event rate to leakage current we arrive at $\sim 0.055\,\mathrm{e^-\,pix^{-1}\,d^{-1}}$ which, while consistent with our observed event rate, is likely too high a value if even some of excess dark current is due to elevated temperature as previously discussed. Furthermore, if we look at the distribution of absorbed charge distances, as reported in Fig. 7.36, we notice that photons can travel for 100s of pixels away from their source track and that the shape of this distribution is not consistent with Fig. 7.15 Right. Nevertheless, such a background might play a role in the overall background level and might have to be mitigated by improved screening and shielding in future experiments. In sum, this hypothesis remains a promising avenue for exploration and current GEANT4 simulation work is ongoing within the collaboration.

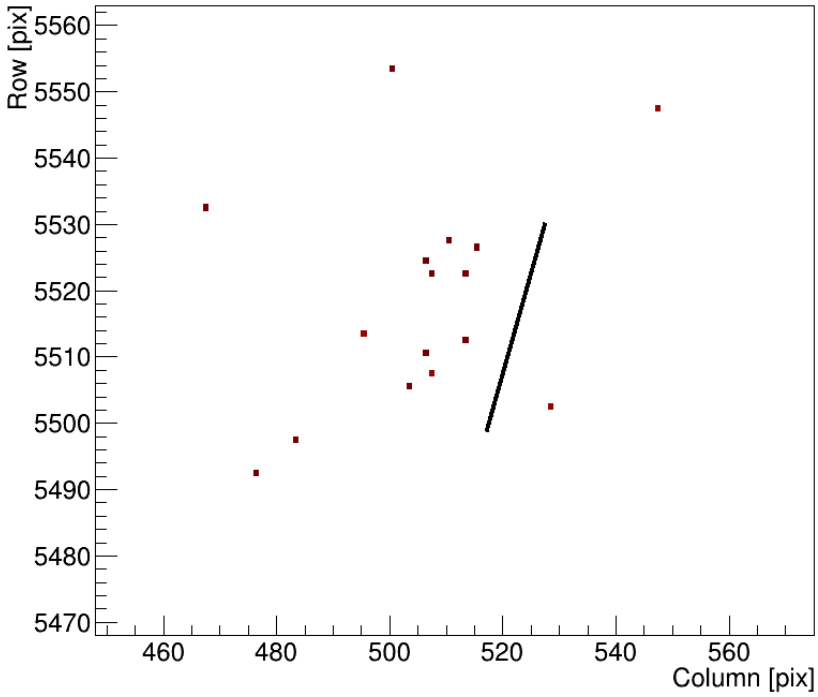

Figure 7.35: Simulation result, zoomed in around a muon track (black line) showing pixels that contain charge from Cherenkov photons absorbed within the media.

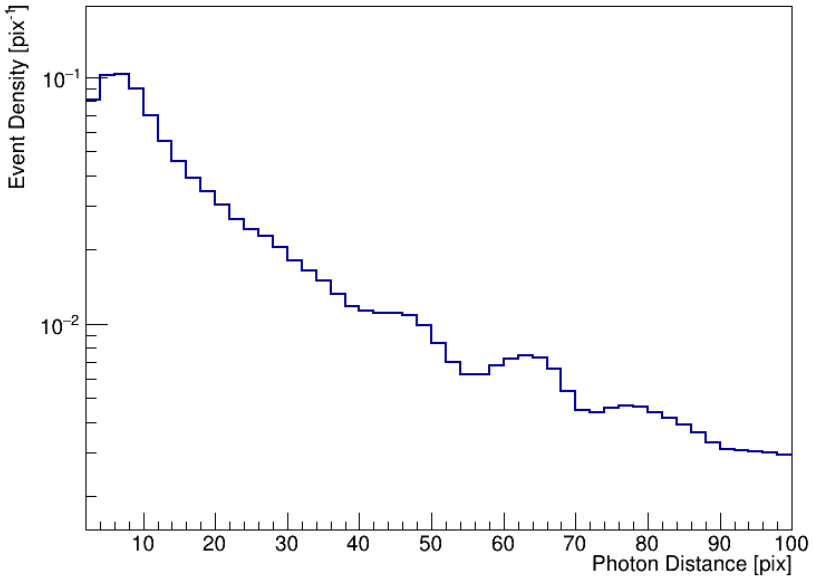

Figure 7.36: Photon density as a function of pixel distance of Cherenkov photons from the source muon track.

7.7.2 Transition Radiation

Transition radiation is the electromagnetic radiation emitted by a particle that traverses between 2 interfaces with different dielectric values. One can think of it as the homogenizing

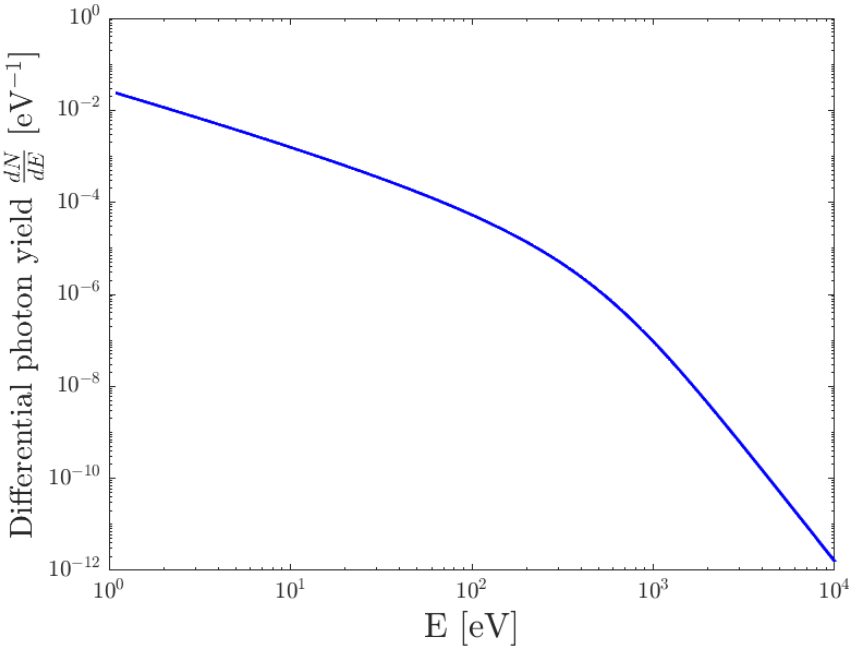

Figure 7.37: Differential yield of transition radiation, under the assumption of $\omega_p = 20$ eV showing logarithmic divergence at low energies and steep dropoff after a few hundred eV.

factor "shaken off" as EM radiation between the two independent solutions of Maxwell's equations for the transiting particle on either side of the boundary. The radiation is forward or backward beamed at an emission angle of $\theta \propto 1/\gamma$ and will arise in our setup from muons passing through the Copper box, and their subsequent entry and exit from the CCD itself. The differential rate for such radiation is derived in Ref. [13] and is:

$$\frac{dN}{d\omega} = \frac{\alpha}{\pi\omega}\left[(1+2\nu^2)\log\left(1+\frac{1}{\nu^2}\right) - 2\right] \tag{7.11}$$

where N is the radiation quanta emitted per interface, ω the energy of the emitted radiation, and $\nu \equiv \omega/(\gamma\omega_p)$ with ω_p being the plasmon energy of the material. Assuming $\omega_p = 20$ eV on average we get the differential spectrum shown in Fig. 7.37. Integrating the differential intensity, we get a total energy emitted per interface of 2 eV with a yield of $\langle N \rangle$=0.07 photons per track. Expressing this as a DC rate, assuming 3× crossings and perfect separation of these photons during clustering, we get 6.9×10^{-4} e$^-$ pix^{-1} d^{-1}, a value 2 orders of magnitude lower than the Cherenkov contribution. In addition, for the Lorentz factors discussed in this section, the emission angles are tight with only 1 pix separation after a 675um of travel suggesting difficulty in disambiguation of transition radiation photons from the bulk of the track.

7.7.3 Local Heating

Finally we consider the less plausible scenario of localized heating releasing long wavelength IR photons into the CCD through something like blackbody radiation. For the former case, suppose a generic particle interaction deposits energy E_0 in a region of length scale R. We suggest, following the work or Ref. [14], that the change in temperature T can be modeled as:

$$\frac{dE}{dT} \sim C(T) \approx c_0 R^3 \left(\frac{T}{T_D}\right)^2 \implies \Delta T = \left(\frac{3T_D^3 E_0}{c_0 \pi R^3}\right)^{1/4} \tag{7.12}$$

where $c_0 = 1.63$ J cm^{-3} K is the volume-specific heat capacity for Silicon and T_D is a temperature scale for the assumed cubic dependence at initially cryogenic temperatures, taken here to be the material Debye temperature of 650K. Computing out this curve for a range of energy deposits, under the assumption that R is pointlike at $\mathcal{O}(1$ nm) we can then work out the blackbody emittance $j = \sigma T^4$ (energy per area) where σ is the Stefan-Boltzmann constant. Accounting for cooling via thermal diffusivity, we model the lifetime of the hot region as $\tau \sim R^2/\alpha$ with $\alpha = 0.8$ cm^2 s^{-1} for Silicon. Putting these concepts together we get the result of Fig. 7.38. Casting this in the framework of muon interactions, we can immediately see from the (Left) plot that the total energy emitted, per interaction of the muon, is $\ll$ eV for deposits in the eV to MeV range and thus an unlikely contributor to any elevated event rate in the detector. We can refine this intuition by noting that absorbable peak wavelengths (Middle) occur only for energies greater than a keV, and finally (Right) that the expected number of photons for an entire track is < 1 even if we preferentially deposited $\mathcal{O}$(keV) per interaction. In sum, this channel is highly unlikely to contribute to our observed excess.

There might be an alternate channel, such as a phonon-photon coupling that produces similar IR photons. We do know from the discrepancy in the band-gap of Silicon (1.1 eV) and the ionization energy (3.7 eV) that the dominant down-conversion mode of any energy deposit is in the emission of optical phonons (63 meV). We leave to the literature and future work to explore couplings of this form.

7.8 Future science capabilities with a Skipper CCD

While we have not presented any new science results from using these Skipper CCDs, hopefully this chapter has demonstrated the impressive nature of the devices. We will close out

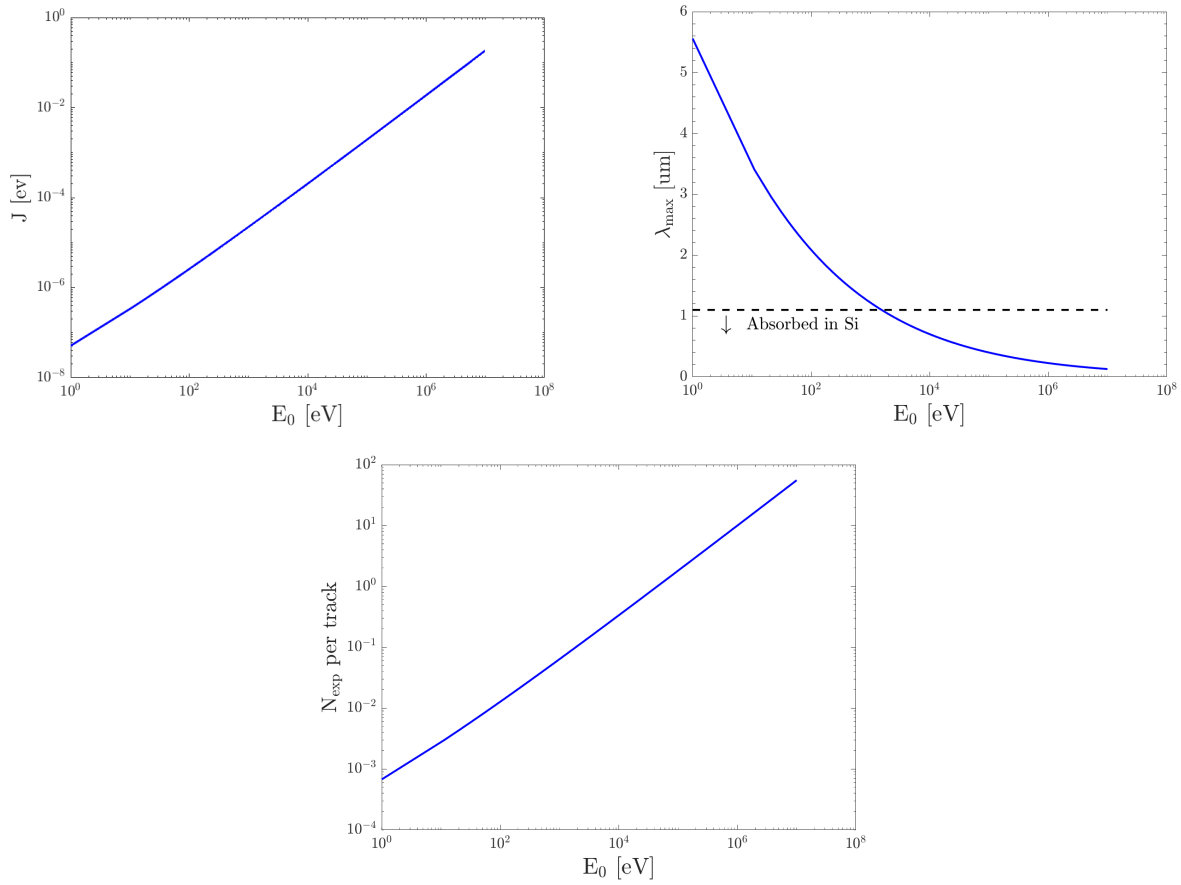

Figure 7.38: Left: energy radiated J, assuming Stefan-Boltzmann blackbody properties for a nm-scale pointlike deposit, for a given deposit energy E_0. Right: Peak wavelength of emitted radiation; note that only wavelengths less than 1.1 um are able to be absorbed. Bottom: Expected number of emitted photons, assuming constant energy deposition E_0 for a muon interaction rate of $4\,\mu\text{m}^{-1}$ over a 675 μm thick travel distance.

our discussion by highlighting two campaigns to utilize Skippers, one under construction and the other proposed.

DAMIC-M: As introduced in Chap. 2, DAMIC-M experiment will be located in Modane, France and be comprised of a stack of 50 Skipper CCDs for a total mass of approx. 1 kg. The experiment can be visualized in Fig. 7.39 Left, along with projections for achievable world leading constraints on electron recoil Dark Matter. The assumption of a leakage current in line with the SNOLAB experiment is highly achievable, especially given the findings of this chapter. The deep underground location of the device will fully mitigate any background by cosmogenic MIPs, while the care taken in dealing with radioactive contamination to the level of 0.1 dru should furthermore fully mitigate any leakage current

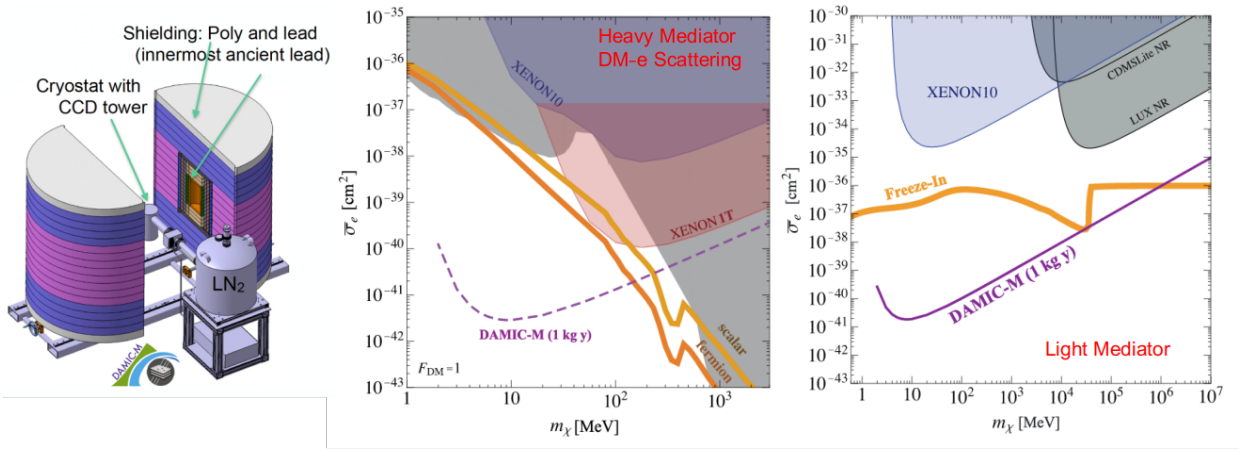

Figure 7.39: Left: Visualization of the proposed DAMIC-M experiment, currently funded for construction and operation. Right: Projections for constraints on Dark Matter electron scattering by the DAMIC-M experiment, assuming 1 kg yr of exposure, backgrounds of 0.1 dru and a leakage current in line with the SNOLAB experiment. Plots taken from Ref. [15].

caused by radiogenic electrons. Thermal concerns will hopefully be resolved by improved cryogenic systems under consideration, including LN_2 cooling and improved cryo-coolers.

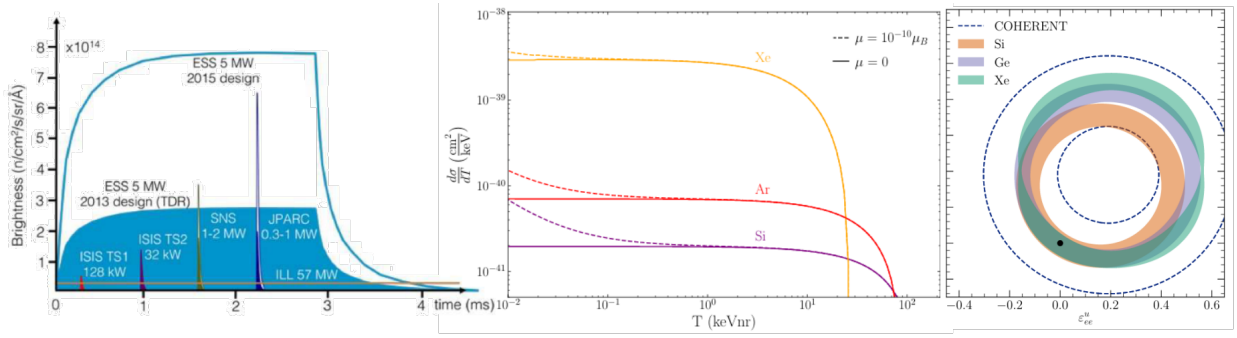

Figure 7.40: Left: Neutron brightness of the European Spallation Source as compared to currently operational beams. Middle: Expected differential energy spectrum for a non-negligible neutrino magnetic moment, with Silicon target rates shown in purple. Right: Beyond Standard Model physics phase space for two parameters that might be non-zero, with probe-able regions for Silicon outlined in orange.

European Spallation Source (ESS): The ESS is a forthcoming pulsed neutron beam in Sweden that will generate a significant increase in neutron brightness (see Fig. 7.40 Left), and concurrently in neutrino yield (from proton spallation byproduct pion decay). As Baxter et al. [16] lay out, these intense high energy ($\mathcal{O}$)(MeV) pulsed neutrinos can be interrogated by a Skipper CCD setup to measure important parameters like the weak-mixing angle or to answer beyond Standard Model questions like whether neutrinos have a non-negligible

magnetic moment (see Fig. 7.40 Right). With a first light of 2022, Skipper CCDs may prove to be invaluable detectors in this campaign with their sub-electron resolution. The biggest roadblock will be reading out the CCDs in concert with the rapid 14 Hz pulsed beam. This would require an entire CCD to be read out in just under 35 ms if we wanted to capture full results during the pulse dead-time. In the best case scenario to achieve useful single electron resolution we estimate needing about 100 skips, and even with 4 amplifiers reading out separate portions of a 4k x 4k image, a *single pixel read* would have to be done in a fraction of a nanosecond — impossible under even the most optimistic scenarios. The solutions are as diverse as instrumenting CCDs with more amplifiers or reading out integrated exposures over many pulses, with considerations ongoing.

References

[1] James R Janesick, Tom S Elliott, Arsham Dingiziam, Richard A Bredthauer, Charles E Chandler, James A Westphal, and James E Gunn. New advancements in charge-coupled device technology: subelectron noise and 4096 x 4096 pixel ccds. In *Charge-Coupled Devices and Solid State Optical Sensors*, volume 1242, pages 223–237. International Society for Optics and Photonics, 1990.

[2] Charles E Chandler, Richard A Bredthauer, James R Janesick, and James A Westphal. Sub-electron noise charge-coupled devices. In *Charge-Coupled Devices and Solid State Optical Sensors*, volume 1242, pages 238–251. International Society for Optics and Photonics, 1990.

[3] Shuopei Wang, Congli He, Jian Tang, Xiaobo Lu, Cheng Shen, Hua Yu, Luojun Du, Jiafang Li, Rong Yang, Dongxia Shi, et al. New floating gate memory with excellent retention characteristics. *Advanced Electronic Materials*, 5(4):1800726, 2019.

[4] S Haque, F Dion, R Frost, R Groulx, SE Holland, A Karcher, WF Kolbe, NA Roe, G Wang, and Y Yu. Design of low-noise output amplifiers for p-channel charge-coupled devices fabricated on high-resistivity silicon. In *Sensors, Cameras, and Systems for Industrial and Scientific Applications XIII*, volume 8298, page 82980X. International Society for Optics and Photonics, 2012.

[5] Jing Zhou. *Direct dark matter detection with the DAMIC experiment at SNOLAB*. PhD thesis, The University of Chicago, 2015.

[6] Robert W Leach and Frank J Low. Ccd and ir array controllers. In *Optical and IR Telescope Instrumentation and Detectors*, volume 4008, pages 337–343. International Society for Optics and Photonics, 2000.

[7] C Bebek. 4k x 2k and 4k x 4k ccd technical manual. *LBNL*, 2007.

[8] SM Tulloch and VS Dhillon. On the use of electron-multiplying ccds for astronomical spectroscopy. *Monthly Notices of the Royal Astronomical Society*, 411(1):211–225, 2011.

[9] James R Janesick. *Scientific charge-coupled devices*, volume 83. SPIE press, 2001.

[10] Stephen E Holland, Chris J Bebek, Kyle S Dawson, JH Emes, Max H Fabricius, Jessaym A Fairfield, Don E Groom, A Karcher, William F Kolbe, Nick P Palaio, et al. High-voltage-compatable fully depleted ccds. In *High Energy, Optical, and Infrared Detectors for Astronomy II*, volume 6276, page 62760B. International Society for Optics and Photonics, 2006.

[11] M. Tanabashi et al. Review of particle physics. *Phys. Rev. D*, 98:030001, Aug 2018. doi: 10.1103/PhysRevD.98.030001. URL `https://link.aps.org/doi/10.1103/PhysRevD.98.030001`.

[12] Martin A Green and Mark J Keevers. Optical properties of intrinsic silicon at 300 k. *Progress in Photovoltaics: Research and applications*, 3(3):189–192, 1995.

[13] John David Jackson. *Classical electrodynamics*. John Wiley & Sons, 2007.

[14] Philip C. Bunting, Giorgio Gratta, Tom Melia, and Surjeet Rajendran. Magnetic bubble chambers and sub-gev dark matter direct detection. *Phys. Rev. D*, 95:095001, May 2017. doi: 10.1103/PhysRevD.95.095001. URL `https://link.aps.org/doi/10.1103/PhysRevD.95.095001`.

[15] Mariangela Settimo. Search for low-mass dark matter with the damic experiment. *arXiv preprint arXiv:2003.09497*, 2020.

[16] D Baxter, JI Collar, P Coloma, CE Dahl, I Esteban, P Ferrario, JJ Gomez-Cadenas, MC Gonzalez-Garcia, ARL Kavner, CM Lewis, et al. Coherent elastic neutrino-nucleus scattering at the european spallation source. *Journal of High Energy Physics*, 2020(2): 1–38, 2020.

CONCLUSION

This work represents a deep-dive into developing and using scientific grade CCDs, under the umbrella of the DAMIC experiment, with an eye towards understanding detector response when searching for very low energy signals from light dark matter.

Using a setup at the University of Chicago we investigated one of the dominant sources of background in solid state detectors — that of small-angle Compton scattered γ-rays, with particular interest in what happens below a few hundred eV. By exposing a CCD to ^{241}Am and ^{57}Co radioactive sources, we identified and characterized several theoretically motivated, but heretofore unobserved, step-like structural features of Compton scattering and validated the results with an MCNP simulation. We parametrized these features between 60 eV and 4 keV and reported the parameter evolution as a function of γ-ray energy. The model, based on a modified Impulse Approximation, however fails to describe the data for energies $<$0.2 keV with a lower-than-measured softening of the L-step. This discrepancy highlights the need for future precise experimental studies to both confirm and characterize the deviation. Our results are directly applicable to any dark matter search that employs silicon detectors.

Next we explored the microphysics of ionization and charge yield production in a silicon detector by appealing to well-measured laboratory data after a thorough literature review. We constructed and fitted a Monte-Carlo based ionization response model, combining impact ionization and a very simplified model of silicon band structure, valid between $\sim$1.2–8 eV and further motivated an extension into the UV-gap (12-50 eV) in which there are no current measurements. We provided ionization probability curves p_n and argued that these are more appropriate than just a single calibration constant and Fano factor when evaluating the response of a detector material.

We then extended the reach of the DAMIC experiment into constraining hidden photon dark matter and light dark matter recoiling off electrons by using the novel idea of interpreting leakage current in the detector as coming from a flux of light dark matter particles. We constructed models of the leakage current and other noise sources and traded these against LDM models derived from literature. In addition to reporting the lowest measured leakage current in a silicon device ($4 \times 10^{-22}\,\mathrm{A\,cm^{-2}}$) we established the best direct-detection limits on dark matter-electron scattering between 0.6 and 100 MeV c^{-2} and hidden photon dark matter with masses in the range 1.2–9 eV c^{-2}. This generic methodology can be extended to any particle, for instance even a flux of very light WIMPs, with the only issue being the reduced sensitivity versus a conventional approach.

Finally, we discussed Skipper CCDs and reported on R&D progress at the University of Chicago in deploying these novel devices for future science goals. We demonstrated their

impressive $0.07\,\mathrm{e}^-$ charge resolution and delved into some current operational limitations, particularly their high leakage current (up to $10^{-19}\,\mathrm{A\,cm}^{-2}$) compared to SNOLAB devices. We presented plausible mechanisms for this elevated charge (e.g. temperature effects or external cosmic radiation) and validated these ideas either through experimental measurements or by simulation.

In sum, this thesis sits at an inflection point between maximizing the scientific output of conventional CCDs and exploring the unique capabilities of next generation devices. Regardless, the issues discussed will remain strongly relevant since the impact of radiogenic backgrounds, accurate charge yield measurements, and reducing leakage current will only grow in importance as direct-detection experiments push down the energy scale.